



12-2017

Advanced Focused Beam-Induced Processing for Nanoscale Synthesis and 2D Materials Device Architectures

Michael Garrison Stanford

University of Tennessee, mstanfo3@vols.utk.edu

Follow this and additional works at: https://trace.tennessee.edu/utk_graddiss

Recommended Citation

Stanford, Michael Garrison, "Advanced Focused Beam-Induced Processing for Nanoscale Synthesis and 2D Materials Device Architectures. " PhD diss., University of Tennessee, 2017.
https://trace.tennessee.edu/utk_graddiss/4815

This Dissertation is brought to you for free and open access by the Graduate School at TRACE: Tennessee Research and Creative Exchange. It has been accepted for inclusion in Doctoral Dissertations by an authorized administrator of TRACE: Tennessee Research and Creative Exchange. For more information, please contact trace@utk.edu.

To the Graduate Council:

I am submitting herewith a dissertation written by Michael Garrison Stanford entitled "Advanced Focused Beam-Induced Processing for Nanoscale Synthesis and 2D Materials Device Architectures." I have examined the final electronic copy of this dissertation for form and content and recommend that it be accepted in partial fulfillment of the requirements for the degree of Doctor of Philosophy, with a major in Materials Science and Engineering.

Philip D. Rack, Major Professor

We have read this dissertation and recommend its acceptance:

Jason D. Fowlkes, David G. Mandrus, Thomas Z. Ward

Accepted for the Council:

Dixie L. Thompson

Vice Provost and Dean of the Graduate School

(Original signatures are on file with official student records.)

**Advanced Focused Beam-Induced Processing for Nanoscale Synthesis and 2D
Materials Device Architectures**

**A Dissertation Presented for the
Doctor of Philosophy
Degree
The University of Tennessee, Knoxville**

**Michael Garrison Stanford
December 2017**

Copyright © 2017 by Michael Garrison Stanford.
All rights reserved.

ACKNOWLEDGEMENTS

All work presented in this dissertation was a collaborative effort between an innumerable amount of people, some of which contributed through personal support rather than research. I would first like to thank my wife, Kathleen, for providing love, support, and understanding which made the completion of research much easier. I also thank my parents (and in-laws) for support and love which has guided me along the way and shaped my life. Thank you also to my siblings, Russell, Allison, and Alan who have also been influential as well as close friends.

Of course, all of my work has been strongly influenced by my research advisor and co-workers. A special thanks is owed to my advisor and friend Dr. Philip Rack for his guidance throughout my graduate studies. I couldn't have asked for a better mentor in research, career advice, or life decisions. Dr. Jason Fowlkes has also been an excellent friend and mentor during my graduate studies. Dr. Rack and Dr. Fowlkes have provided excellent models for young researchers, such as myself, to emulate. I also would like to thank all of the students, postdocs, and research professors whom I have collaborated with and shared many fun times with. I especially acknowledge Brett Lewis and Kyle Mahady who are not only excellent research collaborators, but great friends as well.

I thank the University of Tennessee and the Department of Materials Science and Engineering for providing an excellent academic and research environment for motivated students to excel. I also owe acknowledgement to the Center for Nanophase Materials Sciences at Oak Ridge National Laboratory. Much of my research was conducted at this facility and would not have been possible without their excellent staff and scientists.

Finally, I would like to thank my doctoral committee members: Dr. Philip Rack, Dr. Jason Fowlkes, Dr. David Mandrus, and Dr. Zac Ward. You have been valuable mentors and research collaborators during my graduate studies.

ABSTRACT

Nanofabrication has come to prominence over recent years due to miniaturization of electronic devices as well as interesting physical phenomena that arise in material systems at the nanoscale. Particle beam induced processing enables additive as well as subtractive nanoprocessing techniques. Focused beam induced processing facilitates direct-write processing, thus making it a common technique for fabrication and synthesis on the nanoscale and is typically carried out with charged particles such as electrons or ion species, each of which offer distinct capabilities. This dissertation addresses several challenges which currently plague the focused beam-induced processing community and explores novel applications.

Chapter I explores laser based purification strategies for electron beam induced deposition. This addresses the challenge of material purity, which currently limits broader application of the nanofabrication technique. Chapter II covers advanced helium ion beam induced processing using a Gas Field Ionization source. This chapter explores novel applications for the helium ion beam as well as the mitigation of helium-induced subsurface damage, which currently prevents ubiquitous adoption of the helium ion microscope as a nanofabrication tool. Chapter III studies defect introduction in 2D materials under helium ion irradiation, which proves to be an ideal nanoprocessing application for the helium ion beam.

TABLE OF CONTENTS

INTRODUCTION	1
Electron Beam-Induced Processing	2
Ion Beam-Induced Processing	3
Helium Ion Beam Processing.....	4
CHAPTER I Laser based purification of electron beam induced deposits.....	5
1.1 Purification of Nanoscale Electron Beam Induced Platinum Deposits via Pulsed Laser Induced Oxidation Reaction	6
1.1.1 Abstract.....	6
1.1.2 Introduction.....	6
1.1.3 Results and Discussion	8
1.1.4 Conclusions.....	12
1.1.5 Methods.....	13
1.1.6 Appendix.....	15
1.1.6.1 Supporting Information.....	15
1.1.6.2 Figures.....	25
1.1.6.3 Tables.....	41
1.2 Inert Gas Enhanced Laser-Assisted Purification of Platinum Electron-Beam-Induced Deposits.....	42
1.2.1 Abstract.....	42
1.2.2 Introduction.....	43
1.2.3 Results and Discussion	45
1.2.4 Conclusions.....	52
1.2.5 Methods.....	53
1.2.5.1 Electron-Beam-Induced Deposition.....	53
1.2.5.2 Pulsed Laser Reactive Gas Anneal	53
1.2.5.3 Reactive Laser Assisted Electron-Beam-Induced Deposition	54
1.2.5.4 Sequential or Layer-by-Layer EBID Plus Laser Reactive Gas Anneal	54
1.2.5.5 Energy Dispersive Spectroscopy (EDS) Analysis	55
1.2.6 Appendix.....	57
1.2.6.1 Supporting Information.....	57
1.2.6.2 Figures.....	60
1.2.6.3 Tables.....	73
CHAPTER II Advanced ion beam induced processing using a Gas Field Ionization source	74
2.1 In situ Mitigation of Sub-Surface and Peripheral Focused Ion Beam Damage via Simultaneous Pulsed Laser Heating.....	75
2.1.1 Abstract.....	75
2.1.2 Introduction.....	76
2.1.3 Results and Discussion	78
2.1.4 Conclusions.....	83
2.1.5 Methods.....	84
2.1.5.1 Synchronized Laser Probe	84

2.1.5.2 Helium Ion Microscope/Patterning.....	85
2.1.5.3 TEM Preparation and Imaging.....	85
2.1.5.4 Simulations	85
2.1.5.5 Raman Spectroscopy of Graphene.....	86
2.1.6 Appendix.....	87
2.1.6.1 Supporting Information.....	87
2.1.6.2 Figures.....	92
2.1.6.3 Tables.....	104
2.2 Laser Assisted Focused He ⁺ Ion Beam Induced Etching with and without XeF ₂ Gas Assist	
.....	106
2.2.1 Abstract.....	106
2.2.2 Introduction.....	107
2.2.3 Results and Discussion	109
2.2.4 Conclusions.....	114
2.2.5 Methods.....	115
2.2.5.1 Helium Ion Beam.....	115
2.2.5.2 Gas Injection System	115
2.2.5.3 Laser Delivery System.....	115
2.2.5.4 Monte Carlo Simulation.....	116
2.2.6 Appendix.....	117
2.2.6.1 Supporting Information.....	117
2.2.6.2 Figures.....	121
2.2.6.3 Tables.....	131
2.3 Tungsten Diselenide Patterning and Nanoribbon Formation by Gas-Assisted Focused Helium Ion Beam Induced Etching.....	133
2.3.1 Abstract.....	133
2.3.2 Introduction.....	134
2.3.3 Results and Discussion	135
2.3.4 Conclusions.....	143
2.3.5 Methods.....	143
2.3.5.1 Focused Ion Beam Induced Etching	143
2.3.5.2 Visual Endpoint Monitoring	144
2.3.5.3 WSe ₂ Field Effect Transistor Device Fabrication	145
2.3.5.4 Raman Measurements.....	145
2.3.5.5 STEM Imaging.....	145
2.3.5.6 Monte Carlo Damage Simulations.....	146
2.3.6 Appendix.....	147
2.3.6.1 Supporting Information.....	147
2.3.6.2 Figures.....	148
2.3.6.3 Tables.....	161
CHAPTER III Tunable material properties via Defect engineering in 2D materials by ion beam irradiation.....	162
3.1 Focused Helium-Ion Beam Irradiation Effects on Electrical Transport Properties of Few-Layer WSe ₂ : Enabling Nanoscale Direct Write Homo-junctions	163

3.1.1 Abstract	163
3.1.2 Introduction	164
3.1.3 Results and Discussion	165
3.1.4 Conclusions	171
3.1.5 Methods	172
3.1.5.1 Helium Ion Irradiation	172
3.1.5.2 WSe ₂ Device Fabrication and Characterization	172
3.1.5.3 Raman Spectroscopy	173
3.1.5.4 Energy Dispersive X-ray Spectroscopy	173
3.1.5.5 Microscopy	173
3.1.6 Appendix	174
3.1.6.1 Supporting Information	174
3.1.6.2 Figures	177
3.1.6.3 Tables	195
3.2 High Conduction Hopping Behavior Induced in Transition Metal Dichalcogenides by Percolating Defect Networks: Toward Atomically Thin Circuits	196
3.2.1 Abstract	196
3.2.2 Introduction	197
3.2.3 Results and Discussion	198
3.2.4 Conclusions	204
3.2.5 Methods	205
3.2.5.1 Material Synthesis	205
3.2.5.2 Helium Ion Irradiation	205
3.2.5.3 Raman and Photoluminescence	205
3.2.5.4 Device Fabrication	206
3.2.5.5 Scanning Transmission Electron Microscope Imaging	206
3.2.5.6 STEM Image K-Means Cluster Analysis	206
3.2.5.7 Density Functional Theory	206
3.2.6 Appendix	208
3.2.6.1 Supporting Information	208
3.2.6.2 Figures	210
CONCLUSION	220
LIST OF REFERENCES	221
APPENDIX	246
List of Publications	247
VITA	250

LIST OF TABLES

Table 1. Various parameters used in the thermal simulation emulating PtC ₅ heating as well as parameters relevant to the simulation of electric field propagation and absorption in the Pt/PtC ₅ /SiO ₂ /Si multi-layers.....	41
Table 2. Details and parameters of various LAEBID patterns.	73
Table 3. Relevant parameters for He ⁺ and Ne ⁺ exposures as well as pulsed laser parameters. ..	104
Table 4. Relevant parameters for simulation of laser heating on a silicon substrate.....	105
Table 5. Estimated XeF ₂ and He ⁺ parameters for FIBIE processes at varies He ⁺ dwell times. All patterning was conducted with a 25keV He ⁺ beam and a 0.25 nm pixel pitch.....	131
Table 6. Material and laser parameters for the thermal simulations.....	132
Table 7. Estimated XeF ₂ and He ⁺ parameters for FIBIE processes with 30 μs and 100 ns dwell times with a 0.25 nm pixel pitch and for a FIBIE process with a 100 ns dwell time and a 4.0 nm pixel pitch.	161
Table 8. the doses required to etch through the WSe ₂ and SiO ₂ at various dwell times. These values were extracted by analysis of the VEM as well as correlation with recorded videos of the etch process.	161
Table 9. Raman peak assignments of few-layer WSe ₂	195
Table 10. EnvizION Monte Carlo simulation sputter yields and Se/W sputter ratio for WSe ₂ of varying thicknesses.	195

LIST OF FIGURES

Figure 1. (a) EBID: the nonvolatile dissociation products form the deposit growing coaxially into the beam. Volatile fragments are pumped away. (b) EBIE: the surface adsorbed molecules dissociate under electron impact into reactive species and react to volatile compounds with the substrate material. Reprinted with permission from Ref ⁴ . Copyright 2008, American Vacuum Society.	3
Figure 2. (a) Schematic of the laser annealing setup with approximately 100 μm laser spot size under O_2 flow. (b) EDS measurements of a ~ 140 nm thick PtC_5 EBID deposit annealed with 100 μs pulses at 0.1% duty cycle as a function of exposure times. (c) Images of laser annealed patterns at different exposure times. The deposit annealed for 0.1s exposure time was also cross-sectioned and pictured here.	25
Figure 3. (a) Carbon content as a function of exposure time (duty cycle \times process time, bottom axis) and process time (top axis) for 1 μs at 1% duty cycle, (b) 10 μs at 1% duty cycle, and (c) 100 μs at 0.1% duty cycle. Initial pad thicknesses were ~ 80 , 140, 260, and 350 nm thick, respectively.	26
Figure 4. Scanning electron images of PtC_5 deposits of varying thicknesses and anneal pulse widths that were annealed for 0.1 s of laser exposure time.	27
Figure 5. (a) Time-temperature thermal profile for deposits of varying thickness (inset) irradiated with a 100 μs laser pulse. (b) Simulated thermal profiles of deposit surface as a function of pure platinum top layer thickness (which represents purification) for a deposit which was initially 360 nm prior to annealing. Inset figure displays the maximum temperature at the deposit surface as a function of Pt top layer thickness and original deposit thickness.	28
Figure 6. (a) Cross-section SEM images (at 52°) of a 360 nm thick PtC_5 deposit annealed at 10 μs pulse width, 1.0% duty cycle conditions at various exposure times (exposure times and superimposed edge positions are inset in images). (b) Purification depth as a function of exposure time for 1, 10, and 100 μs pulse width laser conditions with superimposed penetration depth of pure Pt (dotted line).	29
Figure 7. EDS spectra for ~ 80 nm thick (1000 pass) PtC_5 deposit annealed for 60 s process time with 100 μs , 0.1% DC conditions with and without O_2 flux.	30
Figure 8. EDS spectra of $\sim \text{PtC}_5$ deposit grown with 2000 electron passes (originally ~ 140 nm) deposits purified with (a) 1 μs , 1% duty cycle, (b) 10 μs , 1% duty cycle, (c) 100 μs , 0.1% duty cycle laser conditions at varying exposure times.	30
Figure 9. Purification rates as a function of exposure time for deposits with different initial thickness (80 nm, 140 nm, 260 nm, 360 nm for the 1000, 2000, 4000, and 8000 pass deposits, respectively) for (a) 1 μs 1% duty cycle, and (b) 10 μs 1% duty cycle conditions.	31
Figure 10. Scanning electron micrographs of PtC_5 line patterns annealed with 1 μs at 1% duty cycle, 10 μs at 1% duty cycle, and 100 μs at 0.1% duty cycle laser conditions at different exposure times. Lines have different initial thicknesses (50, 70, 95, and 150 nm increasing from left to right).	32
Figure 11. (a) 3D schematic of the computational simulation domain in r - z coordinates. The simulation domain consists of both cylindrical and annular disk volume elements. (b) The	

primary mesh in the simulation domain is defined by the solid yellow grid points. Temperature estimates are reported in the final simulation results at these points. In addition, each mesh point has uniquely defined materials parameters including density, heat capacity, thermal conductivity and optical properties such as the real (n) and imaginary (κ) indices of refraction. The volume element for each mesh node is defined by the surrounding midway points (open yellow circles) located between adjacent mesh nodes in both the (r) and (z) dimensions. Distinct volume elements are indicated by the alternating shades of blue in the panel. (c) The index system shown in the magnified schematic of the simulation domain refers to the (radial,depth) coordinates, respectively. Heat flux balances are calculated at mesh interfaces in order to account for variable material properties in the spatial coordinate and those locations are indicated by fractional indices. 33

Figure 12. Thin film stack optical properties calculated by Rouard's method¹. The title included for both panels (a) and (b) indicates the topmost film-to-substrate in order of left-to-right. (a) The reflectivity of the PtC₅ surface as a function of the PtC₅ film thickness, the transmission through the 100nm SiO₂ film, and the total absorption in the stack are shown. (b) The reflectivity of the PtC₅ surface as a function of buried Pt film thickness, the transmission through the 100nm SiO₂ film, and the total absorption in the stack are shown. 34

Figure 13. Electric field distribution in the thin film stack structure at an arbitrary time. The real component of the electric field (blue) is provided along with the imaginary component (black). The film widths were 915nm (vacuum), 80nm (PtC₅), 20nm (Pt), 100nm (SiO₂) and 500nm (Si). 35

Figure 14. The laser irradiance (intensity) in the thin film stack structure normalized to the incident intensity. The blue curve shows the results for the 80nmPtC₅/ 10nmPt/ 100nmSiO₂/ Si substrate stack. The dotted line is provided for reference and shows the intensity for the same stack but ignoring interface reflections. Reflections from the PtC₅/Pt and Pt/SiO₂ interfaces lead to enhanced absorption in the PtC₅ and Pt films, respectively, as is evident by comparing the solid and dotted blue curves; the intensity drop across these films is larger when considering these reflections. The red intensity profile shows the case for light propagating through an 80nmPtC₅/ 20nmPt/ 100nmSiO₂/ Si substrate stack. For this case, less light is reflected at the initial, vacuum-PtC₅ interface. Yet, the absorption of light in the PtC₅ is greater because the reflectivity at the PtC₅/Pt interface is larger for the thicker, 20nm buried Pt layer, relative to the 10nm layer. 36

Figure 15. Simulated thermal profiles at the deposit surface as a function of pure platinum top layer thickness (which is intended to emulate the deposit composition at various stages of purification). Underlying PtC₅ thicknesses are shown in light gray. Care was taken to conserve the total Pt atomic content in order to capture the expected contraction of the deposit with increasing pure Pt layer thickness. For example, the loss of carbon in the top layer as well as the density change between PtC₅ and Pt were accounted for. 37

Figure 16. (a) Schematic of optical coupling in which PtC₅ is deposited half-on an underlying pure Pt layer. Images of PtC₅ deposits annealed for 30 s which demonstrates optical coupling to the underlying Pt layer of varying thicknesses. (b) 5 nm, (c) 10 nm, (d) 20 nm. (e) Image of PtC₅ deposit annealed under same condition on SiO₂ substrate. 38

Figure 17. (a) Image and EDS spectra of preferentially cured deposit. Region 1 is the area in which the PtC ₅ overlaps the underlying Pt substrate. Region 2 is the area in which the PtC ₅ deposit lies directly on top of SiO ₂ . (b) Simulated thermal profiles of laser anneal for various deposit thicknesses as a function of laser pulse time. Threshold temperature is denoted in plot (dotted line). (c) Fraction of time above the threshold temperature for an 80 nm PtC ₅ deposit as a function of pure Pt under-layer thickness.	39
Figure 18. Scanning electron images of PtC ₅ patterns annealed with 1 μ s at 1% duty cycle, 10 μ s at 1% duty cycle, and 100 μ s at 0.1% duty cycle laser conditions and then cross-sectioned. Times listed are laser exposure time during the anneal.	40
Figure 19. Schematic of the (a) EBID + pulsed laser reactive gas anneal, (b) reactive laser assisted electron-beam-induced deposition, and (c) sequential or layer-by-layer EBID plus laser reactive gas anneal purification processes.	60
Figure 20. Schematic of deposition and annealing experimental setup from (a) tilted and (b) plan view. The laser delivery system, focused electron beam, precursor GIS, and reactive gas GIS converge to a single point. During reactive LAEBID processes the precursor GIS needle is in the “retracted” position (dotted red line) which is withdrawn to ~8 cm vertically and ~5 cm horizontally from the point of interest to reduce precursor flux at the substrate. During the sequential deposition plus annealing process the needles are configured in the as-shown inserted states.	61
Figure 21. (a) EDS spectra of Pt EBID deposits which were annealed with 10 μ s and 1% duty cycle laser conditions for a cumulative laser exposure time of 0.3 s. Spectra shown include an as-deposited pattern, a deposit anneal under chamber ambiance, and a deposit annealed under localized Ar gas flow. (b) RGA spectra showing the residual chamber gas species present as well as during Ar flow.	62
Figure 22. (a) Carbon content, from EDS measurements, as a function of laser exposure time (duty cycle x processing time, bottom axis) and processing time (top axis) for 10 μ s at 1% laser duty cycle. The deposit thicknesses were approximately 240 nm, 90 nm, 50 nm, 25 nm which correspond to 8000, 4000, 2000, and 1000 passes, respectively. Normalized carbon content of 1, is that of a standard PtC ₅ EBID deposit. (b) SEM images of an annealed deposit that was initially ~ 90 nm as-deposited. Inset time reflects the total laser exposure time for each anneal.	63
Figure 23. (a) SEM cross section images of deposits annealed with reactive gas for 0.2 s and 1.5 s of total laser exposure time. (b) Purification thickness from an originally ~ 240 nm thick PtC ₅ deposit as a function of pulsed laser exposure time for a 10 μ s, 1% duty cycle anneal while under Ar gas flow. Inset figure shows the plot and linear regression of purification thickness squared versus time which is consistent with a diffusion limited purification regime.	64
Figure 24. (a) SEM tilt image of a typical laser assisted electron beam induced deposition (LAEBID) pattern deposited with co-flow of hydrogen reactive gas. Specifically, this deposit was created 100 μ s and 0.1% duty cycle laser conditions. The electron beam and gas conditions were as listed in the experimental details. (b) SEM image of a LAEBID pattern deposited with 100 μ s and 0.5% duty cycle laser conditions, which shows contribution from LCVD. The deposit retains shape with high fidelity. (c) Comparison of LAEBID patterns deposited with various laser and refresh parameters. Refresh denotes extra time between	

LAEBID passes to enhance the laser-on time relative to the EBID time. Additional process parameter information may be found in the supporting information.....	65
Figure 25. Normalized carbon content for standard EBID deposits annealed in reactive gas only (black) and a co-flow with approximately equal localized pressure of reactive gas plus the organometallic MeCpPtMe ₃ precursor (red). Deposits were annealed with 100 μs, 0.1% laser duty cycle conditions.....	66
Figure 26. Schematic of proposed purification retardation mechanism. (a) EBID PtC ₅ deposit is composed of Pt nanoparticles suspended with in an amorphous carbon matrix. (b) Under a flux of molecular H ₂ O only, there are many adsorption sites for the purification reaction to occur. (c) With a co-flow of H ₂ O and MeCpPtMe ₃ , the MeCpPtMe ₃ precursor gas dominates the surface coverage due to the long residence time and occupies many adsorption sites and reduces purification rate.....	67
Figure 27. Sequential deposit fabricated from 5 cycles with approximately 70 monolayers deposited per cycle (a) before and (b) after 100 μs smoothing pulses were applied to reduce porosity of the deposit. Inset dashed square denotes original pattern shape prescribed by EBID raster sequence. c) SEM tilted image (52°) of the sequential deposit.	68
Figure 28. (a) EDS spectra of Pt EBID deposits which were annealed with 10 us and 1% duty cycle laser conditions for a cumulative laser exposure time of 0.9 s. Spectra shown include a deposit annealed under localized Ar flow and a deposit annealed under non-localized Ar gas flow. The partial pressure of the Ar flow was approximately 1.0E-6 mbar for both anneals. (b) RGA spectra showing the chamber gases species present during both of the anneal processes.	68
Figure 29. Synchronization map of electron beam and laser pulses during the reactive gas assisted LAEBID process. EBID patterns were deposited using a raster scan. The beam scanning initiates in the bottom left corner and terminates at the top right corner. Pixel spacing of the electron dwells are 13.55 nm in the x and y direction. A blue pixel indicates that the electron beam and laser are both simultaneously on and importantly the laser is irradiating the entire box whereas the electron is addressing only single pixels. A white pixel indicates that the laser is off during the 10 μs electron beam dwell on that pixel. The synchronization is shown for LAEBID with 10 μs laser pulses at (a) 1%, (b) 3%, and (c) 6% duty cycles.	69
Figure 30. (a) SEM image of LAEBID pattern deposited with 100 μs pulse width and 0.5% duty cycle synchronized pulsed laser. Island growth surrounding the deposit was induced by laser assist chemical vapor deposition (LCVD) of the precursor and reactive gas co-flow. (b) EDS spectrum of the LCVD platinum.	70
Figure 31. Images of patterns deposited using the cyclic deposition technique with (a) 50, (b) 130, and (c) 230 monolayers per cycle. Each pattern was deposited using a total of 6 cycles. (d) EDS spectrum the 130 monolayer/cycle deposit.....	71
Figure 32. Patterns deposited using the sequential method (a) before and (b) after twenty 100 μs laser smoothing pulses were applied.....	72
Figure 33. Schematic of helium ion exposures (a) without and (b) with pulsed laser-assist to photothermally enhance implanted ion diffusion and defect annihilation. Grey pixels in the raster pattern represent pixels irradiated solely with He ⁺ whereas red pixels are	

- simultaneously irradiated with the laser and He^+ . Cross-section TEM images illustrate the amorphized silicon region (a) and damage mitigated (b) by the in situ laser-assist. Overlaid on the TEM images are calculated helium, vacancy and interstitial concentrations, illustrating photothermally enhanced diffusion of He^+ and vacancies with the pulsed laser-assist strategy of a photon/ion flux of 1.3×10^6 . Inset in (b) is the simulated time-temperature profile of a single 100 μs laser pulse irradiated on Si. 92
- Figure 34. TEM cross sections of 25 keV He^+ exposures of varying dose (a-d) without and (e-h) with a pulsed laser-assist of 1.3×10^6 photon/ion flux. Exposure doses are inset in the images. High-resolution TEM images showing ion beam induced damage without (i) and with (j) laser-assist for a dose of 5×10^{17} He^+/cm^2 collected from the regions denoted by hatched red boxes in (c) and (g), respectively. k) SAED patterns and (l) TEM cross section of an exposure of 1×10^{18} He^+/cm^2 with 5 times higher (6.6×10^6) photon/ion flux than (h). Dashed circles denote where SAED was conducted. 93
- Figure 35. TEM cross sections of 15 keV He^+ exposure (a) without and (b) with laser-assist of 1.3×10^6 photon/ion at a dose of 1×10^{18} He^+/cm^2 . Dashed line in (a) denotes region amorphized by 25 keV He^+ beam. (c) Reproduction of Figure 34h which shows a 25 keV exposure at a dose of 1×10^{18} He^+/cm^2 with a laser assist of 1.3×10^6 photons/ion for comparison purposes. TEM cross sections of 25 keV He^+ exposure (d) without and (e) with laser-assist at a dose of 1×10^{16} He^+/cm^2 . (f) Reproduction of Figure 34a which shows a 25 keV He^+ exposure at a dose of 1×10^{16} He^+/cm^2 with a laser assist of 1.3×10^6 photons/ion for comparison purposes. 94
- Figure 36. Simulated cross-section helium concentration profiles for 1×10^{16} He^+/cm^2 dose at 15 keV He^+ in silicon (a) without and (b) with laser-assist of 1.3×10^6 photon/ion. Cross-section of calculated helium concentration profiles for 1×10^{16} He^+/cm^2 dose at 25 keV He^+ in silicon (c) without and (d) with laser-assist. (e) Plot of the calculated maximum He^+ concentration as a function of photon/ion flux and implantation energy for a dose of 1×10^{16} He^+/cm^2 . The photon/ion fluxes used for experimental exposures include 0, 1.3×10^6 , and 6.6×10^6 photon/ion. A plot of the maximum He^+ concentration as a function of aerial dose for each of the experimental exposure conditions is inset. 95
- Figure 37. HIM images of channels milled into single layer graphene on SiO_2 without (a) and with (b) laser-assist where the photon/ion flux was $\sim 1.6 \times 10^6$. Scale bar is 500 nm. SEM images confirm the confined channels were cut at a width of ~ 50 nm both (c) with and without (d) laser-assist. Scale bar is 200 nm. (e) Raman spectra of graphene as-receive and irradiated at a dose of 1×10^{14} ions/ cm^2 with (red) and without (black) laser-assist. 96
- Figure 38. (a) TEM image of a 5×10^{17} He^+/cm^2 exposure with no laser assist and a beam energy of 25 keV. High-resolution TEM images of the regions denoted by the red box (b) and the blue box (c) in image (a). These regions represent areas which borders the irradiation induced amorphous Si border and amorphous Si core respectively. (d) TEM image of a 5×10^{17} He^+/cm^2 exposure with a laser assist of 1.3×10^6 photon/ion and a beam energy of 25 keV. High-resolution TEM images of the regions denoted by the red box (e) and the blue box (f) in image (d). 97
- Figure 39. (a) Sub-surface damage accumulation region in Si of a (a) 5×10^{17} and (b) 1×10^{18} He^+/cm^2 exposure with 25 keV He^+ and no laser assist. Small nano-bubbles begin forming in (a) and expand to become clearly visible in (b) with an increase in exposure dose. 98

Figure 40. Simulated cross-sectional concentration distribution of (a-d) implanted He concentration, (e-h) interstitial Si, and (i-l) Si vacancies for a Si substrate irradiated with 25 keV He ⁺ at a dose of 1x10 ¹⁶ He ⁺ /cm ² . The defect distributions are shown for different aerial square exposure patterns with side lengths of 10 nm (1 st row), 50 nm (2 nd row), 100 nm (3 rd row), and 200 nm (4 th row).	99
Figure 41. (a) Maximum defect concentration as a function of side length of an aerial square pattern. All concentrations are simulated for a 1x10 ¹⁶ He ⁺ /cm ² exposure with 25 keV He ⁺ in a Si substrate. (b) Schematic illustrating that when the aerial pattern dimensions reach the lateral range of the defects generated, saturation in maximum concentration occurs.	100
Figure 42. SEM images of 25 keV He ⁺ patterns at a dose of 1x10 ¹⁸ ions/cm ² which were annealed in a (a) post He ⁺ exposure anneal and (b) in-situ manner with 100 μs, 1% DC laser conditions. The right-most pattern in each image was irradiated with no synchronized laser exposure.	101
Figure 43. Cross section concentration profile of the Si interstitials generated from 15 keV He ⁺ in silicon (a) without and with (b) laser-assist of 1.3x10 ⁶ photon/ion. Cross section concentration profile of the Si interstitials generated from 25 keV He ⁺ in silicon (c) without and with (d) laser-assist. (e) Plot of the maximum Si interstitials concentration as a function of aerial dose for each of the exposure conditions.....	102
Figure 44. TEM cross section of Si irradiated with (a) 15 keV and (b) 25 keV He ⁺ and synchronized laser superimposed onto simulations results. TEM cross sections are for a dose of 5x10 ¹⁷ He ⁺ /cm ² whereas the simulations are for a dose of 1x10 ¹⁶ He ⁺ /cm ²	103
Figure 45. (a) Schematic of the focused ion beam induced etching (FIBIE) setup. The focused 785 nm laser beam, focused He ⁺ beam, and gas injection nozzle share a common confocal point on the Ti film surface. (b) In-chamber digital photograph of the experimental setup with the beam, laser probe, and gas sources indicated. The GIS needle is retracted in this image. (c) Schematic of a He ⁺ milling process of Ti. (d) Schematic of a FIBIE process with the XeF ₂ chemical assist. (e) Schematic of a laser assisted FIBIE process.	121
Figure 46. (a) He ⁺ milling of a 200 nm thick Ti film at various doses ranging from 1x10 ¹⁸ —3.7x10 ¹⁹ He ⁺ /cm ² . (b) in situ, pulsed laser assisted milling with a 478 kW/cm ² laser irradiance, 100 ns pulse width and 100 kHz frequency. (c) in situ pulsed laser assisted milling with a 478 kW/cm ² laser irradiance, 300 ns pulse width and 100 kHz frequency. (d) Finite-element simulation of the peak Ti film temperature induced by the 478 kW/cm ² laser irradiance as a function of time for 100 and 300 ns laser pulses.	122
Figure 47. Focused ion beam induced etching (FIBIE) of Ti film as a function of the localized etchant flux of (a) 0, (b) 9.7x10 ¹⁶ , (c) 1.3x10 ¹⁷ , and (d) 1.5x10 ¹⁷ XeF ₂ molecules-cm ⁻² s ⁻¹ . The FIBIE experiments were conducted using a 1 μs He ⁺ dwell time, a 0.25 nm pixel pitch and an ion dose of 1x10 ¹⁹ He ⁺ /cm ²	123
Figure 48. Simulated cross sections of (a) the damage function (the number of damage events per lattice site), (b) the deposited nuclear energy per lattice site, and (c) the implanted He ⁺ ion concentration. The left column corresponds to a milling simulation (11,250,000 ion dose), and the right to an “etching” simulation (2,812,500 ion dose). Additional simulation parameters are listed as follows; 15 nm long line scan, 25 keV beam energy, 1 nm pitch, 2.4 pA current, and 0.45 μs dwell time.....	124

Figure 49. (a) Comparison of FIBIE process and LA-FIBIE process using a 50 μs He^+ beam dwell time. (b) Titanium etch yield of the FIBIE and LA-FIBIE processes as a function of He^+ beam dwell time. LA-FIBIE was conducted with 100 ns laser pulses at an irradiance of 55 kW/cm^2 and a frequency of 50 kHz (0.5 % duty cycle).	125
Figure 50. (a) Simulated peak temperature as a function time for a 100 ns pulse at various laser irradiance. (b) Arrhenius $\ln(\text{etch yield})$ vs $1000/T$ plots for the La-FIBIE process with varying laser irradiance. Each temperature corresponds to temperature achieved with a 100 ns pulse at a laser irradiance of 0, 55.5, 96.7, and 214 kW/cm^2 . (c) Etch yield as a function of laser duty cycle (pulse width x frequency) for 100 ns laser pulses at 55.5 kW/cm^2 irradiance. All etches conducted here used a constant 1 μs He^+ dwell time (additional conditions can be found in Table 5).	126
Figure 51. Photograph of the laser delivery system installed on a high angle port near the load lock of the Zeiss Orion NanoFab helium ion microscope. Optical probe (silver) mounted through the nanomanipulator (black) are indicated within the white ellipse. Only one of the two optical fibers was used in these experiments.	127
Figure 52. Patterns milled into Ti using the La-FIBIE process at varying synchronized laser powers (inset across the top). The laser pulsewidth was 100 ns and the frequency was 50 kHz (0.5 % duty cycle).	128
Figure 53. Patterns milled into Ti using the La-FIBIE process at varying synchronized laser duty cycle, or frequency. The laser pulse width was held at a constant 100 ns and the frequency was varied from 25 – 500 kHz (0.25 – 5.0 % duty cycle) to control the duty cycle.	128
Figure 54. Visual endpoint monitoring of FIBIE (black) and LA-FIBIE (red) processes. Endpoint signal is an averaged greyscale value reflecting the number of secondary electrons collected at the detector after each patterning loop. The scale of the y-axis is in arbitrary units. Inset helium ion microscope images show how the mill progresses with the endpoint signal. ..	129
Figure 55. Average ratio of three measures of subsurface damage between the milling and etching simulations, as a function of depth within the target (see Figure 48). The average ratio for all of these measures over the whole computational domain is approximately four, reflecting the fact that the milling simulation has four times the ion dose of the etching simulation.	130
Figure 56. Schematic of (a) a He^+ milling process, (b) XeF_2 gas injection, and (c) focused ion beam induced etching of WSe_2 . (d) SEM image of WSe_2 nanoribbons created with the FIBIE process. Scale bar is 40 nm.	148
Figure 57. (a) SEM image of He^+ milling of ~ 24 nm thick WSe_2 at doses ranging from 5×10^{17} – 5×10^{18} He^+/cm^2 . Scale bar is 400 nm. (b) FIBIE of WSe_2 with He^+ dwell time of 30 μs . (c) FIBIE of WSe_2 with He^+ dwell time of 100 ns. All patterns are 50 nm x 500 nm. (d) Etch yield of the FIBIE process as a function of dwell time for WSe_2 as well as SiO_2 . (e) Etch yield of the FIBIE process at a constant 100 ns dwell time as a function of patterning pixel spacing.	149
Figure 58. HAADF STEM images of a WNR. (a) Macro image of a single ribbon. (b-c) High-resolution images of the ribbon edge showing high crystallinity in close proximity to the etched surface. (d) Fourier transformations of 10 nm x 10 nm sub-areas were performed and the width of $\{110\}$ type reflections were measured in units per nm. Six measurements from each sub-area were used to find the average spot width and standard deviation. We use this	

width as the measure of crystallinity. The broadening of the reflection indicates that the crystal has been perturbed by the helium ion irradiation. After about 120 nm, the value of the unperturbed crystal is reached.....	150
Figure 59. Simulated (a) aerial view (x-y plane) and (b) cross-section (y-z plane) of the deposited nuclear energy, associated with scanning a 25 keV He ⁺ ion beam on a WSe ₂ layer occupying the top 10 nm, with a 15 nm thick carbon layer underneath. The equivalent areal dose is 3.0x10 ¹⁷ He ⁺ /cm ² . The simulation domain and He ⁺ dose correspond to the experimental conditions used in Figure 58. Note that the plot is on a log scale. (c) Aerial view (x-y plane) and (d) cross-section (y-z plane) of the deposited nuclear energy into 10 nm of WSe ₂ on top of a bulk Si substrate. The scan parameters are 15 nm by 1 μm.....	151
Figure 60. (a) SEM image of an array of 20 nm WNRs. (b) Raman spectra of WNR array normalized to the Si peak as a function of angle between polarization angle of the incident laser spot and the nanoribbon direction. The angular dependence of the Raman anisotropy of the E _{2g} ¹ mode is shown in the inset.	152
Figure 61. (a) Schematic of WNR TFT from side and top view. (b) SEM image of a FET device fabricated with an array of WNRs which are 1 μm long. Scale bar is 3 μm. Inset are SEM images of WNR devices fabricated using standard He ⁺ milling (HIM-WNR) and the FIBIE process (FIBIE-WNR). Scale bar is 300 nm. (c) Normalized channel currents as a function of gate bias (IDS vs VGS) for pristine WSe ₂ (solid curves) and HIM-WNR and FIBIE-WNR (dotted curves) devices. The effective channel width of FIBIE-WNR devices are normalized to fill factor. (d) Ratio of ON state currents of the FIBIE-WNRs to that of pristine WSe ₂ devices as a function WNRs widths for both electron transport (red) and hole transport (black). The ON state currents for electron are measured at +60 V gate bias, while for hole are measured at -60 V gate bias with 1.0 V source-drain excitation.	153
Figure 62. Helium ion microscope images of frames from video recorded during FIBIE to monitor etch progress. Timestamp of frames are used to determine etch dose and hence etch yield.	154
Figure 63. AFM image of flake where milling experiments were conducted. A thickness line profile is displayed which shows that flake thickness was approximately 24.15 nm.....	155
Figure 64. Raman spectra for a pristine WSe ₂ flake as well as Raman spectra for 20 nm WNRs as different orientations to the polarized laser source axis. Significant Raman anisotropy is observed for the WNRs but not for the pristine WSe ₂	156
Figure 65. SEM images of three FIBIE-WNR devices and a HIM-WNR device. The nanoribbon widths shown here are 120, 65, and 25 nm.	157
Figure 66. (a) SEM image of a WNR device composed of an array of 25 nm WNRs. (b) SEM image of the WNR array. (c) Transfer curve of the transistor before (pristine) and after the fabrication of the 25 nm aligned WNR array.....	158
Figure 67. (a) 64 nm x 64 nm HAADF image analyzed for the disorder measurements. The red square, 10nm x 10 nm, is arbitrarily placed and represents the sub-area used to find specific spatial information from within the total image. (b) Fast Fourier transforms FFT) of the sub-area with the -110 reflection circled and the red line marking the path of the intensity profile. (c) FFT Intensity profile. The width of these peaks are used as the measure of material order/disorder.....	159

- Figure 68. EELS from the WNR on amorphous carbon membrane. Integrating under the Se $L_{2,3}$ Edge we get that Se is 712 Se atoms/nm² and Se in WSe₂ with P6/mmc symmetry has a volume density of 65.9 Se atoms/nm³. The layer density is 44.8 Se atoms/nm². It was determined the WSe₂ flake thickness shown in STEM images was approximately 10 nm. 160
- Figure 69. (a) Raman spectra of WSe₂ showing the LA(M) peak at ~ 118 cm⁻¹. (b) Spatially resolved Raman map of the LA(M) peak superimposed onto an optical micrograph. Rectangular He⁺ exposures on the flake are denoted by inset dotted lines. (c) Normalized intensity of LA(M) mode along a line scan on the patterned WSe₂ flake. 177
- Figure 70. HAADF STEM images of suspended WSe₂ which was irradiated with He⁺ at doses of (a) 2×10^{13} , (b) 1×10^{15} , (c) 1×10^{16} , and (d) 1×10^{17} ions/cm². Field of view is 16 nm. SAED patterns are inset for each exposed dose. 178
- Figure 71. (a) Schematic of the WSe₂ field effect transistor (FET) device irradiated with He⁺. (b) Optical micrograph of the WSe₂ FET on SiO₂/Si substrate. The scale bar is 10 μ m. (c) AFM micrograph of the fabricated WSe₂ FET device. The inset represents the height profile along the dotted line shown in the Figure. (d) The transfer characteristics (I_{DS} vs V_{GS}) at two different drain-source voltages (black curves for $V_{DS} = -0.1$ V and red curves for $V_{DS} = -1.1$ V) before (solid curves) and after (dashed curves) He⁺ irradiation at a dose of 1.5×10^{15} ions/cm² on WSe₂ channel region. The measured transfer characteristic clearly shows the ambipolar characteristics of the WSe₂ FET device before He⁺ irradiation, while the device after He⁺ irradiation loses its p-type characteristics. (e) Double log plot of electrical resistivity as a function of He⁺ irradiation dose for mechanically exfoliated few layers WSe₂ flakes on SiO₂/Si substrate. Gradually insulating behavior arose with the initial increasing dose applied, while metallic behavior was observed with the further increase in dose applied. The gate tunability of the WSe₂ device was completely reduced as seen in inset, at a dose of 1×10^{17} ions/cm². 179
- Figure 72. (a) Schematic of the WSe₂ field effect transistor (FET) device irradiated with He⁺ over half of the channel length to induce a homo-junction. (b) Spatially resolved Raman map of He⁺ irradiated junction (1×10^{15} ions/cm²) on a WSe₂ flake. Map shows ratio of integrated peak area of LA(M) (associated with defects) to the main Raman peak E'_{2g} . The inset in the upper left corner shows an optical micrograph of WSe₂ device. The measured transfer characteristics of a WSe₂ FET device (c) before and (d) after, He⁺ irradiation was used to create a homo-junction at a dose of 1×10^{15} ions/cm². 180
- Figure 73. (a) Kelvin Probe Force Microscopy (KPFM) image of a WSe₂ TFT with symmetric Ti/Au electrodes in which half of the channel with exposed with a dose of 5×10^{14} He⁺/cm². (b) Tapping mode AFM image of the same exposed WSe₂ TFT, which shows no topographical evidence of exposure. (c) KPFM line scan, denoted by a black dotted line in (a), which shows band bending at the interface of exposed and pristine WSe₂. (d) Band diagram of a WSe₂ flake, which has a junction created by He⁺ exposure. 181
- Figure 74. (a) The photoresponse of a device with the lateral homojunction created by a dose of 1×10^{15} He⁺/cm² in WSe₂ at zero gate bias. The semi-log plot of I_{DS} vs V_{DS} with and without light exposure shows the photoresponse with noticeable photovoltage as high as 220 mV. (b) Open circuit voltage extracted from devices under light condition as a function of He⁺ dose used to create the homo-junction. 182

Figure 75. The semi-log plot of output characteristics (I_{DS} vs V_{DS}) of asymmetric electrodes (Pd in one side and Ti/Au in other side) of few-layer WSe ₂ devices, before (left panel a & c) and after (right panel b & d) He ⁺ irradiations at two different doses (1×10^{14} and 1×10^{15} He ⁺ /cm ² , respectively). Preferential hole injection in the WSe ₂ channel is clearly seen from the asymmetric nature of I_{DS} – V_{DS} curves (a & c) due to the ohmic contact between the Pd electrode and valence band of WSe ₂ flake and a possible Schottky barrier at Ti/Au contact. The hole transport is still significantly suppressed compared to electron transport (Fig. b and d) on WSe ₂ channel after the He ⁺ irradiation. The images on the top of the Figure depict an optical micrograph (left) and schematic (right) of the device structure studied.	183
Figure 76. Raman spectra of few-layer WSe ₂ at various He ⁺ exposure doses.	184
Figure 77. HAADF STEM images of suspended WSe ₂ which was irradiated with He ⁺ at doses of (a) 2×10^{13} , (b) 1×10^{15} , (c) 1×10^{16} , and (d) 1×10^{17} ions/cm ² . Images have 8 nm field of view.	185
Figure 78. Indexed diffraction pattern taken from WSe ₂ flake exposed with a dosage of 2×10^{13} He ⁺ /cm ²	186
Figure 79. Figure compares the changes in the WSe ₂ crystal structure when subjected to varying doses of ion irradiation. This has been done by STEM Z-contrast imaging, Fourier transformations of each respective Z-contrast image, and selected area electron diffraction patterns that correspond to each region. Fourier transformations of the Z-contrast images agree well with SAED results.	187
Figure 80. (a) SEM image of a single layer WSe ₂ flake on a holey silicon nitride membrane. Inset doses denote the dose applied to each suspended region with units of ions/cm ² . (b) Plot of the ratio of the relative peaks intensities of W – M and Se – L as a function of He ⁺ dose.	188
Figure 81. (a) Raw EDS spectra for suspended WSe ₂ exposed with He ⁺ of various doses. (b) SEM image of the exposed suspended flake on silicon nitride where regions 1-6 were exposed with doses of 1×10^{12} , 1×10^{17} , 5×10^{16} , 1×10^{16} , 1×10^{15} , and 3×10^{17} respectively. (c-e) EDS maps of Se + W, only Se, and only W respectively.	189
Figure 82. The typical hysteresis in measured I_{DS} vs V_{GS} curves at $V_{DS} = 0.1$ V, before (black) and after (red) He ⁺ irradiation at the dose of 1.0×10^{15} ions/cm ² . The corresponding leakage currents (dotted lines) are also plotted in the same graph.	190
Figure 83. Field effect hole mobility extracted from the transfer characteristic curves for few-layer WSe ₂ devices as a function of flake thickness.	191
Figure 84. Measured I_{DS} vs V_{DS} normalized to channel W/L ratio, for the different thickness of WSe ₂ flakes at three different gate voltages, (a) $V_{GS} = 60$ V, (b) $V_{GS} = 0$ V and (c) $V_{GS} = -60$ V. All flakes were exposed in the channel region with a dose of 1×10^{15} He ⁺ /cm ²	192
Figure 85. Using our EnvizION ¹⁰³ ion-solid Monte Carlo simulation we simulated varying thickness WSe ₂ films (7, 16, and 26 nm) which were exposed with 25 keV He ⁺ to a dose of 1×10^{15} He ⁺ /cm ² . In this simulation, the WSe ₂ is assumed to be amorphous with the stoichiometric W/Se ratio of 1/2 and using the bulk properties of crystalline WSe ₂ . The He ⁺ was simulated as a 25 nm cylindrical beam. Green pixels represent Se atoms, blue pixels represent W atoms, light green pixels represent displaced Se atoms, light blue pixels represent displaced W atoms, and red pixels represent unfilled vacancies created by sputtering events.	192

- Figure 86. Time dependence of transistor ON current at $V_{DS} = 1.1\text{ V}$ and $V_{GS} = 60\text{ V}$, for few-layer WSe_2 device irradiated with He^+ ion dose at 1×10^{14} up to 30 days. No recovery on transistor ON currents has been observed by exposing the irradiated sample in ambient conditions. The red open circle represents the channel current prior to He^+ exposure..... 193
- Figure 87. Photo-response of one of the pristine few-layer WSe_2 device (without He^+ irradiation) at various gate potentials. No significant photovoltaic effect has been observed in few-layer WSe_2 device. 194
- Figure 88. He^+ dose dependent electrical properties. (a) Optical micrograph of a standard WSe_2 FET device. Scale bar is $10\text{ }\mu\text{m}$. (b) Transfer curves for exposed FETs with $V_{DS} = -1.1\text{ V}$. (c) Plot of the current ratio: current of the exposed device to current of pristine device at $V_{GS} = 10$ and -60 V . (d) Temperature-dependent transfer curves for WSe_2 exposed with a dose of $1 \times 10^{16}\text{ He}^+/\text{cm}^2$. (e) Arrhenius plot of the device current (I_{DS}) and fitting results of nearest-neighbor hopping model with an activation energy (E_a) of 36.7 meV 210
- Figure 89. STEM image of exposed WSe_2 . (a) HAADF STEM image of WSe_2 which was exposed with a dose of $1 \times 10^{15}\text{ He}^+/\text{cm}^2$. Field of view is 32 nm . (b) STEM image local crystallography analysis using K-means clustering, on the six-nearest neighbor bond-lengths to each atom. Blue atoms represent a pristine lattice, white atoms are around point defects (light damage), and green atoms are extended defects (heavy damage). Nearest neighbor distribution in real space for (c) pristine (blue) and (d) lightly damaged (white) atoms in the lattice. Lightly damage cluster shows significantly lower counts for neighbors in ‘downward pointing’ trimer, which corresponds with preferentially sputtered Se..... 211
- Figure 90. STEM images and analysis. (a) High angle annular dark field (HAADF) STEM images of WSe_2 irradiated with varying doses of He^+ (text inset in image). (b) K-means cluster analyzed STEM images. (c) Only the vacancy boundary atoms (magenta color in the mid row) from the STEM images (top row). 212
- Figure 91. DFT results for pristine and defective single layer WSe_2 . Calculated electronic band structures of the 5×5 supercell with (a) no defect, (b) a point defect, (c) a pore defect, and (d) edge defect configurations. All band energies are aligned to the vacuum potential for direct comparison. The Fermi level is set at the valence band maximum for each system, as shown by the blue dashed line. The corresponding atomic structure for each configuration is shown above the band structure. The point defect in (b) corresponds to a single Se vacancy, which is indicated by the red dashed circle. 213
- Figure 92. Atomic layer inverters. (a) Schematic of atomic layer inverter created by utilizing exposed and pristine material on a single flake. (b) Optical micrograph of a typical inverter device. Scale bar is $10\text{ }\mu\text{m}$. (c) Input (V_{in}) – Output (V_{out}) voltage characteristics of a WS_2 atomic layer inverter. Circuit diagram for device is inset. (d) Input (V_{in}) – Output (V_{out}) voltage characteristics of a WSe_2 atomic layer inverter. (e) Input (V_{in}) – Output (V_{out}) voltage characteristics of a WSe_2 atomic layer inverter which was gated with an ionic liquid. (f) Voltage gain (dV_{out}/dV_{in}) of inverter reported in figure (e). 214
- Figure 93. Edge contacts for 2D devices. (a) Schematic of edge contact FET. Source and drain are fabricated from NNH WS_2 (exposed to a dose of $1 \times 10^{16}\text{ He}^+/\text{cm}^2$). The FET channel is pristine (unexposed) WS_2 . (b) Raman map of a WS_2 flake plotting the intensity of the 2LA(M) peak. The WS_2 flake was exposed to doses varying from $1 \times 10^{14} - 1 \times 10^{16}\text{ He}^+/\text{cm}^2$ (inset). Scale bar is $10\text{ }\mu\text{m}$. Raman map is overlaid on an optical micrograph. (c) Transfer

curve for a standard WS ₂ FET compared with that of an edge contacted FET in which the source and drain were composed of NNH WS ₂	215
Figure 94. Transfer curves for device before and after irradiation with the He ⁺ beam. Doses range reported are (a) 1x10 ¹⁴ He ⁺ /cm ² , (b) 1x10 ¹⁵ He ⁺ /cm ² and (c) 1x10 ¹⁶ He ⁺ /cm ²	216
Figure 95. (a) Raman spectra for WSe ₂ as a function of He ⁺ exposure dose. (b) Photoluminescence spectra for WSe ₂ as a function of He ⁺ exposure dose. Log-scale spectra is inset.	216
Figure 96. Temperature dependent output curves with a V _{GS} of (a) 80 V and (b) -80 V. The device was exposure with a dose of 1.0x10 ¹⁶ He ⁺ /cm ² prior to measurement.	217
Figure 97. EELS spectra showing a decrease in the area under the selenium L _{2,3} edge with increasing He ⁺ dose. This is directly correlated to the areal density of the specific element.	217
Figure 98. (a) Transfer curves for the WS ₂ transistor which was part of the logic gate. (b) Transfer curves of the metallic-like resistor portion of the inverter which demonstrates no effect of gate modulation. (c) I-V characteristic of the resistor.	218
Figure 99. (a) Transfer curves for the WSe ₂ transistor which was part of the logic gate. The device was gated with a high dielectric-constant ionic liquid. (b) Transfer curves of the metallic-like resistor portion of the inverter which demonstrates no effect of gate modulation.	218
Figure 100. Schematic of a WSe ₂ inverter device with IL gating.	219

INTRODUCTION

Focused beam induced processing (FBIP) has emerged as a viable technique for materials processing and synthesis on the nanoscale. In the context of this dissertation, focused beam induced processing is defined a materials processing method which is initiated by exposure to a focused beam of charge particles. The emergence of focused beam induced processing has largely been motivated by the fundamental study of nanoscience. In particular relevance to this work, the processing of nanomaterials as well the downsizing of electrical circuits have played a crucial role in catalyzing the development of new FBIP techniques.

FBIP techniques are typically carried out via irradiation with focused electrons or ions, each of which offer distinct capabilities. The focused electrons (or ions) are typically generated in scanning electron (or ion) microscopes. The scanning electron or ion microscope (SEM or SIM) uses a series of electrostatic lenses and apertures to focus the charged particles to a probe size of commonly < 10 nm. This enables direct-write materials processing or synthesis on the nanoscale. FBIP techniques can be additive, subtractive, or induce some sort of alteration to the target material. FBIP can also rely on a gas-assist for the processing technique or may solely be induced by ion-solid interactions between the charged particle and the target material. Gas-assisted processes generally utilize a gas-injection system to locally inject a precursor molecule into the SEM or SIM chamber. Inelastic interactions of the electron (or ion) beam with the precursor molecule drives dissociation of molecule which chemically assisted the FBIP process¹. This will be further discussed in this introduction. Alternatively, ion-solid interactions alone can be used to initiate a FBIP processing. Energetic particles can transmit energy to target atoms by means of nuclear or electronic energy loss. Nuclear energy loss occurs when the energetic particle interacts with the charged nucleus of an atom in an elastic manner. Electronic energy loss occurs with the energetic particle interacts with electrons resulting in an inelastic interaction. These energy loss mechanisms can be utilized in FBIP processes in a variety of different manners. Energy loss can be used to locally introduce heat into the system, generate defects in the target material, implant charged particles into the target material, and sputter target atoms, to name a few. A more comprehensive review on FBIP processes can be found in REFs^{2,3}.

This dissertation will largely focus on a number of FBIP processes utilizing focused electron (e^-) and focused helium ion (He^+) beams. The FBIP techniques include gas-assisted and

non-gas-assisted processes. Here background is provided on a number of processes which are relevant to this dissertation.

Electron Beam-Induced Processing

Focused electron beam-induced processing (FEBIP) may be thought of as the non-invasive variant in comparison with focused ion beam-induced processing (FIBIP), owing to the fact that an electron has a much lower mass compared to all ion species and generally does not induce a large concentration of defects in the underlying substrate by knock-on collisions. Additive and subtractive processes with FEBIP are typically chemical-assisted techniques. Electron beam-induced deposition (EBID) is generally carried out by introducing a precursor gas into a scanning electron microscope (SEM) in close proximity to a substrate. The precursor gas then physisorbs onto the substrate and impinging primary electrons from the focused beam, and particularly secondary electrons generated from the substrate, cause the precursor molecule to dissociate through inelastic collisions with the electrons. Non-volatile dissociation by-products generated from the dissociation event condense on the substrate creating a direct-write deposit whose geometry is dictated by the focused beam's raster pattern. Incomplete dissociation of the precursor molecule (typically organometallic) results in unwanted ligands being incorporated into the deposits. This results in low purity deposits. A schematic of this process is shown in **Figure 1a** and reprinted from Ref⁴.

Analogous to EBID, electron beam-induced etching (EBIE) can be carried out in a similar manner in which a precursor molecule is dissociated via an inelastic collision with an electron. In this case, the selected precursor dissociation by-products form a volatile compound with the substrate material, thereby removing or etching the substrate material. Of course, the precursor molecules are carefully selected with the proper chemistry to deposit a pattern of desired composition or generate an etchant of proper composition. Typically, CVD precursors are used as EBID precursor molecules, but recent work strives to create precursor molecules specifically tailored for FEBIP and FIBIP^{5,6}. Additionally, high energy e^- beams have been utilized to introduce defects into material lattices⁷, however defect introduction via electron beam irradiation at energies commonly available in SEMs is generally very low yield and will not be discussed further in this dissertation.

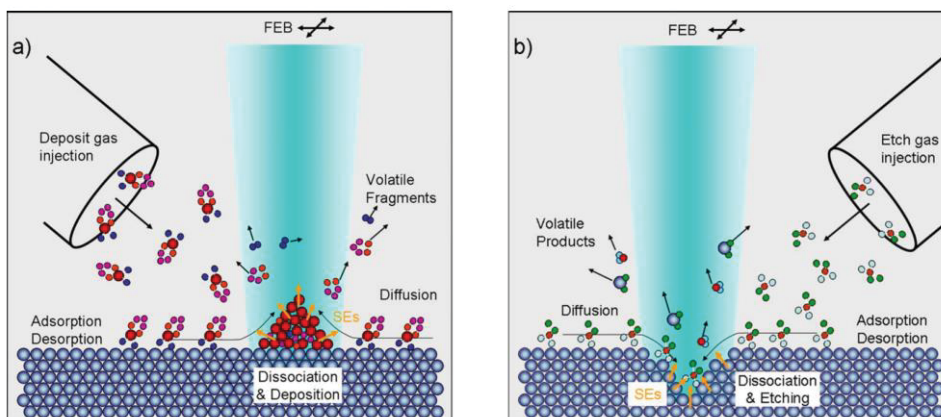


Figure 1. (a) EBID: the nonvolatile dissociation products form the deposit growing coaxially into the beam. Volatile fragments are pumped away. (b) EBIE: the surface adsorbed molecules dissociate under electron impact into reactive species and react to volatile compounds with the substrate material. Reprinted with permission from Ref⁴. Copyright 2008, American Vacuum Society.

Ion Beam-Induced Processing

FIBIP is very similar to FEBIP, however an ion species is generated and used for processing. Typical FIBIP either takes place in a dual-beam SEM or a focused ion microscope (FIM). The most elementary FIBIP technique is subtractive sputtering of a target material via bombardment with the ion species. This occurs when momentum transfer between the ion species and the target atoms are sufficient to eject the target atoms. The sputter rate will depend upon the primary ion beam energy, ion mass, target mass, and binding energy amongst other variables. These solid-ion interactions are well studied as sputtering techniques are a common technique for thin film deposition. However, as the primary ion enters the substrate, a cascade of knock-on collisions occur which may introduce a high concentration of subsurface point defects, which may be undesired for some nanoscale direct-write processes.

Analogous to EBID and EBIE, Ion beam-induced deposition (IBID) and etching (IBIE) can be used as additive and subtractive synthesis processes, respectively. Similar to the electron beam equivalent, these processes are carried out by injecting precursor molecules in close proximity to the substrate surface, where inelastic collisions with the primary ion beam and

generated secondary electrons dissociate the precursor molecule to form a non-volatile by-product (IBID) or a by-product which forms a volatile compound with the substrate material (IBIE). Since the secondary electron yield (Y_{SE}) from the substrate is much greater for ion beams in comparison to electron beams, IBID and IBIE rates are generally greater than EBID and EBIE for comparable beam current. However, undesired subsurface substrate damage, “staining” from some metallic ion species (such as Ga^+), and resolution limits provide restrictions for FIBIP.

Helium Ion Beam Processing

Ga^+ ion beams, which utilize liquid metal ion sources (LMIS), have been the industry standard for FIBIP for a number of years, due to source stability and brightness. However, the LMIS typically results in a beam with a large emission angle (30°) and an energy spread on the order of 15 V. This results in a large amount of chromatic aberration and ultimately limits the resolution of the focused beam. In recent years, He^+ and Ne^+ focused ion beam imaging and processing from the Gas Field Ion Source (GFIS) has emerged as a higher resolution variant, due to low energy spread, low beam convergence angle, and small wavelength (in comparison to e^-). Helium ion beam synthesis and imaging has been used for a variety of applications such as nanolithography⁸, 2D material editing and defect manipulation^{9–12}, nanopore synthesis for DNA sequencing¹³, selective lattice straining¹⁴, the direct-write deposition of high resolution nanowires¹⁵, high aspect ratio pillar deposition⁸, high resolution milling for fabrication of plasmonic nanostructures^{16–18}, selective defect introduction^{10,12,19}, and is being explored as a next-generation instrument for nanoscale circuit editing/debugging^{20,21}. Clearly, there are broad applications for He^+ processing which are of general interest to the fields of materials science and nanoscience. Chapter II explores several applications for advanced focused beam induced processing utilizing He^+ . Chapter III will detail focused beam induced processing with the He^+ beam geared specifically toward 2D materials. Each chapter and subsection provides additional relevant background information.

CHAPTER I
LASER BASED PURIFICATION OF ELECTRON BEAM INDUCED
DEPOSITS

1.1 Purification of Nanoscale Electron Beam Induced Platinum Deposits via Pulsed Laser Induced Oxidation Reaction

A version of this chapter was originally published by M. G. Stanford et al.:

Stanford, M. G.; Lewis, B. B.; Noh, J. H.; Fowlkes, J. D.; Roberts, N. A.; Plank, H.; Rack, P. D. Purification of Nanoscale Electron-Beam-Induced Platinum Deposits via a Pulsed Laser-Induced Oxidation Reaction. *ACS Appl. Mater. Interfaces* **2014**, 6, 21256–21263.

Michael G. Stanford and Brett B. Lewis conducted experiments reported in this manuscript. Michael G. Stanford conducted subsequent data analysis and characterization. All co-authors discussed the results and formulated the purification mechanism reported in the manuscript. Reprinted with permission. Copyright 2014 American Chemical Society.

1.1.1 Abstract

Platinum-carbon deposits made via electron beam induced deposition were purified via a pulsed laser induced oxidation reaction and erosion of the amorphous carbon to form pure platinum. The purification proceeds from the top down and is likely catalytically facilitated via the evolving platinum layer. Thermal simulations suggest a temperature threshold of ~ 485 K, and the purification rate is a function of the PtC₅ thickness (80-360 nm) and laser pulse width (1-100 μ s) in the ranges studied. The thickness dependence is attributed to the ~ 235 nm penetration depth of the PtC₅ composite at the laser wavelength and the pulse width dependence is attributed to the increased temperatures achieved at longer pulse widths. Remarkably fast purification is realized at cumulative laser exposure times of less than 1 second.

1.1.2 Introduction

Electron beam induced deposition (EBID) is a synthesis technique which is dictated by a focused electron beam and stimulates a localized reaction of precursor species^{1,3,22}. The result is a nanoscale synthesis technique which can conveniently grow materials “on-demand” via a prescribed electron beam raster sequence. Significant advances have been made by elucidating the critical electron-precursor-solid interactions^{23–27} that occur in the EBID process, which has

enabled better control and higher resolution. Thus, several applications have emerged for nanostructured materials grown via electron beam induced deposition, such as: specialized scanning probe tips^{28,29}, nanomagnetic logic and devices^{30,31}, nanophotonics^{32,33}, field emission emitters^{34,35}, new sensor concepts exploiting nanogranular behavior^{36,37}, maskless lithography^{38–41}, lithography mask editing^{42–45}, superconducting nanostructures^{46,47}, and electrical contacts on-demand⁴⁸ to name a few.

While the field has experienced significant growth over the past decade, one of the main liabilities of focused electron (and ion) beam induced processing has been the inclusion of unwanted by-products into the deposits. The by-product inclusion occurs because EBID is typically performed at room temperature and the standard chemical vapor deposition precursors utilized do not volatilize completely under the electron beam. For instance, one of the most common precursors used is the trimethyl(methylcyclopentadienyl)platinum(IV) ($\text{MeCpPt}^{\text{IV}}\text{Me}_3$) precursor which, depending on the electron beam parameters used, deposits PtC_x material where $5 \leq x \leq 8$ ^{49,50}. To address this limitation, several groups around the world have explored in-situ and ex-situ methods to purify EBID materials (see Botman for review¹). While not an exhaustive list, some approaches that have been used include: post-synthesis annealing^{51–53}, more volatile precursors^{54–56}, mixing reactive gases to stimulate by-product desorption^{57–59}, in-situ substrate heating with reactive gases^{51,60}, and post-electron irradiation with^{61,62} and without reactive gases^{63,64}.

Selective optical coupling of EBID deposits could enable photo-thermal purification to be achieved with minimal damage to surrounding features or substrates. For instance, we have investigated an in-situ synchronized pulsed laser-assisted electron beam induced deposition (LAEBID) process in which an intermittent pulsed laser was used to thermally assist the desorption of carbonaceous by-products from the $\text{MeCpPt}^{\text{IV}}\text{Me}_3$ ⁶⁵ and $\text{W}(\text{CO})_6$ ⁶⁶ precursors during growth. To add to our understanding of conditions which affect the LAEBID process, here we investigate a post-growth laser annealing process. Though similar to many of the post-heating studies that have been performed, the optical coupling can be tuned to be minimally invasive to the substrate or devices due to small laser spot size and precise control of pulsing conditions which as we will show lead to a relatively short cumulative heating time.

In this study, we used an infrared laser delivery system integrated onto our dual electron-ion beam system⁶⁶ to irradiate PtC_x (where x=5) deposits in the presence of a localized O₂ flow from a gas-injection system (**Figure 2a**) (see methods for details). As we will show, the laser irradiation couples to the PtC₅ matrix and photo-thermally heats the deposit and stimulates a reaction of carbon with the localized flux of O₂ molecules. Converse to our in-situ synchronized process demonstrated previously⁶⁵, no observable purification was accomplished without O₂ flow for the ex-situ laser anneal (see supporting information).

1.1.3 Results and Discussion

Figure 2b illustrates EDS measurements of a ~140 nm thick, 500x500 nm² square pattern of PtC₅ that was progressively laser irradiated with a 100 μs pulse width, 0.1% duty cycle and ~165 W/cm² optical power density under O₂ flux. Note that the laser exposure time (product of the processing time and duty cycle), is 0.1% of the actual processing times. Clearly, the carbon peak (0.277 keV) in the 5 keV beam interaction region rapidly decreases with time and suggests the purification from the PtC₅ deposit to pure platinum (in the detection limits of the EDS). A small shoulder remains in this energy range but as described previously by ref⁶¹ the small residual peak can be attributed to the Pt-N peak. Images of the progressive purification are presented in **Figure 2c**. The onset of platinum grain coarsening occurs rapidly (< 0.3 s laser exposure time) as the carbon is reduced and continues until carbon removal is complete at approximately 1.0 s. Peripheral nanoparticles appear around the edges of the deposits once exposed to the laser anneal. These particles are a result of peripheral deposition during the EBID process and can be minimized by careful selection of electron beam parameters during deposition^{67,68}.

Subsequent to the initial laser series, three laser conditions (1 and 10 μs at 1% duty cycle and 100 μs at 0.1% duty cycle) were used to simultaneously anneal 500x500 nm² PtC₅ EBID deposits of varying thicknesses (~80, 140, 260, 360 nm). **Figure 3a** illustrates the integrated and normalized carbon EDS peak of the PtC₅ deposits as a function of the effective laser exposure time for 1 μs-1% duty cycle pulses (see supporting information for EDS spectra and estimated purification rates). Higher duty cycle was used for the lower pulse width to accelerate the purification. Interestingly, the thick deposits (260 and 360 nm) were rapidly purified, whereas the thin deposits (80 and 140 nm) were unaffected by this laser treatment. **Figure 3b** illustrates

that the 10 μ s-1% laser treatment purifies the PtC₅ faster; however, thinner deposits again cure at slower rates than the thicker deposits. For deposits laser treated with the 100 μ s-0.1% duty cycle conditions (**Figure 3c**), the anneal rate was effectively independent of initial deposit height, and very quick in comparison with 1 and 10 μ s pulses.

We entertained the possibility of both pyrolytic and photolytic mechanisms for purification of the PtC₅. **Figure 4** compares SEM micrographs, normalized to a constant laser exposure time, which demonstrate the purification progression as a function of deposit thickness and laser pulse width. All deposits shown were subjected to an exposure time of 0.1 s. As illustrated in **Figure 3**, the thicker samples are purified at a higher rate than the thinner samples for 1 and 10 μ s pulse widths, whereas the deposits irradiated with 100 μ s pulses are all effectively annealed. Hence, the increase in purification rate using 100 μ s pulses is attributed to the thermal profile of the laser pulse which reaches higher temperature than the 1 and 10 μ s pulses. We conclude that photolytic purification mechanisms are not dominant, as indicated by the differences in purification with varying pulse widths at a constant exposure time. Complementary EBID lines with variable thicknesses also clearly illustrate the thickness/laser pulse width dependence on the purification (see SEM images in supporting information).

In order gain a better understanding of the laser annealing behavior, we estimated the optical and thermal properties of the PtC₅ via a simple Maxwell-Garnett model of a Pt and amorphous carbon composite. The refractive index (n) and extinction coefficient (κ) for PtC₅ material were estimated to be 1.88 and 0.31, respectively, thus the optical penetration depth ($((4\pi\kappa/\lambda)^{-1})$) was estimated to be ~ 235 nm for the PtC₅ deposits. Details of the methods used for estimating the relevant PtC_x material properties and a description of the subsequent finite difference numerical approximation method used to perform the thermal simulations may be found in the supporting information. **Figure 5a** illustrates simulated temperature profiles as a function of laser pulse width and different PtC₅ thicknesses. Clearly, the pulse width temperatures do not reach steady-state in the experimental pulse width range as the temperature for each thickness rises over the entire range studied. Due to the PtC₅ penetration depth, and low thermal conductivity, the thicker deposits are photo-thermally heated to higher temperatures relative to the optically thin deposits. Also, optically transparent SiO₂ is a good thermal insulator

and minimizes silicide formation relative to Si. These factors explain the faster annealing of the thicker deposits at short pulse widths.

We attribute the photo-thermal purification of the PtC₅ deposits to a basic reaction of the carbon matrix with the localized oxygen flux. Thus the process depends on both the temperature and oxygen concentration at the reaction front. Clearly a threshold temperature must be reached in order to drive the reaction and erosion of the carbonaceous matrix. This is evident because the laser anneal processes which result in lower simulated temperature per pulse (i.e. thin deposits at short pulse widths) do not effectively remove the carbon, despite having the same exposure time. Thermal chemical erosion of amorphous hydrogenated carbon has been shown to have a threshold of approximately 650 K⁶⁹. Furthermore high purity Pt films via chemical vapor deposition (CVD) using the MeCpPt^{IV}Me₃ precursor can be grown as low as 475 K, however an interesting enhanced growth mode is observed at ~ 550 K which is driven by an autocatalytic oxidation decomposition reaction⁷⁰. Comparing the thermal simulations with our observable purification of the PtC₅, reveals an erosion threshold of approximately 485 K for carbon in the PtC₅ deposits. The difference in the threshold temperature could be due to underestimating κ and/or overestimating n in our effective media approximation as there are different literature values in particular for amorphous carbon. Additionally, and consistent with the autocatalytic CVD process, the purification may be facilitated by catalytic O₂-Pt reactions whereby O₂ dissociatively adsorbs to create atomic oxygen, which is much more reactive and could lower the reaction temperature⁷⁰⁻⁷². The catalytic contribution will be considered more thoroughly in a future model description of the process, but recently it has been suggested in a thermally activated PtC_x purification process in which an O₂ flux is periodically pulsed⁷³. Qualitatively, the results indicate that the O₂-carbon does not effectively react in the thin deposits at 1 μ s pulse width, whereas 10 and 100 μ s laser pulse widths can effectively induce carbonaceous erosion in all of the deposit thicknesses tested here because each exceed the temperature threshold.

Figure 6a are SEM cross-sections of laser treated ~360 nm thick PtC₅ deposits at different laser exposure times (10 μ s 1% DC) which illustrates the increase in the Pt layer thickness from the top-down (see supporting information for complementary images of the other laser conditions). The asymmetric purification (left face favored purification) observed in **Figure 6a** is attributed to the geometry of the gas injection and laser delivery as both are

delivered from the left side of the SEM image. **Figure 6b** plots the resultant Pt thickness versus the laser exposure time for each laser treatment. The estimates show that for the thick deposit, each laser condition converges towards the same thickness at 0.1 s exposure time, though difficult to conclusively measure because of the topology that develops. This is consistent with the fact that each condition exceeds the activation temperature and while higher temperatures can accelerate the reaction rate, the oxygen flux eventually limits the extent of the reaction. Interestingly beyond ~ 10 nm the apparent growth rates diverge which we will address below.

Mechanistically, the picture that emerges is that each laser pulse rapidly heats the deposit, which thermally stimulates the reaction of the amorphous carbon matrix with the O_2 flux and to forms CO_x volatile by-products. Reduction of carbon in the PtC_5 deposits causes an anticipated $\sim 70\%$ volume reduction which is evident in **Figure 2c** and **Figure 6a**⁶¹. Due to the relatively high concentration of O_2 impinging on the surface, an outer shell of pure Pt initially forms. After formation of the outer Pt shell, O_2 must permeate through platinum grains and the nanoscale porosity that develops in order to sustain the purification process in the deposit interior. As the pure platinum layer nucleates and grows, the optical coupling changes due to the optical and thermal properties of pure Pt. **Figure 5b** shows simulated surface time-temperature profiles of progressively thicker platinum layers with the concomitant 70% reduction in the PtC_5 layer due to the carbon loss for a deposit with a 360 nm initial thickness (surface time-temperature profiles for other thicknesses studied in this work are reported in supporting information). The inset illustrates the simulated temperature as a function of Pt layer thickness for the different original PtC_5 thickness. An interesting interplay occurs as the platinum layer grows which varies for different original PtC_5 thickness. For the two optically thick PtC_5 deposits, the growing Pt layer decreases the temperature over the entire Pt thickness range; however the surface temperature fluctuates. At 10 nm the slight initial decrease is due to the high Pt reflectivity, which is partially compensated by the high absorption as the film thickness is close to the penetration depth of the 915 nm radiation. As the Pt layer increases beyond the penetration depth, the temperature further decreases due to the thermal mass of the additional Pt layer. We suggest that the reduced growth rate beyond 10 nm for the 360 nm thick deposit noted in **Figure 6b** is due to the temperature difference at 1, 10 and 100 μs for the thicker Pt layers.

For the optically thin layers, as the thickness approaches the Pt penetration depth (~ 10 nm), there is a positive feedback and the temperature supersedes the original surface temperature due to a significant increase in absorbance of the deposit. As the Pt layer increases beyond the penetration depth, the temperature decreases similar to the thicker deposits due to increased thermal mass.

To further illustrate the importance of the optical coupling, we also deposited 80 nm PtC₅ layers on top of thin Pt layers (5, 10, 20 nm) and irradiated the bi-layers with conditions (10 μ s and 1% DC) that otherwise do not purify the optically thin PtC₅ layers (see supporting information). As expected, the purification rate scaled with the Pt thickness as the enhanced optical coupling and reflectance associated with the pure Pt underlayer increases the temperature in the PtC₅ layer which induces the combustion reaction of the O₂ with the carbon matrix. Importantly in this case, the PtC₅/Pt layer sequence reduces the reflectance and thus increases the overall temperature during the early stages of the purification.

1.1.4 Conclusions

In summary, we have demonstrated a new pseudo-in situ technique to purify the electron beam induced deposition of PtC₅ deposits from the MeCpPt^{IV}Me₃ precursor. At the 165 W/cm² power density studied here, the temperature increases with laser pulse width. Furthermore, the composite PtC₅ material has an estimated absorption depth of 235 nm, thus the temperature is also sensitive to the deposit thickness. A threshold temperature of ~ 485 K was estimated via simulations, which is lower than previously determined amorphous carbon combustion with O₂. The reduced threshold is either an artifact of our effective medium approximation or perhaps the process is catalytically assisted by dissociative adsorption of O₂ into more reactive atomic oxygen. A complex interplay ensues as the Pt layer grows which not only changes the optical coupling and thus the photo-thermal heating, but also the in- and out-diffusion of the oxygen reactant and CO_x product.

As for our perspective on future work, we comment briefly. To purify thicker deposits, a multilayer deposit/purification sequence may be required similar to what Mehendale et al⁶⁰ demonstrated for a heated substrate process. In the limit, we suggest that an atomic layer deposition-like (ALD) process could be viable. While selective ALD deposits have been

demonstrated using EBID deposits to locally catalyze reactions³⁹, a truly direct-write ALD process is envisioned. Namely, the initial nanoscale half-reaction would be stimulated by the focused electron beam in the presence of the $\text{MeCpPt}^{\text{IV}}\text{Me}_3$ precursor to create thin PtC_x patterns. Subsequently a synchronized laser pulse in the presence of oxygen would photo-thermally stimulate the carbon reduction half reaction to create pure nanostructures.

1.1.5 Methods

Electron beam induced deposition (EBID) was performed in an FEI Nova Nanolab 600 Dual Beam system. Silicon substrates with a thermally grown 100 nm SiO_2 oxide were plasma cleaned (XEI Scientific, Inc, Evactron) in the chamber for a minimum of 30 min prior to deposition. All PtC_5 EBID structures in this study were grown with the $\text{MeCpPt}^{\text{IV}}\text{Me}_3$ precursor at a chamber pressure of $\sim 1.2 \times 10^{-5}$ mbar and the gas nozzle $\sim 100 \mu\text{m}$ above the substrate. EBID pads were grown to varying thicknesses by changing the number of electron passes or loops (1000, 2000, 4000, and 8000 loops) in a $500 \text{ nm} \times 500 \text{ nm}$ square pattern. The corresponding heights of these deposits are approximately 80, 140, 260, and 360 nm, respectively. Each pad pattern was deposited at 5 keV energy, 98 pA current, 10 μs dwell time, and a pixel pitch of 13.55 nm (50% overlap). Subsequent to deposition, the chamber was pumped for at least 30 minutes prior to laser annealing to minimize residual $\text{MeCpPt}^{\text{IV}}\text{Me}_3$ precursor in the chamber.

A 915 nm wavelength 25 W multi-chip diode laser module (Oclaro, BMU25B-915-01) driven by an IXYS PCX-7410 pulsed diode laser driver was used to anneal the EBID deposits. The laser delivery system (OmniProbe, Inc.) was mounted $\sim 38^\circ$ relative to the substrate normal and precisely delivers a beam size of $\sim 100 \mu\text{m}$ diameter, as schematically shown in **Figure 2a**. During laser irradiation, O_2 gas was delivered to the area of interest with an OmniGIS I (Oxford Instruments) gas injection system, which was positioned $100 \mu\text{m}$ above the substrate and $200 \mu\text{m}$ from the center of the field of view. The gas temperature was set to 25°C and the valve pulse rate was set such that the chamber pressure was 1.2×10^{-5} mbar. Due to the GIS needle position and the $100 \mu\text{m}$ laser spot size, large deposits within the entire laser spot can be annealed in a parallel manner. If larger areas need to be purified, we envision that sequential stage motions could be implemented to raster the area of interest under the focused laser with an appropriate beam overlap strategy employed. During this study, varying laser pulse widths (1, 10, and 100

μs) and duty cycles (0.1% and 1%) were used at a constant optical power density of $\sim 165 \text{ kW/cm}^2$. Pulse width and duty cycle combinations were selected in such a way to provide adequate cooling time between pulses for the substrate to return to room temperature. Obviously the specific laser conditions are a function of the deposit and the substrate and thus different substrates will have different optimum conditions; thus, understanding both the laser absorption and the subsequent thermal diffusion is critical and for extremely delicate substrates, for instance membranes, thermal stresses need to be considered (see ref.⁶⁵ for instance). More information on the laser delivery system can be found in ref.⁷⁴.

Energy dispersive x-ray spectroscopy (EDS) was performed with an EDAX Genesis X-ray Microanalysis System also mounted on the dual beam system, thus the samples were not exposed to atmosphere. Each spectrum was recorded with beam conditions of 5 kV and 1.6 nA and a 30 second acquisition time. A 100 nm SiO_2 coated silicon substrate EDS scan was used to determine background for data analysis and peak fitting (see supporting information for EDS analysis description).

1.1.6 Appendix

1.1.6.1 Supporting Information

O₂ Versus no O₂ Laser Anneal

Figure 7 demonstrates the significance of the O₂ flow to successfully purify PtC₅ deposits. Here, we compare EDS plots of an annealed sample irradiated for 60s with the 100 μ s and 0.1% duty cycle anneal with and without O₂ flow at a chamber pressure of $\sim 1 \times 10^{-5}$ mbar. Clearly, with the O₂ flux, the carbon content was effectively reduced to form a purified Pt deposit. Without the O₂ flux (laser only at a chamber pressure of $\sim 2 \times 10^{-6}$ mbar), no observable purification was achieved. Therefore, we conclude that the purification process involves a photothermally stimulated reaction of O₂ with the amorphous carbon matrix, which forms CO_x volatile by-products and reduces carbon content in the deposit.

EDS Spectra and Quantitative Analysis

Figure 8a-c displays EDS spectra for the 2000 pass (140 nm original height) PtC₅ deposits annealed under various laser conditions. These are examples of the raw EDS spectra used to determine the purity of the deposits. The carbon content, and hence purification, reported in **Figure 3** of the main text was estimated by using a peak fitting technique. Specifically, a background EDS spectra of the SiO₂ substrate was subtracted from each of the raw EDS spectra of the deposits. All EDS peaks (namely carbon (0.277 keV), oxygen (0.523 keV), silicon (1.74 keV), and platinum (2.048 keV)) were then fit with a Gaussian curve:

$$y = y_0 + \frac{Ae^{\frac{-4 \ln(2)(x-x_c)^2}{w^2}}}{w \sqrt{\frac{\pi}{4 \ln(2)}}} \quad [1]$$

where x_c is the center of the EDS peak, A is the amplitude, and w is the full-width at half-maximum. Using equation 1, the area under the curve was taken to be a measure of elemental concentration. Due to difference in EDS yield between carbon and platinum, we report solely the normalized carbon content to give an indication of deposit purity. Hence, when the area of the carbon peak (0.277 keV) was reduced, this indicates purification of the deposit.

Purification Rates Estimated from EDS (Figure 3)

The slopes (instantaneous purification rate) of the normalized carbon intensity versus laser exposure time were measured for each film thickness and laser condition and are illustrated

in **Figure 9** below. The thickness dependence of the purification rate is clearly demonstrated in **Figure 9a** and **b** where the thicker PtC₅ deposits purify to the EDS penetration depth first. While variations in the instantaneous purification rates can be estimated for the 100 µs-0.1% DC anneals, the fluctuations are likely dominated by experimental error. All of the thicknesses appear to purify at a similar rate of ~ 1100 %C/S.

Anneal Progression

Figure 10 is a compilation of scanning electron images of different thickness (50, 70, 95, and 150 nm) lines exposed at progressively longer exposure times and similar laser conditions as in **Figure 3**. EBID line patterns were deposited with 5 kV energy, 28 pA current, 3 µs dwell time, and a pixel pitch of 5 nm. A varying number of electron loops (10,000, 15,000, 20,000 and 50,000) were applied to achieve heights of approximately 50, 70, 95, and 150 nm and widths of approximately 55 nm, 75 nm, 95 nm, and 115 nm, respectively. **Figure 10** corroborates the EDS results for the square pattern EDS results in **Figure 3**; the thicker lines are preferentially purified for 1 and 10 µs pulse widths and 1% duty cycle, whereas all the lines are simultaneously purified at the 100 µs pulse width and 0.1% duty cycle.

Thermal Simulations

T(r,z,t) by finite difference numerical approximation method

The heat equation as it pertains to the particular cylindrical geometry of interest here is;

$$c_p \rho \frac{\partial T(r, z)}{\partial t} = \frac{1}{r} \frac{\partial}{\partial r} \left(r k(r, z) \frac{\partial T(r, z)}{\partial r} \right) + \frac{\partial}{\partial z} \left(k(r, z) \frac{\partial T(r, z)}{\partial z} \right) + Q(r, z, t) \quad [1]$$

where c_p is the heat capacity, ρ is the density, $T(r, z)$ is the radial (r) and depth (z) dependent temperature, $k(r, z)$ is the space-dependent thermal conductivity and $Q(r, z, t)$ includes the applied laser pulse ($J/m^3 s$). The cylindrical coordinate θ is removed for symmetry reasons: cylindrical deposits were considered in numerical simulations as models for the square prism PtC_x structures deposited in real experiments. In the discussion of the numerical approximation used to estimate the time evolving temperature directly below, $Q(r, z, t)$ is omitted for convenience and the details related to this term is presented later. Applying the multi-variable product rule to equation [1] yields;

$$c_p \rho \frac{\partial T(r, z)}{\partial t} = \frac{k(r, z)}{r} \frac{\partial T(r, z)}{\partial r} + \frac{\partial k(r, z)}{\partial r} \frac{\partial T(r, z)}{\partial r} + k(r, z) \frac{\partial^2 T(r, z)}{\partial r^2} + \frac{\partial k(r, z)}{\partial z} \frac{\partial T(r, z)}{\partial z} + k(r, z) \frac{\partial^2 T(r, z)}{\partial z^2} \quad [2]$$

An explicit, time–marching, finite difference numerical approximation method was used to estimate the solution to equation [2] as a function of time and space. A schematic of the numerical mesh used to solve the equation in space is shown in **Figure 11**. A variable mesh spacing was imposed in both the radial and depth coordinates in order to yield a tractable simulation time because the ultraviolet laser absorption depth requires a very small mesh size ($\sim 10 \text{ nm}$) while, e.g., the large radial laser beam size used in experiments (10^4 nm), requires a large maximum radius in order that the constant temperature boundary condition, imposed at the maximum radius, does not influence the final solution. The small mesh size ($\sim 10^1 \text{ nm}$) forces a very small time step so that the only reasonable method to reduce the total simulation time is to reduce the number of interior spatial nodes in the simulation domain.

The mesh geometry shown in **Figure 11a** defines two basic geometrical elements within the simulation domain; (a) cylindrical elements at the ($r = 0$) mesh nodes and (b) annular disks at all other locations. The indices in parentheses indicate the radial and depth coordinates, respectively (see **Figure 11c**). In order to account for the spatial dependence of the thermal conductivity, simulation domain temperatures were estimated at intermediate mesh locations which correspond to the interfaces between the geometrical elements. These interface temperatures were estimated by balancing the heat flux at the mathematical interfaces between the geometrical elements at each time step Δt ;

$$k(r, z) \frac{\partial T(r, z)}{\partial r} \Big|_{[-\delta r]} = k(r, z) \frac{\partial T(r, z)}{\partial r} \Big|_{[+\delta r]} \quad [3]$$

where $-\delta r$ and $+\delta r$ indicate opposing sides of the mathematical interface between elements. In reference to the meshes in **Figure 11b-c**, this equation may be rewritten as;

$$k_{(1,2)} \frac{T_{(\frac{3}{2},2)} - T_{(1,2)}}{\Delta r_1} = k_{(2,2)} \frac{T_{(2,2)} - T_{(\frac{3}{2},2)}}{\Delta r_1} \quad [4]$$

which rearranging, yields

$$T_{(\frac{3}{2},2)} = \frac{k_{(1,2)} T_{(1,2)} + k_{(2,2)} T_{(2,2)}}{k_{(1,2)} + k_{(2,2)}} \quad [5]$$

for the temperature at the boundary between volume elements, but in terms of the primary spatial node positions. In this way, the term including dk/dr in equation [2] may be neglected as it is inherently included by using equations [4] and [5]. Ultimately, this method was used to estimate the temperature change at the interior nodes with the annular disk geometry as shown in equation [6] as will be shown in steps below. Alternatively, equation [2] may be recast in terms of the heat flux across the interfaces of each mesh element while inherently accounting for the temperature dependence of the thermal conductivity material property, e.g., using equation [7] below. This form method was used for the case of the cylindrical elements located at ($r = 0$).

Annular Disk geometry

$$\frac{\partial T_{(2,2)}}{\partial t} = \frac{k_{(2,2)}}{c_{p(2,2)}\rho_{(2,2)}r_2} \frac{\partial T_{(2,2)}}{\partial r} + \frac{k_{(2,2)}}{c_{p(2,2)}\rho_{(2,2)}} \frac{\partial^2 T_{(2,2)}}{\partial r^2} + \frac{k_{(2,2)}}{c_{p(2,2)}\rho_{(2,2)}} \frac{\partial^2 T_{(2,2)}}{\partial z^2} \quad [6]$$

$$\frac{\partial T_{(2,2)}}{\partial t} = \frac{k_{(2,2)}}{c_{p(2,2)}\rho_{(2,2)}} \left\{ \frac{-2\pi r_{c(1)} dh_{(1)} \frac{\partial T_{(2,2)}}{\partial r} \Big|_{[-r]} + 2\pi r_{c(2)} dh_{(1)} \frac{\partial T_{(2,2)}}{\partial r} \Big|_{[+r]} - \pi(r_{c(2)}^2 - r_{c(1)}^2) \frac{\partial T_{(2,2)}}{\partial z} \Big|_{[-z]} + \pi(r_{c(2)}^2 - r_{c(1)}^2) \frac{\partial T_{(2,2)}}{\partial z} \Big|_{[+z]}}{\pi(r_{c(2)}^2 - r_{c(1)}^2) dh_{(1)}} \right\} \quad [7]$$

For example, at the ($r = 0$) nodes, equation [7] may be written as;

Cylindrical geometry

$$\frac{\partial T_{(1,2)}}{\partial t} = \frac{k_{(1,2)}}{c_{p(1,2)}\rho_{(1,2)}} \left\{ \frac{2\pi r_{c(1)} dh_{(1)} \frac{\partial T_{(1,2)}}{\partial r} \Big|_{[+r]} - \pi r_{c(1)}^2 \frac{\partial T_{(1,2)}}{\partial z} \Big|_{[-z]} + \pi r_{c(1)}^2 \frac{\partial T_{(1,2)}}{\partial z} \Big|_{[+z]}}{\pi r_{c(1)}^2 dh_{(1)}} \right\} \quad [8]$$

Taylor series expansions, truncated at the 3rd derivative, were then used to estimate the spatial derivatives required in equations [6] & [8] using the interfacial temperatures described by equation [5]. For example, the first derivative in the radial dimension was estimated for the annular disk geometry and cylindrical geometry using equations [9] and [10];

$$T_{(\frac{3}{2},2)} \cong T_{(2,2)} - \Delta r_1 \frac{\partial T_{(2,2)}}{\partial r} + \frac{\Delta r_1^2}{2} \frac{\partial^2 T_{(2,2)}}{\partial r^2} \quad [9]$$

$$T_{(\frac{5}{2},2)} \cong T_{(2,2)} + \Delta r_2 \frac{\partial T_{(2,2)}}{\partial r} + \frac{\Delta r_2^2}{2} \frac{\partial^2 T_{(2,2)}}{\partial r^2} \quad [10]$$

Multiplication of equation [9] by $-\Delta r_2^2$, multiplication of equation [10] by Δr_1^2 and then solving both equations simultaneously for the first derivative yielded;

$$\frac{\partial T_{(2,2)}}{\partial r} \cong \frac{\Delta r_1^2 T_{(\frac{5}{2},2)} - (\Delta r_1^2 - \Delta r_2^2) T_{(2,2)} - \Delta r_2^2 T_{(\frac{3}{2},2)}}{\Delta r_1 \Delta r_2^2 + \Delta r_1^2 \Delta r_2} \quad [11]$$

Inserting the interface temperatures into equation [11] gives;

$$\frac{\partial T_{(2,2)}}{\partial r} \cong \frac{\Delta r_1^2 \left[\frac{k_{(2,2)}T_{(2,2)} + k_{(3,2)}T_{(3,2)}}{k_{(2,2)} + k_{(3,2)}} \right] - (\Delta r_1^2 - \Delta r_2^2)T_{(2,2)} - \Delta r_2^2 \left[\frac{k_{(1,2)}T_{(1,2)} + k_{(2,2)}T_{(2,2)}}{k_{(1,2)} + k_{(2,2)}} \right]}{\Delta r_1 \Delta r_2^2 + \Delta r_1^2 \Delta r_2} \quad [12a]$$

Similarly, equation [12a] applies to the depth dimension;

$$\frac{\partial T_{(2,2)}}{\partial z} \cong \frac{\Delta h_1^2 \left[\frac{k_{(2,2)}T_{(2,2)} + k_{(2,3)}T_{(2,3)}}{k_{(2,2)} + k_{(2,3)}} \right] - (\Delta h_1^2 - \Delta h_2^2)T_{(2,2)} - \Delta h_2^2 \left[\frac{k_{(2,1)}T_{(2,1)} + k_{(2,2)}T_{(2,2)}}{k_{(2,1)} + k_{(2,2)}} \right]}{\Delta h_1 \Delta h_2^2 + \Delta h_1^2 \Delta h_2} \quad [12b]$$

In a similar procedure, the second derivative may be estimated from equations [9] and [10];

$$\frac{\partial^2 T_{(2,2)}}{\partial r^2} \cong 2 \frac{\Delta r_1 T_{(\frac{5}{2},2)} - (\Delta r_1 + \Delta r_2)T_{(2,2)} + \Delta r_2 T_{(\frac{3}{2},2)}}{\Delta r_1 \Delta r_2^2 + \Delta r_1^2 \Delta r_2} \quad [13a]$$

and in the depth coordinate;

$$\frac{\partial^2 T_{(2,2)}}{\partial z^2} \cong 2 \frac{\Delta h_1 T_{(2,\frac{5}{2})} - (\Delta h_1 + \Delta h_2)T_{(2,2)} + \Delta h_2 T_{(2,\frac{3}{2})}}{\Delta h_1 \Delta h_2^2 + \Delta h_1^2 \Delta h_2} \quad [13b]$$

An estimate of the temperature change for the annular disk geometry resulted from combining equations [5], [6], [12a], [13a] and [13b];

$$\begin{aligned} \frac{\Delta T_{(2,2)}}{\Delta t} \cong & \frac{k_{(2,2)}}{c_{p(2,2)}\rho_{(2,2)}r_2} \frac{\Delta r_1^2 \left[\frac{k_{(2,2)}T_{(2,2)} + k_{(3,2)}T_{(3,2)}}{k_{(2,2)} + k_{(3,2)}} \right] - (\Delta r_1^2 - \Delta r_2^2)T_{(2,2)} - \Delta r_2^2 \left[\frac{k_{(1,2)}T_{(1,2)} + k_{(2,2)}T_{(2,2)}}{k_{(1,2)} + k_{(2,2)}} \right]}{\Delta r_1 \Delta r_2^2 + \Delta r_1^2 \Delta r_2} \\ & + \frac{k_{(2,2)}}{c_{p(2,2)}\rho_{(2,2)}} 2 \frac{\Delta r_1 \left[\frac{k_{(2,2)}T_{(2,2)} + k_{(3,2)}T_{(3,2)}}{k_{(2,2)} + k_{(3,2)}} \right] - (\Delta r_1 + \Delta r_2)T_{(2,2)} + \Delta r_2 \left[\frac{k_{(1,2)}T_{(1,2)} + k_{(2,2)}T_{(2,2)}}{k_{(1,2)} + k_{(2,2)}} \right]}{\Delta r_1 \Delta r_2^2 + \Delta r_1^2 \Delta r_2} \\ & + \frac{k_{(2,2)}}{c_{p(2,2)}\rho_{(2,2)}} 2 \frac{\Delta h_1 \left[\frac{k_{(2,2)}T_{(2,2)} + k_{(2,3)}T_{(2,3)}}{k_{(2,2)} + k_{(2,3)}} \right] - (\Delta h_1 + \Delta h_2)T_{(2,2)} + \Delta h_2 \left[\frac{k_{(2,1)}T_{(2,1)} + k_{(2,2)}T_{(2,2)}}{k_{(2,1)} + k_{(2,2)}} \right]}{\Delta h_1 \Delta h_2^2 + \Delta h_1^2 \Delta h_2} \quad [14] \end{aligned}$$

A forward differencing scheme was required to approximate the first derivative at the interior radial boundary node ($r = 0$) in order to retain numerical approximation accuracy in the absence of an internal nearest neighbor node. In this case, the following truncated Taylor series equations used were;

$$T_{(\frac{3}{2},2)} \cong T_{(1,2)} + \Delta r_1 \frac{\partial T_{(1,2)}}{\partial r} + \frac{\Delta r_1^2}{2} \frac{\partial^2 T_{(1,2)}}{\partial r^2} \quad [15]$$

$$T_{(2,2)} \cong T_{(1,2)} + 2\Delta r_1 \frac{\partial T_{(1,2)}}{\partial r} + \frac{4\Delta r_1^2}{2} \frac{\partial^2 T_{(1,2)}}{\partial r^2} \quad [16]$$

Multiplying equation [15] by -4 and then solving equations [15] and [16] for the first derivative yields;

$$\frac{\partial T_{(1,2)}}{\partial r} = \frac{T_{(2,2)} - 4T_{(\frac{3}{2},2)} + 3T_{(1,2)}}{-2\Delta r_1} \quad [17]$$

Inserting the relevant interface temperatures into equation [17] and rearranging gives;

$$\frac{\partial T_{(1,2)}}{\partial r} = \frac{\left[1 - 4 \frac{k_{(2,2)}}{k_{(1,2)} + k_{(2,2)}}\right] T_{(2,2)} + \left[3 - 4 \frac{k_{(1,2)}}{k_{(1,2)} + k_{(2,2)}}\right] T_{(1,2)}}{-2\Delta r_1} \quad [18a]$$

Similarly, equation [18a] applies to the depth dimension;

$$\frac{\partial T_{(2,1)}}{\partial z} = \frac{\left[1 - 4 \frac{k_{(2,2)}}{k_{(2,1)} + k_{(2,2)}}\right] T_{(2,2)} + \left[3 - 4 \frac{k_{(2,1)}}{k_{(2,1)} + k_{(2,2)}}\right] T_{(2,1)}}{-2\Delta h_1} \quad [18b]$$

An estimate of the temperature change for the cylindrical element geometry resulted from combining equations [8], [13b] and [18a];

$$\frac{\Delta T_{(1,2)}}{\Delta t} = \frac{k_{(1,2)}}{c_{p(1,2)}\rho_{(1,2)}} \left\{ \frac{2\pi r_{c(1)} dh_{(1)} \left(\frac{\left[1 - 4 \frac{k_{(2,2)}}{k_{(1,2)} + k_{(2,2)}}\right] T_{(2,2)} + \left[3 - 4 \frac{k_{(1,2)}}{k_{(1,2)} + k_{(2,2)}}\right] T_{(1,2)}}{-2\Delta r_1} \right)}{\pi r_{c(1)}^2 dh_{(1)}} \right. \\ \left. + 2 \frac{\Delta h_1 \left[\frac{k_{(2,2)} T_{(2,2)} + k_{(2,3)} T_{(2,3)}}{k_{(2,2)} + k_{(2,3)}} \right] - (\Delta h_1 + \Delta h_2) T_{(2,2)} + \Delta h_2 \left[\frac{k_{(2,1)} T_{(2,2)} + k_{(2,2)} T_{(2,2)}}{k_{(2,1)} + k_{(2,2)}} \right]}{\Delta h_1 \Delta h_2^2 + \Delta h_1^2 \Delta h_2} \right\} \quad [19]$$

Constant temperature boundary conditions were applied at the maximum radius and maximum depth;

$$T(r = r_{max}) = 298K \quad T(z = z_{max}) = 298K \quad [20]$$

An insulating boundary conditions was applied at ($z = 0$);

$$\frac{\partial T(z = 0)}{\partial z} = 0 \quad [21]$$

Pulsed Laser Irradiation

The laser beam intensity I (J/m^2s) was included in the simulation using the following expression;

$$I(r, z) = (1 - R) \frac{P(t)}{2\pi\sigma^2} e^{-\frac{r^2}{2\sigma^2}} e^{-\alpha(r,z)dz} \quad [22]$$

where R is the thin film stack reflectivity, $P(t)$ is the time-dependent laser beam power, σ determines the radius of the beam, and $\alpha(r,z)$ is material dependent absorption coefficient. The reflectivity of the thin film stack was determined using Rouard's method¹ (**Figure 12**). The optical constants of PtC_5 were estimated using the Maxwell-Garnett effective medium approximation assuming that Pt was the inclusion phase and amorphous carbon the matrix constituent². Pt occupies 14% of the available volume in PtC_5 (based on $\rho_{Pt}=21.1$ and $\rho_{a-C}=1.25$

g/cm^3) with $n=3.2$ and $\kappa=5.4$ while $n=1.5$ and $\kappa=0.2$ for the α -C (amorphous carbon) matrix. Application of the Maxwell–Garnett effective medium approximation yielded $n=1.87$ and $\kappa=0.31$ for PtC_5 . The laser power was assumed to exhibit a linear rise (τ_{rise}) over the initial $250ns$ after initiating the laser pulse up to maximum power of $12W$. Beyond $250ns$, the power was held constant over the complete temporal pulse width (τ_{beam}) which was variable in this study from $1\mu s$ to $100\mu s$. The beam power was set to zero immediately after τ_{beam} . The spatially dependent absorption depth;

$$\alpha(r, z) = \frac{4\pi\kappa(r, z)}{\lambda} \quad [23]$$

was calculated using electromagnetic simulations of the electromagnetic field propagation in the thin film stack using FlexPDE® a finite element numerical solver. This additional simulation was necessary to account for a complex electric field absorption profile in the thin film stacks due to the multiple reflecting interfaces present. The electric field distributed in the thin film stack was solved using two partial differential equations considering the real (E_r) and imaginary (E_i) components of the electric field, respectively;

$$\nabla^2 E_{xr}(z) = -\frac{4\pi^2 c^2 \mu_o \epsilon_o (n(z)^2 - \kappa(z)^2)}{\lambda^2} E_{xr}(z) - \frac{4\pi c \mu_o n(z) \kappa(z) \epsilon_o}{\lambda} E_{xi}(z) \quad [24a]$$

$$\nabla^2 E_{xi}(z) = -\frac{4\pi^2 c^2 \mu_o \epsilon_o (n(z)^2 - \kappa(z)^2) \epsilon_o}{\lambda^2} E_{xi}(z) + \frac{4\pi c \mu_o n(z) \kappa(z) \epsilon_o}{\lambda} E_{xr}(z) \quad [24b]$$

A monochromatic plane wave was set to impinge at normal incidence to the stack surface where the stack depth coordinate was (z) and the electric field oscillated in the (x) coordinate. The complementary magnetic induction in the (y) coordinate was then calculated from the solution of [24a] and [24b] using;

$$B_{yr}(z) = \frac{\lambda}{2\pi c} \frac{\partial E_{xi}}{\partial z} \quad [25a]$$

$$B_{yi}(z) = -\frac{\lambda}{2\pi c} \frac{\partial E_{xr}}{\partial z} \quad [25b]$$

The simulation domain consists of a vacuum region beginning at $z = 0$ and extending to a width equal to the wavelength of the incident light, e.g., $915nm$. The thin film stack begins at $z = \lambda$. The vacuum boundary condition was set to;

$$E_{xr}(z = 0) = -\sqrt{2\mu_o c \frac{P}{\pi \sigma^2}} \left[\frac{V}{m} \right] \quad [26a]$$

$$E_{xi}(z = 0) = 0 \quad \left[\frac{V}{m} \right] \quad [26b]$$

The tangential component of the electric field was continuous at the thin film stack interfaces as required by Maxwell's equations. The final film stack layer was the Si substrate. Electric field profiles for a light wave with a 915nm wavelength irradiating the $80\text{nm PtC}_5/20\text{nmPt}/100\text{nmSiO}_2/\text{Si}$ stack is provided in **Figure 13**. The non-reflecting boundary condition was imposed at this boundary in order to avoid artificial reflections back into the film stack;

$$\frac{\partial E_{xr}(z = z_{\max})}{\partial z} = \frac{2\pi n_{\text{Si}}}{\lambda} E_{xi} \quad [27a]$$

$$\frac{\partial E_{xi}(z = z_{\max})}{\partial z} = -\frac{2\pi n_{\text{Si}}}{\lambda} E_{xr} \quad [27b]$$

The time-averaged intensity in the film was estimated from the electric and magnetic fields;

$$\bar{I} = \frac{1}{2\mu_0} \left\{ \frac{1}{T} \int_T (E_{xr}(z)\cos(\omega t) - E_{xi}(z)\sin(\omega t))(B_{yi}(z)\sin(\omega t) - B_{yr}\cos(\omega t)) dt \right\} \left[\frac{W}{m^2} \right] \quad [28]$$

Intensity profiles in two experimentally relevant thin film stacks are shown in **Figure 14**. These complex intensity profiles within the thin film stack layers were then fitted in each material region in order to derive a more accurate form of $I(r, z)$, e.g., replacing equation [22], when necessary. In the case of a buried *Pt* layer lying underneath the *PtC*₅ deposit, intensity profiles diverged significantly from a simple prediction using, for example, the Beer-Lambert approach (dotted blue curve, **Figure 14**) where finite element simulations revealed that more absorption is expected in the *PtC*₅ layer due to a relatively high reflectivity at the *PtC*₅/*Pt* interface.

Thermal Profiles

Optical and thermal properties calculated using the Maxwell-Garnett model, described above, were used to simulate temperature profiles for the deposits of varying thicknesses. The volumetric reduction of deposits with carbon removal (~70%), and the nucleation of a pure *Pt* shell during the purification process was taken into effect to generate time-temperature profiles with varying pure *Pt* shell thickness. **Figure 15** reflects the dynamic thermal profiles of the deposits during the purification process (as the pure *Pt* shell thickens). The complicated interplay between light absorption, light reflection, and the pure *Pt* shell thermal mass combine to result in a thermal profile which varies with the thickness of the outer *Pt* shell. As the shell becomes exceedingly thick, a larger thermal mass limits the maximum temperature achieved per pulse. The limited temperature, along with a relatively low gas diffusion coefficient in the pure *Pt* layer, act in concert to reduce the purification rate deep within the deposit.

Optical Coupling

To illustrate optical coupling of the laser to the region of interest, $1\ \mu\text{m} \times 1\ \mu\text{m}$ thin Pt boxes (which have a high absorption coefficient at 915 nm $k = 5.4$ and a penetration depth of $\sim 13.5\ \text{nm}$) were synthesized and then optically thin ($\sim 80\text{nm}$) PtC_5 layers were deposited half-on and half-off the Pt layers (see S10a for schematic). The thin Pt layers were synthesized via EBID patterning PtC_5 on the Si/SiO₂ substrate which was subsequently purified under electron-beam irradiation and 25°C O₂ flux to achieve a pure Pt deposit. An 80 nm PtC_5 EBID deposit was subsequently deposited half-on and half-off of the pure Pt deposit to test the effects of optical coupling to the underlying substrate (thin Pt vs. SiO₂). **Figure 16** demonstrates the preferential purification of the PtC_5 deposit after 0.3 s exposure time with a 10 μs pulse width and 1% duty cycle as a function of the Pt substrate thickness ($\sim 5, 10, 20\ \text{nm}$). As the underlying pure Pt substrate increases in thickness, the preferential purification of the top PtC_5 deposit increases. EDS spectra of this purification is demonstrated in **Figure 17a**. The visual increase in purification with underlying Pt thickness is because the photon penetration depth of 915 nm wavelength light in pure Pt is $\sim 13.5\ \text{nm}$, therefore as shown in simulated time-temperature simulations (**Figure 17b**), the photothermal heating in the thicker Pt substrate is greater. Clearly, the high absorption of the underlying Pt layer causes a significant increase in photothermal heating of the deposit in comparison to the 80 nm deposit on SiO₂. Substrate-dependent preferential curing may provide a method to use lithographically patterned thin films as nucleation sites for preferential or selective curing of EBID patterns using otherwise mild laser conditions. **Figure 17c** further illustrates the fraction of laser pulse time which exceeds the threshold temperature for an 80 nm PtC_5 deposit, as a function of Pt coupling layer thickness. The underlying coupling layer significantly increases the time above threshold temperature for all pulse widths and accelerates the purification process.

Deposit Cross-sections

Figure 18 shows cross-section images of thick PtC_5 deposits at a variety of times and laser conditions. The purification of the PtC_5 deposits during the laser-O₂ anneal is a top-down process. As illustrated, oxygen molecules are necessary to react with the carbonaceous matrix in order for purification to occur. As the deposits are annealed, the outer surface of the deposit first reacts and densifies which creates a pure Pt shell. As the dense shell thickens, optical coupling is

enhanced up to the penetration depth which likely facilitates the diffusion of O₂ into the deposit to enable further purification. **Figure 6** (in the main text) illustrates the purification thickness versus laser exposure time for the 3 laser conditions attempted. Clearly the purification rate (slope) decreases with increasing exposure time. This is due to a combination of effects such as slower in- and out-diffusion of the reactants and products and as demonstrated in **Figure 3** and discussed in the text, as the platinum layer thickens the temperature actually decreases due to the increased thermal mass of the Pt layer. In our experimental setup, the gas injection system was mounted at a high-angle port in the SEM chamber, and gas flux and the laser irradiation comes from the left side of the deposits with respect to the images reported here. Clearly, the left side of the deposits purified at a higher rate than the right side since incident gas flux provides reactive species for purification. This is further proof of the necessity of O₂ flux during the purification process and suggests an O₂ mass transport limited regime. The laser conditions also had a noticeable effect on the progression of the deposit purification. Particularly profound is the morphology of the pure Pt for deposits annealed with 100 μ s and 10 μ s versus deposits annealed at 1 μ s. The deposits annealed with 1 μ s pulse width forms channels of pure Pt, as opposed to a smooth shell. This is likely because, shorter laser pulse widths (and lower temperatures) do not allow grain growth and coalescence of Pt grains to form the smooth Pt film.

1.1.6.2 Figures

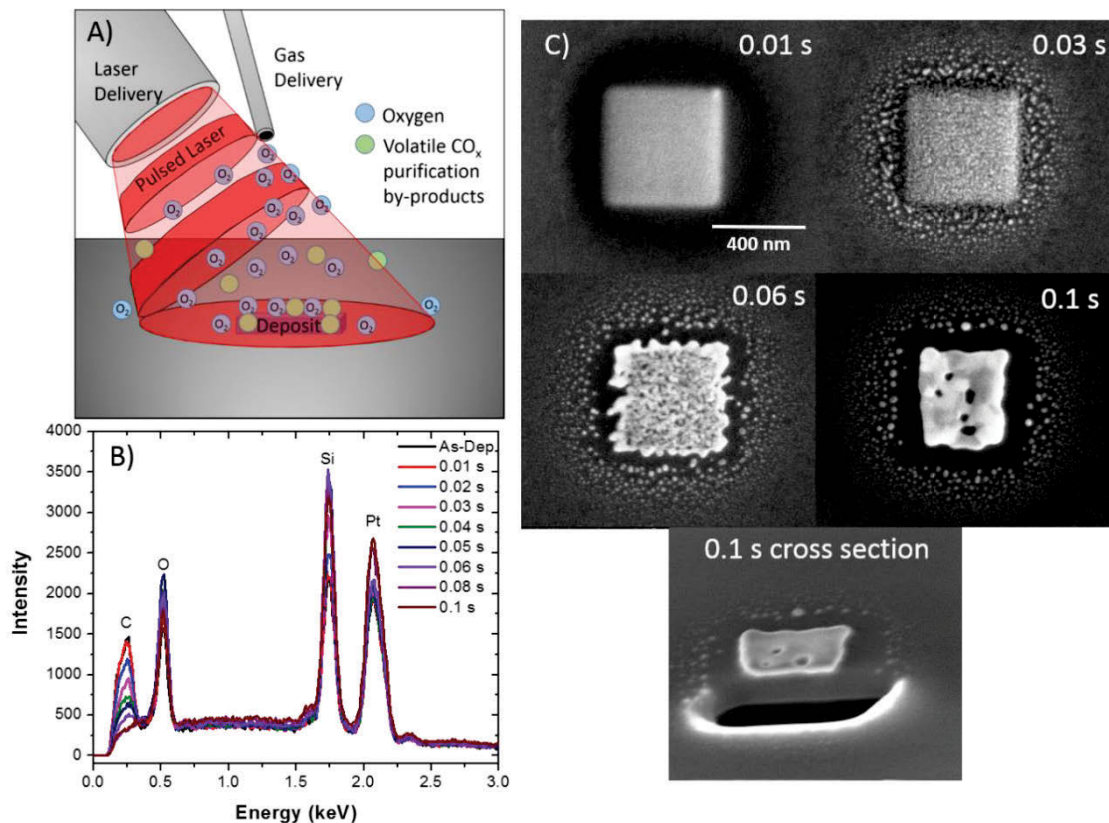


Figure 2. (a) Schematic of the laser annealing setup with approximately 100 μm laser spot size under O₂ flow. (b) EDS measurements of a ~ 140 nm thick PtC₅ EBID deposit annealed with 100 μs pulses at 0.1% duty cycle as a function of exposure times. (c) Images of laser annealed patterns at different exposure times. The deposit annealed for 0.1s exposure time was also cross-sectioned and pictured here.

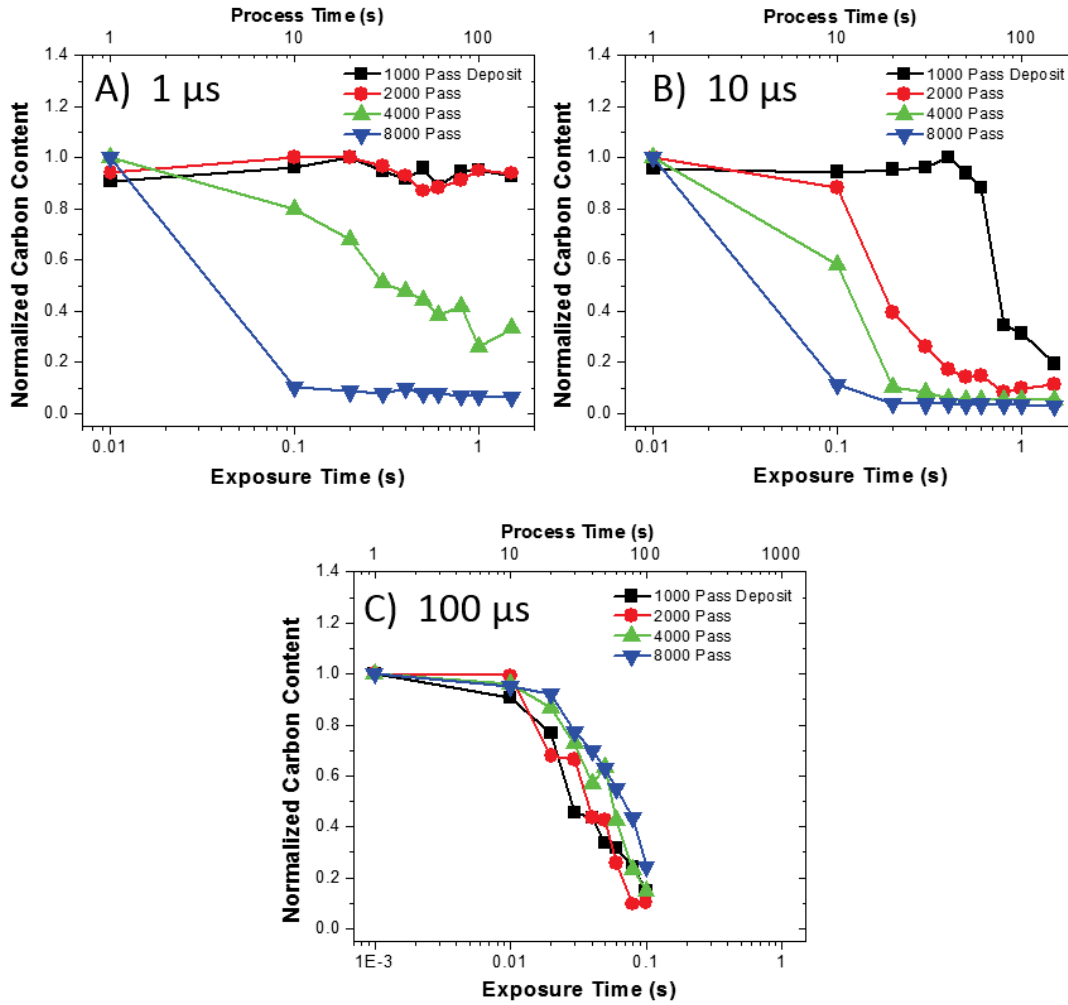


Figure 3. (a) Carbon content as a function of exposure time (duty cycle x process time, bottom axis) and process time (top axis) for 1 μ s at 1% duty cycle, (b) 10 μ s at 1% duty cycle, and (c) 100 μ s at 0.1% duty cycle. Initial pad thicknesses were \sim 80, 140, 260, and 350 nm thick, respectively.

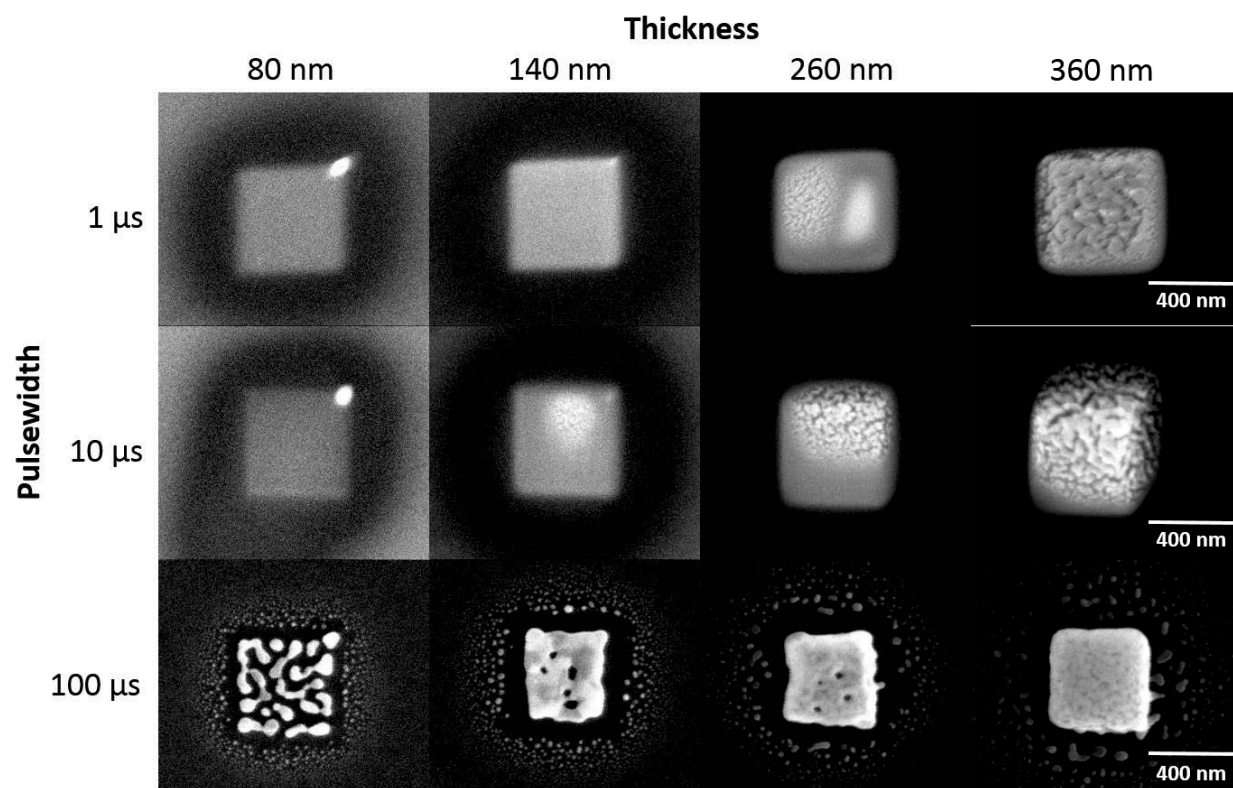


Figure 4. Scanning electron images of PtC₅ deposits of varying thicknesses and anneal pulse widths that were annealed for 0.1 s of laser exposure time.

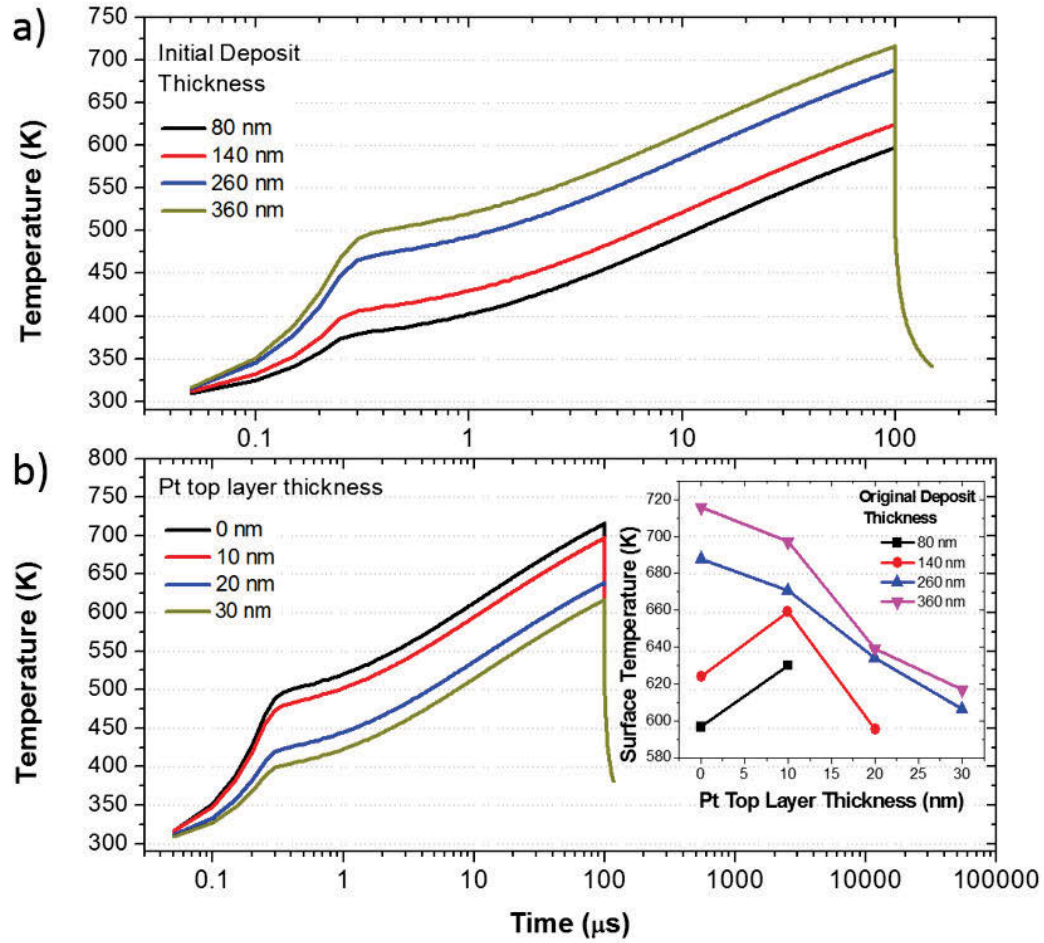


Figure 5. (a) Time-temperature thermal profile for deposits of varying thickness (inset) irradiated with a 100 μ s laser pulse. (b) Simulated thermal profiles of deposit surface as a function of pure platinum top layer thickness (which represents purification) for a deposit which was initially 360 nm *prior* to annealing. Inset figure displays the maximum temperature at the deposit surface as a function of Pt top layer thickness and original deposit thickness.

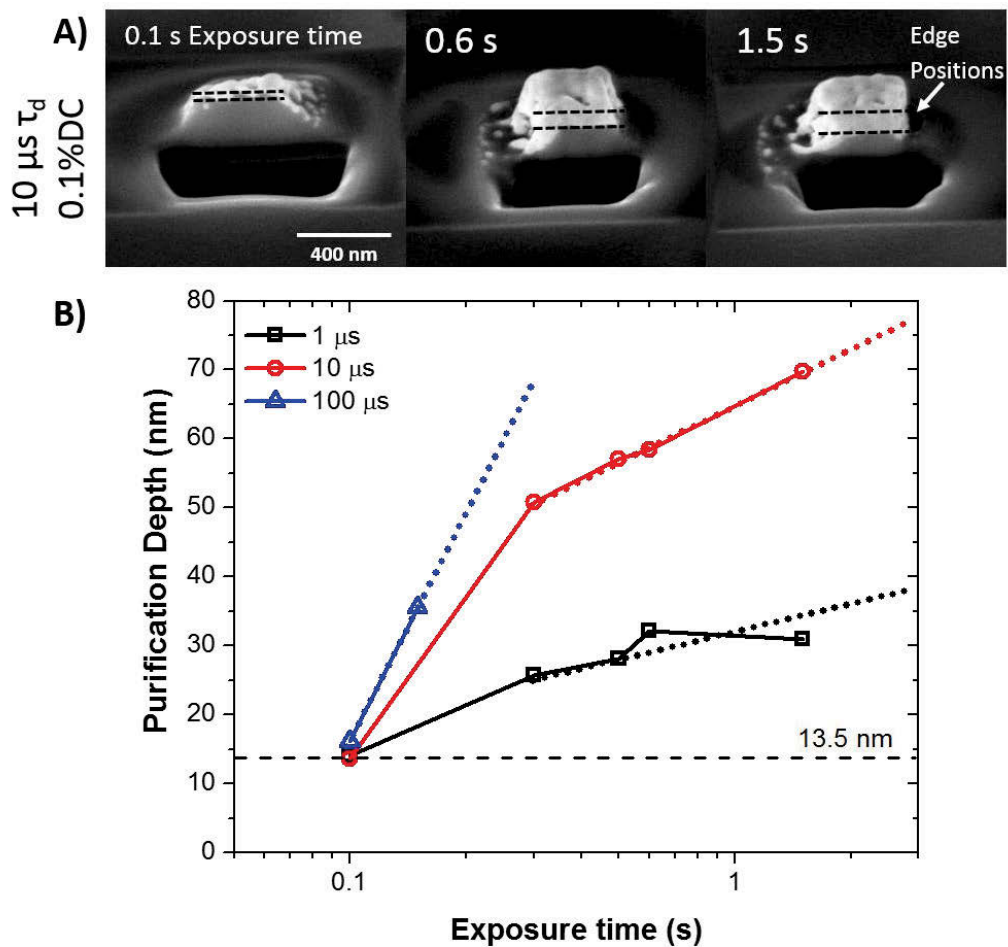


Figure 6. (a) Cross-section SEM images (at 52°) of a 360 nm thick PtC₅ deposit annealed at 10 μs pulse width, 1.0% duty cycle conditions at various exposure times (exposure times and superimposed edge positions are inset in images). (b) Purification depth as a function of exposure time for 1, 10, and 100 μs pulse width laser conditions with superimposed penetration depth of pure Pt (dotted line).

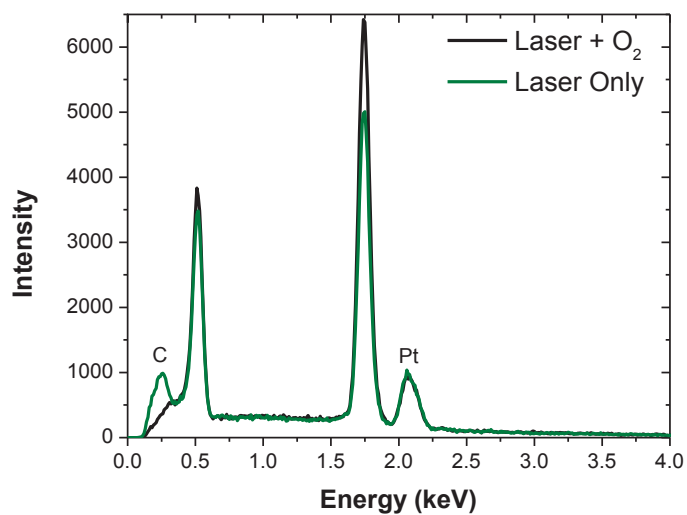


Figure 7. EDS spectra for ~80 nm thick (1000 pass) PtC₅ deposit annealed for 60 s process time with 100 μ s, 0.1% DC conditions with and without O₂ flux.

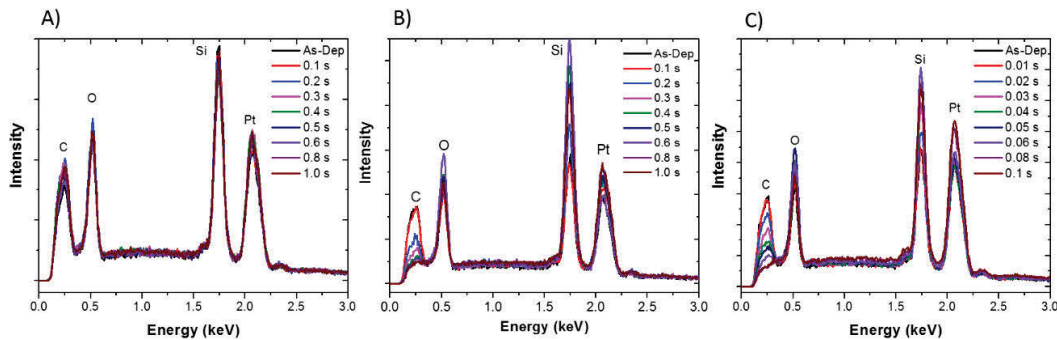


Figure 8. EDS spectra of ~PtC₅ deposit grown with 2000 electron passes (originally ~ 140 nm) deposits purified with (a) 1 μ s, 1% duty cycle, (b) 10 μ s, 1% duty cycle, (c) 100 μ s, 0.1% duty cycle laser conditions at varying exposure times.

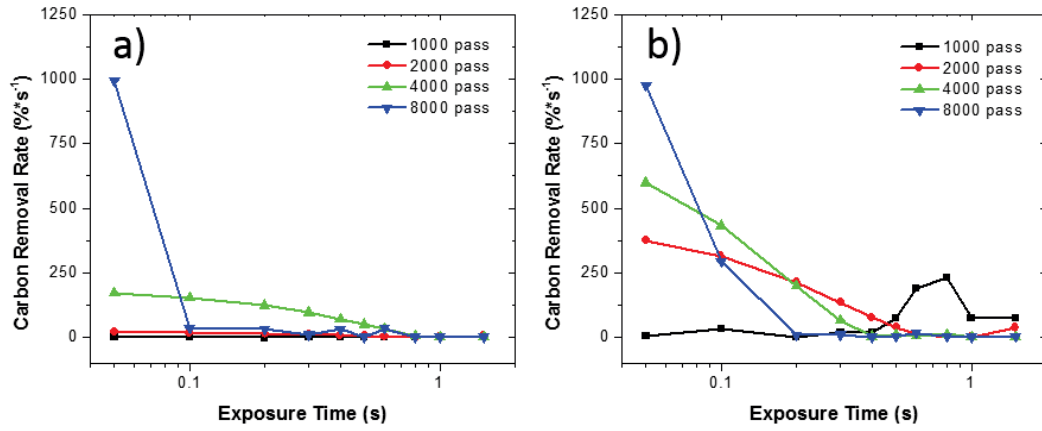


Figure 9. Purification rates as a function of exposure time for deposits with different initial thickness (80 nm, 140 nm, 260 nm, 360 nm for the 1000, 2000, 4000, and 8000 pass deposits, respectively) for (a) 1 μ s 1% duty cycle, and (b) 10 μ s 1% duty cycle conditions.

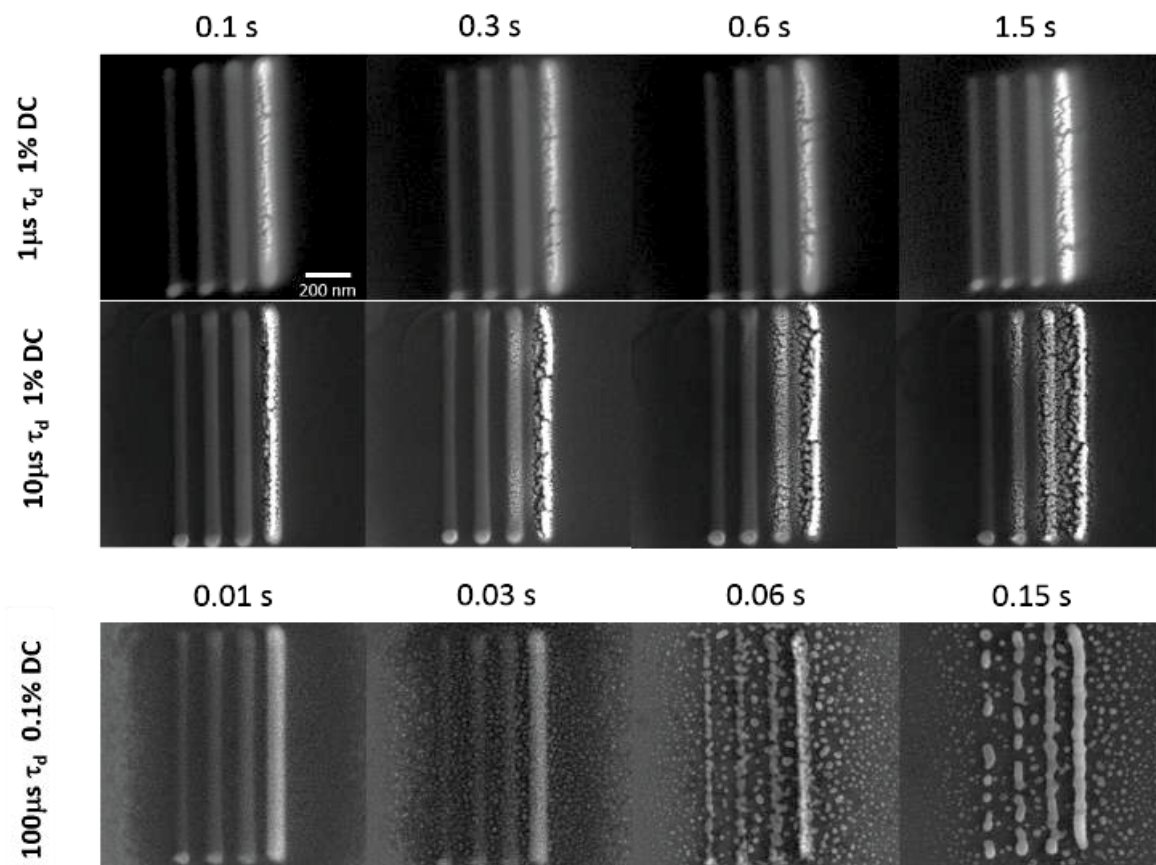


Figure 10. Scanning electron micrographs of PtC₅ line patterns annealed with 1 μs at 1% duty cycle, 10 μs at 1% duty cycle, and 100 μs at 0.1% duty cycle laser conditions at different exposure times. Lines have different initial thicknesses (50, 70, 95, and 150 nm increasing from left to right).

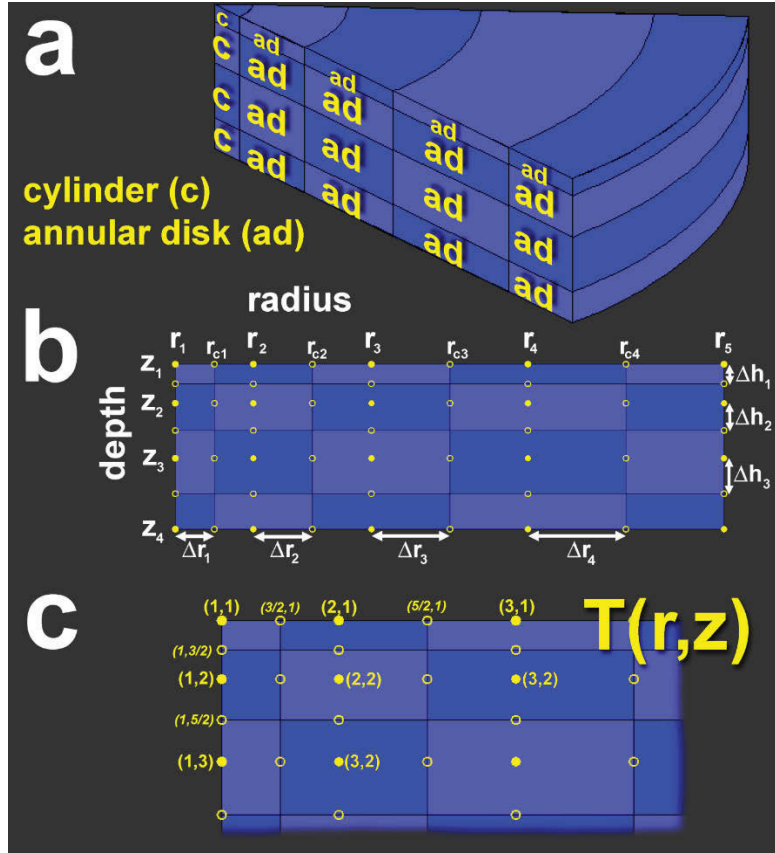


Figure 11. (a) 3D schematic of the computational simulation domain in r - z coordinates. The simulation domain consists of both cylindrical and annular disk volume elements. (b) The primary mesh in the simulation domain is defined by the solid yellow grid points. Temperature estimates are reported in the final simulation results at these points. In addition, each mesh point has uniquely defined materials parameters including density, heat capacity, thermal conductivity and optical properties such as the real (n) and imaginary (κ) indices of refraction. The volume element for each mesh node is defined by the surrounding midway points (open yellow circles) located between adjacent mesh nodes in both the (r) and (z) dimensions. Distinct volume elements are indicated by the alternating shades of blue in the panel. (c) The index system shown in the magnified schematic of the simulation domain refers to the (radial,depth) coordinates, respectively. Heat flux balances are calculated at mesh interfaces in order to account for variable material properties in the spatial coordinate and those locations are indicated by fractional indices.

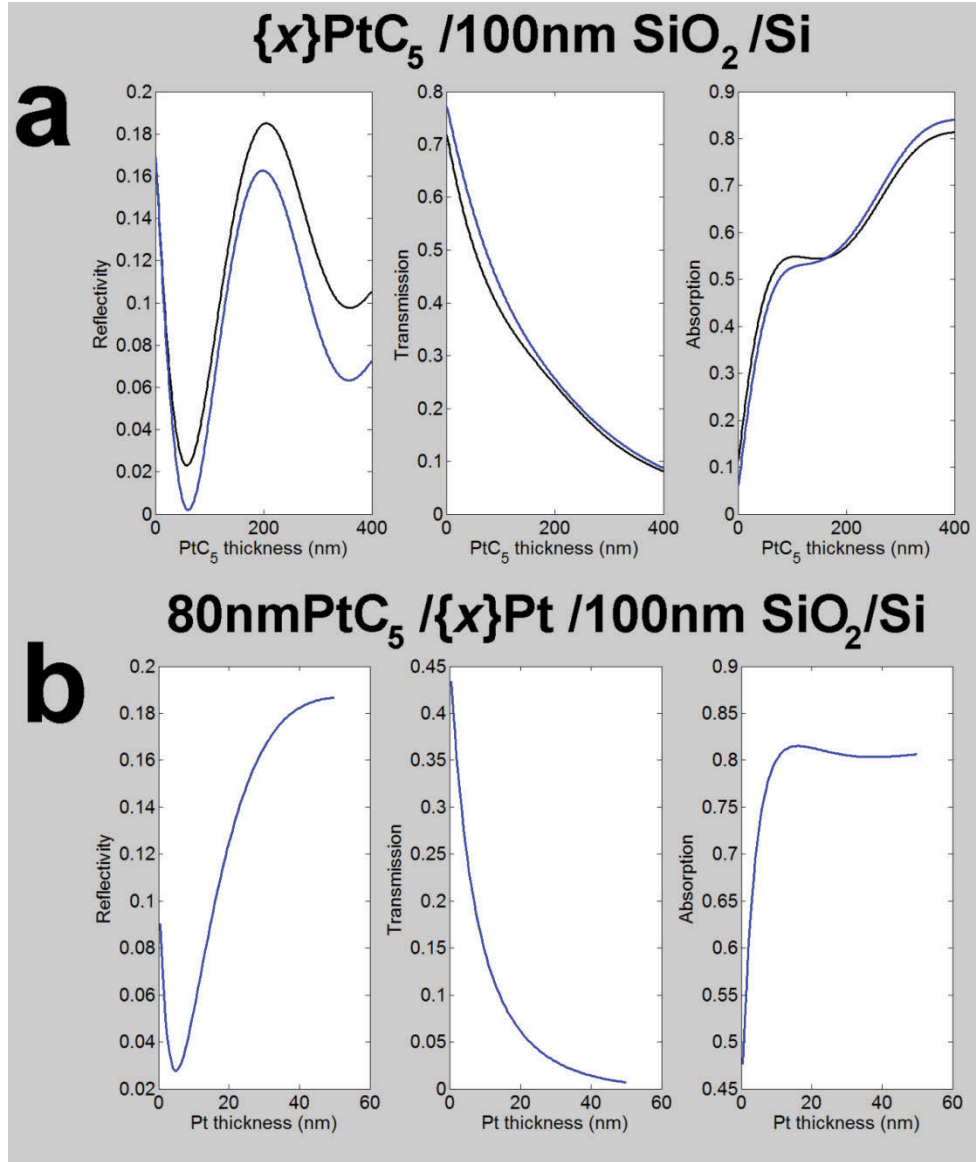


Figure 12. Thin film stack optical properties calculated by Rouard's method¹. The title included for both panels (a) and (b) indicates the topmost film-to-substrate in order of left-to-right. (a) The reflectivity of the PtC_5 surface as a function of the PtC_5 film thickness, the transmission through the 100nm SiO_2 film, and the total absorption in the stack are shown. (b) The reflectivity of the PtC_5 surface as a function of buried Pt film thickness, the transmission through the 100nm SiO_2 film, and the total absorption in the stack are shown.

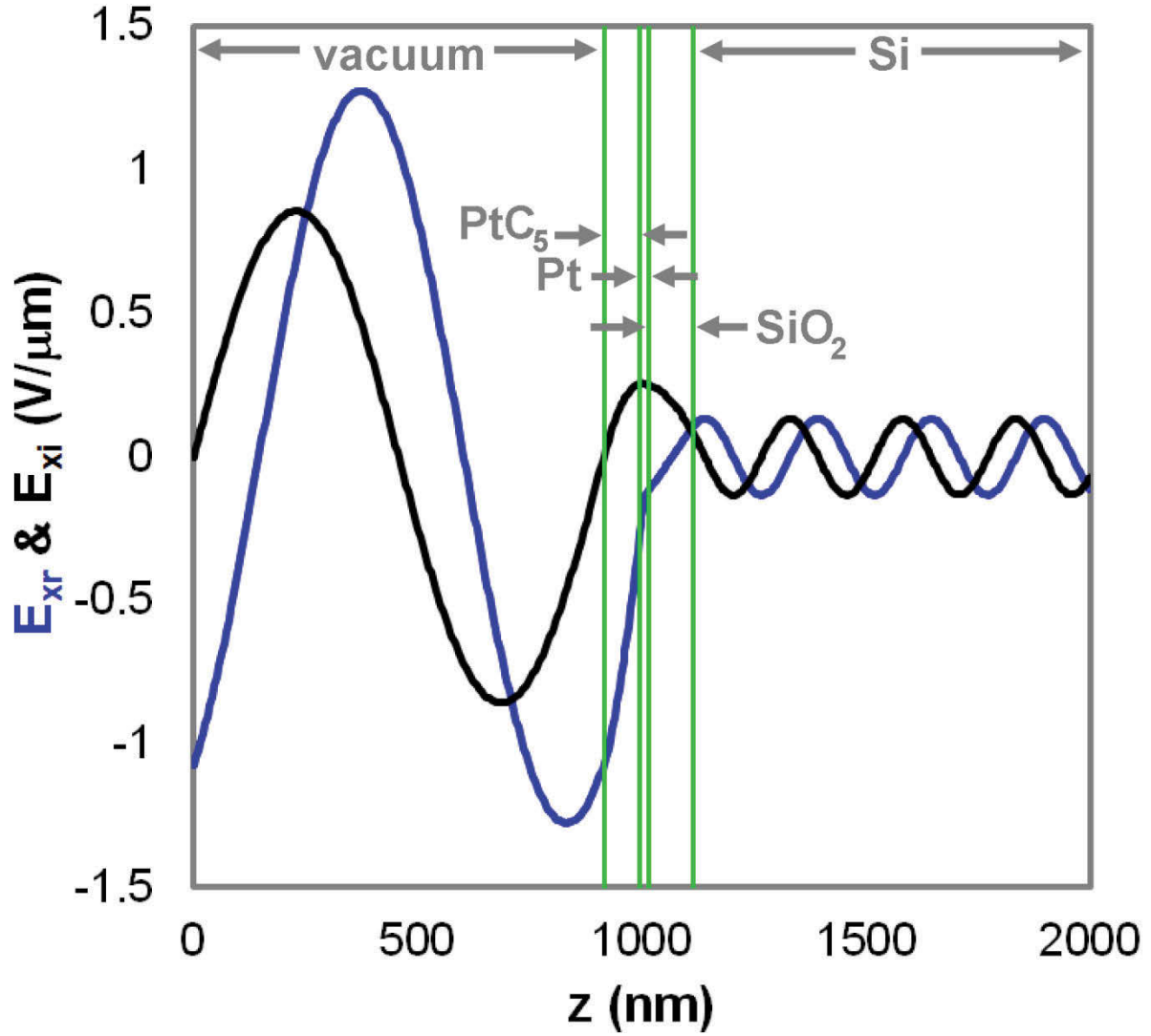


Figure 13. Electric field distribution in the thin film stack structure at an arbitrary time. The real component of the electric field (blue) is provided along with the imaginary component (black). The film widths were 915nm (vacuum), 80nm (PtC₅), 20nm (Pt), 100nm (SiO₂) and 500nm (Si).

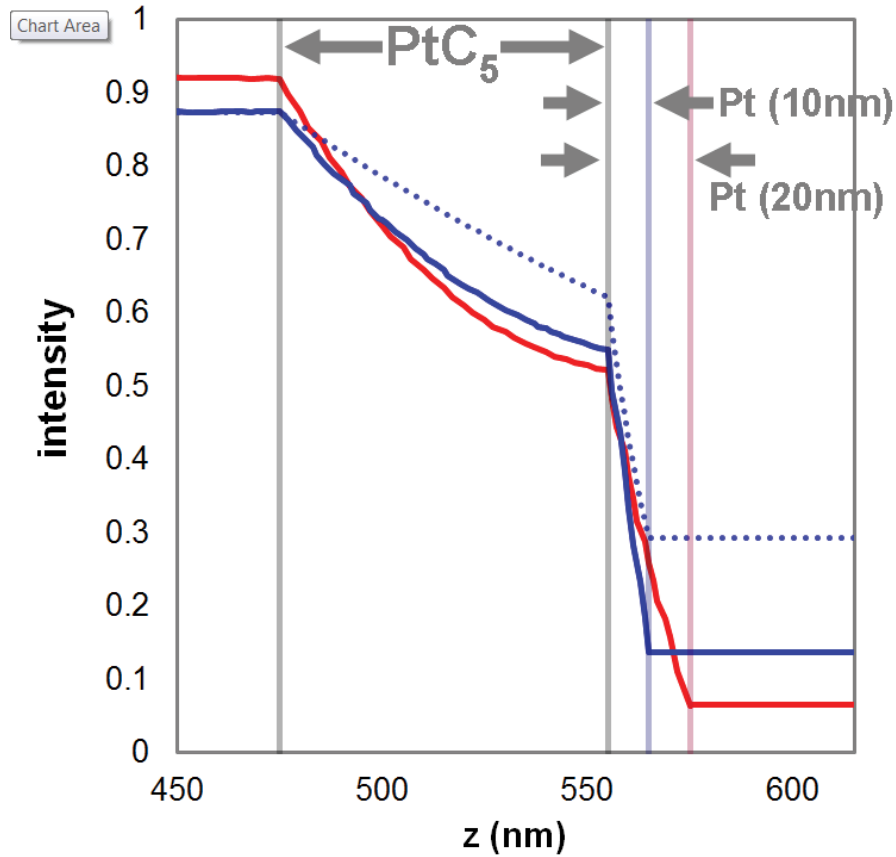


Figure 14. The laser irradiance (intensity) in the thin film stack structure normalized to the incident intensity. The blue curve shows the results for the 80nmPtC₅/ 10nmPt/ 100nmSiO₂/ Si substrate stack. The dotted line is provided for reference and shows the intensity for the same stack but ignoring interface reflections. Reflections from the PtC₅/Pt and Pt/SiO₂ interfaces lead to enhanced absorption in the PtC₅ and Pt films, respectively, as is evident by comparing the solid and dotted blue curves; the intensity drop across these films is larger when considering these reflections. The red intensity profile shows the case for light propagating through an 80nmPtC₅/ 20nmPt/ 100nmSiO₂/ Si substrate stack. For this case, less light is reflected at the initial, vacuum–PtC₅ interface. Yet, the absorption of light in the PtC₅ is greater because the reflectivity at the PtC₅/Pt interface is larger for the thicker, 20nm buried Pt layer, relative to the 10nm layer.

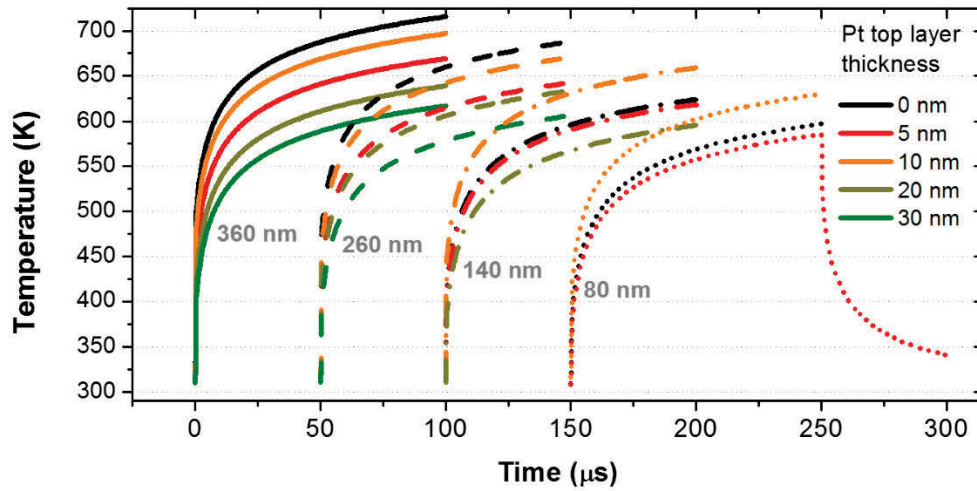


Figure 15. Simulated thermal profiles at the deposit surface as a function of pure platinum top layer thickness (which is intended to emulate the deposit composition at various stages of purification). Underlying PtC_5 thicknesses are shown in light gray. Care was taken to conserve the total Pt atomic content in order to capture the expected contraction of the deposit with increasing pure Pt layer thickness. For example, the loss of carbon in the top layer as well as the density change between PtC_5 and Pt were accounted for.

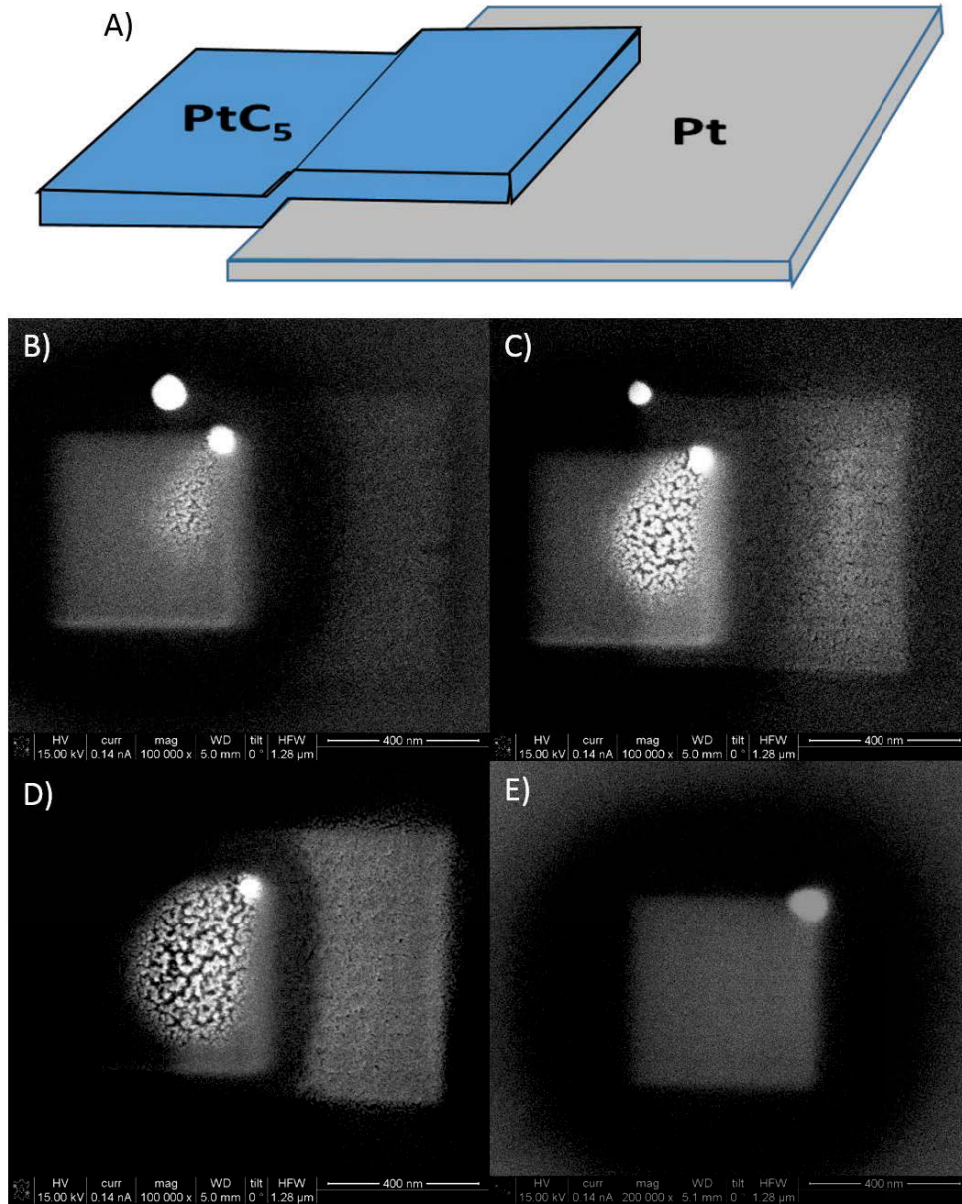


Figure 16. (a) Schematic of optical coupling in which PtC_5 is deposited half-on an underlying pure Pt layer. Images of PtC_5 deposits annealed for 30 s which demonstrates optical coupling to the underlying Pt layer of varying thicknesses. (b) 5 nm, (c) 10 nm, (d) 20 nm. (e) Image of PtC_5 deposit annealed under same condition on SiO_2 substrate.

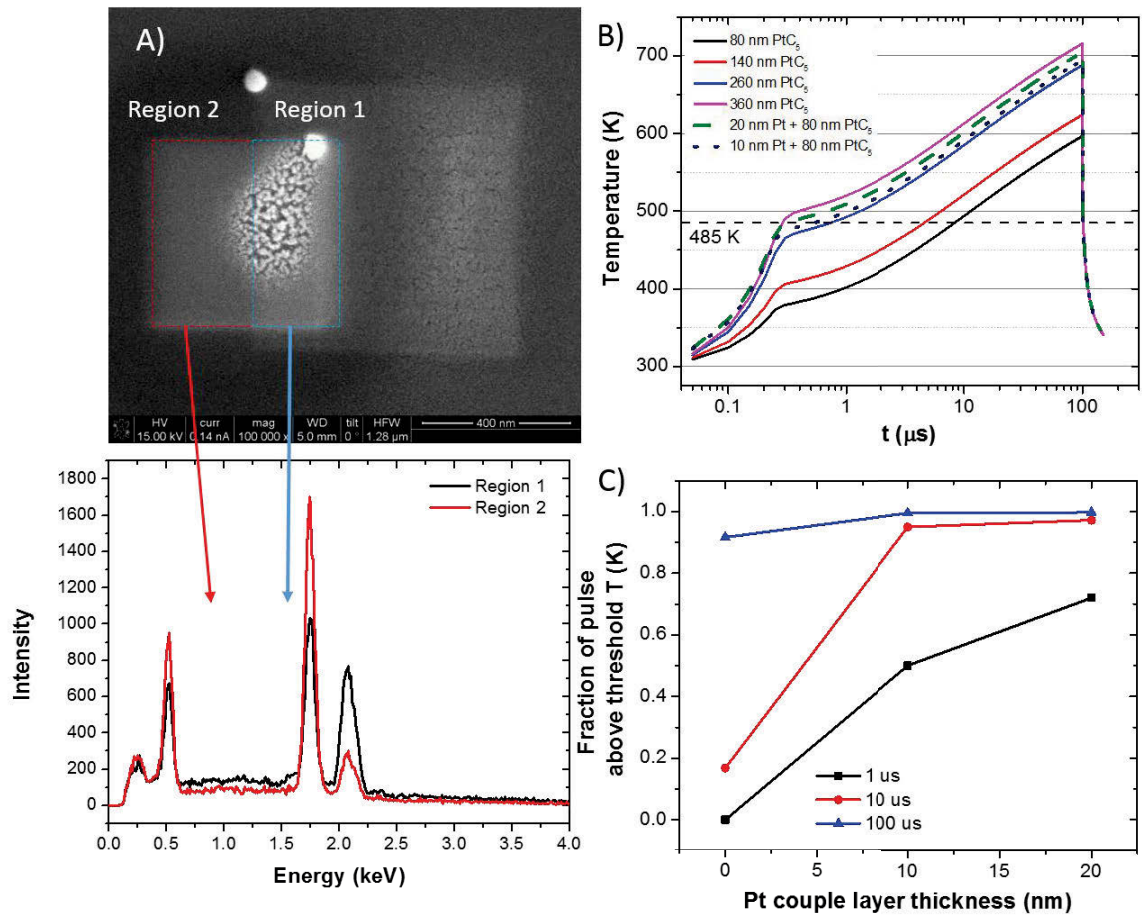


Figure 17. (a) Image and EDS spectra of preferentially cured deposit. Region 1 is the area in which the PtC_5 overlaps the underlying Pt substrate. Region 2 is the area in which the PtC_5 deposit lies directly on top of SiO_2 . (b) Simulated thermal profiles of laser anneal for various deposit thicknesses as a function of laser pulse time. Threshold temperature is denoted in plot (dotted line). (c) Fraction of time above the threshold temperature for an 80 nm PtC_5 deposit as a function of pure Pt under-layer thickness.

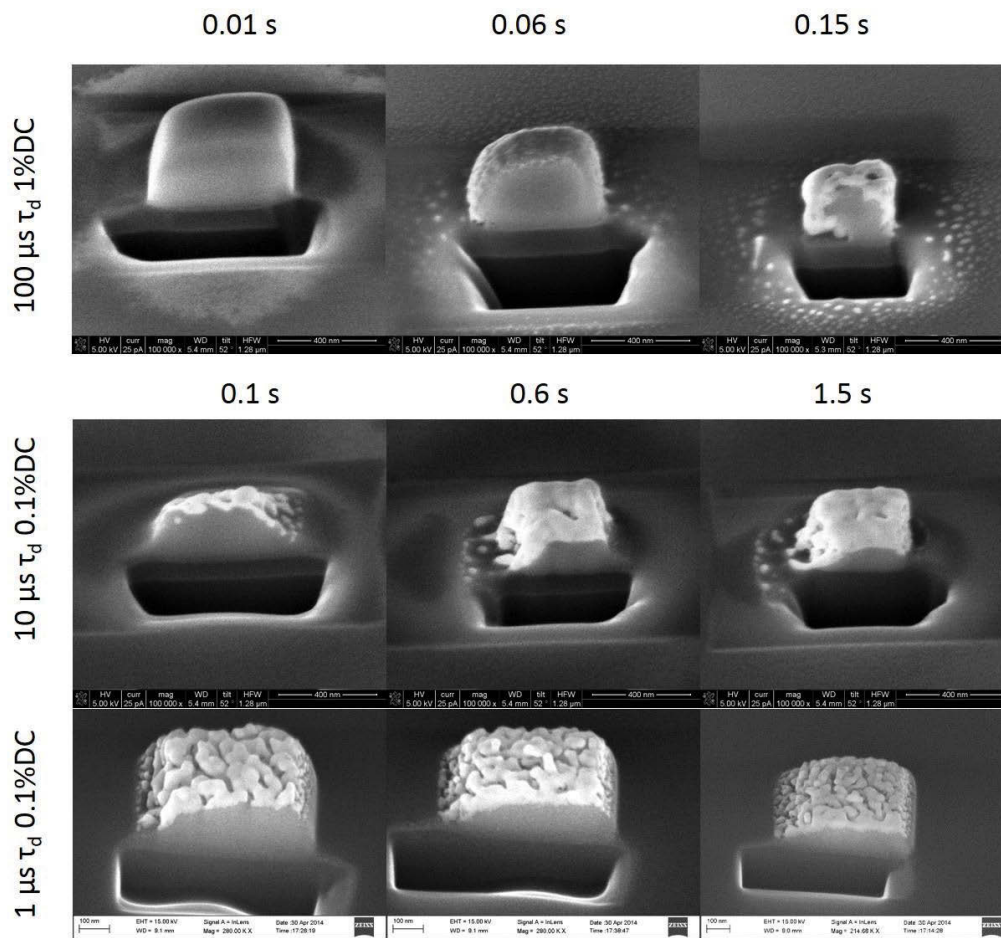


Figure 18. Scanning electron images of PtC_5 patterns annealed with $1\ \mu\text{s}$ at 1% duty cycle, $10\ \mu\text{s}$ at 1% duty cycle, and $100\ \mu\text{s}$ at 0.1% duty cycle laser conditions and then cross-sectioned. Times listed are laser exposure time during the anneal.

1.1.6.3 Tables

Table 1. Various parameters used in the thermal simulation emulating PtC₅ heating as well as parameters relevant to the simulation of electric field propagation and absorption in the Pt/PtC₅/SiO₂/Si multi-layers.

	units	PtC ₅	Pt	SiO ₂	Si
thermal conductivity (k)	<i>W/m K</i>	8.6	72	1	150
heat capacity (c _p)	<i>J/kg K</i>	360	130	1000	800
density (ρ)	<i>kg/m³</i>	4550	21100	2600	2300
real index of refraction (n)		1.87	3.18	1.62	3.63
imaginary index (κ)		0.311	5.44	1x10 ⁻⁵	2.3x10 ⁻³
laser beam diameter (FW90)	<i>μm</i>	100			
laser wavelength	<i>nm</i>	915			
laser power	<i>W</i>	12			
laser ramp time (τ _{ramp})	<i>ns</i>	250			

1.2 Inert Gas Enhanced Laser-Assisted Purification of Platinum Electron-Beam-Induced Deposits

A version of this chapter was originally published by M. G. Stanford et al.:

Stanford, M. G.; Lewis, B. B.; Noh, J. H.; Fowlkes, J. D.; Rack, P. D. Inert Gas Enhanced Laser-Assisted Purification of Platinum Electron-Beam-Induced Deposits. *ACS Appl. Mater. Interfaces* **2015**, 7, 19579–19588.

Michael G. Stanford and Brett B. Lewis conducted experiments reported in this manuscript. Michael G. Stanford conducted subsequent data analysis and characterization. All co-authors discussed the results and formulated the purification mechanism reported in the manuscript. Reprinted with permission. Copyright 2015 American Chemical Society.

1.2.1 Abstract

Electron beam-induced deposition patterns, with composition of PtC₅, were purified using a pulsed laser induced purification reaction to erode the amorphous carbon matrix and form pure platinum deposits. Enhanced mobility of residual H₂O molecules via a localized injection of inert Ar-H₂ (4%) is attributed to be the reactive gas species for purification of the deposits. Surface purification of deposits was realized at laser exposure times as low as 0.1 s. The ex-situ purification reaction in the deposit interior was shown to be rate-limited by reactive gas diffusion into the deposit, and deposit contraction associated with the purification process caused some loss of shape retention. To circumvent the intrinsic flaws of the ex-situ anneal process, in-situ deposition and purification techniques were explored which resemble a direct write atomic layer deposition (ALD) process. First, we explored a laser assisted electron beam induced deposition (LAEBID) process augmented with reactive gas which resulted in a 75% carbon reduction compared to standard EBID. A sequential deposition plus purification process was also developed and resulted in deposition of pure platinum deposits with high fidelity and shape retention.

1.2.2 Introduction

Focused electron-beam-induced processing (FEBIP) is capable of directly depositing and etching material with nanoscale resolution^{1,3,75}. Electron-beam-induced deposition (EBID) occurs when a precursor species is decomposed by a focused electron beam, resulting in a condensed deposit and some volatile reaction byproducts. This technique enables 3-dimensional direct write of nanoscale structures via an intelligent control of the focused electron beam raster sequence. An improved understanding of the fundamental electron-precursor-solid interactions have led to advances in growth rate and resolution of the EBID process^{23–25,27}. These advancements have enabled the emergence of many applications for materials grown via the EBID technique such as direct write plasmonic structures^{32,76}, field-emission emitters^{34,35}, maskless lithography^{38–41}, lithography mask editing^{42–44,45}, scanning probe tips^{28,29}, superconducting nanostructures^{77,78}, electrical contacts⁴⁸, and nanomagnetic logic^{30,31} to list a few.

Although EBID has been used for the aforementioned applications, a major liability has been the inclusion of unwanted byproducts in the final deposit. Since EBID is typically carried out at room temperature using standard chemical vapor deposition precursors, the precursor ligands do not completely volatilize via electron stimulated reactions. This results in the inclusion of unwanted ligands and ligand fragments in the deposit⁷⁹. In the case of the commonly used organometallic trimethyl(methylcyclopentadienyl)-platinum(IV) ($\text{MeCpPt}^{\text{IV}}\text{Me}_3$), incomplete volatilization during the EBID process results in the inclusion of methyl ligands and other carbon rich byproducts. Hence the final deposit is a PtC_x material with $5 \leq x \leq 8$ ^{49,50}, that consist of platinum nanoparticles embedded within a hydrogenated amorphous carbon matrix. Many purification techniques have been explored to address the EBID contamination issue with varying success⁷⁵. Some of these approaches include post and in-situ electron irradiation^{61,62,80,81,82,83}, use of more easily volatilized precursors^{84–86}, post deposition annealing^{51–53}, reactive gas co-flow^{57,59,87}, and in-situ substrate heating^{51,60} to name a few. Martin et al. have recently demonstrated that inert gas flow can enhance electron-beam-induced etch rates of carbon, by increasing the flow of residual chamber reactive gases⁸⁸.

Recently, we have demonstrated enhanced purification of EBID deposits using an in-situ laser anneal technique. In this process, so-called laser assisted electron beam induced deposition

(LAEBID), synchronized laser pulses were used to intermittently assist in the thermal desorption of byproducts after each electron beam pass⁶⁵. This method was successful in improving deposit purity as well as spatial resolution of the direct write EBID process, however LAEBID could not completely purify the deposits. To promote further purification of EBID patterns deposited from the MeCpPtMe₃ organometallic precursor, we recently demonstrated an in-chamber pulsed laser-induced oxidation purification process⁸⁹. The process was able to fully purify deposits in a minimally invasive manner via a photothermal oxidation reaction. Adversely, a 70% volumetric reduction upon removal of carbonaceous byproducts resulted in a loss in precise shape retention and fidelity of deposits.

To increase purity, shape retention, and fidelity of EBID deposits, here we have developed a laser-induced purification reaction using residual H₂O molecules as a reactive gas species whose mobility to the EBID reaction zone is enhanced by a localized flow of Ar or Ar-H₂ (4%). Furthermore, we explored in-situ strategies to deposit pure patterns which have cyclic deposition and purification steps. Specifically, we use an infrared pulsed laser delivery system mounted on a high angle port of a dual beam system to irradiate EBID deposits under a localized ambient of inert Ar-H₂ (4%) or Ar gas. While initially we attributed the purification process to be due to a localized hydrogenation from the localized 4% H₂, subsequent experiments demonstrated that a pure Ar flow also results in purification. Thus, as described below, the enhanced reaction is attributed to enhanced surface diffusion of residual H₂O molecules to the EBID deposit via the localized Ar gas injection. The deposits are photothermally heated and facilitate the dissociation of the H₂O molecules into O^{*}, H^{*}, and OH^{*} radicals and the radicals subsequently react with the carbonaceous matrix in the PtC_x to form volatile byproducts. Hence, hydrogenation and oxidation reactions are attributed with the removal of the carbonaceous matrix. We also demonstrate an in-situ reactive gas-assisted LAEBID process as well as a sequential deposition and purification technique. The later succeeds in depositing pure patterns with high shape retention and resembles a direct write ALD process with a first half-reaction driven by electron beam induced deposition and the second half-reaction driven by the photothermal hydrogenation reaction with the carbon byproducts. In this work, the terminology “ALD” is not used to reflect that an exact monolayer of material is deposited per cycle. Rather “ALD” is used in the sense described by Kanarik et al.⁹⁰ which states that the process benefits

from separate self-limiting half reactions with atomic-scale fidelity. Schematics illustrating the purification techniques studied here are shown in **Figure 19**.

1.2.3 Results and Discussion

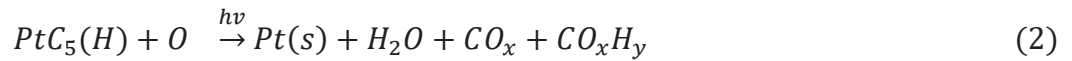
Figure 21 displays the EDS spectra of EBID PtC₅ deposits which were irradiated with the 165 W/cm² optical power density, 10 μs pulse width, and 1% duty cycle laser conditions for 0.3 s of laser exposure time. Two conditions are compared where the deposits were laser annealed 1) in the presence of residual chamber gases at a chamber base pressure of 5.2E-6 mbar, in which H₂O is the dominant residual gas, and a 2) localized flow of inert Ar gas. Clearly, the deposit that was annealed under localized Ar ambient experienced greater reduction in carbon content. The localized Ar gas species is inert thus not suspected to contribute to the chemical etching of the carbonaceous matrix within the deposits, however inert gas flow has been shown to increase concentration of residual H₂O adsorbates in the area of localized flux⁸⁸. Hence, the purification mechanism envisioned is a multistep process where (1) Ar gas is locally injected by a GIS, (2) the localized Ar bombards substrate surfaces and enhances the H₂O diffusion rate, (3) H₂O diffuses onto the EBID deposit, and (4) thermal energy supplied by the laser facilitates the dissociation of H₂O into radicals which react with the carbon matrix in PtC₅ deposits and forms volatile compounds which subsequently desorb.

Residual H₂O that contributes toward the thermally driven purification reaction have multiple possible origins from within the system. Specifically H₂O molecules may be supplied from (1) outgassing of chamber walls, (2) outgassing of the substrate, or (3) from contamination in the inert gas line. **Figure 21b** compares residual gas analysis (RGA) taken of residual chamber gases and during localized Ar flow. Minimal differences in the chamber partial pressure of H₂O (18 amu) molecules with and without localized Ar (20 and 40 amu) flow suggests that the H₂O species which contribute toward the purification process are not delivered from the inert gas line. Inert gas flow localized to the substrate as well as non-localized flow should have similar effect at facilitating H₂O outgassing at the chamber walls. Additional laser anneals of PtC₅ deposits with non-localized Ar flow shows minimal purification (see supporting information), and thus rules out enhanced contribution from H₂O from the chamber wall. Hence, we conclude that the localized Ar gas flux supplied from the GIS needle facilitates the localized enhanced surface

diffusion of H₂O from the substrate, which is the dominant contributor toward the purification reaction.

Figure 22 illustrates the integrated normalized carbon EDS peak for various PtC₅ deposit thicknesses as a function of laser exposure (and process) time. The deposits were irradiated with 165 W/cm² optical power density, 10 μs pulse width, and 1% duty cycle laser conditions in the localized Ar ambient. The PtC₅ EBID deposits used in this study had a 500 x 500 nm² area with variable deposit thickness (~25, 50, 90, and 240 nm by varying the number of EBID passes). As shown previously⁸⁹, laser annealing with no localized gas flow does not eliminate the carbon. We also demonstrated, for O₂-laser annealing, that the PtC₅ deposit purification as a function of total laser exposure time (duty cycle x process time) is highly dependent on the initial deposit thickness; thicker deposits anneal faster due to enhanced optical coupling of the laser to the PtC₅ (see supporting info of Ref ⁸⁹ for detailed explanation of the role of these material parameters on the laser purification process). A similar behavior is demonstrated here, where the thicker deposits anneal at a faster rate due to enhanced photothermal heating of the deposit.

The purification evolution as a function of depth into EBID deposits were examined in **Figure 23**. Specifically, 240 nm thick PtC₅ deposits were irradiated with the 10 μs, 1% duty cycle pulsed-laser under flux from Ar inert gas. Deposit cross-sections are shown for 0.2 s and 1.5 s laser exposure times. For these exposure times, the purification front progresses into the deposit, but does not anneal the entire deposit. The proposed purification reactions upon the formation of radicals from H₂O dissociation are as follows:



for the (1) hydrogenation and (2) oxidation purification reactions, respectively, where PtC₅(H) denotes the hydrogenated PtC₅ deposits. It is worth noting that a self-hydrogenation co-reaction may also play a role during purification due to residual hydrogen present in the amorphous carbon from the original EBID process. Under laser-irradiation and applied heat, dehydrogenation of some ligands result in the hydrogenation and hence volatilization of other ligands producing CH_x or CO_xH_y by-products⁹¹, thus possibly contributing a secondary role in the purification. Dehydrogenation of the amorphous carbon matrix can also result in the formation of

additional water molecules under oxygen flux, which may also be tertiary reactions contributing toward the overall purification reaction⁶².

Figure 23b is a plot of the purified platinum thickness as a function of laser exposure time for the pulsed laser purifications. To sustain the top-down subsurface purification reaction, the transport of the reactive gas to the reaction front is envisioned to occur via a two-step process, namely: (1) the reactive gas radicals adsorb onto the purified Pt surface after thermal dissociation of H₂O molecules and (2) subsequently diffuses to the purification front through the nanoscale porosity that develops. There is also likely purification contribution from H₂O molecules which adsorb and diffuse into the deposit prior to dissociation. Since Pt serves as a catalyst for many hydrogenation and oxidation reactions^{92,93}, these species will readily chemisorb onto the deposit surface. Therefore, as the Pt surface layer thickens, diffusion of the reactive species to the purification front is expected to be the rate limiting transport mechanism. Recently, purification simulations interrogating the PtC₅/O₂ interaction have revealed that transport is dictated by the cyclic process of dissociation chemisorption/associative desorption on Pt surfaces coupled with O₂ diffusion between Pt interactions⁹⁴. This combined process can be described using an effective diffusion coefficient which is typically much smaller than the diffusion of the gas alone. We suspect that the coupled diffusion process is similar for both reactive gas radicals active here, O and H. The inset plot in **Figure 23b** plots the purification depth squared as a function of laser exposure time. Since the diffusion depth of the reactive gas species into a material has a \sqrt{Dt} dependence, the linearity ($R^2 = 0.9998$) of the plot is consistent with a diffusion limited purification rate. Hence the diffusion limited purification rate reveals the need for in-situ deposition and purification processes for thick deposits because the time required for diffusion of reactive gas species into the interior of the deposit follows a squared dependency with the depth.

Roberts et al. developed a pulsed-laser assisted process for in-situ purification of EBID deposits, namely Laser Assisted Electron-Beam-Induced Deposition (LAEBID)^{65,66}. In this work, laser pulses were synchronized with EBID passes and the highest purity (~37 at% Pt) was achieved when the EBID layer thickness per laser pulse was approximately a monolayer of deposited material. Importantly, the deposits were grown on a titanium film which facilitates the optically coupling and subsequent heating necessary for the thermally driven purification.

Nonetheless, even with a monolayer-by-monolayer purification approach, carbon content remained in the deposits (optimum purification realized $\sim \text{PtC}_2$). To try promoting further purification, here we introduce a reactive gas to the LAEBID process. We envision the reactive gas assisted LAEBID process as a direct-write atomic layer deposition (ALD) process with an electron-beam dictated first half-reaction followed by a reactive gas purification second half-reaction dictated by laser heating. Ar inert gas was injected simultaneous with the precursor gas to provide a co-flow (using two individual injection systems) of species necessary for deposition and purification, where once again, the Ar species increases the localized diffusion of H_2O reactive to the deposit. Notably, subsequent studies revealed that precise synchronization and laser pulsing during the refresh time of the EBID layer is not necessary since the electron beam is only irradiating a single pixel while the laser pulse irradiates the entire deposit. This effectively gives refresh time for the other pixels, which have no interaction with the electron beam at that moment in time. Thus the results presented here were not synchronized with the refresh time.

Figure 24a shows a SEM image of a deposit following reactive LAEBID (100 μs pulse width and 0.1% duty cycle). The deposit demonstrates exceptional shape retention and smoothness. In addition, a decrease in carbon content relative to standard PtC_5 EBID resulted (**Figure 24b**). A variety of laser conditions were explored for the reactive LAEBID process in an attempt to promote further purification of the deposits. Changing the duty cycle from 0.1% to 0.5% for 100 μs pulse width (red bars) resulted in a decrease in carbon content from 53 % (relative to standard EBID) to 38 % by providing a greater laser exposure time during deposition. To increase the laser exposure time relative to the EBID half-reaction, an additional 13 ms refresh time after each pass of deposition (yellow bars) was added to further purify the deposits. During the refresh time, the electron beam was blanked and only the laser anneal half-reaction occurs. The added refresh time resulted in a further reduction of carbon. However, the increase in cumulative laser exposure also resulted in laser-assisted chemical vapor deposition (LCVD) in the laser irradiation area ($\sim 100\mu\text{m}$) as shown in **Figure 24b**. Therefore, the deposit thickness evolves from a convolution of LAEBID and LCVD processes and results in a loss of deposit shape retention. Additional information on the competing LCVD phenomenon is detailed in the Supporting Information.

The reactive LAEBID process was also attempted with a pulse width of 10 μ s and a variable duty cycle of 1, 3, and 6 % (blue bars). The 10 μ s pulse width yields a lower maximum deposit temperature (\sim 490 K) relative to the 100 μ s pulse width (\sim 600 K) due to the non-steady state behavior of the laser heating⁸⁹. Higher duty cycles can be tolerated at 10 μ s, relative to 100 μ s, since less time is required for recovery to room temperature between pulses. Thermal pulse interactions are intentionally avoided in order to both simplify the interpretation of results and avoid a steady state temperature transient over the process time which can favor both LCVD and thermal drift.

Increasing the duty cycle of the 10 μ s pulses to 6 % resulted in a reduction in the carbon content of the deposit from 60 % to 25 % relative to standard EBID, which represents the highest purity obtained in our Pt LAEBID deposits that excludes LCVD effects. Beyond 6 % duty cycle resulted in steady state heating and thermal drift during the LAEBID process. Summarily, reactive LAEBID realized a reduction in carbon content of 75 % relative to standard EBID, however complete carbon removal was not achieved. The challenges preventing complete purification are addressed below.

To understand the effect that the MeCpPtMe₃ precursor gas had on the photo-thermal half-reaction in the LAEBID process, standard EBID PtC₅ patterns were grown and subsequent laser anneals were carried out with (1) the Ar inert gas flow alone, and (2) a co-flow of Ar reactive gas and MeCpPtMe₃ precursor where the precursor nozzle was positioned at approximately 7 mm from the center of field of view and 5 mm above the substrate, sufficient to significantly decrease the MeCpPtMe₃ flux as evidenced by a significant decrease in the EBID growth rate at this position. **Figure 25** is a plot of the normalized carbon content of the laser annealed deposits as a function of laser exposure time irradiated with 100 μ s pulse width and 0.1% duty cycle pulses. Clearly, when annealed with the Ar flow alone, the purification rate is fast relative to the sample laser annealed with the precursor gas co-flow. It is therefore deduced that the presence of the precursor molecule attenuates the purification reaction, thus making complete carbon removal in the reactive gas assisted LAEBID process challenging.

The schematics shown in **Figure 26** illustrate a proposed mechanism for the laser-annealing attenuation exhibited when a co-flow of reactive gas/precursor molecules is used.

Figure 26a illustrates the common microstructure of PtC₅ deposits, namely platinum nanograins

are embedded within an amorphous carbon matrix. In the presence of the Ar gas flux, residual H₂O molecules adsorbed to the substrate exhibit enhanced diffusion rates which reduce the reactive gas replenishment time. Radicals created upon dissociation of H₂O molecules, then react with the carbonaceous matrix through hydrogenation and oxidation reactions to reduce embedded carbon content. When a reactive and precursor gas co-flow is used (**Figure 26c**), the relative residence times of the gas molecules on a surface must be considered to realize the resultant equilibrium surface coverage. Large molecules, such as the MeCpPtMe₃ precursor used in this study, have longer residence times on the deposit surface than the dissociation H^{*} and O^{*} radicals. As the schematic illustrates, the precursor molecules dominate the surface coverage on the deposit surface due to their long residence time (τ). This effectively lowers the coverage of the reactive gas by reducing available adsorption sites and attenuates the purification reaction. Understanding that the co-flow of precursor gas in the presence of reactive gas species attenuates the purification reaction helps explain why the complete LAEBID reaction is limited under laser conditions that would otherwise purify an EBID deposit. This suggests that a pulsed gas procedure is necessary for the in-situ growth and purification of EBID deposits, similar to true atomic layer deposition (ALD) process.

To circumvent the apparent gas competition issues with co-flow, a pulsed gas procedure was utilized in a sequential EBID deposition and subsequent laser anneal process. Specifically, precursor gas was injected during the EBID half-reaction, which was subsequently pumped from the chamber. The precursor partial pressure introduced during this half reaction was $\sim 9.0 \times 10^{-6}$ mbar. A 30 keV beam energy was used for EBID to prevent significant peripheral deposition, which is characteristic of a 5 keV beam with larger beam tails (see **Figure 31**). Next, the Ar inert gas was injected at a partial pressure of $\sim 1.2 \times 10^{-5}$ mbar during the photo-thermally induced de-carburization second half-reaction to enhance diffusion of residual water molecules. Importantly, 10 μ s pulse width and 1% duty cycle laser condition were used to anneal the deposit during each cycle, followed by several 100 μ s pulse width smoothing pulses. The 10 μ s pulses facilitate the de-carburization of the deposit, however, the relatively brief pulses prevent significant coalescence of the Pt, thus promoting deposit shape retention. Several 100 μ s pulses are used to promote controlled coalescence after each purification cycle to reduce some deposit porosity whilst maintain shape retention. This cycle was repeated to build a pure deposit of

desired size and shape, as illustrated in **Figure 27c**. Unique to this process compared to a traditional surface reaction limited ALD processes, the number of monolayers deposited per cycle is dictated by EBID half-reaction, which makes sub-monolayer resolution possible. The number of monolayers deposited per cycle largely effects the deposit characteristics as shown in the supporting information (**Figure 31**). Due to the $\sim 70\%$ volumetric loss during the decarburation reaction, significant internal stresses will be exhibited in the deposits if many (> 200) monolayers are deposited per cycle. Large internal stresses may cause the deposit to delaminate from the substrate (**Figure 31c**), hence there is an optimum number of monolayers per cycle that will result in an acceptable deposition rate whilst preventing significant internal stresses from building up during the purification cycle. **Figure 27a** displays a pattern deposited using five cycles and ~ 70 monolayers of deposition per cycle before $100\ \mu\text{s}$ smoothing laser pulses were utilized to reduce porosity of the freshly deposited material from the cycle. **Figure 27b** displays the deposit after the smoothing pulses were applied. The yellow dotted line denotes the EBID raster pattern. Clearly, precise shape retention is achieved using this sequential deposition technique. **Figure 27c** is a tilted scanning electron image (52°) of the deposit, and the total thickness of the purified deposit is estimated to be $\sim 50\ \text{nm}$ (consistent with the $\sim 70\%$ volume reduction experienced when purifying a PtC_5 deposit). EDS spectra of sequential deposition patterns (supporting information **Figure 31**) reveal that the deposits are pure platinum. Hence the sequential deposition process can be utilized to direct write pure nanostructures.

The throughput of the layer by layer process seems noticeably lower than that of a single EBID deposition followed by a subsequent reactive gas anneal, however the completeness of the anneal must be considered. Since the time for diffusion of a reactive gas species to deposit interior is proportional to the depth squared, it may be quite timely to anneal a single standard EBID deposit in its entirety and may result in the lack of shape retention. The throughput of the sequential layer by layer process also has a similar throughput to the completely insitu LAEBID process. This is because the deposition rate may be hindered in the LAEBID process because the elevated substrate temperature reduces gas residence time (for precursor and reactive gas species). To comment briefly, the throughput of the sequential layer by layer process could be improved with a smaller deposition chamber, similarly to an ALD system. This would increase

the pumping rates between cycles, enable a higher frequency cyclic process, and ultimately increase applicability of the process.

1.2.4 Conclusions

In conclusion, we have demonstrated a localized pulsed laser-induced purification reaction which can be used to purify PtC₅ EBID deposits generated via electron stimulated reactions of the MeCpPtMe₃ precursor. The reactive gas species was supplied by the thermal dissociation of residual H₂O molecules in the chamber, where inert Ar gas was used to enhance H₂O diffusion to the reaction zone. We have also demonstrated two direct write pseudo atomic layer deposition processes. Specifically, we have presented a reactive gas assisted LAEBID process which is capable of depositing patterns from the MeCpPtMe₃ precursor with much greater purity than standard EBID, by utilizing intermittent 915 nm annealing laser pulses and residual H₂O molecules. We have also demonstrated a sequential deposition process to circumvent gas competition for adsorption sites that appears ubiquitous with the LAEBID process. The sequential deposition process utilized a pulsed gas strategy, similar to a traditional ALD process, however for this work, the first half reaction was dictated by electron beam irradiation and the second half reaction was dictated via a photothermally induced purification reaction. The sequential deposition process was successful in deposition of pure nanostructures with high shape retention and fidelity.

As for our perspective on future development of this process, several parameters can surely be further optimized for higher efficiency and throughput. The 915 nm laser is largely transparent to oxide substrates as well as highly reflective on metallic substrates and deposits. Therefore photothermal heating from this laser system is often inefficient. We speculate that lasers in the visible spectrum will heat the substrate or deposits with greater efficiency, thus increasing the throughput of the in-situ and ex-situ annealing strategies of EBID deposits. In the gas co-flow LAEBID process, gas competition for adsorption sites between the reactive gas and precursor gas limits the deposit's purity. This suggests that flux of the reactive gas is not sufficient in comparison to the precursor gas to enable complete deposit purification. A similar setup in an environmental SEM enables the use of pressure regimes (not possible in a standard

SEM) which may provide a gas mixture possible of facilitating complete purification in the LAEBID process.

1.2.5 Methods

1.2.5.1 Electron-Beam-Induced Deposition

EBID was performed using an FEI Nova Nanolab 600 Dual Beam system on a Si substrate with a 200 nm thick thermally grown silicon oxide layer. The chamber was air plasma cleaned with an Evactron system, produced by XEI Scientific Inc., for a minimum of 15 minutes prior to deposition. Unless noted, EBID was carried out by locally injecting MeCpPtMe₃ precursor in close proximity to the area of interest where the GIS needle was positioned ~100 μ m above the substrate and ~200 μ m from the center of the field of view. The MeCpPtMe₃ crucible was heated to approximately 45°C to increase the vapor pressure of the precursor. The chamber pressure was ~1.0 x 10⁻⁵ mbar during injection of the MeCpPtMe₃ precursor into the chamber with a base pressure of ~1.0 x 10⁻⁶ mbar. Each pattern was deposited using 5 keV electron beam energy, 98 pA beam current, 10 μ s dwell time, and a 13.6 nm pixel pitch. The number of EBID passes were varied (1000, 2000, 4000, and 8000) to create deposits that were approximately 25, 50, 90, and 240 nm thick.

1.2.5.2 Pulsed Laser Reactive Gas Anneal

A 915 nm wavelength 25 W multichip diode laser module with model number BMU25B-915-01, produced by Oclaro Inc., was used to anneal the deposits. This laser module was driven by an IXYS PCX-7410 pulsed diode laser driver. A laser delivery system, produced by Omniprobe, Inc. (an Oxford Company), was mounted on a high angle port in the SEM chamber at an angle of 52° relative to the substrate. This system enabled the simultaneous delivery of an approximately 100 μ m diameter laser spot size with a Gaussian distribution to the EBID deposit in the SEM chamber. Inert Ar gas was delivered to the area of interest using an OmniGIS I gas injection system; the inert gas contained a small mixture of H₂ gas (4 volume %). Subsequent comparisons with pure Ar gas, reveal that the H₂ species have no observable contribution toward the purification process. The needle was positioned ~100 μ m above the sample and ~200 μ m from the center of field of view. The chamber base pressure before reactive gas flow was ~1.0 x 10⁻⁶ mbar. The valve pulsing rates in the OmniGIS I, which ultimately control the reactive gas

flux, were set to achieve a chamber pressure of 1.2×10^{-5} mbar when the reactive gas was flowing, and the gas temperature was 25 °C. The needle configuration for deposition and the subsequent purification are illustrated in **Figure 20**. For this work, the optical power density of the laser was constant at $\sim 165 \text{ kW/cm}^2$. Laser pulse width and duty cycle were varied with the laser driver. Additional information on the laser delivery system can be found in reference⁹⁵. The EBID and subsequent pulsed laser reactive gas anneal processes are illustrated in **Figure 19a**.

1.2.5.3 Reactive Laser Assisted Electron-Beam-Induced Deposition

Reactive laser assisted electron beam induced deposition (LAEBID) was carried out by performing EBID to deposit PtC_x patterns while simultaneously irradiating the EBID deposit with the pulsed laser in a Ar inert gas co-flow, where the Ar once again increases flux of the reactive gas (H_2O) to the deposit region. EBID was conducted using 5 keV electron beam energy, 98 pA beam current, 10 μs dwell time, and a 13.6 nm pixel pitch. A schematic of this process is illustrated in **Figure 19b**. Some LAEBID deposits included an additional 13.6 ms refresh time after each EBID pass to lengthen reactive gas annealing time per pass. During the EBID pass, the laser was simultaneously pulsed with either 10 μs or 100 μs pulsewidths. The irradiation duty cycle was varied over the range of 0.1% - 6% (see supporting information for more details and **Figure 29** which shows a schematic illustrating a map of laser and EBID synchronization). For this work, the FEI GIS for the MeCpPtMe_3 precursor gas as well as the OmniGIS I for the inert gas were opened concurrently to establish the co – flow regime. The partial pressures of the Ar inert gas and MeCpPtMe_3 precursor introduced into the chamber were approximately 1.10×10^{-5} mbar and 9.0×10^{-6} mbar, respectively. During the co-flow experiments, the precursor gas nozzle was retracted $\sim 8 \text{ cm}$ vertically and $\sim 5 \text{ cm}$ horizontally while the reactive gas GIS needle was positioned 100 μm above the sample and 200 μm from the center of field of view (see **Figure 20**). By comparison, in the typical EBID experiment the precursor gas nozzle is located in the same close position. Ultimately, this needle configuration significantly decreases the flux of MeCpPtMe_3 precursor gas molecules relative to the reactive gas molecules to slow the EBID growth and enhance the purification of the deposits.

1.2.5.4 Sequential or Layer-by-Layer EBID Plus Laser Reactive Gas Anneal

As will be demonstrated, the co – flow of gases used in the LAEBID process, prohibit complete volatilization of unwanted byproducts in the final deposit. To circumvent the issues of

the co-flow of precursor gas and reactive gas in the LAEBID process, a sequential deposition and purification process was also developed. In this process, precursor gas and Ar inert gas were injected (separately) into the chamber under standard EBID and laser annealing parameters. A 30 keV beam energy and 150 pA beam current were used for deposition in this study to minimize peripheral PtC₅ deposition on the substrate^{67,68}. For the layer-by-layer process, an optimum EBID thickness per cycle was determined to be 70 nm (see supporting information **Figure 31**). After the EBID cycle, the precursor gas was pumped from the chamber until a base pressure of $\sim 2.0 \times 10^{-6}$ mbar was achieved and Ar inert gas was injected into the chamber to enhance flow rate of residual H₂O to the deposit at a pressure of $\sim 1.2 \times 10^{-5}$ mbar. The pulsed laser system was then used to irradiate the sample with 10 μ s pulses at 1% duty cycle for a total laser exposure time of 3.0 s and equivalent process time of 5 minutes. After each cycle, the deposit was irradiated with several 100 μ s laser pulses to initiate the coalescence of any disconnected Pt grains in the deposit. This step was required to mitigate the evolution of porosity in the final morphology. For the sequential approach, the needles for the reactive gas and precursor gas were both positioned 100 μ m above the sample and 200 μ m from the center of field of view (as shown in **Figure 20**). The sequential EBID + laser anneal process was repeated in order to create a pure deposit of desired size and shape and a schematic of this process is shown in **Figure 19c**.

1.2.5.5 Energy Dispersive Spectroscopy (EDS) Analysis

EDS spectra were recorded while irradiating the substrate with a 5 keV energy electron beam at a beam current of 1.6 nA. Analysis to determine the normalized carbon content of each spectra were conducted by first subtracting a background spectra of the underlying SiO₂ substrate. The Pt and C EDS signatures, located at 2.048 keV and 0.277 keV respectively, were then fit with a Gaussian curve of the form shown in equation 1:

$$y = y_0 + \frac{Ae^{\frac{-4 \ln(2)(x-x_c)^2}{w^2}}}{w \sqrt{\frac{\pi}{4 \ln(2)}}} \quad [1]$$

where x_c is the center of the EDS peak, A is the amplitude, and w is the full-width at half-maximum. The area under the curve was taken to be a measure of the elemental concentration of the deposit. Due to variability in EDS yield of the different elements, we solely report the carbon content normalized to a standard EBID deposit's carbon content to give an indication of the

deposit purity. It is well known that the Pt-N and C-K EDS peaks overlap. The Pt-N/Pt-M peak ratio was experimentally determined to be approximately 0.03 for our EDS system. This is notably lower than the Pt-N/Pt-M determined by other work to be 0.09, and is likely attributed to a difference in sensitivity of the lower energy portion for the detector. This proportionality constant was used to determine contribution of the Pt-N peak from the Pt-M peak located at 2.048 keV. The estimated contribution of the Pt-N peak was then subtracted from the EDS peak located at 0.277 keV to produce a more accurate estimate of the actual carbon EDS peak.

1.2.6 Appendix

1.2.6.1 Supporting Information

Purification Reaction with Localized and Non-Localized Gas Flow

H₂O is an abundant residual gas which has been shown to purify Pt EBID deposits⁶². Here we use inert Ar gas flow to enhance the surface diffusion of residual H₂O molecules to facilitate the laser assisted purification reaction with the PtC₅ EBID patterns. The source of the residual H₂O which contributes toward purification reactions may be (1) outgassing of chamber walls, (2) outgassing of the substrate, or (3) from contamination in the inert gas line. **Figure 28a** compares the EDS spectra of PtC₅ deposits which were laser annealed under flux of localized and non-localized Ar gas, with 10 μ s and 1% duty cycle laser conditions. Clearly, the localized gas flux was more effective in purifying the deposits, as indicated by a significant reduction in the carbon content. **Figure 28b** displays RGA spectra which show that the chamber gas composition was very similar for the two laser anneals. Inert gas flow localized to the substrate as well as non-localized flow should have similar effect at facilitating H₂O outgassing at the chamber walls. Minimal purification with non-localized Ar flux rules out enhanced contribution from H₂O from the chamber wall. **Figure 21** indicates that the inert gas line has minimal H₂O contamination. We therefore conclude that the localized Ar gas flux supplied from the GIS needle facilitates the localized enhanced surface diffusion of H₂O from the substrate.

Reactive Gas Assisted LAEBID Synchronization

Figure 29 illustrates the synchronization of the LAEBID process for 500 nm x 500 nm deposits for a single LAEBID pass, where a single pass consists of an electron beam raster sequence in which each pixel is serially addressed. Specifically, the schematics reported here are for LAEBID which utilized 10 μ s laser pulse width at 1%, 3%, and 6% duty cycle. The electron beam was set to raster from the top left of the pattern to the bottom right, with an x- and y-axis pixel spacing of 13.55 nm and a 10 μ s dwell time. In the schematic, the blue boxes represent pixels when the electron beam and laser pulses are irradiating simultaneously. All other white boxes represent pixels where the electron beam is on and no laser irradiation occurs. Importantly, during laser irradiation (blue pixels), the laser spot size is large enough that the entire deposit is simultaneously irradiated. The ratio of laser pulse on-time per LAEBID pass, as well as other experimental parameters for the LAEBID processes are reported in Table 2. In this table,

highlighted carbon content denotes that the deposit was compromised by laser induced chemical vapor deposition (LCVD), which deposits Pt in the entire laser spot size. Therefore, the most successful LAEBID conditions not convoluted with the LCVD reaction (10 μ s, 6% DC) were able to deposit a pattern with only ~25 % of the carbon content of a standard EBID deposit (~55.7 at% carbon). It is also clear that there is a trend between Laser/Ebeam “on” time and the carbon content of the deposit. Longer laser exposures, or the H₂O reactive gas anneal 2nd half-reaction, enhance the final purity of the deposit. A large enhancement in material purity (just 25% of carbon compared to standard EBID deposits) was able to be realized using the LAEBID process, and deposits exhibited high fidelity and shape retention.

LCVD

Figure 30a displays a LAEBID pattern deposited with synchronized 100 μ s pulse width and 0.5% duty cycle laser pulses. Clearly, island thin film growth was initiated peripheral to the area patterned by the electron dictated 1st half reaction. This peripheral island growth is attributed to contributions from LCVD which are not prevalent at milder laser conditions. Previous simulations⁸⁹ suggest that the SiO₂ substrate reaches a surface temperature of approximately 300°C, which is similar to common substrate temperatures for Pt CVD and ALD processes^{96–98}. **Figure 30b** displays an EDS spectrum for the LCVD region. There is no distinguishable carbon peak in the spectrum, as the slight low energy peak can be attributed to the Pt-N EDS peak. Thus we conclude that the reactive gas contributes to the CVD process and these conditions realize a simple pyrolytic dissociation of the precursor molecule. The onset of LCVD provides a temperature limitation for the LAEBID process. Specifically, the laser pulses must supply enough photothermal heat to facilitate the purification reaction of the amorphous carbon in the deposit, while remaining below the temperature threshold for the onset of LCVD platinum. A pulsed gas strategy, as opposed to gas co-flow, enables the use of laser conditions that are otherwise not feasible for the reactive gas assisted LAEBID process.

Sequential or Layer-by-Layer EBID Details

Figure 31a-c displays images of patterns deposited using the cyclic deposition technique with a different number of EBID monolayers deposited per cycle. This technique used a pulsed gas strategy where, (1) precursor gas was injected into the chamber for the electron beam dictated deposition 1st half-reaction, (2) the precursor was subsequently pumped from the

chamber and Ar inert gas was injected, and (3) diffusion enhanced residual H₂O molecules facilitate the laser pulse dictated purification 2nd half-reaction. From these images (and complimentary EDS spectra, **Figure 31d**), it is clear that the process succeeds in depositing a controllable number of monolayers per cycle with high purity. This provides an extra degree of freedom over typical surface reaction limited ALD processes. Since multiple monolayers can be deposited per cycle with this cyclic deposition technique, the process time required for deposition of a purified pattern can be drastically reduced. However, thicker deposition per cycle can have adverse effects on the deposit's uniformity and smoothness, as is clear by comparing **Figure 31a** and **Figure 31c**. It is worth noting that the peripheral deposition seen surrounding the deposits can be minimized by careful selection of electron beam parameters⁹⁹, and the growths on top of deposits in **Figure 31a** and **Figure 31c** are a result of an electron beam scanning artifact; neither of these issues are implicit with the cyclic deposition process in general. Converse to **Figure 27**, these patterns were deposited using a 5 keV beam energy, instead of 30 keV. This is responsible for the extensive peripheral or proximity deposition shown here.

Smoothing pulses were used after each cycle of the sequential deposition process to reduce the porosity of the deposits. A deposit before and after twenty 100 μ s smoothing pulses were applied is displayed in **Figure 32a** and **Figure 32b**, respectively. The smoothing pulses allow coalescence of the porous microstructure into a more continuous and smooth microstructure.

1.2.6.2 Figures

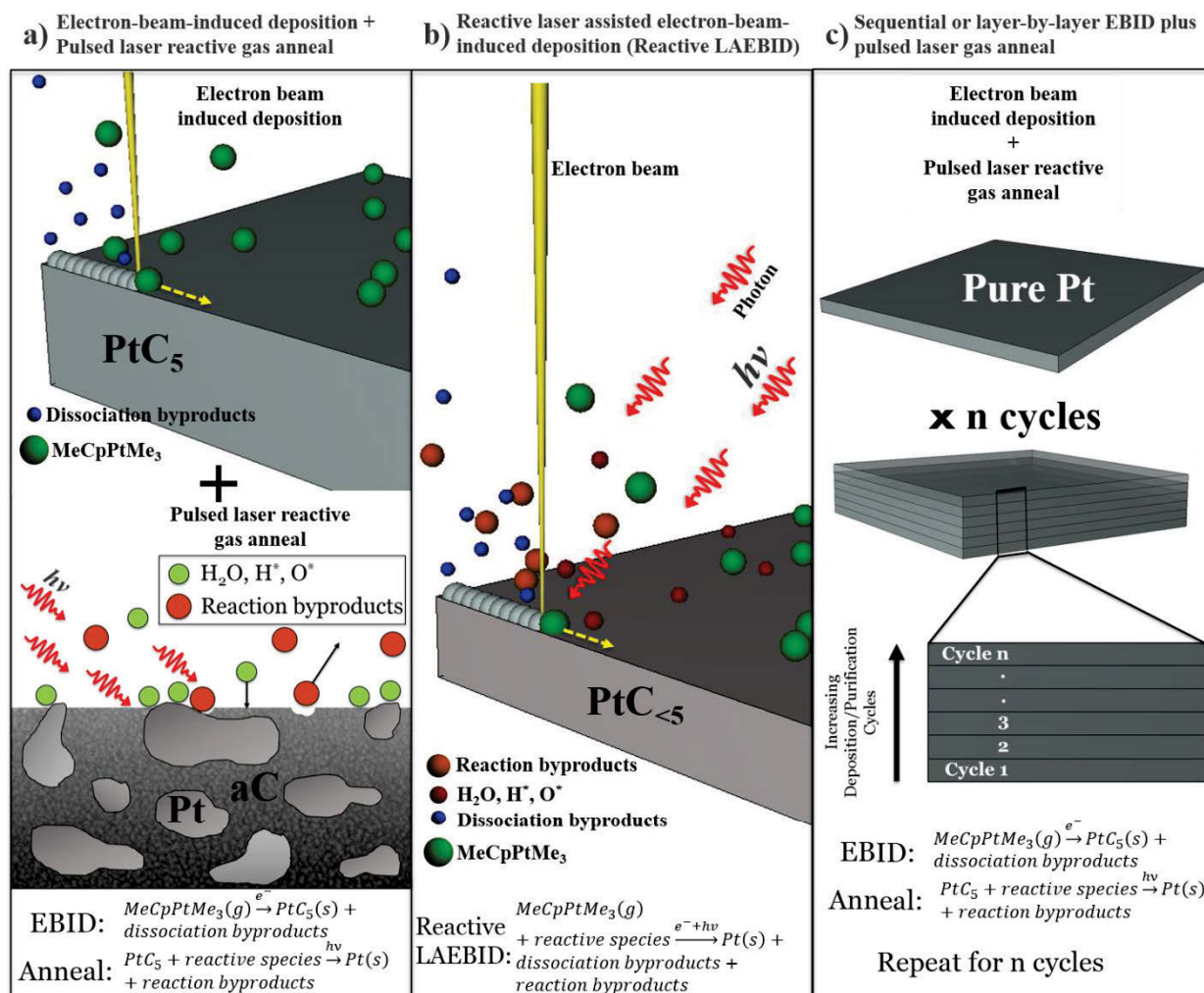


Figure 19. Schematic of the (a) EBID + pulsed laser reactive gas anneal, (b) reactive laser assisted electron-beam-induced deposition, and (c) sequential or layer-by-layer EBID plus laser reactive gas anneal purification processes.

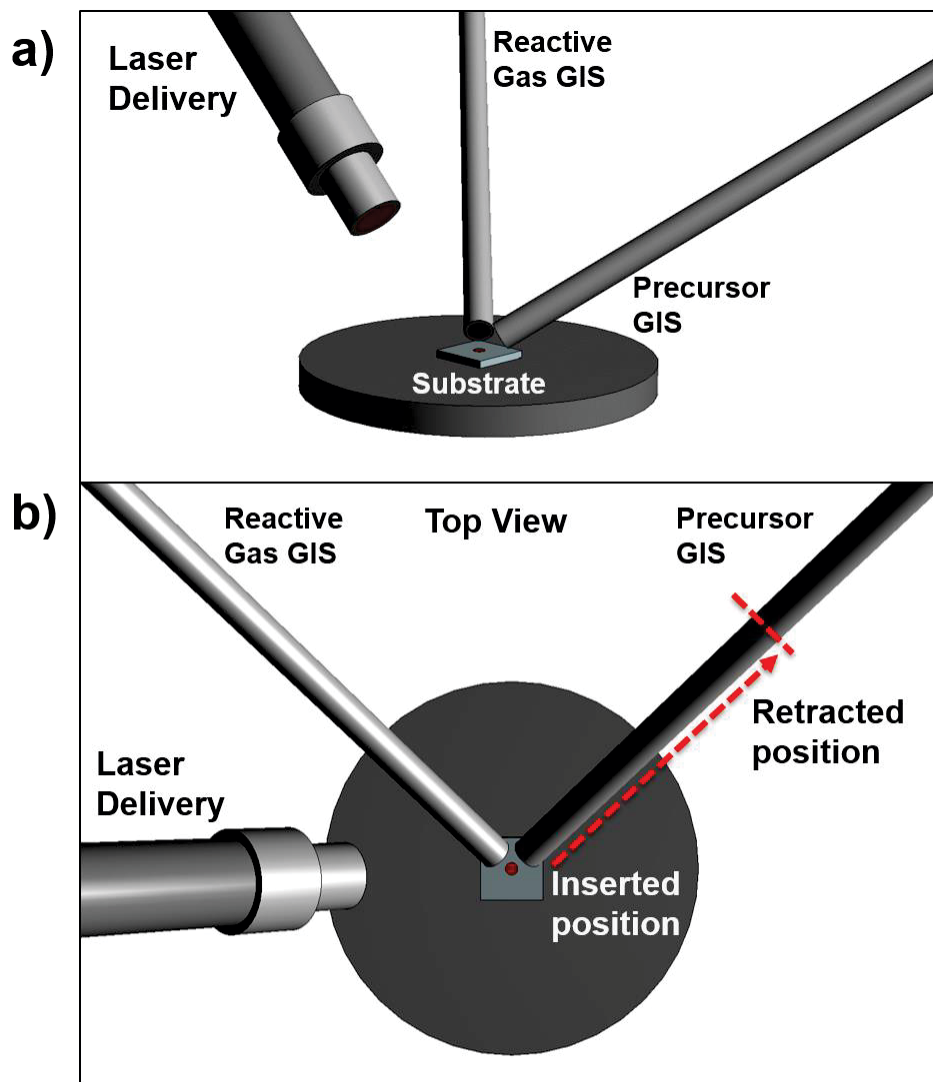


Figure 20. Schematic of deposition and annealing experimental setup from (a) tilted and (b) plan view. The laser delivery system, focused electron beam, precursor GIS, and reactive gas GIS converge to a single point. During reactive LAEBID processes the precursor GIS needle is in the “retracted” position (dotted red line) which is withdrawn to ~8 cm vertically and ~5 cm horizontally from the point of interest to reduce precursor flux at the substrate. During the sequential deposition plus annealing process the needles are configured in the as-shown inserted states.

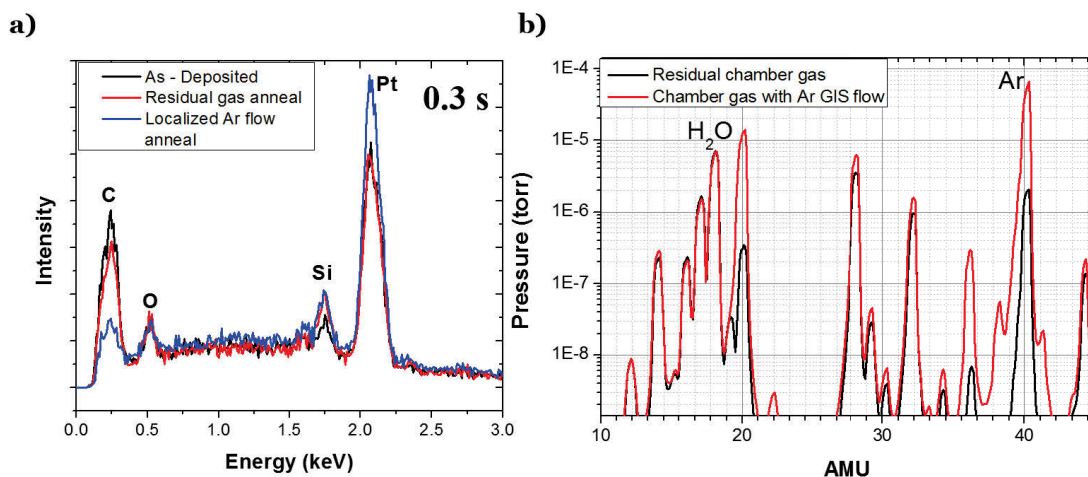


Figure 21. (a) EDS spectra of Pt EBID deposits which were annealed with 10 us and 1% duty cycle laser conditions for a cumulative laser exposure time of 0.3 s. Spectra shown include an as-deposited pattern, a deposit anneal under chamber ambiance, and a deposit annealed under localized Ar gas flow. (b) RGA spectra showing the residual chamber gas species present as well as during Ar flow.

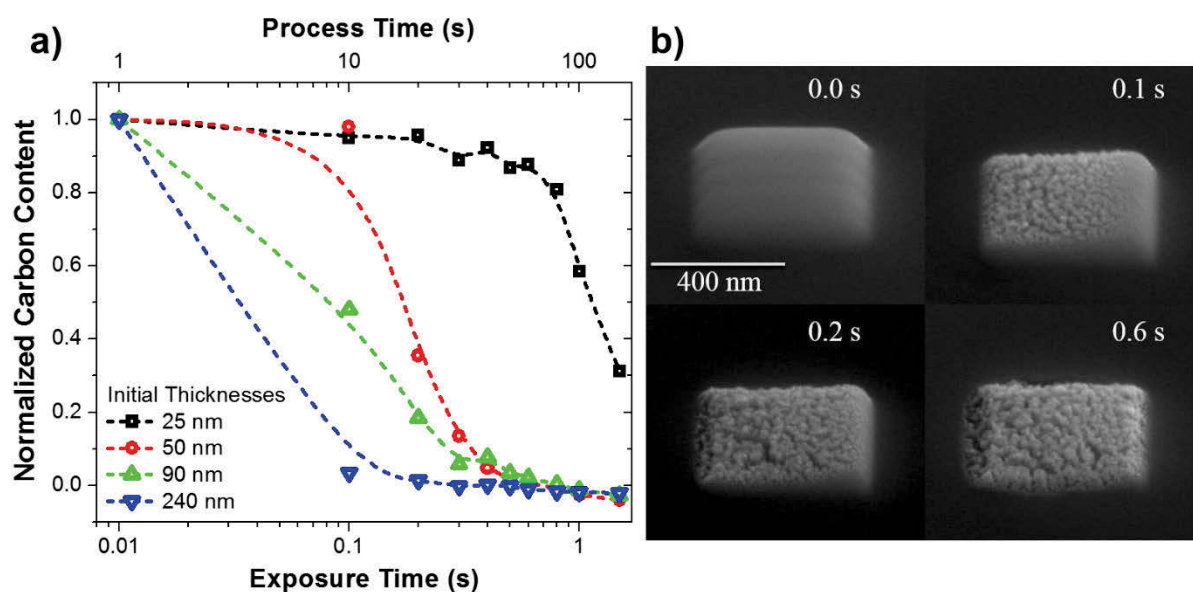


Figure 22. (a) Carbon content, from EDS measurements, as a function of laser exposure time (duty cycle \times processing time, bottom axis) and processing time (top axis) for 10 μ s at 1% laser duty cycle. The deposit thicknesses were approximately 240 nm, 90 nm, 50 nm, 25 nm which correspond to 8000, 4000, 2000, and 1000 passes, respectively. Normalized carbon content of 1, is that of a standard PtC₅ EBID deposit. (b) SEM images of an annealed deposit that was initially \sim 90 nm as-deposited. Inset time reflects the total laser exposure time for each anneal.

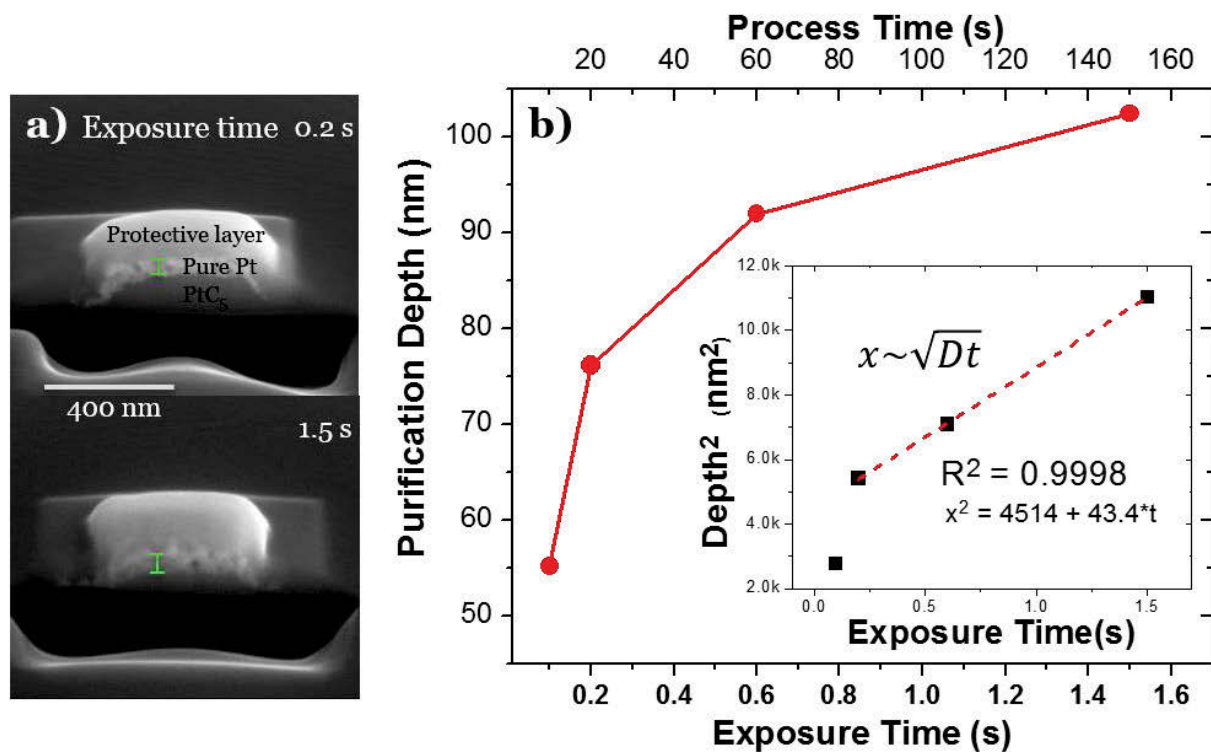


Figure 23. (a) SEM cross section images of deposits annealed with reactive gas for 0.2 s and 1.5 s of total laser exposure time. (b) Purification thickness from an originally ~240 nm thick PtC₅ deposit as a function of pulsed laser exposure time for a 10 μs, 1% duty cycle anneal while under Ar gas flow. Inset figure shows the plot and linear regression of purification thickness squared versus time which is consistent with a diffusion limited purification regime.

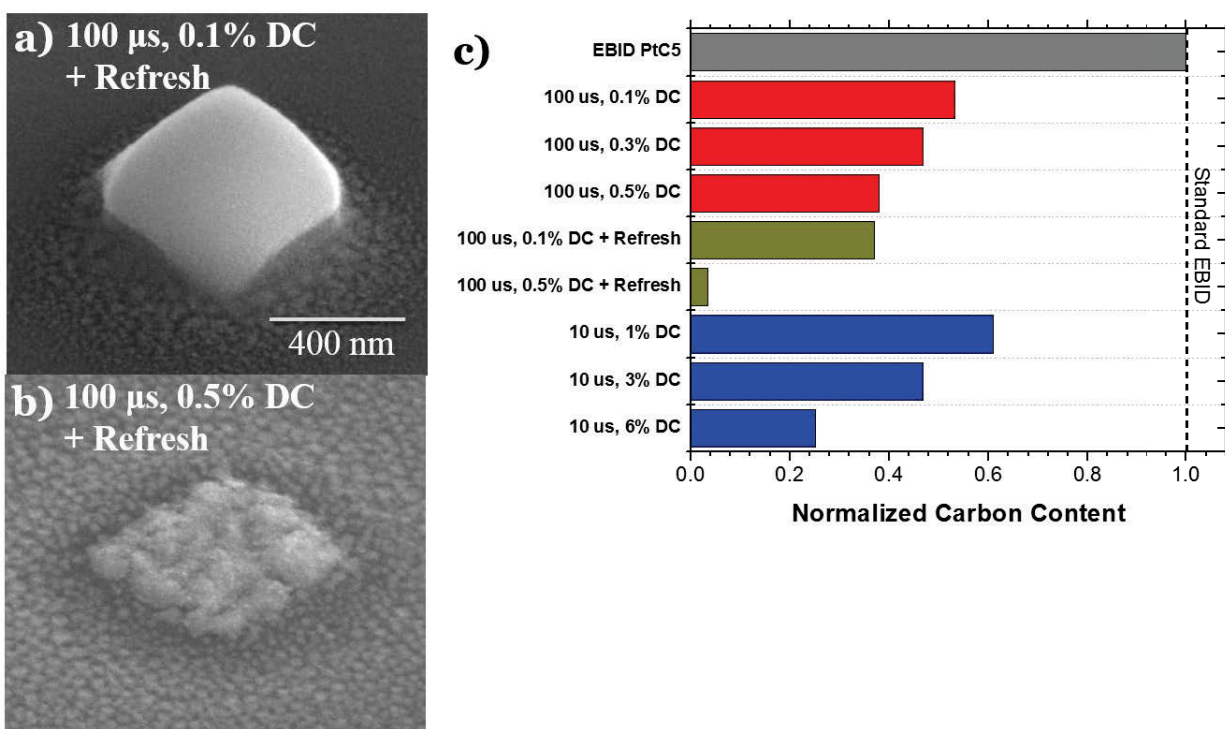


Figure 24. (a) SEM tilt image of a typical laser assisted electron beam induced deposition (LAEBID) pattern deposited with co-flow of hydrogen reactive gas. Specifically, this deposit was created 100 μ s and 0.1% duty cycle laser conditions. The electron beam and gas conditions were as listed in the experimental details. (b) SEM image of a LAEBID pattern deposited with 100 μ s and 0.5% duty cycle laser conditions, which shows contribution from LCVD. The deposit retains shape with high fidelity. (c) Comparison of LAEBID patterns deposited with various laser and refresh parameters. Refresh denotes extra time between LAEBID passes to enhance the laser-on time relative to the EBID time. Additional process parameter information may be found in the supporting information.

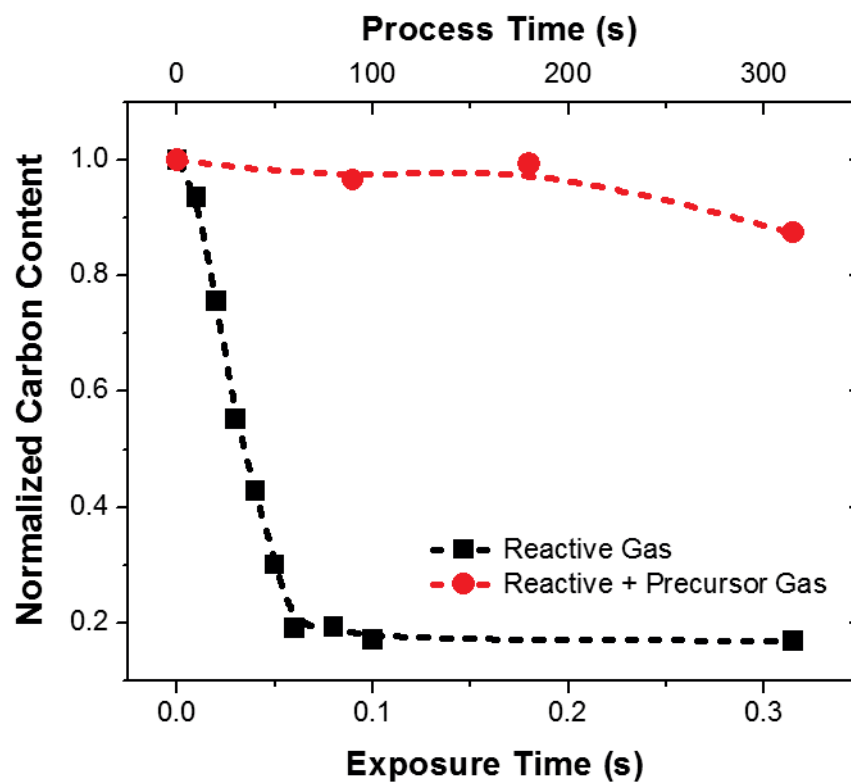


Figure 25. Normalized carbon content for standard EBID deposits annealed in reactive gas only (black) and a co-flow with approximately equal localized pressure of reactive gas plus the organometallic MeCpPtMe₃ precursor (red). Deposits were annealed with 100 μ s, 0.1% laser duty cycle conditions.

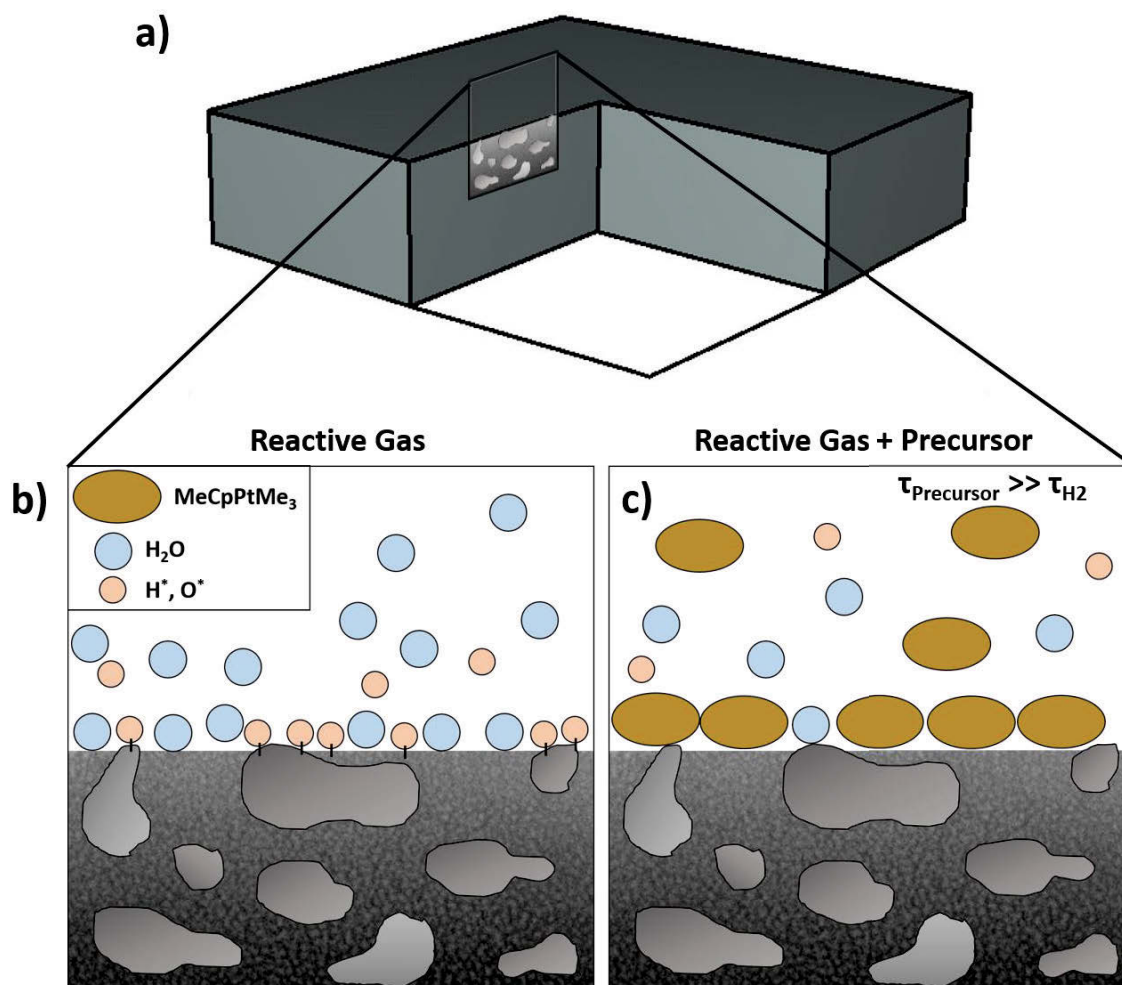


Figure 26. Schematic of proposed purification retardation mechanism. (a) EBID PtC_5 deposit is composed of Pt nanoparticles suspended with in an amorphous carbon matrix. (b) Under a flux of molecular H_2O only, there are many adsorption sites for the purification reaction to occur. (c) With a co-flow of H_2O and MeCpPtMe_3 , the MeCpPtMe_3 precursor gas dominates the surface coverage due to the long residence time and occupies many adsorption sites and reduces purification rate.

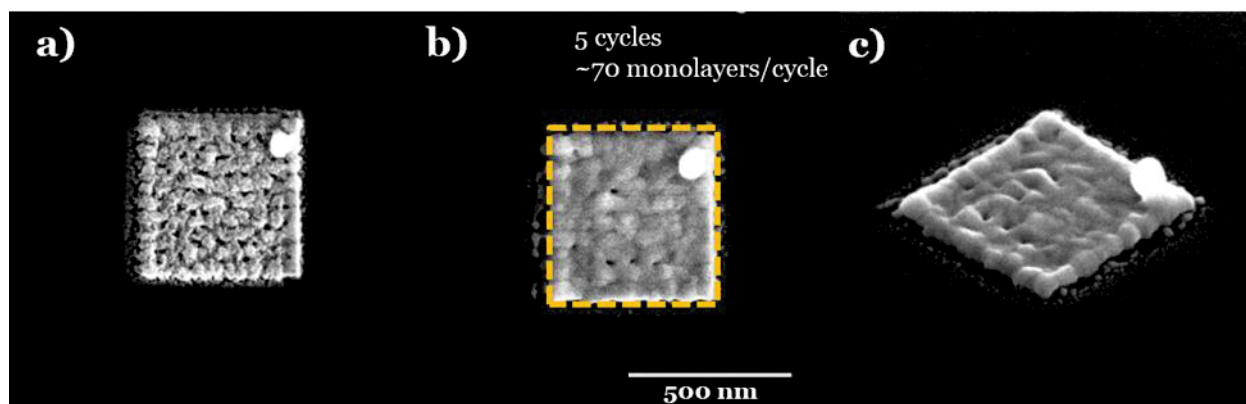


Figure 27. Sequential deposit fabricated from 5 cycles with approximately 70 monolayers deposited per cycle (a) before and (b) after 100 μ s smoothing pulses were applied to reduce porosity of the deposit. Inset dashed square denotes original pattern shape prescribed by EBID raster sequence. c) SEM tilted image (52°) of the sequential deposit.

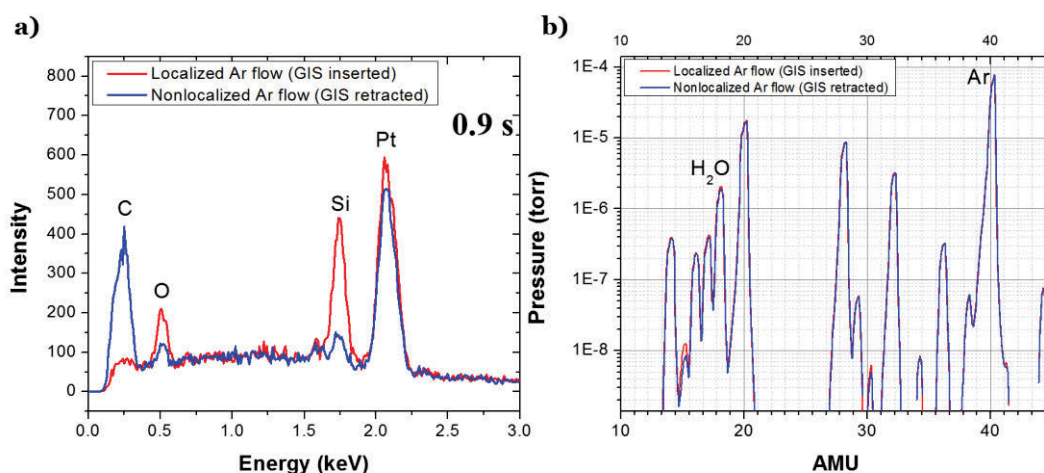


Figure 28. (a) EDS spectra of Pt EBID deposits which were annealed with 10 μ s and 1% duty cycle laser conditions for a cumulative laser exposure time of 0.9 s. Spectra shown include a deposit annealed under localized Ar flow and a deposit annealed under non-localized Ar gas flow. The partial pressure of the Ar flow was approximately 1.0E-6 mbar for both anneals. (b) RGA spectra showing the chamber gases species present during both of the anneal processes.

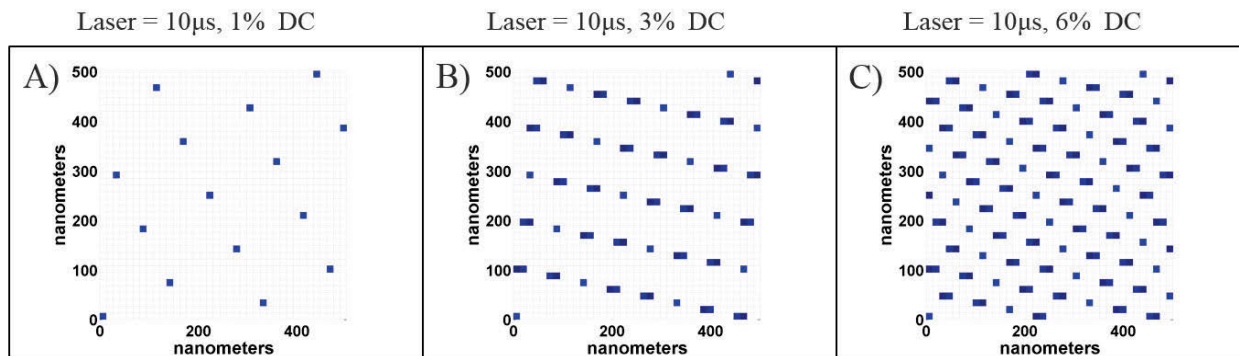


Figure 29. Synchronization map of electron beam and laser pulses during the reactive gas assisted LAEBID process. EBID patterns were deposited using a raster scan. The beam scanning initiates in the bottom left corner and terminates at the top right corner. Pixel spacing of the electron dwells are 13.55 nm in the x and y direction. A blue pixel indicates that the electron beam and laser are both simultaneously on and importantly the laser is irradiating the entire box whereas the electron is addressing only single pixels. A white pixel indicates that the laser is off during the 10 μ s electron beam dwell on that pixel. The synchronization is shown for LAEBID with 10 μ s laser pulses at (a) 1%, (b) 3%, and (c) 6% duty cycles.

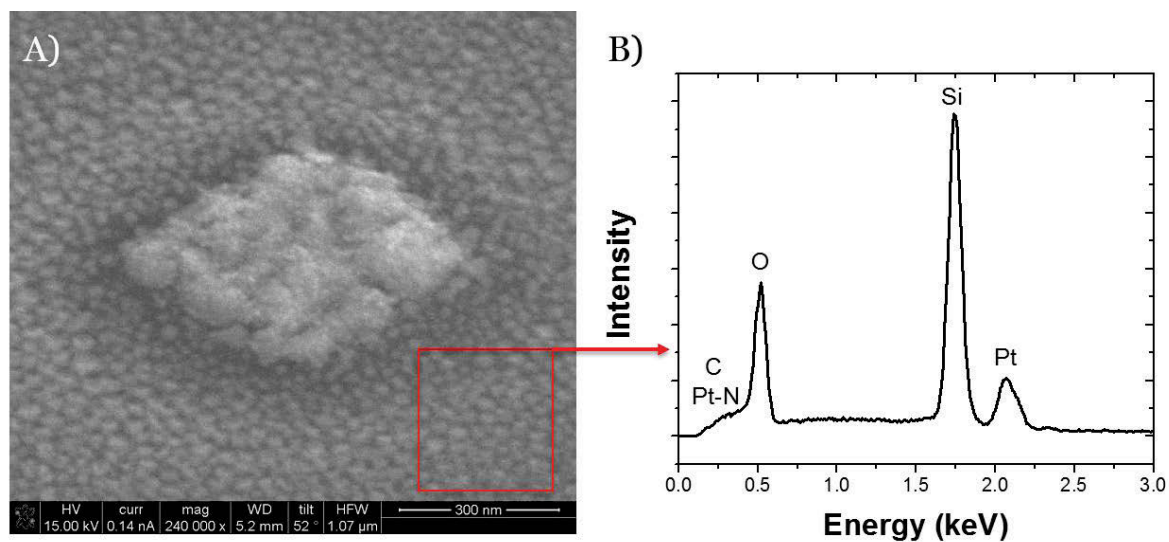


Figure 30. (a) SEM image of LAEBID pattern deposited with 100 μ s pulse width and 0.5% duty cycle synchronized pulsed laser. Island growth surrounding the deposit was induced by laser assist chemical vapor deposition (LCVD) of the precursor and reactive gas co-flow. (b) EDS spectrum of the LCVD platinum.

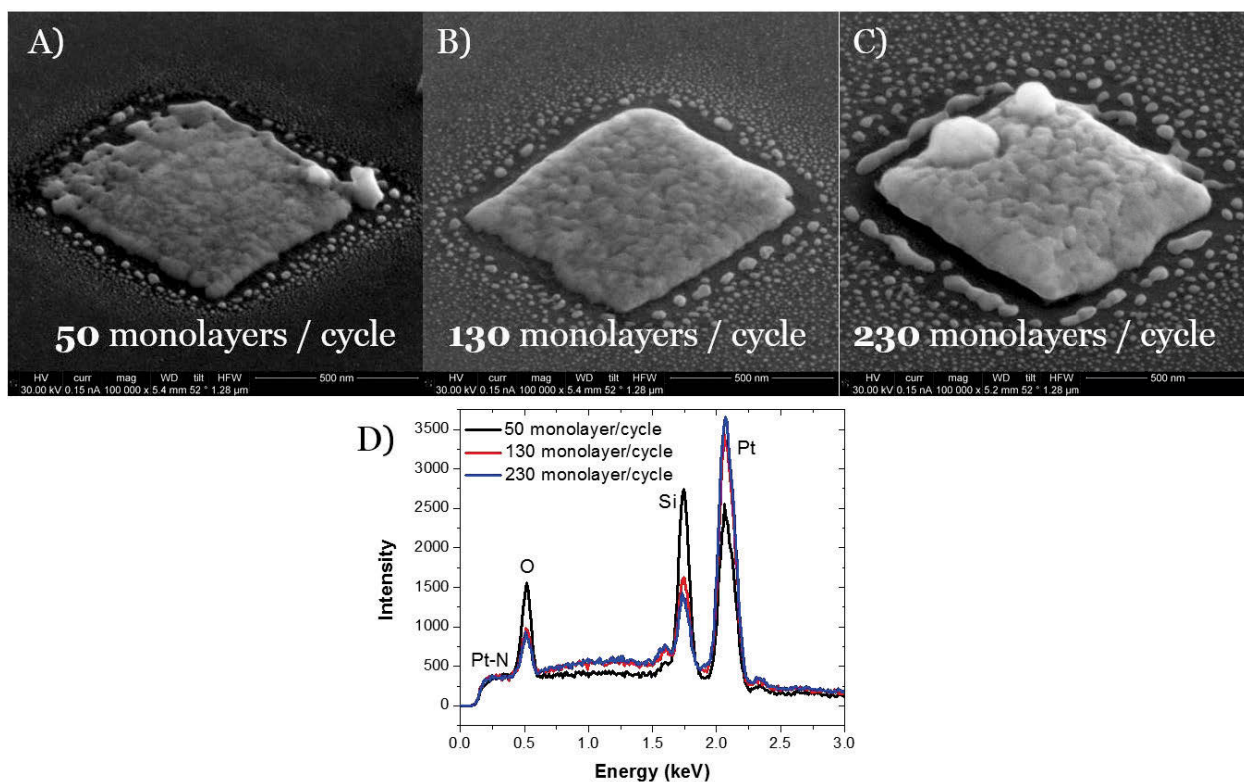


Figure 31. Images of patterns deposited using the cyclic deposition technique with (a) 50, (b) 130, and (c) 230 monolayers per cycle. Each pattern was deposited using a total of 6 cycles. (d) EDS spectrum the 130 monolayer/cycle deposit.

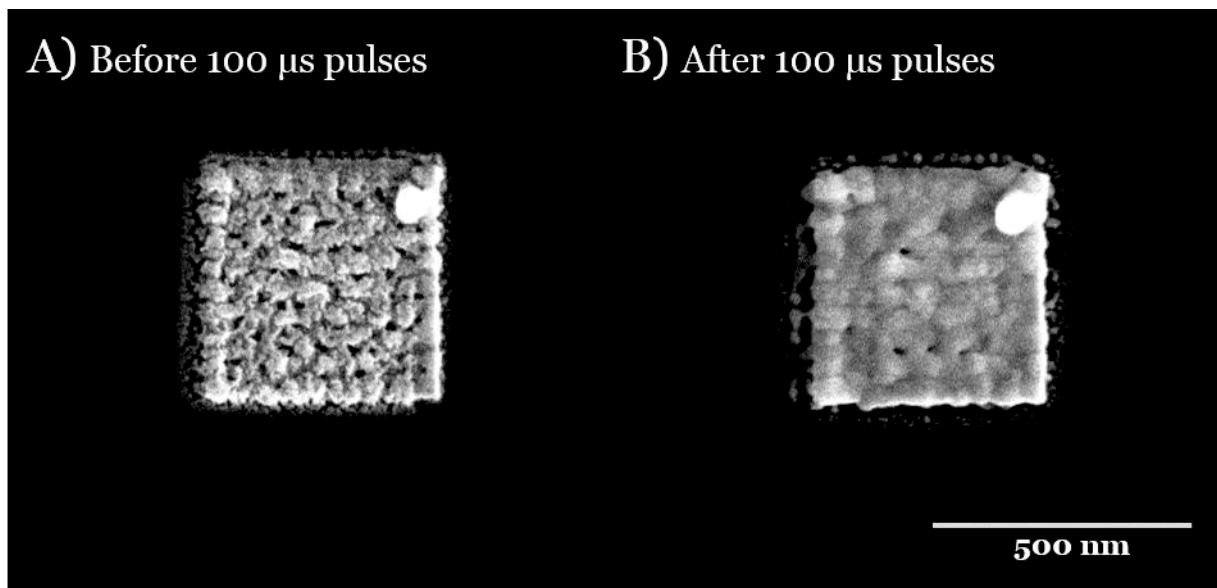


Figure 32. Patterns deposited using the sequential method (a) before and (b) after twenty 100 μ s laser smoothing pulses were applied.

1.2.6.3 Tables

Table 2. Details and parameters of various LAEBID patterns.

Laser Conditions		Gas Conditions		Electron Beam Conditions						
Pulse Width (μs)	Duty Cycle (%)	Inert Gas	Precursor Gas	Beam current (pA)	Beam energy (keV)	Dwell (μs)	Refresh (ms/Ebeam Pass)	Laser pulses per LAEBID pass	Laser On/ Ebeam On (per pixel)	Platinum Content (at%)
100	0.1	Ar	MeCpPtMe ₃	98	5	10	NONE	0.14	1.36	27.3
100	0.1	Ar	MeCpPtMe ₃	98	5	10	13.6	0.14	1.36	35.1
100	0.3	Ar	MeCpPtMe ₃	98	5	10	NONE	0.41	4.08	29.9
100	0.5	Ar	MeCpPtMe ₃	98	5	10	NONE	0.68	6.81	34.5
100	0.5	Ar	MeCpPtMe ₃	98	5	10	13.6	0.68	6.81	85.3
10	1	Ar	MeCpPtMe ₃	98	5	10	NONE	13.62	13.62	24.7
10	3	Ar	MeCpPtMe ₃	98	5	10	NONE	40.85	40.85	29.9
10	6	Ar	MeCpPtMe ₃	98	5	10	NONE	81.70	81.70	44.3

CHAPTER II
ADVANCED ION BEAM INDUCED PROCESSING USING A GAS FIELD
IONIZATION SOURCE

2.1 In situ Mitigation of Sub-Surface and Peripheral Focused Ion Beam Damage via Simultaneous Pulsed Laser Heating

A version of this chapter was originally published by M. G. Stanford et al.:

Stanford, M. G.; Lewis, B. B.; Iberi, V.; Fowlkes, J. D.; Tan, S.; Livengood, R.; Rack, P. D. In Situ Mitigation of Subsurface and Peripheral Focused Ion Beam Damage via Simultaneous Pulsed Laser Heating. *Small* **2016**, *12*, 1779–1787.

Michael G. Stanford, Brett B. Lewis, and Vighter Iberi conducted experiments reported in this manuscript. Shida Tan and Richard Livengood conducted TEM measurements. Michael G. Stanford conducted subsequent data analysis, characterization, simulations, and wrote the manuscript. All co-authors discussed the results and formulated the mechanism for sub-surface damage mitigation.

2.1.1 Abstract

Focused helium and neon ion beam processing has recently been used to push resolution limits of direct-write nanoscale synthesis. The ubiquitous insertion of focused He^+/Ne^+ beams as the next-generation nanofabrication tool-of-choice is currently limited by deleterious subsurface and peripheral damage induced by the energetic ions in the underlying substrate. Here, we demonstrate the *in situ* mitigation of subsurface damage induced by He^+/Ne^+ ion exposures in silicon via a synchronized infrared pulsed laser-assist process. The pulsed laser-assist provides highly localized *in situ* photothermal energy which reduces the implantation and defect concentration by greater than 90 %. The laser-assisted exposure process is also shown to reduce peripheral defects in He^+ patterned graphene, which makes this process an attractive candidate for direct-write patterning of 2D materials. These results offer a necessary solution for the applicability of high resolution direct-write nanoscale material processing via focused ion beams.

2.1.2 Introduction

Focused ion beam induced processing of materials has long been the tool-of-choice for nanoscale direct-write additive and subtractive materials synthesis.⁴ Additive approaches involve the injection of precursor molecules which are locally adsorbed onto the substrate and dissociated by the primary ion beam and secondary electrons generated by the primary ion. Subtractive approaches include direct sputtering from the focused ion beam as well as gas-assisted etching. Liquid gallium sources have historically been the industry standard, however in recent years He^+ and Ne^+ focused ion beam imaging and processing from the Gas Field Ion Source (GFIS) has emerged as a higher resolution variant. Helium ion beam synthesis and imaging has been used for a variety of applications such as nanolithography¹⁰⁰, 2D material editing and defect manipulation^{9–12}, nanopore synthesis for DNA sequencing¹³, selective lattice straining¹⁴, and is being explored as a next-generation instrument for nanoscale circuit editing/debugging.^{20,21} While the GFIS source provides higher resolution, the more ubiquitous application of helium and neon ion beam induced synthesis is still in question. The main liability of nanoscale processing with a GFIS source is the notable sub-surface damage accumulation that occurs during irradiation of a substrate^{101–104}, which ultimately limits the fidelity and resolution of direct-write processing capabilities. While the distribution and concentration of defects and implanted species are a function of beam energy and ion/target type, the progression of defects ranging from dislocation bands to the coalescence of sub-surface He microbubbles, as a function of dose, was recently observed in the He^+/Si system with transmission electron microscopy (TEM)¹⁰²: 1×10^{15} ions/cm² – dislocation bands, 1×10^{16} ions/cm² – onset of amorphization, 1×10^{17} ions/cm² – coalescence of sub-surface He nanobubbles, 1×10^{18} ions/cm² – coalescence of sub-surface He microbubbles.

Conveniently, the He^+/Si system is well-studied as cavities formed via He^+ implantation can getter metal impurities in silicon and extend the lifetime of semiconductor junctions.¹⁰⁵ Nanobubble formation and the subsequent cavity formation for post-implantation annealed He/silicon has been well-documented and shown to be a complex interaction of the generated vacancies and implanted helium ion distributions.¹⁰⁶ The measurements and modeling of He and H implantation defect formation and temperature dependent recovery/diffusion has been recently reviewed in detail.¹⁰⁷ Summarily, the He^+ implantation damage profile in Si and subsequent

recovery kinetics can be categorized into a low-fluence and high fluence regime¹⁰⁸ for implant energies on the order of tens of keV. The transition between the two regimes is an aerial dose on the order of 1×10^{16} ions/cm² which for 20keV He⁺ in silicon yields a peak concentration $\sim 3.5 \times 10^{20}$ He⁺/cm³. Temperature programmed desorption of He in the low fluence regime has simple first order kinetics with a maximum desorption peak at ~ 300 °C, whereas higher fluence spectra have higher order kinetics with multiple temperature peaks. In the low fluence regime for a 5×10^{15} ions/cm² dose and 20 keV He⁺ energy, the damage profile contains a peak in the helium concentration at ~ 200 nm deep into the silicon whereas the silicon vacancy concentration extends from the surface to ~ 70 nm deep.^{109,110} Time-dependent low-temperature annealing (250 °C) reveals that helium diffuses towards the sample surface which temporarily fills vacancies in the near surface region before effusing out of the sample. Higher temperature anneals (~ 600 °C) are required to totally annihilate the vacancies, which at low fluence do not coalesce to form voids or cavities.

At higher fluence (for instance 2×10^{16} He/cm²), the peak He⁺ ion concentration is again ~ 200 nm deep and the vacancy concentration extends from the surface to ~ 100 nm deep. Electron microscopy does not reveal bubbling at this concentration, but rather a high density of extended defects peaking at ~ 130 nm deep – consistent with a SRIM/TRIM simulated peak in the displaced silicon atoms. Annealing kinetics in the higher fluence regime is complicated by the strain fields produced by the higher concentration of vacancies and helium which interact to form higher order extended and more stable vacancies, He-vacancy complexes, and eventually helium bubbles. Helium effusion from coalesced bubbles occurs at a higher activation energy (1.8 eV)¹¹¹, which leads to the formation of stable empty cavities or voids embedded within the target material. To mitigate the high-fluence damage regime, thermal energy must be sufficient to drive diffusion in order to avoid the critical helium and defect concentration levels that lead to irreparable void formation.

Here we demonstrate an *in situ* pulsed laser-assisted focused ion beam approach in which an intermittent pulsed laser with an appropriate power density and duty cycle can photothermally mitigate undesired helium and neon ion-beam induced subsurface damage. Specifically, during the focused ion beam exposure a pulsed laser (~ 100 μ s pulse width) is periodically irradiated ($\sim 1\%$ duty cycle or 100 Hz frequency) onto the beam-exposed region and a fraction (depending on

the indices of refraction at the laser wavelength) of the laser light is absorbed which heats the substrate. Clearly the damage mitigation is a function of the time-temperature profile of the pulsed laser heating. We demonstrate the effects of total ion dose, photon/ion flux ratio, and ion energy in the He⁺/Si system and compare the effect of ion type in the Ne⁺/Si system. Finally, He⁺ milled graphene channels are also compared with and without the laser-assist and lower defect concentrations were observed. The pulsed laser-assisted ion exposure approach promises to enable a plethora of high-resolution ion beam nanomachining techniques where subsurface and peripheral damage cannot be tolerated.

2.1.3 Results and Discussion

Figure 33 is a schematic illustrating the pulsed laser delivery system which is mounted onto the gas field ion microscope. A) depicts a He⁺ exposure for the prescribed raster pattern whereas b) illustrates the relevant He⁺ and laser beam irradiation sequences where the focused helium ion beam is scanned and the pulsed laser is periodically exposed to the entire region. The schematic cross section in **Figure 33a** demonstrates the simulated room temperature helium, vacancy and interstitial concentration profiles of a 1×10^{16} He⁺/cm² dose overlaid on an experimental TEM image. Simulation details can be found in experimental details, supporting information, and will be discussed further in this work. The schematic cross-section in **Figure 33b** illustrates the simulated concentration profiles resulting from the same dose with the photothermal laser-assist. As illustrated, the *in situ* laser exposure intermittently heats the exposed region and facilitates helium and vacancy diffusion as well as interstitial-vacancy annihilation. It is worth noting that the uncoupled simulation does not account for interstitial/vacancy annihilation, therefore the reported Si interstitial/vacancy concentrations represent the hypothetical maximums of each. **Figure 34** compares TEM cross section micrographs of a silicon sample exposed to variable He⁺ areal doses ranging from 1×10^{16} to 1×10^{18} He⁺/cm² without a-d) and with e-h) the simultaneous pulsed laser irradiation at a ion beam energy of 25 keV. Examination of the TEM images a-d) demonstrate the typical damage accumulation noted in silicon¹⁰², namely a clear progression from vacancy and dislocation generation (as evidenced by the slight contrast in the 1×10^{17} He⁺/cm² dose), amorphization (observed in the 5×10^{17} He⁺/cm² dose), and helium bubble formation (noted in the 1×10^{18}

He⁺/cm² dose image d) and is accompanied by surface swelling at doses of 5x10¹⁷ He⁺/cm² and 1x10¹⁸ He⁺/cm². See Supporting Information for high-resolution images of some of the defect signatures. Interestingly, the typical defect signatures are realized at slightly higher areal doses because the scanned ion width is less than the radial range of the beam (helium straggle at 25keV = 123 nm); thus the defect and implant concentrations are effectively smaller (detailed in Supporting Information).

Simultaneous pulsed laser irradiation has a profound effect on the subsurface damage accumulation (**Figure 34e-h**), and significantly attenuates the onset of Si amorphization. The averaged photon/ion flux used for this laser-assisted exposure was 1.3x10⁶ photon/ion. The simulated temporal profile of the silicon surface temperature induced by a single laser pulse is illustrated in the **Figure 33b** inset where the maximum temperature reached is ~ 700 K. **Figure 34** also shows high-resolution TEM images collected of He⁺ exposed Si without i) and with j) *in situ* laser-assist at an ion dose of 5x10¹⁷ He⁺/cm², and clearly demonstrates a significant reduction in subsurface damage with the *in-situ* laser-assist. Specifically, near surface amorphization of the Si is obvious in **Figure 34i** when no laser assist is used. However, the Si maintains its near surface crystallinity when a laser assisted exposure technique is used, as shown in **Figure 34j**. **Figure 34k** are selected area electron diffractograms (SAED) of an unexposed silicon region and a region exposed to a helium dose of 1x10¹⁸ He⁺/cm² at a photon/ion flux ratio 5x higher (see **Figure 34l** where dashed circles denote the SAED regions) relative to the damage profile shown in **Figure 34h**. Comparison of the SAEDs reveals that while defects remain, as evidenced by the distorted spots, the laser heating annihilates much of the damage accumulated during ion irradiation and the single crystal silicon is maintained. Atomic resolution TEM images which confirm the maintained crystalline structure of Si after a laser-assisted exposure can be found in Supporting Information **Figure 38**. Another obvious signature of the irradiation damage at higher doses in silicon is the surface swelling observed in **Figure 34 c,d**. The onset of the swelling is a signature of the crystalline to amorphous transition that occurs as the amorphous silicon density is reduced (increased free volume). At higher doses (**Figure 34d**), the helium concentration increases and the bubble size increases which exacerbates the surface swelling (see references^{101,102}). Importantly, the higher photon/ion flux

ratio further reduces the ion damage and minimal surface swelling is observed even at the 1×10^{18} He^+/cm^2 dose

To demonstrate the influence of beam energy and ion species, **Figure 35** illustrates TEM cross section images of without and with laser-assisted ion beam exposures into silicon samples for **a-b)** 15 keV He, 1×10^{18} He^+/cm^2 and **d-e)** 25 keV Ne^+ , 1×10^{16} Ne^+/cm^2 . The photon/ion flux used was 1.3×10^6 photon/ion for the laser-assisted 15 keV He^+ exposure. The dashed line in **Figure 35a** is a trace of the amorphization zone of the equivalent 25 keV sample (**Figure 34d**). As evident in **Figure 35a** the amorphization zone is shallower at 15 keV because of the higher nuclear energy loss cross section at lower He^+ energy. Thus the peak implantation and defect concentrations at an equivalent ion dose is higher at 15 keV than 25 keV. Therefore one expects that the laser-assisted defect mitigation will be less effective at lower beam energy. **Figure 35b** and **Figure 35c** compare 15 keV and 25 keV regions, which have the same ion dose and photon/ion flux ratios and, as expected, the residual ion damage (swelling/surface protrusion) in the 15 keV sample is more severe.

Figure 35 also compares TEM micrographs of 25 keV Ne^+ exposures at 1×10^{16} Ne^+/cm^2 dose without **d)** and with **e)** laser-assist during the exposure. The mass of the Ne^+ (20 amu) is much higher than He^+ (4 amu) and consequently has a higher nuclear energy loss cross section and a significantly reduced implant range. Thus, the number of silicon interstitials and vacancies generated are $\sim 3.8 \times$ higher per ion and the reduced range results in a higher peak implant concentration for Ne^+ relative to equivalent energy He^+ . A comparison of **Figure 35d** and **Figure 35f** illustrates that at the exposure dose of 1×10^{16} He^+/cm^2 at 25 keV, very little cumulative damage has occurred, whereas for Ne^+ under identical conditions, full amorphization has occurred to a depth of ~ 100 nm. Because the defect generation rate of Ne^+ is significantly higher and the larger neon atom has a lower diffusion coefficient in silicon, a photon/ion flux $12 \times$ higher was tested (1.6×10^7 photon/ion). **Figure 35e** illustrates that while the amorphization region is significantly reduced, a higher photon/ion flux ratio is needed for the Ne^+/Si system. As discussed above, post-annealing studies of helium implantation into silicon reveals that irreparable voids form at a critical exposure dose of $\sim 1 \times 10^{16}$ He^+/cm^2 . While the implanted helium can be driven out of the bubbles, voids/pores remain in the silicon. Importantly, in these studies the implantation is over a large area and thus the helium and defect gradients and

subsequent transport are confined mostly to a single dimension along the implant axis. However, in our reduced geometry a pseudo 2-dimensional diffusion gradient exists; diffusion in the z – coordinate as well and perpendicular to the long scan axis dominate mass flow. In order to mitigate void formation it is important to have appropriate laser conditions in which the implanted ions diffuse and vacancies/interstitials annihilate before this critical dose is reached. For example, comparable laser exposure *after* ion irradiation yields much less damage mitigation compared with the *in situ* process (see Supporting Information).

The damage mitigation in the He^+/Si system during ion irradiation is a complex process involving the distributions, diffusion and interaction of the implanted helium atoms, interstitial Si, and Si vacancies. The helium, vacancy and interstitial concentration profiles of a $25 \text{ keV } 1 \times 10^{16} \text{ He}^+/\text{Si}$ implantation dose is illustrated in **Figure 33a**. Indeed, the helium distribution penetrates deepest into the silicon substrate relative to the interstitial silicon and silicon vacancies. The process is further complicated by the fact that the He-Si vacancy interactions change with increasing dose. For simplicity, we have modeled the uncoupled diffusion of the helium ions as well as silicon interstitials and vacancies to illustrate how the *in situ* laser irradiation affects the distributions and helps facilitate out-diffusion of helium. The Si vacancy and interstitials are thus reported as the maximum hypothetical concentrations, since the uncoupled simulation does not account for Si vacancy/interstitial annihilation. The activation energies and pre-exponential factors for silicon vacancies (0.1 eV , $1.18 \times 10^{-4} \text{ cm}^2/\text{s}$)¹¹², interstitials (1.37 eV , $1.58 \times 10^{-1} \text{ cm}^2/\text{s}$)¹¹² and He (0.58 eV , $5.1 \times 10^{-4} \text{ cm}^2/\text{s}$)¹¹³ are assumed.

In context to this work, the experimental results illustrated in **Figure 34a-h** reach a $1 \times 10^{16} \text{ He}^+/\text{cm}^2$ dose in $\sim 1.78 \text{ s}$ and thus the series in **Figure 34e-h** experiences ~ 178 laser pulses during the critical exposure dose of $1 \times 10^{16} \text{ He}^+/\text{cm}^2$, where previous literature suggests defect concentration levels that lead to irreparable void formation¹⁰⁵. **Figure 36** compares the simulated helium concentration profiles of an exposure dose of $1 \times 10^{16} \text{ He}^+/\text{cm}^2$ for 15 keV a) without and b) with laser-assist as well as 25 keV c) without and d) with laser-assist. **Figure 36e** compares the maximum implanted He concentration as a function of photon/ion flux for 15 and 25 keV beam energy exposures at a dose of $1 \times 10^{16} \text{ ions}/\text{cm}^2$. Clearly, higher photon/ion flux reduces the maximum concentration of implanted He by promoting diffusion. Interestingly, at low photon/ion flux, the implanted 15 keV He^+ concentration is greater than that of 25 keV He^+

due to a smaller interaction volume. A crossover point in the implanted ion concentrations of the two beam energies occurs at $\sim 1.3 \times 10^6$ photon/ion, beyond which the laser-assist is more effective reducing the He concentration for 15 keV He⁺. This is due to the first-order He desorption kinetics at the surface of the Si substrate as 15 keV He⁺ implantation is distributed more closely to the substrate surface than 25 keV He⁺. The He concentration as a function of exposure dose during the exposure is inset in **Figure 36e**, which further illustrates the effectiveness of the pulsed laser in facilitating helium diffusion and thus mitigation of helium coalescence and bubble formation. Also included in the inset of **Figure 36e** is a simulation for the 5x higher photon/ion flux ratio (6.6×10^6 photon/ion) for the exposure conditions shown in **Figure 34l**. Over one order of magnitude reduction in the helium concentration is realized at a dose of 1×10^{16} He⁺/cm², and extrapolating the diverging plots to higher dose clearly realizes higher concentration differences as dose increases. Simulations of the laser-assisted vacancy and interstitial diffusion were also performed and are included in the Supporting Information. The monovacancy activation energy yields very fast diffusion (even at room temperature) and thus, the simple model assumed here predicts almost complete out-diffusion of the vacancies. Conversely, the interstitial activation energy is relatively high, therefore interstitials realize very little laser assisted-diffusion. The interstitial diffusion could feasibly be enhanced by achieving higher temperatures with the pulsed laser heating. The observed photothermal defect mitigation is to be assumed dominated by vacancy diffusion to Si interstitials and subsequent interstitial-vacancy recombination/annihilation. The results are consistent with tight binding molecular dynamics simulations which reveal that at low temperature (< 1050 °C) vacancy diffusion dominates and interstitial-vacancy annihilation occurs with an activation energy of ~ 1.13 eV.¹¹² It is worth noting that while high photon/ion flux is apparently more effective at He out-diffusion for 15 keV He⁺ beams, the induced Si vacancy and interstitial concentrations are greater relative to the 25 keV He⁺ beam due to the reduced interaction volume. This accounts for the increased surface protrusion associated with amorphization of the Si exposed with 15 keV He⁺ (**Figure 35b**) relative to 25 keV He⁺ (**Figure 35c**).

Finally, we demonstrate anecdotally reduced defect generation by comparing progressively narrower channels cut into single layer graphene supported on Si via the He⁺ ion beam. He⁺ induced defects in graphene has been previously reported^{12,114} and in particular the

proximal defect generation caused by backscattered ions.¹¹⁵ Recently, it was demonstrated that the contrast in HIM imaging of supported graphene can be used as an *in situ* visualization of conductance in graphene¹¹ due to the positive charging and subsequent darkening of the image that occurs if inadequate conduction channels exist. **Figure 37** compares HIM and SEM images of identical confined channels that were cut into graphene with a helium ion beam with and without the pulsed laser-assist. The confined channels were cut with dimensions of 150, 100, 50 nm (from bottom to top). Clear evidence of darkening is observed in the HIM image of the 50 nm wide channel generated without the laser-assist which is consistent with proximal defect generation from backscattered ions and a lowering of the channel conductance (**Figure 37a**). Conversely, the 50 nm channel generated with the pulsed laser-assist does not darken (**Figure 37b**), which suggests a high-conductance channel suitable to minimize positive charging in the HIM. **Figure 37e** shows Raman spectra, using an excitation wavelength of 532 nm, of He⁺ exposures on graphene at a dose of 1×10^{14} He⁺/cm² with and without laser-assist. A dose of 1×10^{14} He⁺/cm² was used to emulate the low proximal dose delivered from backscattered ions in the periphery of the exposure pattern. There is a clear reduction in the D peak intensity when simultaneous laser pulses irradiate the graphene during the exposure. The reduction in the D peak is indicative of increased order in the graphene, fewer point defects, and hence greater conductivity. Therefore, at high photon/ion flux, proximity damage associated with ion patterning can be healed *in situ* while still allowing the primary beam to pattern the material with a prescribed raster pattern, thus effectively increasing the patterning resolution. Patterning 2D materials with greater photon/ion flux could serve as a method to further reduce undesired peripheral damage. Future work will focus on optimization of proximal laser-assisted defect mitigation of 2D materials patterned with He⁺ and Ne⁺ and their effects on device performance.

2.1.4 Conclusions

In summary, focused ion beam-induced nanoscale synthesis has played an important role in nanoscience and technology. The impact that this technique will have in the future depends on improved ion source solutions that can extend the resolution towards the atomic scale. Beyond resolution, solutions to the deleterious peripheral damage induced during direct-write processes must be developed as defects introduced into device regions cannot be tolerated. To

this end, we have demonstrated that a pulsed laser-assist can mitigate the damage introduced via focused helium and neon ion beam irradiation. The damage mitigation is intuitively a function of the photon/ion flux ratio as well as a function of the ion beam energy and ion species. Ultimately, a balance in the damage creation and diffusion/recovery of the implanted ions, and vacancies and interstitials generated must be reached. While at a fixed laser wavelength the pulse-width and duty cycle of the laser can be adjusted to modulate the effective photothermal load, a variable wavelength source is an intriguing option to optimize the laser-solid coupling to maximize the absorption and heating in the near surface region. To this end, we are developing a multi-wavelength source which can be spectrally tuned across the visible spectrum to optimize the photothermal laser-assist process. Furthermore, both laser-assisted focused ion beam-induced deposition and laser-assisted focused ion beam gas-assisted etching will be investigated. It is believed that not only will the sub-surface damage be mitigated, but deposited material purity will be enhanced as we have demonstrated in laser-assisted focused electron beam induced deposition.^{65,116–118} Furthermore, it is expected that laser-assisted and gas-assisted etching, in a similar fashion as laser-assisted focused electron beam induced etching¹¹⁹ can realize higher etching rates.

2.1.5 Methods

2.1.5.1 Synchronized Laser Probe

The laser delivery system⁹⁵ utilizes a 915 nm wavelength 25 W multichip diode laser module (BMU25B-915-01, Oclaro Inc.) and is mounted on a high angle port (52° relative to the sample stage) on the helium/neon ion microscope (HIM/NIM). The laser probe was aligned such that the focal distance was confocal with the ion beam at a working distance of 7.5 mm with respect to the HIM pole piece. This setup enables delivery of a maximum power of ~165 kW/cm² with a laser spot size of ~100 μm. The small spot size enables highly localized pulsed heating that is confined spatially on the substrate as well as in the near-surface region. This minimizes thermal drift, which is associated with continuous heating, and makes *in situ* ion and photon irradiation possible with high spatial resolution.

2.1.5.2 Helium Ion Microscope/Patterning

Scanning helium and neon exposures and imaging were performed with a Zeiss ORION Nanofab HIM/NIM. An accelerating voltage of 25 keV was used for all imaging, whereas accelerating voltages of 15 and 25 keV were used for the patterned exposures. Beam currents varied from 0.3 – 0.9 pA in order to modify the photon/ion flux ratio (see Supporting Information Table 3 for a summary of all experimental parameters). A silicon substrate with a ~3 nm native oxide layer was used for ion beam exposures and subsequent TEM imaging. A 100 nm x 1,000 nm rectangular pattern geometry was used for the ion beam exposures. All patterns in this study were exposed with a 1 μ s dwell time and a 1 nm pixel spacing. Patterns were generated using a Fibics NPVE pattern generator as well the Zeiss Athena pattern generator. During laser-assisted ion beam exposures, 100 μ s laser pulses, driven at frequencies ranging from 100 – 200 Hz (1-2 % duty cycle), were synchronized to begin and end with the ion exposure patterns. The photon/ion flux ratio was carefully controlled by varying beam current, laser duty cycle, and refresh times.

2.1.5.3 TEM Preparation and Imaging

The ion beam exposure sites were characterized using a FEI Tecnai F20 TEM operating at 200 keV. Samples were prepared using an FEI Strata 400 Dual Beam FIB/SEM. The boundaries of the amorphous to crystalline regions are easily visible in bright field TEM due to differences in diffraction of electrons in the crystalline vs. amorphous regions.¹²⁰ The electron beam diffraction pattern was studied to analyze the crystallinity of the ion implanted region annealed with in-situ laser.

2.1.5.4 Simulations

Simulations of the laser-induced heating effects as well as diffusion of implanted ions and point defects were performed using COMSOL Multiphysics 5.0, which is a commercial finite element method (FEM) software package. Specifically, a backward differentiation formula time-stepping method with strict time steps was used to generate the temporal temperature evolution for silicon during laser irradiation with the 915 nm laser. The temperature profile was used to determine the temperature dependent diffusion of implanted He interstitials, as well as silicon vacancies and interstitials generated by knock-on collisions with the energetic He⁺. The multifrontal massively parallel sparse direct solver was used for evaluation of the diffusion

equation and an open boundary was used at the substrate surface for Helium to mimic the low activation energy of the helium desorption. The diffusion simulations conducted were uncoupled, meaning that the diffusion of each defect type (He interstitials, Si interstitials, and Si vacancies) was independent of one another and does not account of defect interactions such as vacancy/interstitial annihilation. Additional simulation details can be found in the supporting information.

2.1.5.5 Raman Spectroscopy of Graphene

Confined channels were milled into CVD grown single-layer graphene, which was supported by a SiO₂ coated Si substrate, with 25 keV He⁺. Raman spectroscopy was performed in a Renishaw inVia micro-Raman system using a 532 nm excitation laser. A 100X magnification objective was used for spectral acquisition with a 5 second acquisition time. Laser spot size was approximately 0.6 μm. Data analysis was conducted with WIRE v3.4 software. Raman spectra of the graphene prior to He⁺ exposure were consistent across the substrate, and suggest uniformity in the quality of the graphene.

2.1.6 Appendix

2.1.6.1 Supporting Information

Exposure Parameters

For all He⁺ and Ne⁺ exposures, multiple parameters were used to control the photon/ion flux. The parameters include: laser duty cycle, ion beam current, and ion beam refresh time between patterning passes. Table 3 includes relevant parameters for all experiments, which have a critical effect on the evolution of the subsurface damage with ion exposure. Photon/ion flux is reported relative to conditions for a 1.3x10⁶ photon/ion exposure.

Simulation Details

Laser Heating Simulation

Simulations of the laser-induced heating effects were performed using COMSOL Multiphysics 5.0, which is a commercial finite element method (FEM) software package. The expression for heat delivered to the substrate from the laser is derived from the Beer-Lambert law:

$$Q_{in}(x, y, z) = Q_0(1 - R_c) * \frac{A_c}{\pi\sigma_x\sigma_y} * G(x, y) * \text{Exp}(-A_c z) \quad (1)$$

where Q_0 is the optical power of the laser, R_c is the reflection coefficient, A_c is the absorption coefficient, $G(x, y)$ is the 2-dimensional Gaussian laser profile, σ_x and σ_y are the 1/e radii of the Gaussian laser profile, and z is the depth from the substrate's surface. A linear 100 ns laser ramp time was assumed for this simulation and a laser pulse width of 100 μ s was applied. The following time dependent heat equation was used to simulate the heat transfer throughout the silicon substrate:

$$\rho C_p \frac{dT}{dt} + \rho C_p \mathbf{u} \cdot \nabla T = \nabla \cdot (k \nabla T) + Q(x, y, z) \quad (2)$$

where ρ is the material density, C_p is the heat capacity at constant pressure, \mathbf{u} is the velocity vector for thermal transport, and κ is the thermal conductivity. Convective heat transfer to the surrounding atmosphere was neglected since irradiation conditions were under high vacuum and T_0 was defined as 293.15 K. A backward differentiation formula time-stepping method with strict time steps was used to generate the temporal temperature evolution for silicon during laser irradiation.

Table 4 reports relevant simulation and material parameters used to simulate the temperature temporal evolution in a silicon substrate which is heated with 100 μ s 915 nm laser pulse. The 1/e radii of the Gaussian shaped beam was treated as 45 μ m along the x-axis and 60 μ m along the y-axis. This produces a beam diameter of 90 μ m along the x-axis and 120 μ m along the y-axis. This accounts for the angle of the port from which the laser is mounted in the chamber and results in an elongated spot. All other parameters listed are experimental or material parameters that are relevant to simulate the time-temperature profiles.

A single 100 μ s laser pulse heats the substrate to approximately 700 K and then rapidly decays to room temperature (RT). All experimental laser conditions used for this study used a duty cycle of < 2%, thus each laser pulse returns to RT well before the subsequent laser pulse. This prevents thermal drift and additive heating effects. The profile inset in **Figure 33** of the main text was used to calculate the temperature-dependent diffusion coefficients.

SRIM/TRIM

SRIM/TRIM Monte Carlo simulations were used to generate the subsurface ion implantation profiles, and our EnvizION variant¹⁰³ was used to generate the vacancy and interstitial profiles. In order to generate statistically accurate profiles, 500,000 ion trajectories were traced in a point source and the simulated implantation and defect profiles of the 1000 nm x 100 nm exposure geometry were approximated by rastering the SRIM or EnvizION generated profiles (500,000 ions) over the entire 1,000 nm x 100 nm scan area. The concentration of the central slice perpendicular to the long scanning axis was used as the distribution profiles of the implanted ions and defects.

Diffusion Simulations

COMSOL Multiphysics 5.0 was used to simulate the temperature-driven diffusion of implanted ions and point defects in silicon induced by the focused He⁺ beam exposures. The diffusion coefficients of the aforementioned point defects were expressed as:

$$D(t) = D_0 \text{Exp} \left(-E_a / RT(t) \right) \quad (3)$$

where D_0 is the diffusion prefactor, E_a is the activation energy, and T is the previously simulated time-dependent temperature profile in the near surface region of our substrate (T vs t profile is found in the inset of **Figure 33**). Since ion exposures were conducted in a region much smaller

than the laser spot size and the simulated temperature difference over the implant range was negligible, the temperature was assumed to be spatially constant with only a time-dependence. The implantation and defect spatial profiles generated by SRIM/TRIM and EnvizION were imported as a source term and scaled to match the dose rate of experiments and synchronized with the appropriate number of laser pulses. The time-dependent diffusion expression was taken as:

$$\frac{\partial D}{\partial t} + \nabla \cdot (-D \nabla D) = f \quad (4)$$

where D is the diffusion coefficient and f is the source term for defect generation. A generalized alpha time-stepping method was applied to the simulation with strict time steps. The multifrontal massively parallel sparse direct solver was used for evaluation and an open boundary was used at the substrate surface for Helium to mimic the low activation energy of the helium desorption.

Damage Mitigation and Defect Signatures

Figure 38 shows a comparison of a $5 \times 10^{17} \text{ He}^+$ exposure without (a) and with (d) the use of a laser-assist. Atomic resolution TEM images (b) and (c) show the regions denoted by the red and blue boxes in (a), respectively. In (b), it is clear that the region which experienced damage accumulation from the He^+ irradiation underwent an amorphous transition, while the region not exposed to a large extent of damage accumulation remains crystalline. In comparison, there is no amorphization of Si in the near surface region when a laser assist was used (e). **Figure 38c** shows a TEM image taken from the core of the He^+ irradiation induced amorphized Si. This region is characterized by high atomic disorder with no evidence of crystalline structure. In comparison, (f) shows the peak damage accumulation region of Si exposed with the laser-assist. Although noticeable defects are present, crystalline atomic structure is evident. This confirms that synchronized the laser-assisted exposure technique greatly mitigates the formation of subsurface damage.

Figure 39 shows TEM images of the subsurface damage accumulation regions for a He^+ exposure at a dose of (a) 5×10^{17} and (b) $1 \times 10^{18} \text{ He}^+/\text{cm}^2$. In **Figure 39a**, amorphization of the Si is clear, and small nano-bubbles are visible. As the dose increases to $1 \times 10^{18} \text{ He}^+/\text{cm}^2$, the bubbles expand with the accumulation of He and become more visible.

Scanning Dimension Effects

Figure 40 shows the simulated cross-sectional concentration distribution of a-d) implanted He^+ , e-h) interstitial Si, and i-l) Si vacancies for a Si substrate irradiated with 25 keV He^+ at a dose of $1 \times 10^{16} \text{ He}^+/\text{cm}^2$. The defect distributions are shown for different aerial square exposure patterns with side lengths of 10 nm (1st row), 50 nm (2nd row), 100 nm (3rd row), and 200 nm (4th row). Clearly, as the side length of the square aerial exposure pattern increases, the maximum defect concentration also increases. This effect is summarized in **Figure 41a**, which plots the maximum defect concentration as a function of the side length of the square exposure pattern. The concentration of defects increases until the size of the exposure pattern reaches the lateral range of the defects generated for a single exposure pixel. The maximum defect concentration saturates once the exposed region exceeds the dimensions of the lateral range. A schematic of this concept is shown in **Figure 41b**, which illustrates that overlap stops once dimensions of the aerial dose pattern exceed the lateral range of defects generated. Hence, the pattern dimensions as well as the aerial dose and beam conditions have significant contributions to the maximum subsurface defect concentration when the pattern size is below the lateral range of defects generated.

In-situ Anneal vs. Post Anneal

Figure 42 displays SEM images comparing the effects of a laser post anneal relative to an in-situ laser assist during ion beam irradiation. **Figure 42a**, shows 5 patterns which were patterned with the ion beam and subsequently irradiated with the laser, whereas the patterns in **Figure 42b** were patterned and irradiated with the laser in-situ at a flux of $6.6 \times 10^6 \text{ photon/ion}$. For comparison the bottom right pattern in **Figure 42b** was exposed to the same dose and experiences no in situ nor ex situ laser exposure. Clearly an in-situ anneal (**Figure 42b**) is more effective at reducing subsurface damage in comparison with a pattern which experienced a post exposure anneal with the same laser exposure (16 min laser anneal process time, with 100 μs pulse width and 1% duty cycle). This is because for mitigation of void formation it is critical, where appropriate in situ laser exposure enables the helium atoms to diffuse and vacancies/interstitials annihilate before this critical dose is reached. Once a critical implantation concentration of ions and defects are reached, stable subsurface bubbles and defect clusters are formed which amorphize the silicon and require much higher activation energies to annihilate.

Silicon Interstitial Diffusion

Figure 43a and **Figure 43c** show the distribution of Si interstitials generated from knock-on collisions with 15 and 25 keV He⁺ at an aerial dose of 1E16 ions/cm³. **Figure 43b** and **Figure 43d** show the Si interstitial profiles for exposures with a simultaneous pulsed laser synchronization of 100 μs and 1% duty cycle (1.3x10⁶ photon/ion). The maximum interstitial concentration is shown as a function of the aerial exposure dose in **Figure 43e**. The thermal energy supplied from the pulsed laser system drives minimal diffusion of the interstitial Si, which has an activation energy of 1.37 eV and a diffusion pre-factor of 1.58x10⁻¹ cm²/s.¹¹² To comment briefly, vacancy diffusion within the Si substrate has an activation energy of 0.10 eV and a diffusion prefactor of 1.18x10⁻⁴ cm²/s. Therefore the vacancy mobility is much greater than that of Si interstitials at elevated temperature (~ 700 K). Vacancies can annihilate the interstitial Si. Hence the dominant mechanisms for in-situ defect healing under pulsed laser irradiation within the Si substrate include 1) the enhanced diffusion of implanted interstitial He⁺ and 2) the enhanced diffusion of vacancies which facilitates interstitial annihilation.

Experimental and Simulation Comparison

Figure 44 shows cross section TEM images of silicon exposed with a) 15 and b) 25 keV He⁺ to a dose of 5x10¹⁷ He⁺/cm² with the synchronized laser assist. The images are superimposed onto the FEA simulation results to show the correlation between the predicted simulation He⁺ profile and the experimental profile.

2.1.6.2 Figures

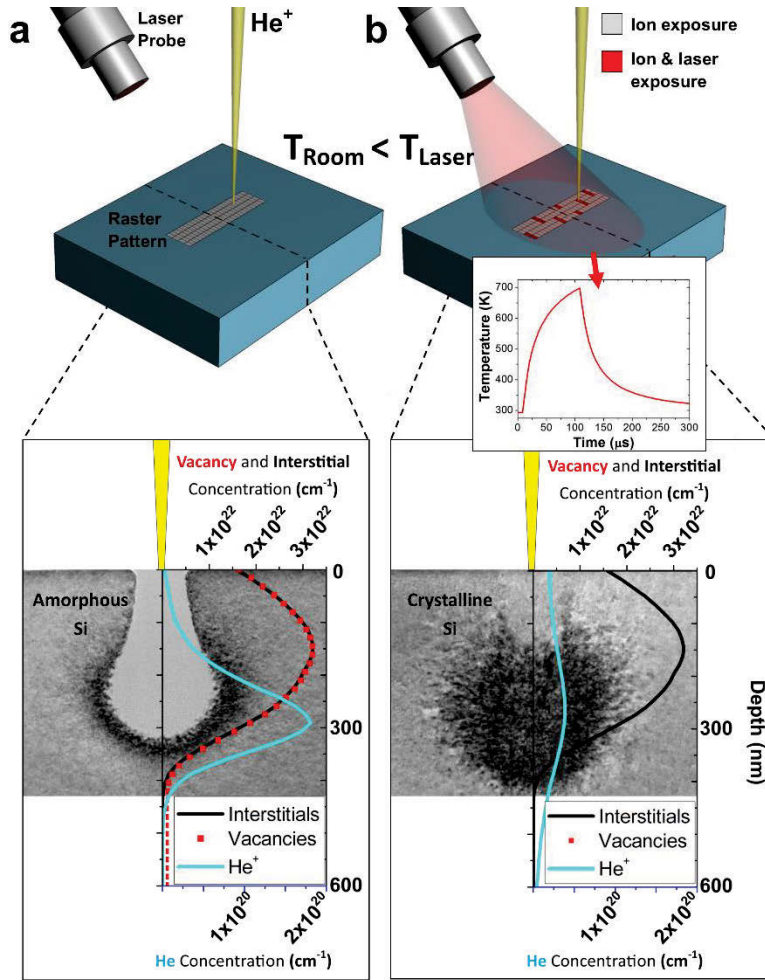


Figure 33. Schematic of helium ion exposures (a) without and (b) with pulsed laser-assist to photothermally enhance implanted ion diffusion and defect annihilation. Grey pixels in the raster pattern represent pixels irradiated solely with He^+ whereas red pixels are simultaneously irradiated with the laser and He^+ . Cross-section TEM images illustrate the amorphized silicon region (a) and damage mitigated (b) by the in situ laser-assist. Overlaid on the TEM images are calculated helium, vacancy and interstitial concentrations, illustrating photothermally enhanced diffusion of He^+ and vacancies with the pulsed laser-assist strategy of a photon/ion flux of 1.3×10^6 . Inset in (b) is the simulated time-temperature profile of a single 100 μs laser pulse irradiated on Si.

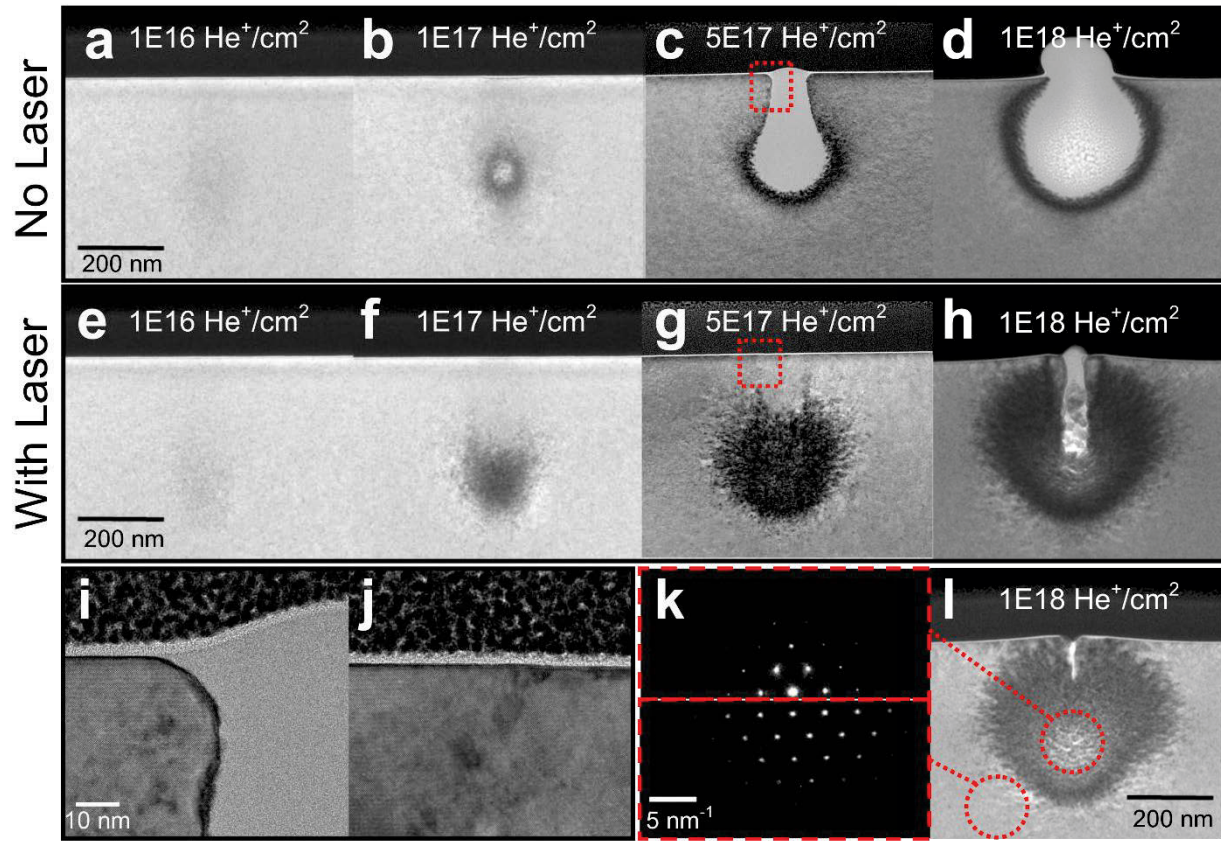


Figure 34. TEM cross sections of 25 keV He^+ exposures of varying dose (a-d) without and (e-h) with a pulsed laser-assist of 1.3×10^6 photon/ion flux. Exposure doses are inset in the images. High-resolution TEM images showing ion beam induced damage without (i) and with (j) laser-assist for a dose of $5 \times 10^{17} \text{ He}^+/\text{cm}^2$ collected from the regions denoted by hatched red boxes in (c) and (g), respectively. k) SAED patterns and (l) TEM cross section of an exposure of $1 \times 10^{18} \text{ He}^+/\text{cm}^2$ with 5 times higher (6.6×10^6) photon/ion flux than (h). Dashed circles denote where SAED was conducted.

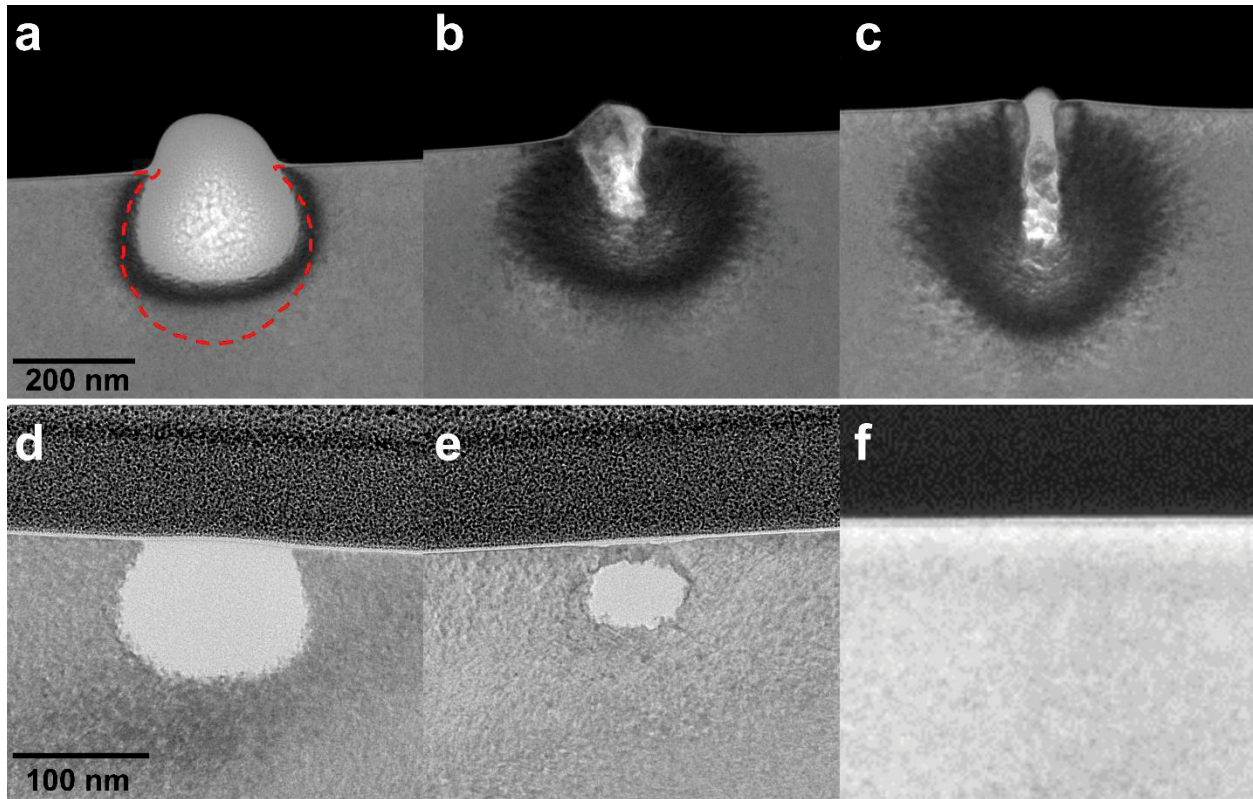


Figure 35. TEM cross sections of 15 keV He^+ exposure (a) without and (b) with laser-assist of 1.3×10^6 photon/ion at a dose of $1 \times 10^{18} \text{ He}^+/\text{cm}^2$. Dashed line in (a) denotes region amorphized by 25 keV He^+ beam. (c) Reproduction of Figure 34h which shows a 25 keV exposure at a dose of $1 \times 10^{18} \text{ He}^+/\text{cm}^2$ with a laser assist of 1.3×10^6 photons/ion for comparison purposes. TEM cross sections of 25 keV Ne^+ exposure (d) without and (e) with laser-assist at a dose of $1 \times 10^{16} \text{ He}^+/\text{cm}^2$. (f) Reproduction of Figure 34a which shows a 25 keV He^+ exposure at a dose of $1 \times 10^{16} \text{ He}^+/\text{cm}^2$ with a laser assist of 1.3×10^6 photons/ion for comparison purposes.

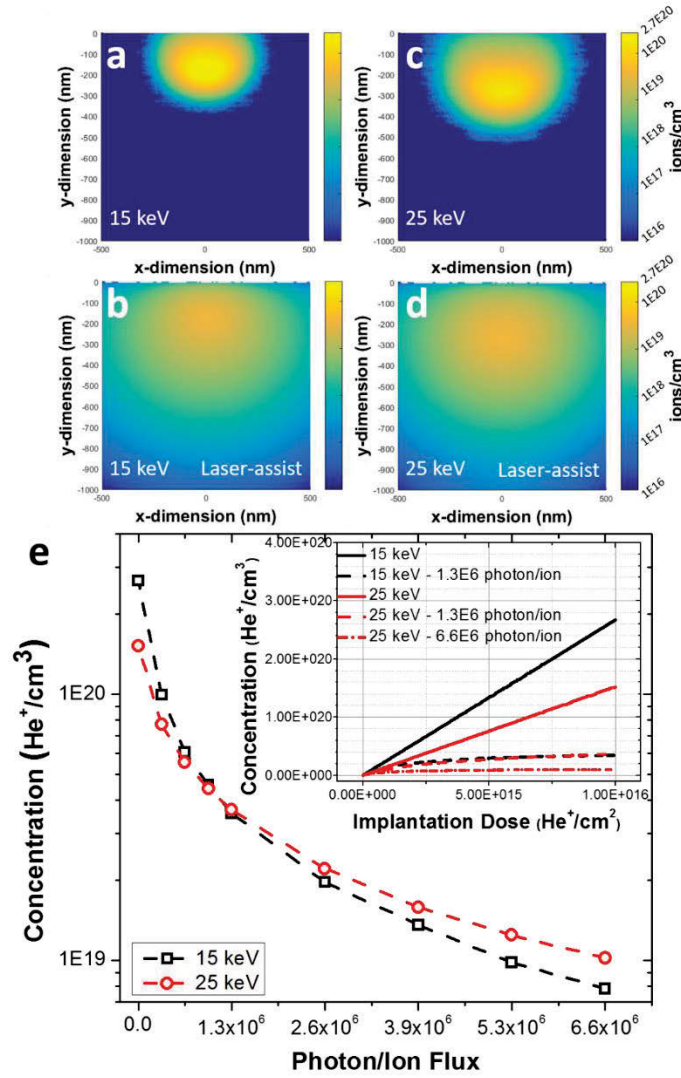


Figure 36. Simulated cross-section helium concentration profiles for 1×10^{16} He⁺/cm² dose at 15 keV He⁺ in silicon (a) without and (b) with laser-assist of 1.3×10^6 photon/ion. Cross-section of calculated helium concentration profiles for 1×10^{16} He⁺/cm² dose at 25 keV He⁺ in silicon (c) without and (d) with laser-assist. (e) Plot of the calculated maximum He⁺ concentration as a function of photon/ion flux and implantation energy for a dose of 1×10^{16} He⁺/cm². The photon/ion fluxes used for experimental exposures include 0, 1.3×10^6 , and 6.6×10^6 photon/ion. A plot of the maximum He⁺ concentration as a function of aerial dose for each of the experimental exposure conditions is inset.

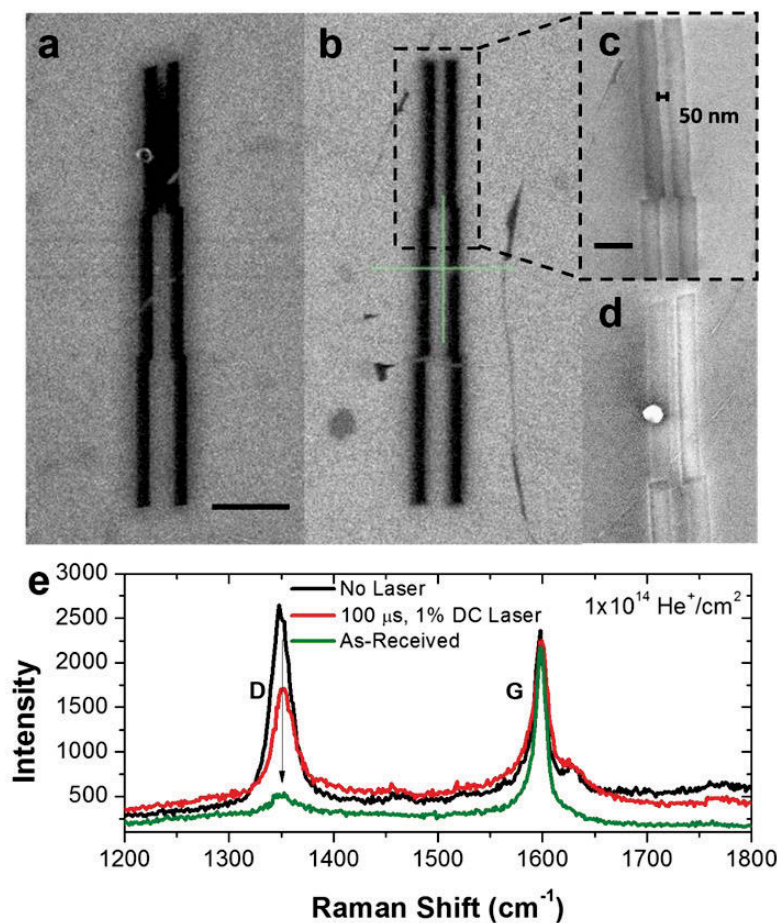


Figure 37. HIM images of channels milled into single layer graphene on SiO₂ without (a) and with (b) laser-assist where the photon/ion flux was $\sim 1.6 \times 10^6$. Scale bar is 500 nm. SEM images confirm the confined channels were cut at a width of ~ 50 nm both (c) with and without (d) laser-assist. Scale bar is 200 nm. (e) Raman spectra of graphene as-receive and irradiated at a dose of 1×10^{14} ions/cm² with (red) and without (black) laser-assist.

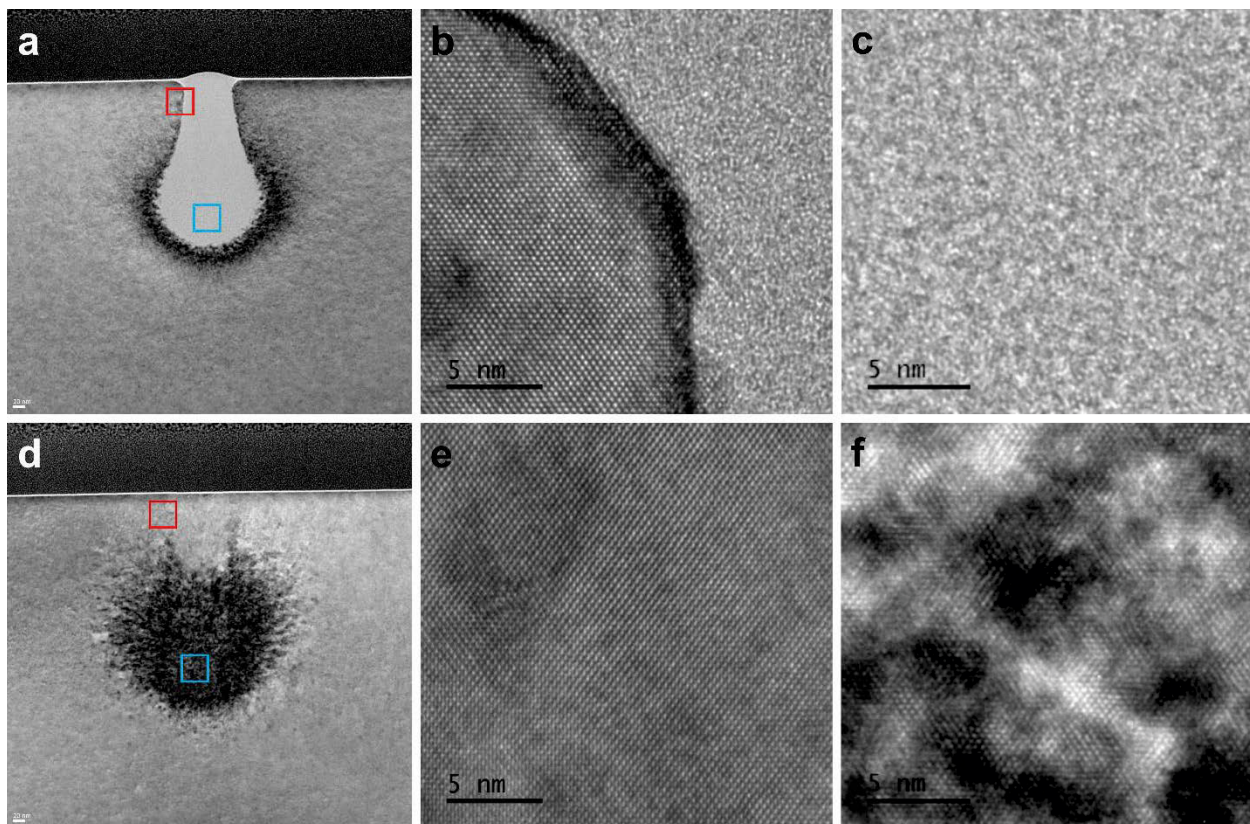


Figure 38. (a) TEM image of a $5 \times 10^{17} \text{ He}^+/\text{cm}^2$ exposure with no laser assist and a beam energy of 25 keV. High-resolution TEM images of the regions denoted by the red box (b) and the blue box (c) in image (a). These regions represent areas which borders the irradiation induced amorphous Si border and amorphous Si core respectively. (d) TEM image of a $5 \times 10^{17} \text{ He}^+/\text{cm}^2$ exposure with a laser assist of $1.3 \times 10^6 \text{ photon/ion}$ and a beam energy of 25 keV. High-resolution TEM images of the regions denoted by the red box (e) and the blue box (f) in image (d).

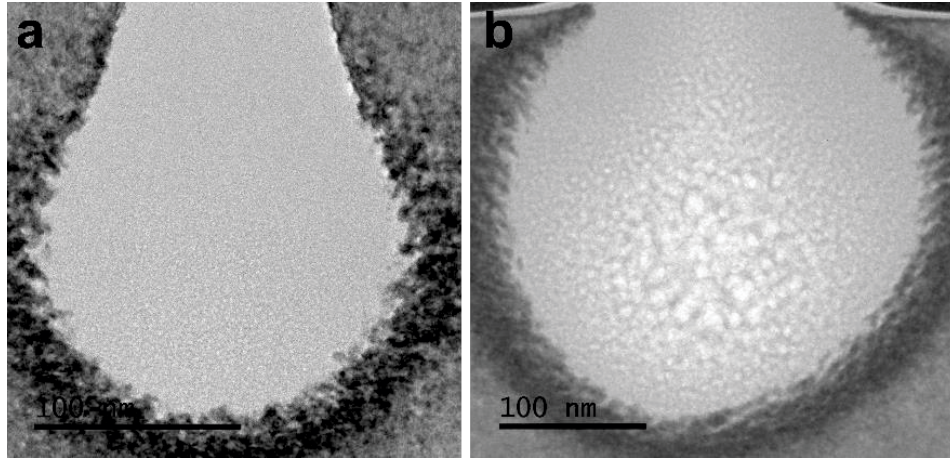


Figure 39. (a) Sub-surface damage accumulation region in Si of a (a) 5×10^{17} and (b) 1×10^{18} He^+/cm^2 exposure with 25 keV He^+ and no laser assist. Small nano-bubbles begin forming in (a) and expand to become clearly visible in (b) with an increase in exposure dose.

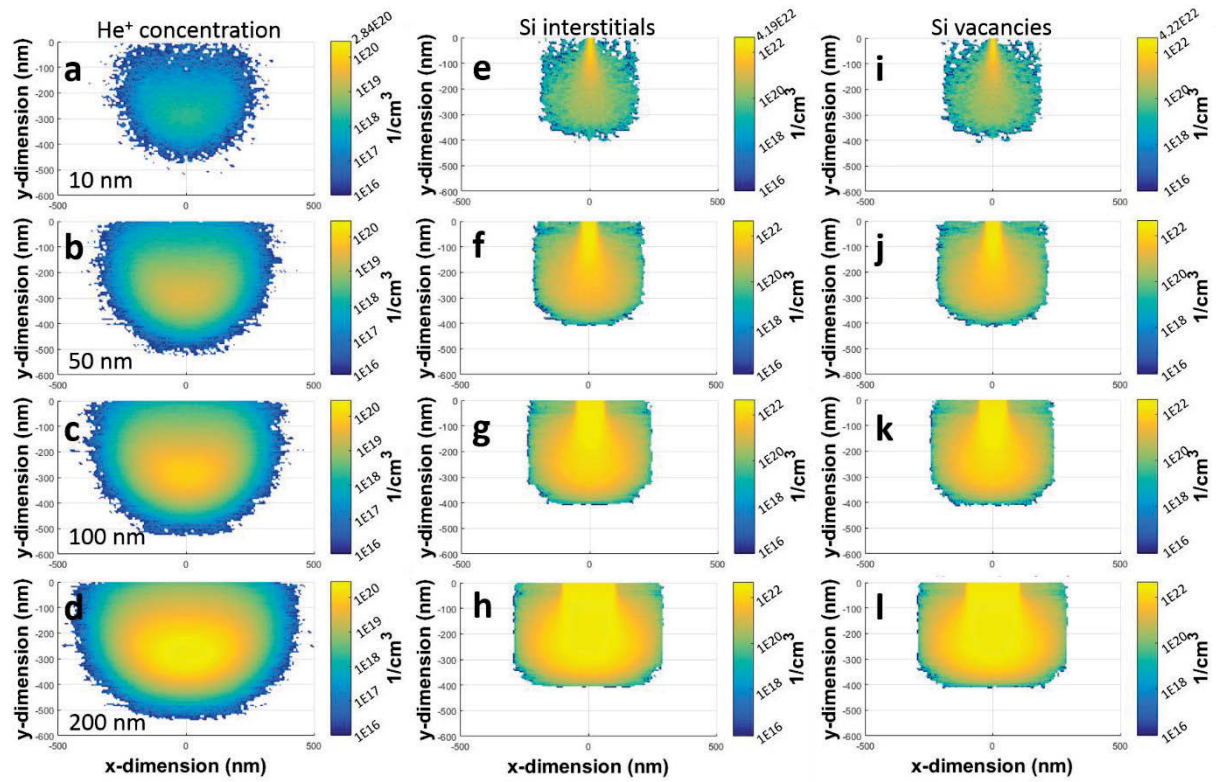


Figure 40. Simulated cross-sectional concentration distribution of (a-d) implanted He concentration, (e-h) interstitial Si, and (i-l) Si vacancies for a Si substrate irradiated with 25 keV He⁺ at a dose of 1×10^{16} He⁺/cm². The defect distributions are shown for different aerial square exposure patterns with side lengths of 10 nm (1st row), 50 nm (2nd row), 100 nm (3rd row), and 200 nm (4th row).

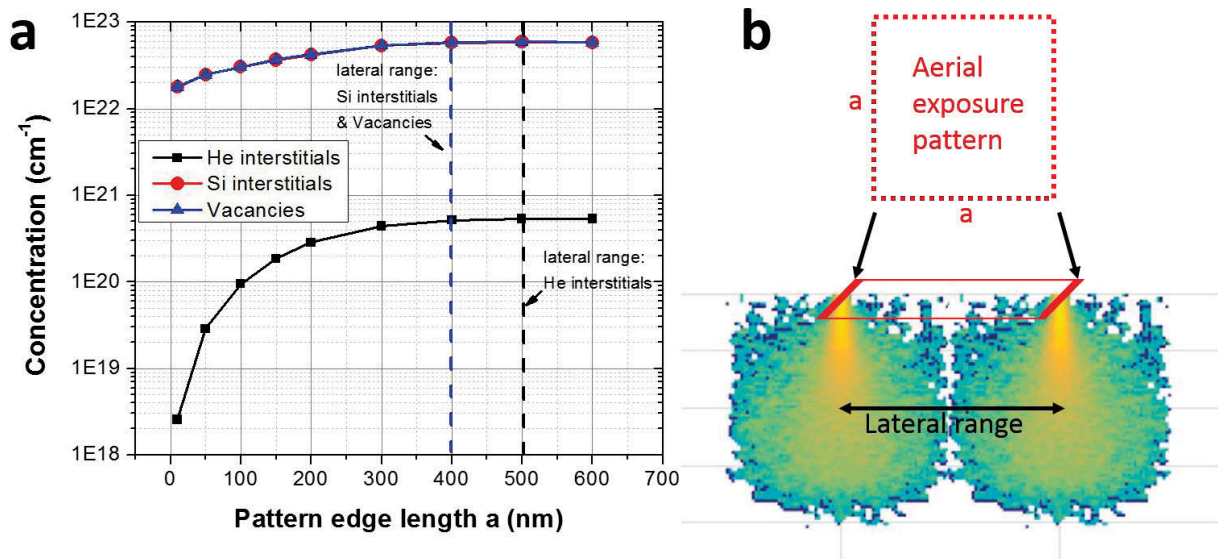


Figure 41. (a) Maximum defect concentration as a function of side length of an aerial square pattern. All concentrations are simulated for a $1 \times 10^{16} \text{ He}^+/\text{cm}^2$ exposure with 25 keV He^+ in a Si substrate. (b) Schematic illustrating that when the aerial pattern dimensions reach the lateral range of the defects generated, saturation in maximum concentration occurs.

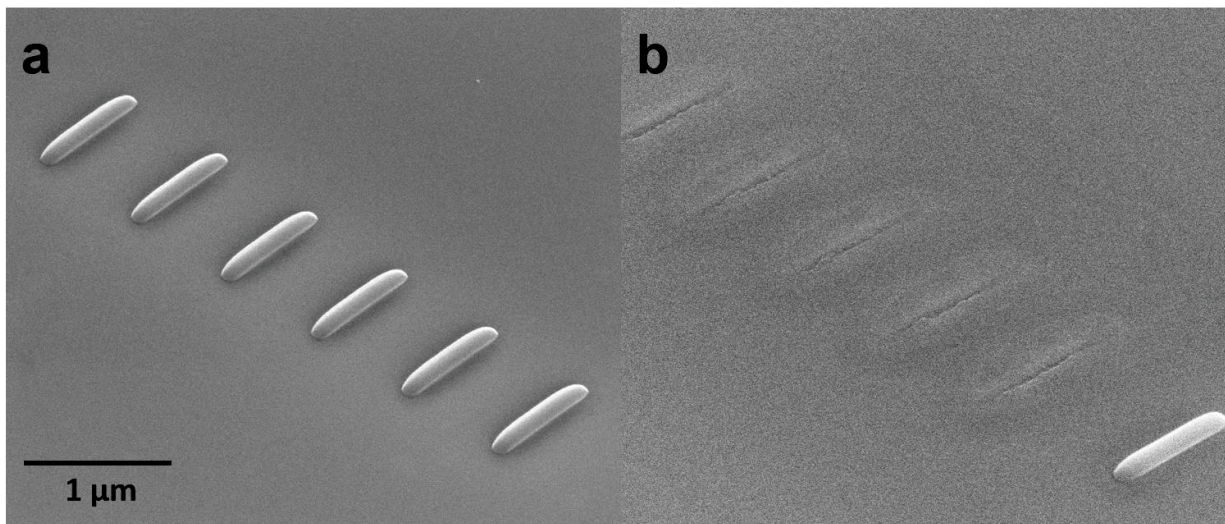


Figure 42. SEM images of 25 keV He^+ patterns at a dose of 1×10^{18} ions/cm³ which were annealed in a (a) post He^+ exposure anneal and (b) in-situ manner with 100 μs , 1% DC laser conditions. The right-most pattern in each image was irradiated with no synchronized laser exposure.

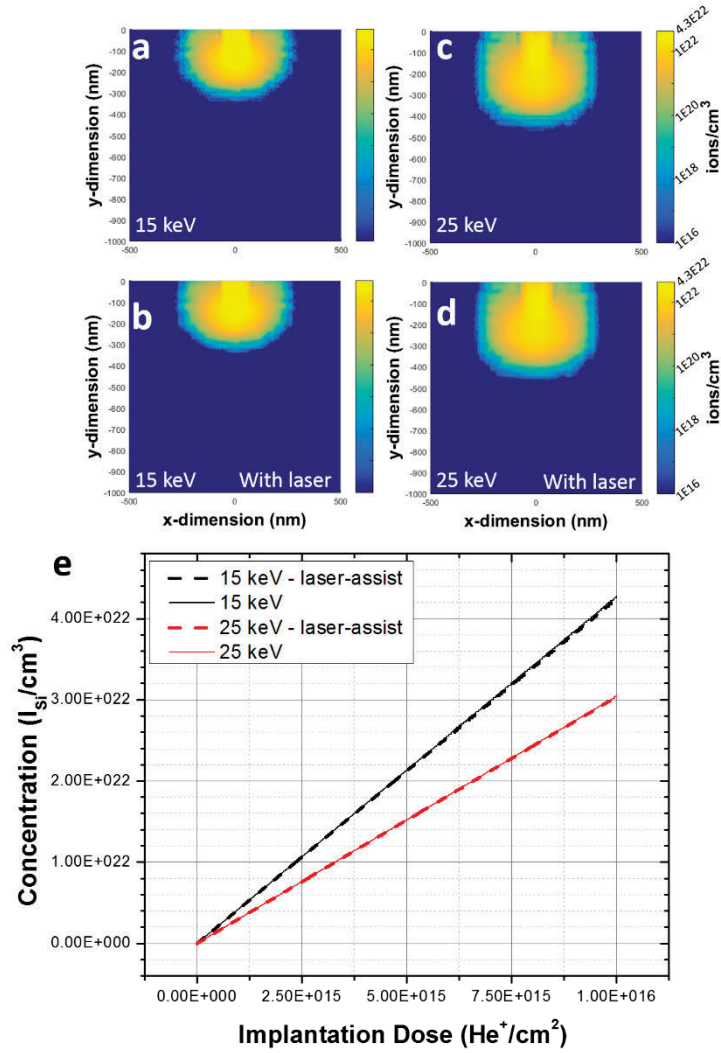


Figure 43. Cross section concentration profile of the Si interstitials generated from 15 keV He⁺ in silicon (a) without and with (b) laser-assist of 1.3×10^6 photon/ion. Cross section concentration profile of the Si interstitials generated from 25 keV He⁺ in silicon (c) without and with (d) laser-assist. (e) Plot of the maximum Si interstitials concentration as a function of aerial dose for each of the exposure conditions.

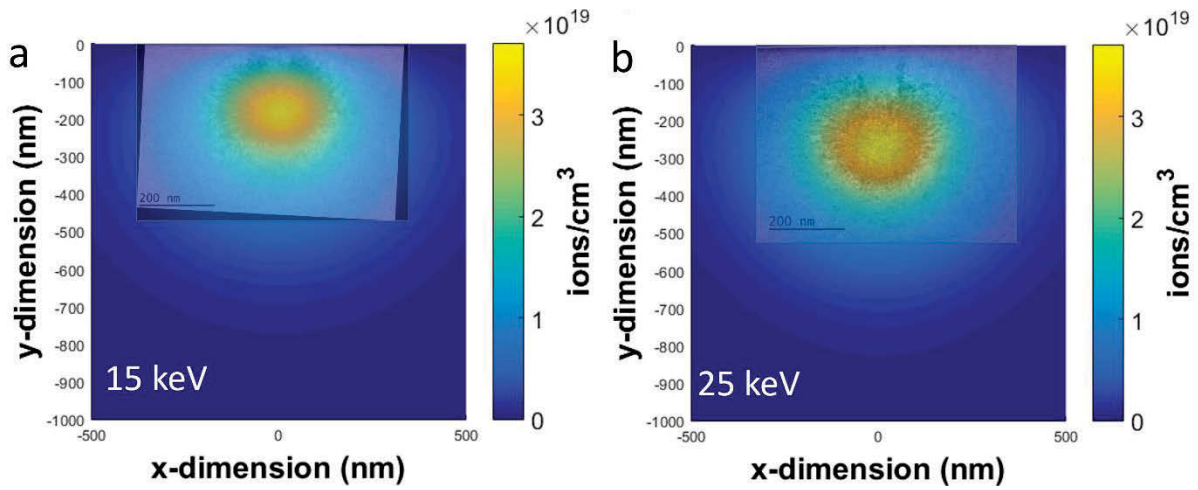


Figure 44. TEM cross section of Si irradiated with (a) 15 keV and (b) 25 keV He⁺ and synchronized laser superimposed onto simulations results. TEM cross sections are for a dose of 5×10^{17} He⁺/cm² whereas the simulations are for a dose of 1×10^{16} He⁺/cm².

2.1.6.3 Tables

Table 3. Relevant parameters for He⁺ and Ne⁺ exposures as well as pulsed laser parameters.

Figure	Ion species	Doses (ions/cm ²)	Beam energy (keV)	Beam current (pA)	Beam dwell time (μs)	Pattern pixel spacing (nm)	Laser pulse width (μs)	Laser duty cycle	Multiplicity (refresh)	Relative photon/ion flux
2A	He	1.00E+16	25	0.9	1	1 x 1	N/A	0%	1	0
2B	He	1.00E+17	25	0.9	1	1 x 1	N/A	0%	1	0
2C	He	5.00E+17	25	0.9	1	1 x 1	N/A	0%	1	0
2D	He	1.00E+18	25	0.9	1	1 x 1	N/A	0%	1	0
2E	He	1.00E+16	25	0.9	1	1 x 1	100	1%	1	1
2F	He	1.00E+17	25	0.9	1	1 x 1	100	1%	1	1
2G	He	5.00E+17	25	0.9	1	1 x 1	100	1%	1	1
2H	He	1.00E+18	25	0.9	1	1 x 1	100	1%	1	1
2I	He	5.00E+17	25	0.9	1	1 x 1	N/A	0%	1	0
2J	He	5.00E+17	25	0.9	1	1 x 1	100	1%	1	1
2L	He	1.00E+18	25	0.9	1	1 x 1	100	1%	5	5
3A	He	5.00E+17	15	0.9	1	1 x 1	N/A	0%	1	0
3B	He	5.00E+17	15	0.9	1	1 x 1	100	1%	1	1
3C	Ne	1.00E+16	25	0.15	1	1 x 1	N/A	0%	1	0
3D	Ne	1.00E+16	25	0.15	1	1 x 1	100	2%	1	12

Table 4. Relevant parameters for simulation of laser heating on a silicon substrate.

Simulation Parameters	Value	Description
σ_x	0.045[mm]	Laser 1/e radii- x
σ_y	0.06[mm]	Laser 1/e radii - y
Rc	0.3226	Reflection coefficient at 915 nm
Ac	315.876 [1/cm]	Absorption coefficient at 915 nm
Q0	22[W]	Laser power
Pulse	100 [us]	Laser pulse width
Cp	700 [J/(kg*K)]	Si heat capacity
ρ	2329 [kg/m ³]	Si density
κ	130 [W/(m*K)]	Si thermal conductivity

2.2 Laser Assisted Focused He⁺ Ion Beam Induced Etching with and without XeF₂ Gas Assist

A version of this chapter was originally published by M. G. Stanford et al.:

Stanford, M. G.; Mahady, K.; Lewis, B. B.; Fowlkes, J. D.; Tan, S.; Livengood, R.; Magel, G. A.; Moore, T. M.; Rack, P. D. Laser-Assisted Focused He⁺ Ion Beam Induced Etching with and without XeF₂ Gas Assist. *ACS Appl. Mater. Interfaces* **2016**, 8, 29155–29162.

Michael G. Stanford conducted experiments, analysis, and thermal simulations reported in this work. Brett B. Lewis also contributed to the collection of experimental data. Michael G. Stanford also wrote the manuscript. Kyle Mahady conducted Monte Carlo simulations. Tom M. Moore and Greg. A. Magel created the laser system utilized in this work. All co-authors contributed to manuscript revision. Reprinted with permission. Copyright 2017 American Chemical Society.

2.2.1 Abstract

Focused helium ion (He⁺) milling has been demonstrated as a high-resolution nanopatterning technique, however it can be limited by its low sputter yield as well as the introduction of undesired sub-surface damage. Here, we introduce pulsed laser and gas assisted processes to enhance the material removal rate and patterning fidelity. A pulsed laser-assisted He⁺ milling process is shown to enable high resolution milling of titanium while reducing sub-surface damage in situ. Gas-assisted focused ion beam induced etching (FIBIE) of Ti is also demonstrated in which the XeF₂ precursor provides a chemical assist for enhanced material removal rate. Finally, a pulsed laser-assisted and gas-assisted FIBIE process is shown to increase the etch yield by ~ 9x relative to the pure He⁺ sputtering process. These He⁺-induced nanopatterning techniques improve material removal rate, in comparison to standard He⁺ sputtering, whilst simultaneously decreasing sub-surface damage, thus extending the applicability of the He⁺ probe as a nanopatterning tool.

2.2.2 Introduction

Focused helium ions have been used for nanoscale synthesis in a variety of applications in recent years and offer an enhanced resolution relative to the standard liquid Ga ion source. This has resulted in synthesis of nanostructures with sub-10 nm resolution via deposition, etching, and lithography.^{121–123} However, due to low sputter yields of He^+ , patterning by material removal requires high doses which results in the formation of undesired sub-surface damage and He bubbling.^{102,124,125} This is undesirable for many applications and limits the effectiveness of focused He^+ as a nanofabrication candidate. Therefore, for robust nanoscale synthesis with the helium ion microscope (HIM), processes should be developed which mitigate sub-surface damage as well as minimize the He^+ dose required for processing.

FIBIE, which utilizes a chemical assist, can be used to enhance the material removal rate relative to a standard sputtering process. Lower dose is required with the enhanced material removal rate thus reducing the extent of deleterious sub-surface damage. During FIBIE, a precursor gas is injected in close proximity to the substrate. The precursor gas physisorbs onto the substrate and establishes an equilibrium coverage. While rastering in a prescribed pattern, the He^+ beam drives the dissociation of precursor molecules into radical species via collisions with primary and backscattered ions, generated secondary electrons, as well as target atoms that experience knock-on collisions. If the radicals generated from the precursor gas form a volatile compound with the substrate material, a chemical assist component can facilitate the sputtering component and enhance material removal. However, the etch rate during a FIBIE process can be restricted by a number of rate limiting mechanisms analogous to electron beam induced etching¹²⁶. The volatile compounds may contain several precursor ligands necessitating relatively larger exposure doses to achieve volatile compound formation. The exposure dose is typically increased using additional charge exposure loops or larger per-pixel dwell times. Additionally, volatile compounds may have a long residence time on the substrate surface after formation causing a reduction in the effective precursor gas surface coverage.

FIBIE has been demonstrated with a number of primary ion beams, of which Ga^+ is the most popular choice¹²⁷. Precursor gases including XeF_2 ^{128–132}, Cl_2 ^{129,130,133–137}, O_2 ^{128,130}, H_2O ^{130,138}, NH_3 ^{130,137}, Br_2 ¹³⁰, and I_2 ^{131,139,140} have been used to chemically aid in material removal, to name a few. The FIBIE process has also been shown to minimize the damage zone

induced by the ion beam in comparison to a standard milling process¹⁴⁰. Therefore, He⁺ FIBIE is an exceptional candidate for high-resolution nanofabrication due to the reduced damage zone and enhanced etching rates associated with FIBIE as well as the impressive resolution of the He⁺ probe.

In this work, we compare and contrast different He⁺ milling and etching processes of a Titanium thin film, including standard He⁺ sputter milling, in situ laser-assisted He⁺ milling, FIBIE with XeF₂, and pulse laser-assisted FIBIE (LA-FIBIE). Schematics of the experimental setup as well as three of the aforementioned processes are shown in **Figure 45a-e**. **Figure 45a-b** is a schematic and digital image of the experimental setup, respectively, which illustrates that the ion, reactive gas, and pulsed laser all converge to common beam interaction region. For the laser system, light from a fiber-coupled semiconductor diode laser is transmitted through a single-mode fiber in a vacuum-sealed probe that is mounted through a motorized nanomanipulator on a port of the helium ion microscope chamber (additional details can be found in the methods and supporting information). **Figure 45c-e** show schematics of standard He⁺ sputter milling, FIBIE with XeF₂, and LA-FIBIE, respectively. Ti was chosen as the model material system in this work as it is a standard refractory metal; Furthermore, XeF₂ electron beam induced etching¹⁴¹ and laser assisted electron beam induced etching has recently been explored¹¹⁹. First, we demonstrate that by synchronizing pulsed laser irradiation with a standard He⁺ milling process, sub-surface He⁺ swelling is significantly reduced and milling quality/fidelity is enhanced. FIBIE with XeF₂ demonstrated high fidelity etching as well as a much greater etch yields as compared to that of a standard milling process. Finally, etch yields were further enhanced (by as much as 9x relative to the standard He⁺ sputtering process) by synchronizing an in situ pulsed laser system with the FIBIE process (LA-FIBIE). Fine tuning of laser parameters, such as irradiance (kW/cm²) and duty cycle (pulse width x frequency), and He⁺ beam parameters provide a method to fine tune Ti etch rates.

Pulsed heating (in this work 0.1 – 3 % duty cycle) is used instead of continuous heating because continuous heating decreases the residence time of the precursor molecule and thus retards the chemical assist component; for instance for electron beam induced deposition, Mulders et al.¹⁴² showed that deposition rates were reduced for a number of precursors that were studied. Conceivably, a continuous wave irradiation could facilitate the ion milling process

(analogous to a stage heater), however, the pulsed laser results in rapid heating and cooling which allows the substrate to return to approximately room-temperature between pulses. This minimizes sample thermal drift, which would limit the resolution of simultaneous processing with the He^+ beam. Additionally, highly localized heating with the pulsed laser system occurs in the near-surface region of the substrate, which may be critical for processing a substrate with heat sensitive components.

2.2.3 Results and Discussion

Standard He^+ milling of Ti was initially performed as a baseline study to compare with the subsequent photothermal and chemically assisted processes. **Figure 46a** are scanning He^+ micrographs, which show 50 x 500 nm channels which were milled into the Ti film using a He^+ beam with an acceleration voltage of 25 keV. The use of relatively large ion exposure doses reflects the relatively low sputtering yield when using He^+ . Significant sub-surface damage and He bubble formation induced swelling outside of the exposure pattern boundary is observed with increasing milling dose. This proximity effect limits the use of He^+ as a candidate for Ti milling, as well as many other materials.

Figure 46b are scanning He^+ micrographs of channels that were milled by He^+ with the simultaneous pulsed laser assist process. The 785 nm pulsed laser conditions were: a 100 ns pulse width, 100 kHz frequency (1% duty cycle), and $\sim 478 \text{ kW/cm}^2$ irradiance (176 mW laser power) for the duration of the He^+ milling processes. The resulting channels exhibit much less swelling, which suggest less sub-surface damage¹⁴³ compared with the standard room temperature milling processes (**Figure 46a**). High fidelity pattern transfer is feasible with the synchronized pulsed laser assist. Recent work has demonstrated that $\sim 90\%$ of sub-surface implanted He concentration can be thermally driven in/out via a pulsed laser assisted He^+ exposure.¹⁴³ Photothermal energy supplied from the laser drives diffusion of implanted He^+ as well as recombination of vacancies and interstitials generated via interactions of the target material with the energetic ion (and subsequent knock-on atoms). The sputter yield (as measured by visual or SE detector endpoint monitoring – see Supporting Information) is also improved to approximately 0.045 atoms/ion with the laser assist, about 1.5x enhancement relative to ~ 0.03 atoms/ion without a laser assist. Sub-surface damage and swelling can be further reduced by

controlling the photon/ion flux from the laser and ion beam¹⁴³. **Figure 46c** is a scanning He⁺ micrograph which shows a channel which was milled with a laser assist of 300 ns pulse width at 100 kHz frequency. The increase in duty cycle, from 1 to 3%, degraded the pattern transfer evidently due to Ti grain coalescence. **Figure 46d** displays the simulated peak Ti film temperatures per pulse for both cases. Additional details on the thermal simulation can be found in the supporting information. Notably, a 300 ns laser pulse induces a temperature rise greater than 950 K. This elevated temperature explains the Ti grain coarsening. The increase in sputter yield during pulsed laser assist was unexpected considering the brief time available for thermal assist using 1% and 3% duty cycles. The likely cause for the effective yield change could be the swelling component which narrows the channel and limits the escape angle for the sputtered target material.

Analogous to a reactive ion etch, the chemical etching during FIBIE typically increases the material etching rate. As a result, lower He⁺ doses are required per unit volume removed. Concurrently, the concentration of He⁺ induced sub-surface damage is reduced, minimizing swelling. **Figure 47a-d** show channels etched into the Ti film under increasing, and localized, XeF₂ fluxes. The He⁺ dose was constant in these experiments (1×10^{19} He⁺/cm²). All experiments were conducted using a 25 keV acceleration voltage and a beam current ranging from 1.7-2.3 pA. Additional experimental details can be found in the Methods section. The etch yield is clearly enhanced (~ 0.17 atoms/ion) with increasing XeF₂ flux up to the highest XeF₂ flux of 1.5×10^{17} cm⁻²s⁻¹ where the Ti film was completely etched through (**Figure 47d**). Increasing the XeF₂ flux increases the equilibrium surface coverage and decreases the coverage time for the XeF₂ molecules on the Ti surface. Both outcomes push the FIBIE process toward a reaction rate limited (RRL) regime¹⁴¹ where etching efficiency is maximized. Notably, surface swelling and sub-surface damage is minimized during the FIBIE process.

The ion milling and chemically-assisted etching processes were simulated using the Monte Carlo simulation code EnvizION^{103,144} in order to elucidate the reduction in sub-surface damage observed during FIBIE. The Ti – Ti surface, and lattice binding energies of the Ti film, were varied to emulate the ion milling and chemically-assisted etching processes (see methods for additional details). Standard energetics are used for the ion milling while the surface and lattice binding energies are reduced to emulate the increased effective sputter yield for the

chemically assisted etching process. For instance, the simulated sputter yield for the typical Ti energetics generates a sputter yield of 0.036 atoms/ion, in good agreement with the experimentally observed value of 0.03 atoms/ion. The reduced energetics were tuned to increase the sputter yield to 0.16, which is in the same range of the chemically assisted Ti etching. The Monte Carlo simulation yields a “damage function,” which is defined as the cumulative number of damage events per lattice site. In addition, we store the nuclear energy deposited in the film by the He^+ ions, and the He^+ implantation concentration. **Figure 48a** shows a cross-section of the damage function for the milling simulation (left) and the chemically-assisted etching simulation (right). For comparison, we found that a damage function of about 0.2 events/lattice sites drives a crystalline to amorphous transition which is observed in silicon¹⁰²; this value is exceeded in the milling simulations up to 150 nm perpendicular to the long scan axis (x-axis in the simulations). Interestingly, the swelling observed in the milled Ti extends approximately 150 nm into the adjacent, unexposed film (**Figure 46a**), though the defect distribution is expected to be different in metallic Ti relative to the covalent silicon lattice. **Figure 48b** shows the deposited nuclear energy for milling (left) and etching (right). As with the damage function, we determined the deposited energy necessary for amorphization of Si. While Bohmayr et al. determined from simulations that Si amorphization occurs at a deposited nuclear energy of 12 eV/atom¹⁴⁵, our simulations suggest an energy of about 5.5 eV/atom. This energy is exceeded by the milling simulation throughout most of the computational domain (or 150 nm perpendicular to the long scan axis), and for the chemically-assisted etching simulation is exceeded in a somewhat smaller region. **Figure 48c** illustrates the He^+ ion implant concentration for milling (left) and chemically-assisted etching (right). Both the damage function and the deposited energy scale linearly with the ion dose for both the chemically-assisted etching and milling simulation: the ratio of the damage function for the milling simulation to that of the etching simulation is 4:1, when averaged over the computational domain, reflecting the fact that the milling simulation has four times the ion dose. Thus, the reduction in sub-surface damage in the chemically-assisted etching simulations can be understood as a reduction in the ion dose needed to etch a channel compared with milling simulations. While the average ratio of the damage function (and deposited energy) between the milling and chemically-assisted etching simulations scales with the dose, there is

some observed sub-surface depth-dependence of these quantities (see supporting information for details).

Previous results of CF₄ reactive ion etching of Ti indicated that the final fluorine insertion of $F + TiF_3 \rightarrow TiF_4$ is the rate limiting step and importantly TiF₃ is a stable solid which is not volatile.^{146,147} The focused electron beam induced etch (FEBIE) rate of Ti with XeF₂ was shown to be enhanced by supplying in situ thermal energy from an infrared pulsed laser;¹¹⁹ the enhanced etch rate was attributed to photothermally enhanced: (1) Ti-F reaction, 2) TiF₄ desorption 3) increased XeF₂ gas surface diffusion to the reaction zone and 4) increased TiF_x surface diffusion from the reaction zone. The thermal energy is expected to also increase the XeF₂ desorption rate which would decrease the overall reaction, however the increasing etch rate mechanisms appears to over-compensate and result in a net increase in the etch rate compared to the un-assisted FEBIE process. Our proposed model is different than what was recently proposed for electron beam induced etching of diamond with an H₂O precursor¹⁴⁸. Martin et al. correlated the anisotropic shape evolution of H₂O/diamond etching to a process rate-limited by the electron stimulated desorption of the CO by-products. Importantly they did not observe any rate or anisotropy difference with increasing temperature as would be expected by this athermal mechanism. Clearly we observe a strong photothermal response and, due to the small polycrystalline grain size and sub-surface damage, no anisotropic surface evolution.

The pulsed laser system was used to study the effects that in-situ thermal energy has on the FIBIE process. **Figure 49a** shows patterns etched into Ti with 25 keV He⁺ using the FIBIE process (top) and the LA-FIBIE process (bottom) at a dose of 1×10^{19} He⁺/cm² for the FIBIE process and 7.0×10^{18} He⁺/cm² for the LA-FIBIE process. The LA-FIBIE process results in a greater etch yield than the FIBIE process, however there is some loss in the lateral resolution of the process due to overetching. **Figure 49b** shows the etch yield of the FIBIE and LA-FIBIE processes as a function of the He⁺ dwell time. The synchronized laser irradiance used for these experiments was 55.5 kW/cm² at a pulse width of 100 ns and a frequency of 50 kHz (0.5% duty cycle). Due to the thermal enhancements previously mentioned, the LA-FIBIE process results in a higher etch yield than the FIBIE process for all dwell times. As the ion dwell time is reduced, the etch yield increases for both processes due to an enhanced precursor coverage during the ion

beam dwell; at longer dwell times, the XeF₂ precursor gets depleted and the chemical assist is limited by subsequent precursor adsorption and/or diffusion of the precursor to the reaction zone.

In order to better understand the FIBIE regimes, we estimated the XeF₂ localized flux and monolayer coverage time, and compared to our ion beam conditions in Table 5. The XeF₂ flux for the He⁺ dwell time experiments was estimated to be $1.6 \times 10^{17} \text{ cm}^{-2} \text{ s}^{-1}$, in accordance to Ref¹⁴⁹. This results in a XeF₂ monolayer coverage time of approximately $8.4 \times 10^3 \text{ } \mu\text{s}$ assuming a unity sticking coefficient. This is much less than the loop time (ranges from $4 \times 10^4 \text{ } \mu\text{s}$ to $2 \times 10^7 \text{ } \mu\text{s}$ for the 100 ns to 50 μs dwell times), or time between subsequent exposures of the same pixel, during the patterning process for all He⁺ dwell times compared. Therefore, we conclude that there is sufficient time between pixel exposures to allow the XeF₂ coverage to re-equilibrate. However, the number of ions that each Ti surface site is exposed to per patterning loop increases with increasing dwell time. For instance, at the 100 ns dwell time, each Ti surface site is exposed to just ~ 1.3 ions per pass. This inhibits the full depletion of the precursor species and results in a more RRL regime. In contrast, a 50 μs dwell time exposes each Ti surface site to ~ 640 ions per pass which severely depletes the local XeF₂ coverage. The longer dwell time results in mass transport limited (MTL) etching behavior, and a reduction in the etch yield. Precursor diffusion, which can be thermally enhanced by the synchronized pulsed laser, can reduce the time required for XeF₂ replenishment during the LA-FIBIE process. This along with enhanced reaction, byproduct desorption, and byproduct diffusion result in a greater etch yield for LA-FIBIE, in particular at longer dwell times (such as 50 μs) which are typically in the MTL regime.

Thermal simulations were conducted to determine the photothermal heating of the pulsed laser induced heating of the Ti films. **Figure 50a** shows the simulated temporal evolution of the surface temperature induced in the Ti film by a single 100 ns laser pulse at various laser irradiances on the 200 nm thick Ti on the thin SiN_x. At the 55.5 kW/cm^2 laser irradiance (**Figure 49**), the Ti temperature is raised modestly to $\sim 325 \text{ K}$. This indicates that relatively small amounts of thermal energy introduced during the LA-FIBIE process can affect the etch yield. **Figure 50b** is an Arrhenius plot of the natural log of the etch yield versus the inverse of the simulated temperature achieved by 100 ns laser pulses during the LA-FIBIE processes with varying laser irradiance (as shown in **Figure 50a**). From the slope of the Arrhenius plot the effective activation energy of the etch process is $\sim 49 \text{ meV}$ for a pulsed process with 0.5 % duty cycle, which is in

good agreement with laser-assisted electron beam induced etching enhancements¹¹⁹. As the laser irradiance, and hence photothermal energy increases, etch yield is enhanced. However, increasing laser irradiance can significantly reduce the lateral resolution of the etch process (shown in Supporting Information). The lower XeF₂ flux of $\sim 1.0 \times 10^{17} \text{ cm}^{-2}\text{s}^{-1}$ in comparison to the data reported in **Figure 49** is responsible for the lower etch yields. **Figure 50c** shows the effect of laser duty cycle on the etch yield. At low duty cycles (0.1 and 0.25%) there is little enhancement in the etch rate in comparison to a standard FIBIE process. However, the etch rate increases above 0.25% duty cycle until saturation occurs at a duty cycle of 1%. Operation at above 1% duty cycle does not allow sufficient time for the material to return to room temperature between subsequent laser pulses. This results in additive heating with each pulse and thermal “runaway”, which facilitates spontaneous decomposition of the XeF₂ and spontaneous etching. This limits the spatial resolution of the etching process, although it remains confined to the dimensions of the laser spot; thus another application for the instrument used in these experiments might be larger area material removal via laser etching. Therefore, the synchronized laser conditions during the LA-FIBIE process, can be chosen to give highest spatial resolution (low laser irradiance and low duty cycle) or greatest etch rate (high laser irradiance and high duty cycle).

2.2.4 Conclusions

In summary, milling rate and fidelity enhancement with focused He⁺ are demonstrated in this work by several methods. First, synchronizing a pulsed laser with a standard He⁺ milling process increases the effective sputter yield of Ti while simultaneously reducing deleterious sub-surface damage and swelling by the introduction of photothermal energy. FIBIE of Ti with the XeF₂ precursor molecule was also demonstrated as a method to enhance material removal rate which also reduces the cumulative damage. Finally, laser assisted-FIBIE was introduced as a method to enhance etch yield in comparison to the standard room temperature FIBIE. These processes demonstrate important advancements in subtractive patterning techniques using the focused helium ion microscope. This increases its applicability as a robust high resolution nanomachining instrument.

2.2.5 Methods

2.2.5.1 Helium Ion Beam

A Zeiss Orion NanoFab helium ion microscope was used for all sputtering and etching experiments. Exposures were conducted with a He^+ beam energy of 25 keV with a beam current ranging from 1.7 – 2.3 pA using the 20 μm aperture. A Fibics NanoPatterning Visualization Engine (NPVE) was used as the pattern generator. For all patterns, a constant pixel spacing of 0.25 nm was used and the dwell times were varied from 100 ns to 50 μs . Experiments were conducted on a 30 nm thick SiN_x membrane which was coated with 200 nm of Ti. This substrate was chosen to mimic some chip repair strategies of thinned backside edits; importantly the thin membrane geometry minimizes thermal conduction relative to bulk substrates.

2.2.5.2 Gas Injection System

An Oxford Instruments OmniGIS I gas injection system (GIS) was used to deliver XeF_2 in close proximity to the substrate. The needle was positioned $\sim 100\ \mu\text{m}$ above the substrate and $\sim 200\ \mu\text{m}$ from the center of the ion beam field of view at an angle of 38° between the needle and the substrate. The XeF_2 precursor gas was cooled to 15°C prior to flow. Gas fluxes were estimated by the method detailed in Ref¹⁴⁹.

2.2.5.3 Laser Delivery System

A small spot on the sample surface centered on the He^+ ion beam was irradiated by a 785 nm wavelength optical beam at incident optical powers up to 176 mW using a prototype laser delivery system provided by Waviks, Inc. (Dallas, TX). Light from a fiber-coupled semiconductor diode laser is transmitted through single-mode fiber and a miniature optical system in a vacuum-sealed probe that is mounted through a motorized nanomanipulator on a high-angle port on the helium ion microscope chamber. The single-mode system projects an approximately Gaussian elliptical laser spot onto the sample having full widths at $1/e^2$ irradiance along the minor and major axes of $7.7\ \mu\text{m}$ x $13.1\ \mu\text{m}$ at optimum focus. The nanomanipulator permits closed-loop submicron positioning of the laser spot on the sample surface under computer control, and is also used to perform focusing of the laser spot. Laser power, pulse length, and repetition rate are all adjustable under computer control.

Additional details on the laser delivery system and optical beam and pulse parameters can be found in the Supporting Information.

2.2.5.4 Monte Carlo Simulation

The ion milling and chemically-assisted etching process were simulated using EnvizION code^{103,144} to elucidate the reduction in sub-surface damage observed during FIBIE. This code uses a Monte-Carlo based method, similar to that of SRIM-TRIM¹⁵⁰, to simulate the ion stopping and recoil process. This Monte-Carlo algorithm is coupled to a voxel based model of the target, which simulates the cumulative removal of material by sputtering, as well as the sub-surface damage. In order to emulate gas-assisted FIBIE, we adjusted the properties of the Ti substrate in order to increase the sputter yield: the surface binding energy was reduced from 4.89 eV to 0 eV, and the lattice binding energy was reduced from 3 eV to 1.5 eV. The surface binding energy is the energy threshold that displaced titanium atoms which have reached the surface must exceed in order to be sputtered; importantly only displaced atoms from ion or knock-on collisions are able exit the material while unperturbed surface atoms remain. The lattice binding energy is the energy expended when a titanium atom is displaced from its position in the lattice. This change in the energetics increases the sputter yield to 0.16, which is in the same range as that observed for FIBIE in **Figure 49b**. We refer to simulations that use the reduced surface and lattice binding energies as “chemically-assisted etching” simulations, and those which use the higher values of the surface and lattice binding energies as “milling” simulations.

We simulated a 15 nm by 1 nm line scan using the standard milling and chemically-assisted etching energetics (where the x-axis is taken to be the scan axis). For both sets of simulations, we simulate the dose sufficient to create a channel approximately 30 nm deep: 11,250,000 ions for milling simulations, and 2,812,500 ions for chemically-assisted etching simulations (i.e., the milling simulation requires four times the ion dose). We measure the sub-surface damage by with a so-called “damage function”, which we define as the cumulative damage events at a lattice site. A damage event consists of either a titanium atom being displaced from its position at the site (vacancy production), or a recoiling atom coming to rest at the site (vacancy elimination). We additionally study the nuclear energy deposited in the target by the He⁺ ions, defined as the energy lost due to elastic collisions between atoms per lattice site.

2.2.6 Appendix

2.2.6.1 Supporting Information

Laser Delivery System Details

A prototype laser delivery system provided by Waviks, Inc. (Dallas, TX) was mounted on a high-angle port of the helium ion microscope at the Center for Nanophase Materials Sciences at Oak Ridge National Laboratory. The system consists of a 785 nm fiber-coupled semiconductor diode laser (Oxxius Model LBX-785-250-FC-SM-PP) connected with single-mode fiber through a vacuum feedthrough into a vacuum probe containing miniature lenses to image the fiber mode onto the sample. The vacuum probe is mounted through a 3-axis motorized nanomanipulator (Oxford Instruments OmniProbe 200) enabling 100 nm closed-loop encoder feedback control of laser spot position with computer control and storage of positions. A photograph of the laser delivery system including nanomanipulator, as installed onto the helium ion microscope, is shown in **Figure 51**. As shown, the prototype system includes two optical fiber channels for two separate laser wavelengths; only the 785 nm channel was used for these experiments.

The focusing optics produce an approximately Gaussian circular laser spot on-axis having a $1/e^2$ irradiance beam waist (radius) w_0 at best focus of 3.85 μm , as measured using a laser beam analyzer. Because the angle of the laser port is 54 degrees away from the ion beam and sample normal, the laser spot on the sample surface is elongated in the y direction (along the plane of incidence) by a factor of $(\cos 54^\circ)^{-1}$ or about 1.7 compared to the spot size in the x direction (normal to the plane of incidence), which was confirmed by marks made on samples at high laser powers.

Including all optical coupling losses, the 785 nm laser power incident on the sample surface can be set under software control to a setpoint value as high as 176 mW, corresponding to a peak laser irradiance at the center of the Gaussian focused laser spot of 478 kW/cm^2 at maximum laser power. The diode laser can be operated continuously (cw) at a setpoint power, or digitally modulated between zero output and the power setpoint with a rise time of under 2 ns, using a computer-controlled pulse generator for complete control of pulse duration and triggering. For the experiments reported here, unsynchronized periodic repetitive pulsing was used, with pulses as short as 100 ns and frequencies (pulse repetition rates) as high as 500 kHz, although these pulsewidths and frequencies are not limited by the apparatus.

LA-FIBIE Images

Laser Power Dependence

Figure 52 shows patterns milled into Ti using the La-FIBIE process with a 1 μs He^+ dwell time, 100 ns laser pulsewidth, and 50 kHz laser frequency (0.5% duty cycle). Laser power was varied and the values are inset in the figure. The laser powers of 79.0, 35.7, and 20.5 mW correspond to peak irradiance levels at the center of the Gaussian laser spot of 88, 44, and 26.4 kW/cm^2 , respectively. The dose for all patterns is approximately $7.5 \times 10^{18} \text{ He}^+/\text{cm}^2$. At the lowest laser power studied (20.5 mW) pattern fidelity is good however the etch yield was lower (**Figure 50** of manuscript). At greater laser power etch yield increased as described in the main text. However, the higher yield associated with greater laser power promotes etching in peripheral regions around the intended patterned area and compromises the pattern fidelity.

Duty Cycle Dependence

Figure 53 shows the dependence of duty cycle on the La-FIBIE process. As duty cycle increases, there is an increase in etch yield (**Figure 50** of manuscript) however at progressively higher duty cycle, the pattern fidelity is again compromised.

Thermal Simulations

Simulations of laser-induced heating of the Ti/SiN_x substrate were performed using COMSOL Multiphysics 5.0, which is a commercial finite element method (FEM) software package. The expression for heat delivered to the substrate from the laser is derived from the Beer-Lambert law:

$$Q_{in}(x, y, z) = P_o(1 - R_c) \frac{2A_c}{\pi w_x w_y} G(x, y) \exp(-A_c z) , \quad (1)$$

where P_o is the optical power of the laser, R is the reflection coefficient, A is the absorption coefficient, $G(x, y)$ is the Gaussian laser irradiance profile, w_x and w_y are the $1/e^2$ irradiance radii of the Gaussian laser profile in the x and y directions, respectively, and z is the depth from the substrate's surface. w_x and w_y were experimentally determined to be 3.85 μm and 5.90 μm , respectively, as described above. A linear 10 ns laser ramp time was assumed for this simulation and the laser pulse width was varied depending upon the experiment. All absorption was assumed to occur in the Ti film, since the extinction coefficient for 785 nm photons in SiN_x is

approximately zero. The following time dependent heat equation was used to simulate the heat transfer throughout the Ti and SiN_x substrates substrate:

$$\rho C_p \frac{dT}{dt} + \rho C_p \mathbf{u} \cdot \nabla T = \nabla \cdot (k \nabla T) + Q(x, y, z) \quad (2)$$

where ρ is the material density, C_p is the heat capacity at constant pressure, \mathbf{u} is the velocity vector for thermal transport, and κ is the thermal conductivity. Convective heat transfer to the surrounding atmosphere was neglected since irradiation conditions were under high vacuum and T_0 was defined as 293.15 K. A backward differentiation formula time-stepping method with strict time steps was used to generate the temporal temperature evolution during laser irradiation.

Table 6 reports relevant simulation and material parameters used to simulate the temperature temporal evolution induced by the 785 nm laser pulse. The Ti and SiN_x heat capacitance and thermal conductivity were approximated for thin films in accordance to Refs^{151,152}.

Visual Endpoint Monitoring

Visual endpoint monitoring (VEM) was used to monitor the progress of the milling or etching through the Ti, and hence the etch yield. VEM measures the cumulative current collected by the detector during a single loop of the patterning process and assigns the value to a unit which reflects the electron collection (y-axis). Therefore, the VEM signal decreases as effective secondary electron (SE) yield decreases. Since the underlying SiN_x has a lower SE yield than the Ti substrate, the VEM plot demonstrably indicates when milling or etching through the Ti is complete and SiN_x milling begins. As shown in **Figure 54**, there is a sharp decrease in the VEM signal once the Ti mill is complete. This method was used to precisely determine all etch and sputter yields.

2.2.6.2 Figures

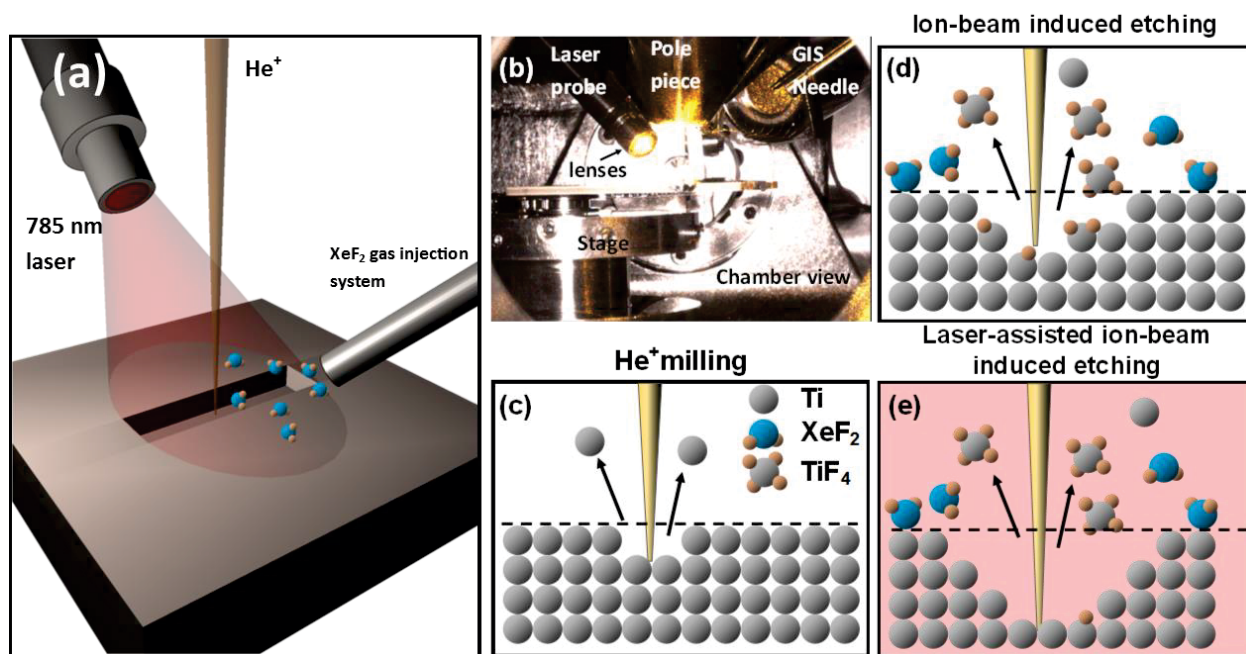


Figure 45. (a) Schematic of the focused ion beam induced etching (FIBIE) setup. The focused 785 nm laser beam, focused He⁺ beam, and gas injection nozzle share a common confocal point on the Ti film surface. (b) In-chamber digital photograph of the experimental setup with the beam, laser probe, and gas sources indicated. The GIS needle is retracted in this image. (c) Schematic of a He⁺ milling process of Ti. (d) Schematic of a FIBIE process with the XeF₂ chemical assist. (e) Schematic of a laser assisted FIBIE process.

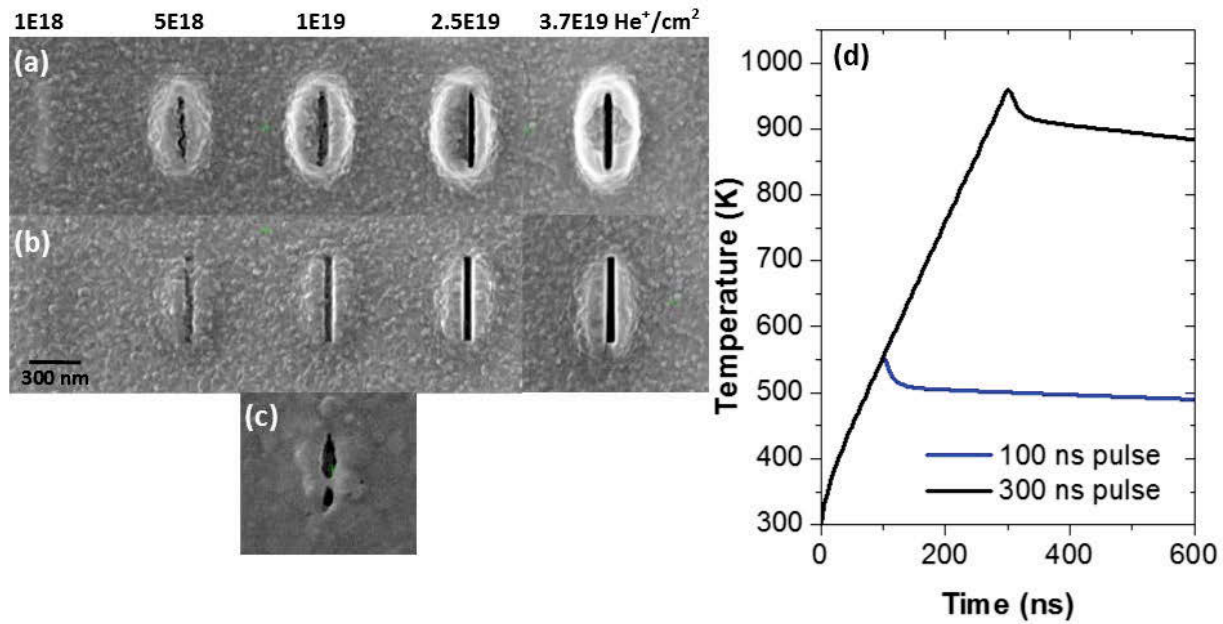


Figure 46. (a) He⁺ milling of a 200 nm thick Ti film at various doses ranging from 1×10^{18} — 3.7×10^{19} He⁺/cm². (b) in situ, pulsed laser assisted milling with a 478 kW/cm² laser irradiance, 100 ns pulse width and 100 kHz frequency. (c) in situ pulsed laser assisted milling with a 478 kW/cm² laser irradiance, 300 ns pulse width and 100 kHz frequency. (d) Finite-element simulation of the peak Ti film temperature induced by the 478 kW/cm² laser irradiance as a function of time for 100 and 300 ns laser pulses.

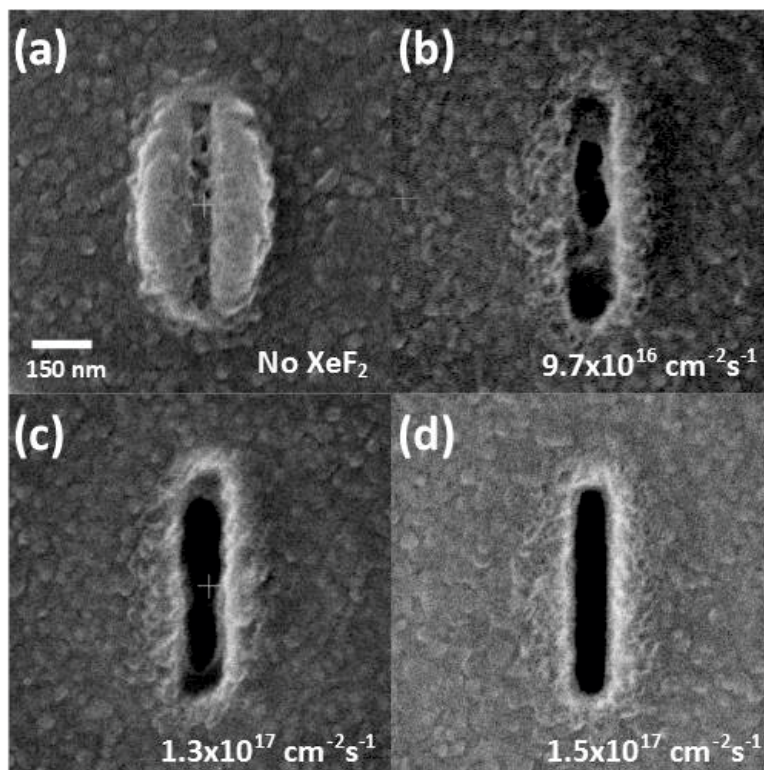


Figure 47. Focused ion beam induced etching (FIBIE) of Ti film as a function of the localized etchant flux of (a) 0, (b) 9.7×10^{16} , (c) 1.3×10^{17} , and (d) 1.5×10^{17} XeF₂ molecules-cm⁻²s⁻¹. The FIBIE experiments were conducted using a 1 μ s He⁺ dwell time, a 0.25 nm pixel pitch and an ion dose of 1×10^{19} He⁺/cm².

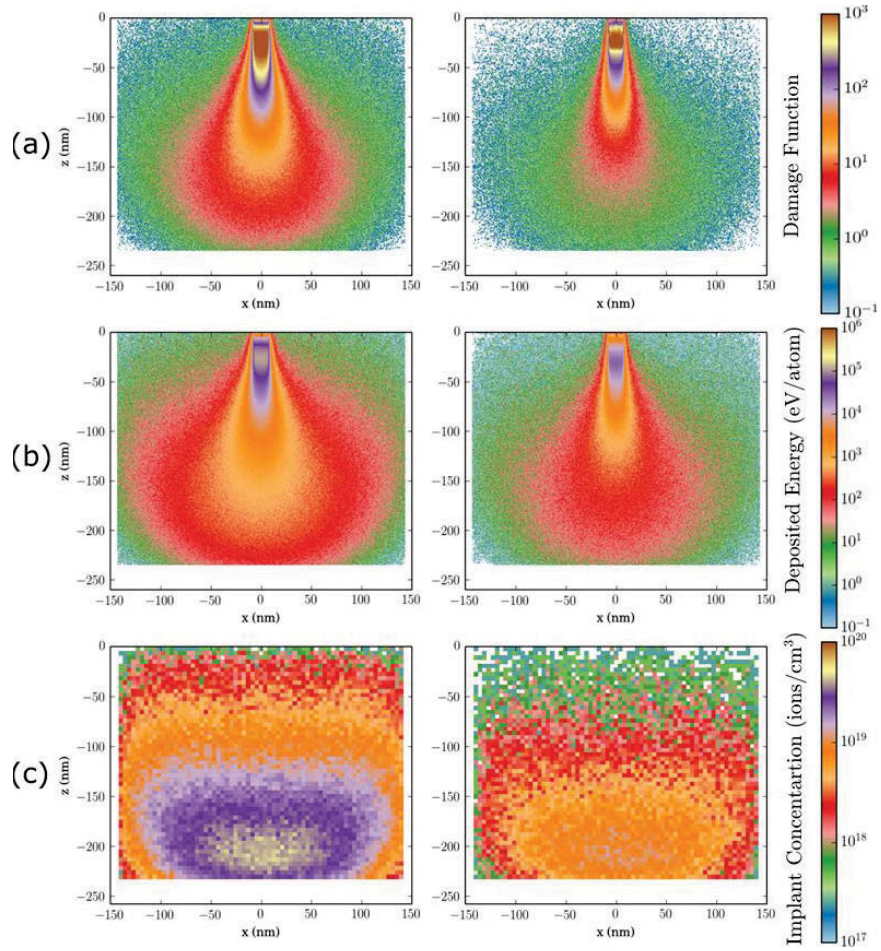


Figure 48. Simulated cross sections of (a) the damage function (the number of damage events per lattice site), (b) the deposited nuclear energy per lattice site, and (c) the implanted He^+ ion concentration. The left column corresponds to a milling simulation (11,250,000 ion dose), and the right to an “etching” simulation (2,812,500 ion dose). Additional simulation parameters are listed as follows; 15 nm long line scan, 25 keV beam energy, 1 nm pitch, 2.4 pA current, and 0.45 μs dwell time.

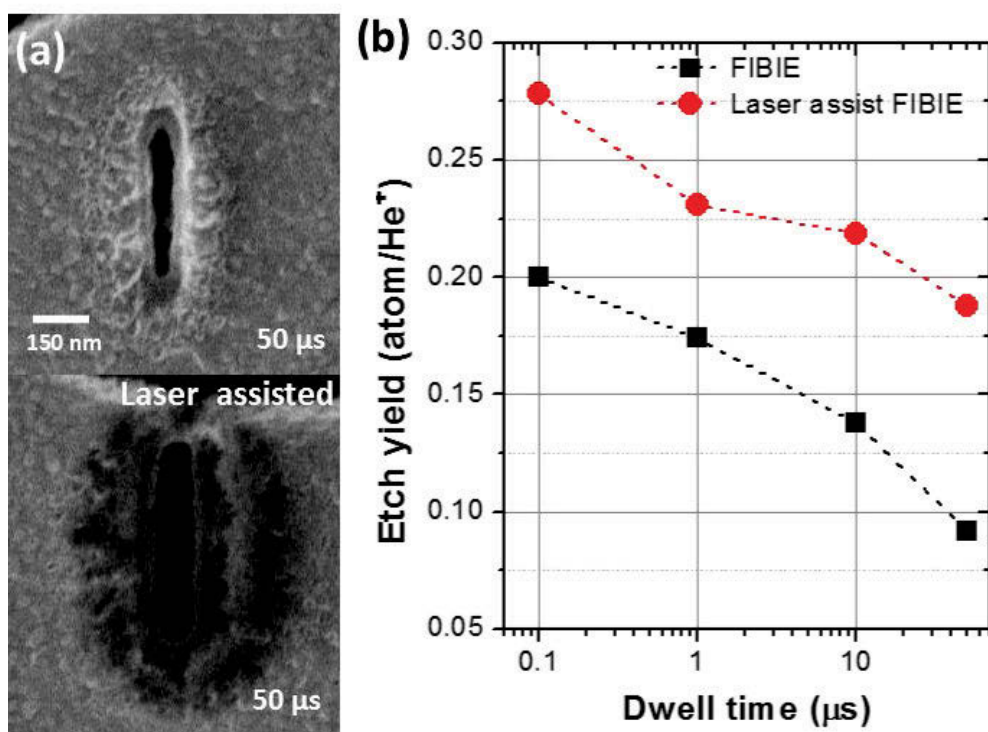


Figure 49. (a) Comparison of FIBIE process and LA-FIBIE process using a 50 μ s He⁺ beam dwell time. (b) Titanium etch yield of the FIBIE and LA-FIBIE processes as a function of He⁺ beam dwell time. LA-FIBIE was conducted with 100 ns laser pulses at an irradiance of 55 kW/cm² and a frequency of 50 kHz (0.5 % duty cycle).

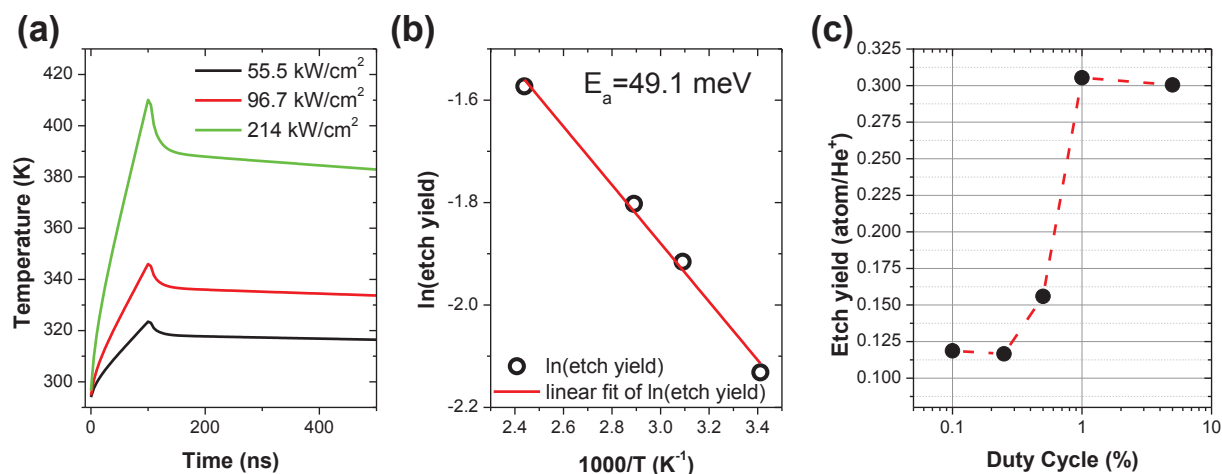


Figure 50. (a) Simulated peak temperature as a function time for a 100 ns pulse at various laser irradiance. (b) Arrhenius ln(etch yield) vs $1000/T$ plots for the La-FIBIE process with varying laser irradiance. Each temperature corresponds to temperature achieved with a 100 ns pulse at a laser irradiance of 0, 55.5, 96.7, and 214 kW/cm². (c) Etch yield as a function of laser duty cycle (pulse width x frequency) for 100 ns laser pulses at 55.5 kW/cm² irradiance. All etches conducted here used a constant 1 μ s He⁺ dwell time (additional conditions can be found in Table 5).

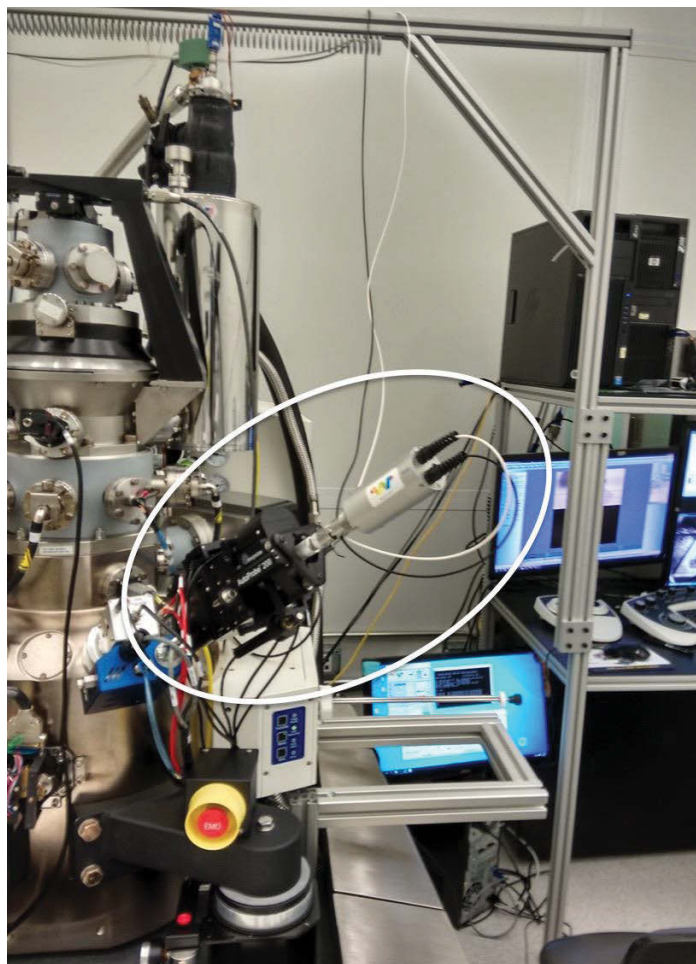


Figure 51. Photograph of the laser delivery system installed on a high angle port near the load lock of the Zeiss Orion NanoFab helium ion microscope. Optical probe (silver) mounted through the nanomanipulator (black) are indicated within the white ellipse. Only one of the two optical fibers was used in these experiments.

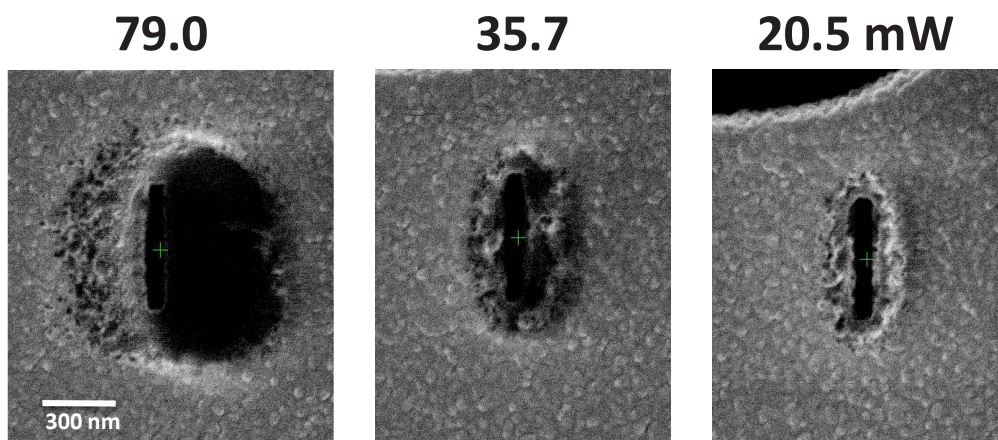


Figure 52. Patterns milled into Ti using the La-FIBIE process at varying synchronized laser powers (inset across the top). The laser pulsewidth was 100 ns and the frequency was 50 kHz (0.5 % duty cycle).

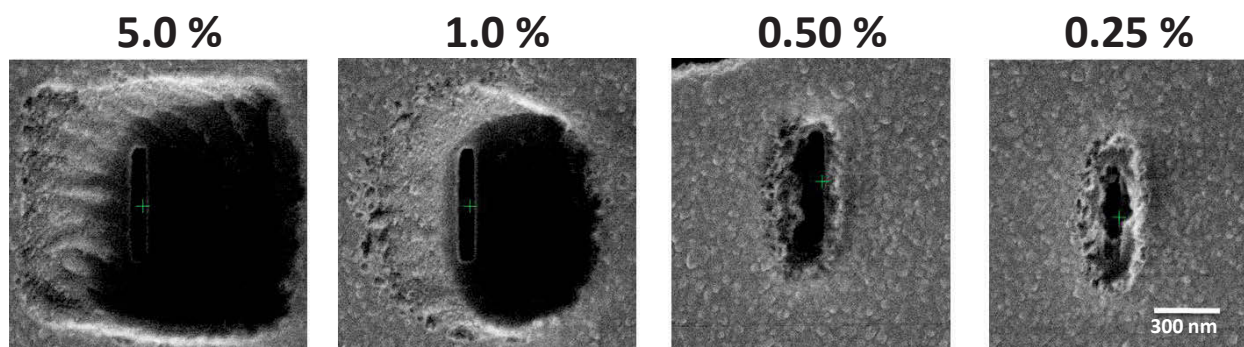


Figure 53. Patterns milled into Ti using the La-FIBIE process at varying synchronized laser duty cycle, or frequency. The laser pulse width was held at a constant 100 ns and the frequency was varied from 25 – 500 kHz (0.25 – 5.0 % duty cycle) to control the duty cycle.

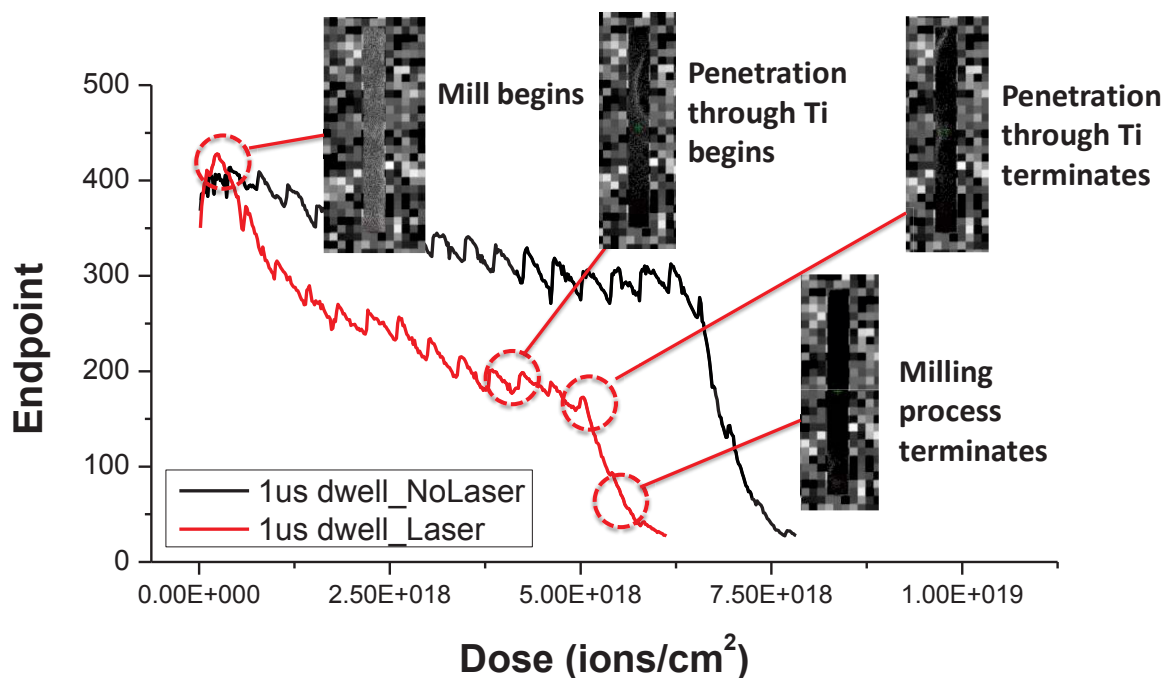


Figure 54. Visual endpoint monitoring of FIBIE (black) and LA-FIBIE (red) processes. Endpoint signal is an averaged greyscale value reflecting the number of secondary electrons collected at the detector after each patterning loop. The scale of the y-axis is in arbitrary units. Inset helium ion microscope images show how the mill progresses with the endpoint signal.

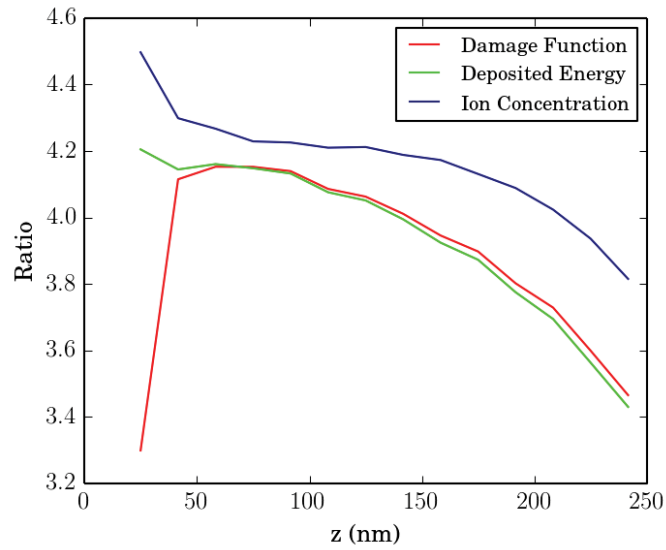


Figure 55. Average ratio of three measures of subsurface damage between the milling and etching simulations, as a function of depth within the target (see Figure 48). The average ratio for all of these measures over the whole computational domain is approximately four, reflecting the fact that the milling simulation has four times the ion dose of the etching simulation.

2.2.6.3 Tables

Table 5. Estimated XeF₂ and He⁺ parameters for FIBIE processes at varies He⁺ dwell times. All patterning was conducted with a 25keV He⁺ beam and a 0.25 nm pixel pitch.

	100 ns	1 us	10 us	50 us
Localized XeF ₂ Flux (cm ² s ⁻¹)	1.6x10 ¹⁷	1.6x10 ¹⁷	1.6x10 ¹⁷	1.6x10 ¹⁷
Monolayer coverage time (μs)	8.4x10 ³	8.4x10 ³	8.4x10 ³	8.4x10 ³
Refresh time (pass time) (μs)	4x10 ⁴	4x10 ⁵	4.0x10 ⁶	2.0x10 ⁷
Ions per pixel per pass (ions)	1.1	10	110	530
Ions per surface site per pass (ions)	1.3	13	130	640

Table 6. Material and laser parameters for the thermal simulations.

Simulation Parameters	Value	Description
w_x	3.85 [μm]	Laser $1/e^2$ irradiance radius - x
w_y	5.90 [μm]	Laser $1/e^2$ irradiance radius - y
R	0.594	Reflection coefficient of Ti at 785 nm
A	5.58E5 [1/cm]	Absorption coefficient of Ti at 785 nm
P_0	176.2 [mW]	Laser power
$Pulse$	varied [μs]	Laser pulse width
$C_p(\text{Ti})$	522 [J/(kg*K)]	Ti heat capacity
$\rho(\text{Ti})$	4506 [kg/m^3]	Ti density
$\kappa(\text{Ti})$	5.63 [W/(m*K)]	Ti thermal conductivity
$C_p(\text{Si}_3\text{N}_4)$	710 [J/(kg*K)]	SiN _x heat capacity
$\rho(\text{Si}_3\text{N}_4)$	3440 [kg/m^3]	SiN _x density
$\kappa(\text{Si}_3\text{N}_4)$	2.1 [W/(m*K)]	SiN _x thermal conductivity

2.3 Tungsten Diselenide Patterning and Nanoribbon Formation by Gas-Assisted Focused Helium Ion Beam Induced Etching

A version of this chapter was originally published by M. G. Stanford et al.:

Stanford, M. G.; Pudasaini, P. R.; Cross, N.; Mahady, K.; Hoffman, A.; Mandrus, D. G.; Duscher, G.; Chisholm, M. F.; Rack, P. D. Tungsten Diselenide Patterning and Nanoribbon Formation by Gas-Assisted Focused Helium Ion Beam Induced Etching. *Small Methods* **2017**, *1*, 1600060.

Michael G. Stanford conducted experiments and performed analysis reported in this work. Michael G. Stanford also wrote the manuscript. Kyle Mahady conducted Monte Carlo simulations. Nicholas Cross and Gerd Duscher perform scanning transmission electron microscopy. David Mandrus synthesized the WSe₂. Pushpa Pudasaini conducted electrical measurements. All co-authors contributed to manuscript revisions.

2.3.1 Abstract

In this work, we introduce a gas-assisted focused helium ion beam induced etching (FIBIE) process, which accelerates direct-write patterning of WSe₂ relative to standard ion milling. The etching process utilizes the XeF₂ precursor molecule to provide a chemical assist for enhanced material removal relative to ion sputtering. The FIBIE process enables high fidelity patterning of WSe₂ with doses 5x lower than standard He⁺ milling. This enables the formation of high-resolution WSe₂ nanoribbons with dimensions less than 10 nm. The WSe₂ nanoribbons demonstrate high Raman anisotropy and nanoribbon electrical measurements are reported for the first time. The normalized on-currents of field-effect transistors reveal that the electron and hole currents are both suppressed and scale with the nanoribbon width, with the electron transport experiencing more degradation. However, on-currents of nanoribbons created by the FIBIE process remain orders of magnitude greater than nanoribbons formed by standard He⁺ milling. Scanning transmission electron microscopy and complementary Monte Carlo ion-solid simulations reveal that the reduced currents are due to ion-induced damage in the WSe₂.

2.3.2 Introduction

The focused helium ion microscope (HIM) has garnered much attention in recent years due to its high resolution imaging and nanoscale synthesis precision.^{153,154} The resolution of the He^+ probe, which is less than 1 nm¹⁵⁵, has enabled the formation of sub-10 nm nanostructures via deposition¹²¹, milling^{16,122,156}, and lithography¹²³, to name a few. However, the small mass of He^+ results in a low sputter yield of target materials in comparison to other ions of larger mass, such as Ga^+ .^{157–159} Energy loss of 25 keV He^+ occurs over a depth and lateral straggle extending hundreds of nanometers in typical target materials, and may result in the formation of extensive deleterious subsurface defects and substrate swelling.^{102,143} Beyond this, backscattered He^+ (BS_{He}) and recoil atoms in peripheral regions around the intended exposed areas can limit the practical resolution of the patterning. This is particularly true when patterning 2-dimensional materials in which relatively small doses, which BS_{He} and recoil atoms are capable of delivering, can drastically change the material's properties.¹¹⁵ For this reason, it is essential to minimize the He^+ dose required for both subtractive and additive nanoscale processing techniques.

Focused ion beam induced etching (FIBIE) can conveniently be used to etch a material in a direct-write manner dictated by the scanning pattern of the ion beam. To chemically assist the sputtering, a precursor gas is introduced into an ion microscope in close proximity to the substrate. The molecules adsorb/desorb to establish an equilibrium coverage based on the localized flux and associated residence time, which is a function of gas-surface interactions and substrate temperature¹⁶⁰. While adsorbed, the precursor gas can be dissociated into radical species via inelastic collisions with: 1) primary/backscattered ions, 2) target atoms that experience knock-on collisions, as well as 3) subsequent secondary electrons. With appropriate selection of the etchant precursor gas, the dissociated radical species form volatile byproducts with near-surface atoms of the substrate. The volatile byproducts desorb from the surface and are pumped out of the system. An added benefit of FIBIE is that ion-solid momentum transfer adds a sputtering component to the etch process, which results in higher etch yield when compared to electron beam induced etching.

The HIM has shown potential to pattern and selectively introduce defects with high resolution into 2-D materials such as MoS_2 ^{9,161}, MoSe_2 ¹⁶², WSe_2 ¹⁶³, and graphene^{11,115,122,164–166}. Of particular interest, transition metal dichalcogenide (TMD) nanoribbons have been theorized to

exhibit unique properties depending upon edge termination^{167–170}. TMDs can be milled when suspended on a TEM grid, which conveniently reduces deleterious subsurface and peripheral damage which occurs on bulk/supported substrates. In this work, we developed a gas-assisted FIBIE process to etch WSe₂ with XeF₂ on a supported substrate and freestanding. WSe₂ was chosen due to its ambipolar transport properties and previous work which details the effects of He⁺ irradiation on the behavior of WSe₂¹⁶³. Additionally, the tungsten metal is known to etch via electron beam induced etching using XeF₂¹⁷¹, thus the cation volatility should not limit the chemically assisted process. As is the case for any focused or large area reactive ion etch process, the viability of the precursor enhancing the sputtering rate depends on the volatility of the cation and anion byproducts that form. Conveniently most of the di-chalcogenide (Ch₂) molecules are volatile as are several chalcogenide-halides and thus an appropriate precursor needs to form volatile TMD cation byproducts. During the FIBIE process, He⁺ irradiation drives the dissociation of XeF₂ which generates fluorine radicals and volatile WF_x and SeF_x byproducts are subsequently formed, where the likely dominant byproduct stoichiometry is x = 6¹⁷². The etch yield achieved with the FIBIE process represents a significant increase over the sputter yield of the He⁺ irradiation alone. Importantly, the doses required to etch few-layer WSe₂ minimizes subsurface damage and swelling compared to the ion milling counterpart. Using the gas-assisted FIBIE technique, we are able to form high resolution and high fidelity WSe₂ nanoribbons (WNRs) with widths of less than 10 nm. The WNRs demonstrate high Raman anisotropy dependent upon the angle between the polarized light source and nanoribbon orientation. The electrical transport measurements show degraded on-currents through the WNRs, which scanning transmission electron microscopy revealed is due to defects generated by the ion-solid interactions. Methods for future enhanced nanoribbon processing are discussed.

2.3.3 Results and Discussion

During focused ion beam milling, as well as gas-assisted FIBIE, the ion beam irradiates a specific array of pixels for a prescribed dwell time and fixed number of loops to realize the appropriate areal dose necessary to mill or etch the prescribed feature, respectively. These processes occur pixel-by-pixel over the entire patterned area. **Figure 56a** shows a simplified schematic of a typical milling procedure. The ion beam irradiates the target material for a prescribed dwell time, which causes sputtering of W and Se atoms, although the smaller mass

chalcogen (Se) atoms preferentially sputter at a greater rate⁹. The sputter yield is quite low however and, depending on the WSe₂ layer thickness, may require doses exceeding 1×10^{18} He⁺/cm² to mill through a few-layer TMD flake. As illustrated in **Figure 56b** the gas-assisted FIBIE utilizes a XeF₂ precursor gas which is locally injected to the beam interaction region with a gas injection system (GIS). Experimental details can be found in the experimental section. Importantly, XeF₂ does not spontaneously¹⁷³ etch WSe₂, however, under He⁺ exposure, as shown in **Figure 56c**, XeF₂ dissociates and fluorine radicals react and form volatile compounds with Se and W. These volatile species remain on the substrate for a residence time before desorbing from the surface. Conveniently, ion bombardment and secondary electron emission can reduce the residence time of the volatile compound and enhance the etch rate. All the while, physical sputtering, which is exclusively operative in a standard ion mill, contributes to the overall etching. **Figure 56d** shows an example of a pattern etched into few-layer WSe₂ with the FIBIE process. Sub-10nm WNRs were created with a fraction of the dose (~20%) required for a standard milling process. Mechanistic details of the etch process are discussed in this work.

Figure 57a shows milled patterns conducted on few-layer WSe₂ (~ 24 nm thick) as a function of irradiation dose. A dose approaching 3.2×10^{18} He⁺/cm² was required for complete milling of the WSe₂, which was exfoliated onto a 290 nm SiO₂ on Si substrate. The dose required to complete the etch process was determined based on the etch time from *in situ* videos of the process and visual endpoint monitoring of secondary electron generation. Areal dose was then calculated by multiplying the etch time by the beam current and dividing by the elementary charge and patterning area. Based on the areal dose, one can estimate the effective etch rate. The volume of WSe₂ and SiO₂ removed during the FIBIE process was estimated by multiplying the patterned area with the AFM determined thickness of the WSe₂ flake and reflectometry determined thickness of the SiO₂. The total atoms removed were estimated by multiplying the densities (9.32 g/cm³ and 2.65 g/cm³ for WSe₂ and SiO₂, respectively) by the etched volume and then dividing by the molecular weight and Avogadro's number. Finally, the sputter and etch yields were determined by dividing the estimated sputtered/etched atoms by the total number of ions (dose \times patterning area), as determined by the endpoint monitoring process and *in situ* videos. For He⁺ milling of WSe₂, the sputter yield was determined to be ~0.04 atoms/ion, which is approximately half of the sputter rate predicted by Monte Carlo simulations (0.097 atoms/ion). At this low sputter yield, and hence high

dose, the underlying substrate experienced major subsurface damage and swelling. This illustrates the need for a chemical assisted process to accelerate the etch rate and reduce the dose required for material removal. An important consideration during the FIBIE process is the precursor gas flux and coverage to the patterning region relative to the He^+ beam current, dwell time, and loop time. At a given gas flux, if the He^+ pixel dose (current \times dwell time / area) is sufficiently large, the XeF_2 species are depleted and the chemical assist is reduced in this mass transport limited regime; in this regime, the chemical enhancement depends on XeF_2 replenishment from the gas flux and surface diffusion from the surrounding area. Furthermore, if the byproduct residence time is long, the He^+ beam can cause re-dissociation of the WF_6 and SeF_6 species which further reduces the etch rate¹²⁶. In contrast, if the He^+ dwell time is relatively short, and XeF_2 coverage high, the etching regime operates in a reaction rate limited regime¹⁷⁴. **Figure 57b** and **Figure 57c** show patterns etched into the WSe_2 using the gas-assisted FIBIE process as a function of dose, with a 30 μs and 100 ns He^+ dwell time, respectively. These patterns have a constant pixel pitch of 0.25 nm and the XeF_2 chamber partial pressure for this study was approximately 6×10^{-6} Torr, which equates to a localized flux of $\sim 1.6 \times 10^{17} \text{ cm}^{-2}\text{s}^{-1}$, calculated in accordance with¹⁴⁹. The SE detector current and *in situ* SE videos during milling/chemically assisted etching gives signatures of when the WSe_2 and SiO_2 layers are etched and can be used to monitor the etch process¹⁷⁵. For instance, when complete etching of the WSe_2 occurs the underlying SiO_2 layer appears brighter due to its larger SE yield and when complete etching of the SiO_2 occurs the underlying Si appears darker due to its smaller SE yield (additional details on visual endpoint monitoring and the etch process can be found in supporting information and experimental section). Using a 30 μs He^+ dwell time, complete removal of the WSe_2 occurs at approximately $1.5 \times 10^{18} \text{ He}^+/\text{cm}^2$, however with a 100 ns dwell time, complete WSe_2 removal occurs at approximately $5.0 \times 10^{17} \text{ He}^+/\text{cm}^2$; thus the 30 μs dwell time is mass transport limited and the 100 ns dwell time is more favorable for achieving a higher etch yield. Importantly, the WSe_2 is completely etched with high fidelity at the lower dose and prevents the onset of surface swelling relative to the He^+ milling. For a constant beam energy (25keV), pixel pitch (0.25 nm), current (1.7 pA), and gas chamber pressure (6×10^{-6} Torr) the etch yields as a function of dwell time are plotted in **Figure 57d** for WSe_2 and SiO_2 . Gas-assisted FIBIE yields of 0.23 atoms/ion and 1.7 atoms/ion for WSe_2 and SiO_2 , respectively, represent a significant enhancement over the He^+ sputter yield (0.04 atoms/ion); this low sputter yield is consistent with

other He^+ -material's sputter yields^{104,157,158,163}. The slope of the curve in **Figure 57d** suggests that the etch yield is not saturated and could be enhanced further by a decreased dwell time, reduced current, or increased pixel pitch. **Figure 57e** shows the effect that pixel pitch has on the etch yield during the FIBIE process with a 100 ns He^+ dwell time and all other parameters similar to **Figure 57d**. As the pixel pitch increases to 8 nm, the FIBIE yields for WSe_2 and SiO_2 increase to 0.42 atoms/ion and 2.8 atoms/ion, respectively. This etch enhancement is attributed to the effective increase in XeF_2 coverage for each pixel during ion irradiation. Saturation of the etch yields as pixel pitch increases suggests we have approached a reaction rate limited (RRL) regime. Thus an etch enhancement of $\sim 10\times$ is realized relative to the He^+ sputtering.

To better understand the FIBIE regimes, we estimated the XeF_2 monolayer coverage time and compared it with the ion beam dwell time and loop time. The XeF_2 flux in the experiments delivered to the working area was estimated to be $1.6 \times 10^{17} \text{ cm}^{-2}\text{s}^{-1}$ (XeF_2 chamber partial pressure $\sim 6.0 \times 10^{-6}$ Torr). Based on our standard etching conditions (25 keV, 1.7 pA, 100 ns dwell time, and 0.25 nm pixel spacing), the number of ions that each pixel is exposed to per pass is 1.1 ions or 1.3 ions on each WSe_2 surface site. The time between subsequent exposures on the same pixel, or the loop time, is $4.0 \times 10^4 \mu\text{s}$, and the monolayer coverage time of XeF_2 molecules (assuming unity sticking coefficient) on the substrate is approximately $8.4 \times 10^3 \mu\text{s}$. Therefore, there is sufficient time between pixel exposures for XeF_2 to fully refresh. This data is summarized in Table 7. On the contrary, when a 30 μs dwell time is used, each pixel is exposed to 320 ions per pass (380 ions per surface site). Although the loop time is sufficiently long to ensure monolayer coverage between pattern passes, the large number of ions delivered to each surface site per loop quickly depletes the XeF_2 coverage and results in a less efficient MTL regime. Clearly there is replenishment via surface diffusion and adsorption during the pixel dwell time as the etch efficiency is only 3x higher for the shorter dwell time; the effective etch yields are approximately 0.07 and 0.23 atoms/ion for 30 μs and 100 ns dwell times, respectively.

Table 7 also compares the gas and ion beam regimes as a function of patterning pixel spacing. Specifically, the table compares a 0.25 nm and 4 nm pixel spacing for the 100 ns dwell time. For a 4.0 nm pixel pitch, there are 4.9×10^{-3} ions per WSe_2 surface site per pass. This condition is in an efficient RRL regime, and results in greater etch efficiency of approximately 0.42 atoms/ion. However, considering that the He^+ probe can be focused to a sub-nanometer size,

using a relatively large pixel spacing (e.g. 4 nm) can limit the resolution of the patterning process at the price of enhanced etching efficiency. This should be considered when high-resolution etching is desired.

Suspended few-layer WNR arrays for STEM imaging were fabricated using the FIBIE process with a 100 ns He^+ dwell time, and a 0.5 nm pixel pitch. The requisite dose to etch the suspended WSe_2 layer was $3.0 \times 10^{17} \text{ He}^+/\text{cm}^2$. These conditions result in high resolution as well as a high etch yield. **Figure 58a** shows a macro HAADF STEM image of a single ribbon, which was determined to be ~ 10 nm thick by Electron Energy Loss Spectroscopy (EELS). This confirms that high-aspect ratio etching can be conducted using the FIBIE process. **Figure 58b** reveals that crystallinity is maintained across the width of the nanoribbon although some disorder is introduced into the crystal lattice. The high-resolution image in **Figure 58c** shows that only a small amorphous region and small edge roughness (< 0.5 nm) exists at the etched edge of the nanoribbon, indicating the sub-nanometer precision of the FIBIE process. Edge termination is not obvious from the STEM which reveals a disordered edge region. Furthermore, the multi-layer WSe_2 may exhibit differing edge roughness/terminations for each layer. **Figure 58d** reports the Bragg spot width versus the distance from the edge of the WNR. The Bragg spot width is directly related to the disorder in the crystal lattice, where the spot width increases with increasing disorder. Additional information on the measurement procedure can be found in the Supporting Information. **Figure 58d** indicates that some damage and point defects extend from the edge of the etched region for a distance up to ~ 120 nm, however distinct Bragg spots indicate that the ribbon lattice remains crystalline. This lateral distance is surprising, considering the total thickness of the WSe_2 and underlying amorphous carbon membrane is only ~ 25 nm. This distribution of minor damage in the interior of the nanoribbon is attributed to interactions with scattered He^+ , displaced target atoms (vacancy production), or moving recoil atoms from the WSe_2 or substrate coming to rest within the film (interstitial production or vacancy elimination, depending on whether the location where the recoil atom comes to rest was empty). Multiple studies have shown that sufficient damage in peripheral regions surrounding the intended ion-beam patterned geometry can be induced, which significantly alters the material's optoelectronic properties^{11,115,176}. Although defects are introduced into the crystal lattice during patterning, the FIBIE process results in a far smaller

distribution of damage in comparison to a standard He^+ milling process, due to the major reduction in the dose required for WSe_2 material removal.

We study the subsurface and peripheral damage associated with etching via our EnvizION simulation code^{103,177–179}. **Figure 59a** shows the deposited nuclear energy (log scale) at an equivalent areal dose of $3.0 \times 10^{17} \text{ He}^+/\text{cm}^2$ and a 15 nm x 1000 nm scan for the x-y plane (at a depth of 10 nm) and **Figure 59b** shows the y-z plane (perpendicular to the scan axis at the $x=0$ position). For context, we note that Bohmayr et al.¹⁴⁵ reports a nuclear energy density of $\sim 12 \text{ eV/atom}$ is required for amorphizing silicon (which is close to our simulated estimates of $\sim 5.5 \text{ eV/atom}$ for silicon). For the simulated thin membrane STEM sample, the nuclear energy loss is on the order of 0.3 eV/atom at a distance of 120 nm from the etch edge which is reasonable and consistent with the discernible damage observed in the STEM images. Therefore, an energy loss of 0.3 eV/atom is the threshold for discernable damage to the lattice. Complementary simulations for a bulk substrate are also shown in **Figure 59c**) x-y plane and **Figure 59d**) y-z plane. Comparing **Figure 59a**) and **b**) to **c**) and **d**) illustrates the enhanced nuclear energy loss and thus defects generated in bulk versus thin substrates. The extended or bulk substrate causes more of the backscattered ion contribution to interact with the WSe_2 layer and thus the nuclear energy loss at the same 120 nm distance from the etched edge is on the order of $\sim 1\text{-}2 \text{ eV/atom}$. Damage in the WSe_2 nanoribbons fabricated on a bulk substrate extends to a distance of $\sim 155 \text{ nm}$ from the edge of the etched region, if a damage threshold of 0.3 eV/atom is assumed. It is worth noting that the TMD damage on bulk substrates will depend on the material where high density and high Z-number materials will typically reduce the interaction volume and low density and low Z-number materials will lead to larger interaction volumes.

Extended arrays of high-fidelity WNRs were fabricated on a SiO_2/Si substrate using the FIBIE process with 100 ns dwell time and 0.25 nm pixel pitch He^+ beam conditions. A high magnification SEM micrograph, shown in **Figure 60a**, of etched WNRs reveal that high fidelity patterns with smooth sidewalls can be fabricated. The FIBIE process can be used to fabricate sub-10 nm highly aligned WNRs (as shown in **Figure 60d**). Notably, high quality large WNR arrays with controllable aspect ratio and ribbon pitch can be fabricated on supported substrates.

Recently, Wu et al.¹⁶¹ have demonstrated that MoS_2 nanoribbons demonstrate highly anisotropic optical behavior. The optical anisotropy and enhanced intensity of the Raman modes

are attributed to anisotropy in optical absorption depending upon NR orientation and NR edges, which break up the translational symmetry of the crystal and relaxes selection rules, respectively. **Figure 60b** shows the Raman spectra of a 20 nm WNR array as a function of angle between polarization angle of the incident laser spot and the nanoribbon direction. As the angle increases from 0° to 90° the intensity of the E_{2g}^1 and A_{1g} modes (which are indistinguishable in the spectra) decrease by a factor of 2.6 when normalized to the Si peak. The angular dependence of the Raman anisotropy of the E_{2g}^1 mode is shown in the inset of **Figure 60b**, which confirms that similar to MoS_2 NRs, WNRs also exhibit high Raman anisotropy.

Transport measurements of WNRs were collected in a bottom-gated field-effect transistor (FET) configuration. A schematic of the device structure is shown in **Figure 61a**. To fabricate the devices, 1 μm long WNR arrays were etched across the entire width of the WSe_2 channel regions. For comparison, WNRs were etched using the FIBIE process (FIBIE-WNR) as well as milled with no chemical assist (HIM-WNR). The details of the WNRs FET fabrication can be found in the experimental section. The etched regions were patterned in parallel, thus optimizing the total loop time of the process, which enhances the XeF_2 coverage between successive passes. For all FIBIE-WNR devices reported here, the doses required to etch the WSe_2 were $1\text{--}2 \times 10^{17} \text{ He}^+/\text{cm}^2$. However, a dose of $\sim 3 \times 10^{18} \text{ He}^+/\text{cm}^2$ was required to fabricate the HIM-WNR device. **Figure 61b** shows an SEM image of a device with a WNR array spanning the entire channel width. Inset images show the FIBIE-WNR and HIM-WNR arrays at higher magnification. Notably, the FIBIE-WNR array is smooth with well-defined sidewalls. In comparison, the HIM-WNR array has rough texture and sidewalls, presumably due to significant damage introduced into the WNR from the large milling dose required. Additional images of the WNR devices can be found in the supporting information. Transfer curves comparing pristine WSe_2 (solid curves) devices and the FIBIE-WNR and HIM-WNR (dotted curves) devices are shown in **Figure 61c**. Clearly, the FIBIE-WNR device can still be modulated by the bottom gate, but the carrier transport across the channel is suppressed beyond the simple reduction of the channel width. This is likely because edges of the WNRs, as well as defects induced by BS_{He} and recoil atoms in the ribbon, serve as scattering sites for charge carriers. However, the $I_{\text{on}}/I_{\text{off}}$ ratio for the FIBIE-WNR is approximately 10^3 in comparison to 10^1 for a HIM-WNR device. This indicates that the extent of damage introduced into the WNR is far less for the FIBIE process, and illustrates

another advantage of the FIBIE process for nanoribbon formation in comparison to the standard ion milling process, which has historically been used. **Figure 61d** reports the ratio of ON state currents of WNR devices to that of few layer pristine WSe₂ devices as a function WNR widths for both electron transport (red) and hole transport (black) with ± 60 V gate bias. Interestingly, electron transport is suppressed to a greater extent than hole transport for all WNR widths tested. In particular, the 120 nm wide WNR device experiences minimal reduction in the hole conduction (negative gate voltage) relative to the electron conduction. The preferential suppression of electron conductivity may arise from several mechanisms. Tungsten vacancies created in the ribbon during the FIBIE process may suppress electron conduction. This vacancy would act as a highly localized p-type dopant and could act as a trap for electrons¹⁸⁰. Fluorine plasma processing has also been used to p-dope MoS₂¹⁸¹. The incorporation of F can induce charge transfer processes due to its strong electronegativity and behave as a p-type dopant. However, complementary EELS measurements (not shown) taken in the STEM show no indication of F doping within detectable limits. The narrower nanoribbons exhibit a greater suppression in hole and electron conductivity in comparison to thicker ribbons, and this trend is expected to continue for narrower nanoribbons than those reported here (see SI for 25 nm WNRs). This is consistent with the greater number of edge states as well as increased damage induced within the nanoribbon from the FIBIE process. While sub-10 nm resolution is demonstrated, drift correction strategies are necessary for generating larger area sub-10 nm nanoribbon arrays.

He⁺ induced FIBIE enables high-resolution patterning of the WSe₂ at higher etch rates and consequently lower doses. Gas-assisted etch rates were enhanced as much as 10x at large pixel pitch relative to He⁺ milling. However, for optimum resolution and etch rate, a 0.5 nm pitch was used to etch the nanoribbons which resulted in a 5x enhancement. The enhanced etch rate and lower He⁺ dose significantly reduced the peripheral damage. However, the amount of defects introduced into the lattice may still be too great for various optoelectronic applications. We have previously demonstrated that laser-assisted graphene nanoribbon patterning with the He⁺ beam can reduce the defect concentration and improve conductivity over a standard He⁺ milling process¹⁴³. Alternatively, focused electron beam-induced etching (FEBIE) could be used to create nanoribbons with a minor reduction in resolution. FEBIE should result in a significantly

reduced defect concentration introduced into the nanoribbon lattice because electrons are not likely to generate lattice displacements due to their small mass. Therefore, laser-assisted FIBIE and FEBIE provide alternative nano-fabrication processes, which may reduce the defect concentration incorporated within the nanoribbons. Finally, post-nanoribbon annealing in a selenium ambient could reduce the ion induced damage and number of selenium vacancies.

2.3.4 Conclusions

In conclusion, we have developed a focused ion beam induced etching process to pattern WSe₂. This enables the direct-write formation of high-resolution nanostructures in WSe₂ including nanoribbons with a sub-10 nm width. For the XeF₂ mediated FIBIE, lower doses are required to etch the WSe₂ compared to standard He⁺ milling which enable the fabrication of WSe₂ nanoribbons on supported substrates which reduces deleterious subsurface damage and surface swelling. STEM imaging reveals that the WSe₂ nanoribbon edges have high-fidelity, however defects are generated up to 120 nm from the nanoribbon edge from the ion-solid interactions in the sample. The fabricated WSe₂ nanoribbons exhibit high intensity anisotropy of Raman modes. WSe₂ nanoribbon field effect transistors were also fabricated and modulated via a bottom-gate bias. The gas-assisted FIBIE process should enable the simple chemical etching strategy for many 2D TMD materials and the reduction of He⁺ dose required to pattern few-layer TMDs can enable the formation of nanoribbons on supported substrates. Of particular interest, edge sites of TMD nanoribbons can exhibit ferromagnetic properties with zig-zag edge termination. This FIBIE as well as alternative laser-assisted FIBIE and electron beam induced etching processes should allow for further experimental studies of interesting magneto-opto-electronic phenomena.

2.3.5 Methods

2.3.5.1 Focused Ion Beam Induced Etching

Focused ion beam induced etching (FIBIE) was carried out using the Zeiss Orion Nanofab helium ion microscope. This system is equipped with an OmniGIS I gas injection system (GIS). The GIS system delivered precursor molecules into the chamber from a solid XeF₂ source. During the gas injection, the XeF₂ source was cooled to 15°C in order to control vapor pressure. The GIS needle was positioned ~ 100 μm above the substrate and ~ 200 μm radially from the center of the microscope's field of view. All FIBIE experiments were conducted with a

XeF₂ partial pressure of $\sim 5\text{-}6 \times 10^{-6}$ Torr. Helium ions (He⁺) were generated with an acceleration voltage of 25 kV. The beam current was held constant for all exposures at 1.7 pA and was controlled by using a 20 μm aperture and changing the spot number keep a constant current. All exposure patterns were generated using the NanoPatterning and Visualization Engine (NPVE) pattern generator produced by Fibics Inc.

Nanoribbons were fabricated using a parallel exposure strategy. Each array consisted of multiple rectangular etch patterns with equal spacing, and during FIBIE each rectangular pattern would be exposed to a single pass before the next one would begin. A 100 ns He⁺ dwell time was used in order to work in a more reaction-rate limited regime. Visual endpoint monitoring was used to determine when the etch process was completed and the patterning was subsequently terminated to prevent severe over etching in the underlying SiO₂. Additional details are provided for the visual endpoint monitoring in the following section.

2.3.5.2 Visual Endpoint Monitoring

In order to track the progress of the FIBIE process, videos were recorded and the detector secondary electron (SE) collection was monitored to reveal the doses required to mill through the WSe₂ and underlying SiO₂, as a method of visual endpoint monitoring (VEM). The contrast of the HIM image is dependent upon the material's SE yield (γ_{SE}), among other factors such as sample geometry. Material with a greater γ_{SE} will emit more SEs under He⁺ irradiation and results in a higher brightness. Conversely, materials with a smaller γ_{SE} will emit less SEs and results in a lower brightness. Changes in the contrast of the HIM images during the FIBIE process were used to determine when material etching was complete. Frames of a typical video recorded during FIBIE are shown in the Supporting Information (**Figure 62**). The dose required to complete the etch process can be determined based on the etch time determined in the videos multiplied by the beam current and divided by the elementary charge and patterning area.

The dose to completely mill through *any portion* of the pattern area and the dose to completely mill through the *entire portion* pattern area were recorded for all etching experiments. This dose was determined by the aforementioned endpoint monitoring of the secondary electron current traces and detailed image analysis of the frame-by-frame videos that were recorded. The dose values were averaged to determine the etch yield and the standard error was calculated and displayed as error bars in **Figure 57**.

2.3.5.3 WSe₂ Field Effect Transistor Device Fabrication

Single crystal WSe₂ flakes were exfoliated onto SiO₂ (290 nm)/Si (heavily doped Si which also serves as a bottom gate electrode) substrate from a bulk WSe₂ single crystal by the ‘Scotch tape’ micromechanical cleavage technique and were identified by their optical contrast. The thicknesses of the exfoliated WSe₂ flakes were measured using an Atomic Force Microscope (AFM). Standard e-beam lithography followed by e-beam evaporation was employed to create the source/drain electrodes for electrical measurements. The contacts consisted of Ti/Au (5/30 nm) metals deposited and subsequently patterned via a lift-off process. The electrical characteristics of the fabricated WSe₂ devices were measured using an Agilent semiconductor parametric analyzer (Agilent Tech B1500 A).

All nanoribbon arrays were fabricated across the entire channel width of the device and with a length of 1 μm . The He⁺ beam conditions of 100 ns dwell time and 0.25 nm pixel pitch were used. Since all of the nanoribbons were patterned in parallel, this resulted in reaction rate limited etching. The XeF₂ flux to the surface of the FET was approximately $1.6 \times 10^{17} \text{ cm}^2 \text{ s}^{-1}$ for all WNR fabrication.

2.3.5.4 Raman Measurements

Raman spectroscopy was performed in a Renishaw inVia micro-Raman system using a 532 nm excitation laser. A 100 \times magnification objective was used for spectral acquisition with a 10 s acquisition time and three acquisitions were averaged together. The laser spot size was approximately 0.6 μm . WSe₂ nanoribbon arrays were incrementally rotated with respect to the polarization axis of the Raman instrument in order to observe the anisotropy of the E_{2g}¹ Raman peak. Data analysis was conducted with the WIRE v3.4 software.

2.3.5.5 STEM Imaging

All STEM microscopy was carried out using a Nion UltraSTEM 200 operating at an accelerating voltage of 200 kV. Flakes of WSe₂ were exfoliated from a bulk crystal on onto films on continuous α -carbon film grids. The sample was baked at 160 $^{\circ}\text{C}$ in an inert atmosphere for 9 hours directly prior to imaging. The few-layer WSe₂ images consist of averaging 20 frames each 512 x 512 pixels with a 4 μs dwell time per pixel.

2.3.5.6 Monte Carlo Damage Simulations

We study the subsurface damage associated with milling by means of our EnvizION simulation code^{103,177–179}. EnvizION simulates the ion stopping and recoiling process using a Monte-Carlo based method similar to SRIM-TRIM¹⁵⁰, with compound energetics based on TRIDYN^{182,183}. We simulated the average nuclear energy deposited per ion, measured as the density of nuclear energy lost in elastic collisions between ions/recoil atoms and target atoms. We simulate the three dimensional deposited nuclear energy as the average per ion of 10 million He^+ ions, with an initial He^+ energy of 25 keV, on a 10 nm layer of WSe_2 on top of a 15 nm layer of carbon and on top of a bulk silicon substrate. To estimate the total subsurface damage, we then raster each of these profiles in a 15 nm by 1 μm in-plane (x-y) pattern, at density dose of 3×10^{17} ions/ cm^2 . Note that this method may over-predict subsurface damage particularly in the thin sample since cumulative sputtering is not taken into account: as material is removed, the WSe_2 layer becomes thinner, which would tend to allow ions to pass more easily into the carbon layer, or out the other side of it.

2.3.6 Appendix

2.3.6.1 Supporting Information

Visual Endpoint Monitoring

In order to track the progress of the FIBIE process, videos were recorded and monitored to reveal the doses required to mill through the WSe₂ and underlying SiO₂, as a method of visual endpoint monitoring (VEM). The contrast of the HIM image is dependent upon the material's secondary electron (SE) yield (γ_{SE}), among other factors such as sample geometry. Material with a greater γ_{SE} will emit more SEs under He⁺ irradiation and results in a greater brightness. Conversely, materials with a smaller γ_{SE} will emit less SEs and results in a lesser brightness. Changes in the contrast of the HIM images during the FIBIE process were used to pinpoint when material etching was complete. Frames of a typical video recorded during FIBIE are shown in **Figure 62**. Dose required to complete the etch process can be determined by based on the etch time determined in the videos and factors such as beam current, pixel pitch, and dwell time. This method, along with AFM measurement of the WSe₂ flake thickness, was used to determine the etch yields reported in **Figure 57** of the main text.

25 nm WNR Device Performance

The pristine device (**Figure 66c**) had abnormally low electron conduction. Consequently, the measured WNRs exhibited an anomalously high $I_{WNR}/I_{pristine}$ and thus we did not include this in **Figure 61** (however, the hole transport ratio follows the trend shown in **Figure 61**).

2.3.6.2 Figures

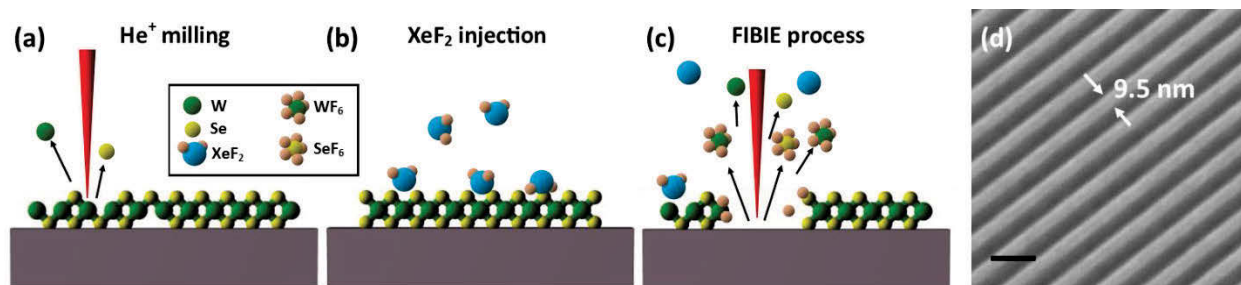


Figure 56. Schematic of (a) a He⁺ milling process, (b) XeF₂ gas injection, and (c) focused ion beam induced etching of WSe₂. (d) SEM image of WSe₂ nanoribbons created with the FIBIE process. Scale bar is 40 nm.

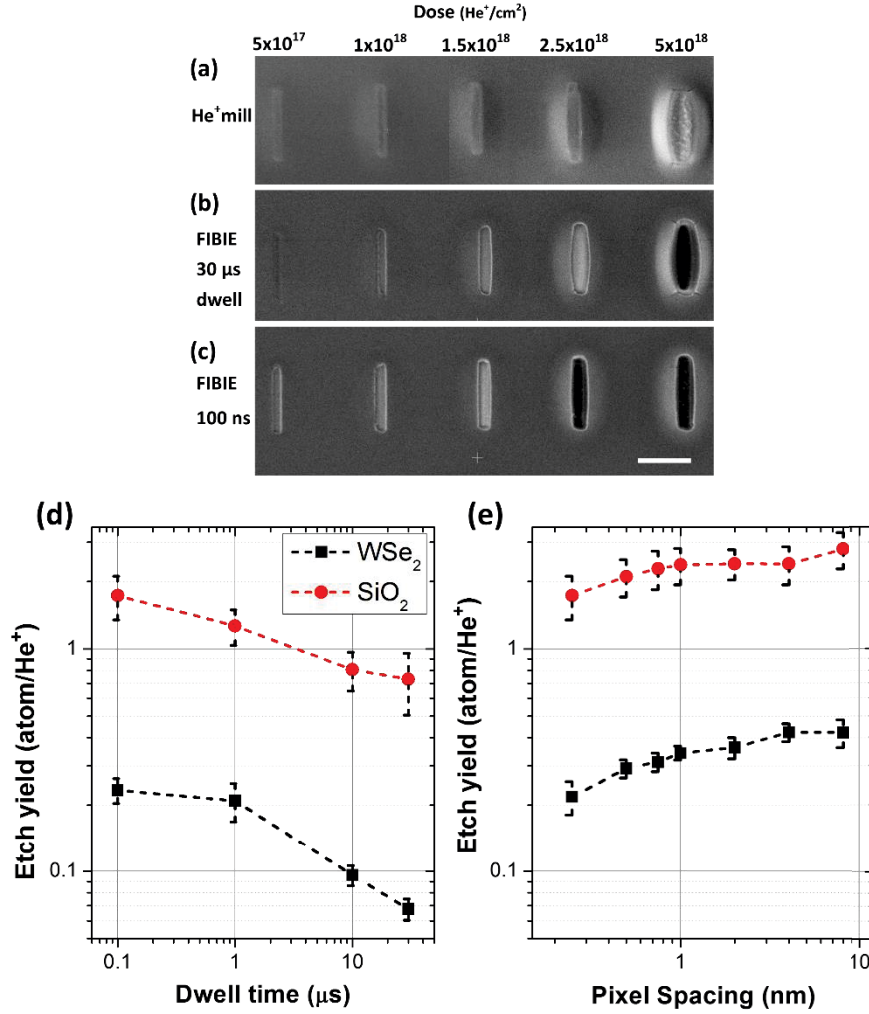


Figure 57. (a) SEM image of He⁺ milling of ~24 nm thick WSe₂ at doses ranging from 5x10¹⁷ – 5x10¹⁸ He⁺/cm². Scale bar is 400 nm. (b) FIBIE of WSe₂ with He⁺ dwell time of 30 μs. (c) FIBIE of WSe₂ with He⁺ dwell time of 100 ns. All patterns are 50 nm x 500 nm. (d) Etch yield of the FIBIE process as a function of dwell time for WSe₂ as well as SiO₂. (e) Etch yield of the FIBIE process at a constant 100 ns dwell time as a function of patterning pixel spacing.

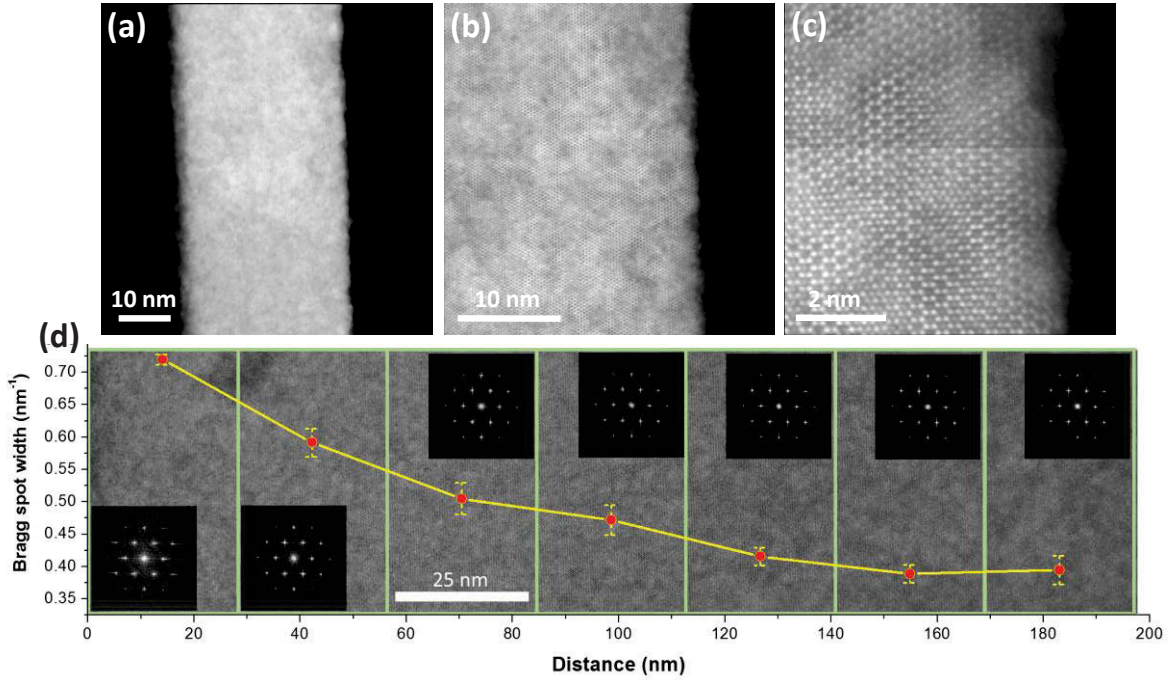


Figure 58. HAADF STEM images of a WNR. (a) Macro image of a single ribbon. (b-c) High-resolution images of the ribbon edge showing high crystallinity in close proximity to the etched surface. (d) Fourier transformations of 10 nm x 10 nm sub-areas were performed and the width of {110} type reflections were measured in units per nm. Six measurements from each sub-area were used to find the average spot width and standard deviation. We use this width as the measure of crystallinity. The broadening of the reflection indicates that the crystal has been perturbed by the helium ion irradiation. After about 120 nm, the value of the unperturbed crystal is reached.

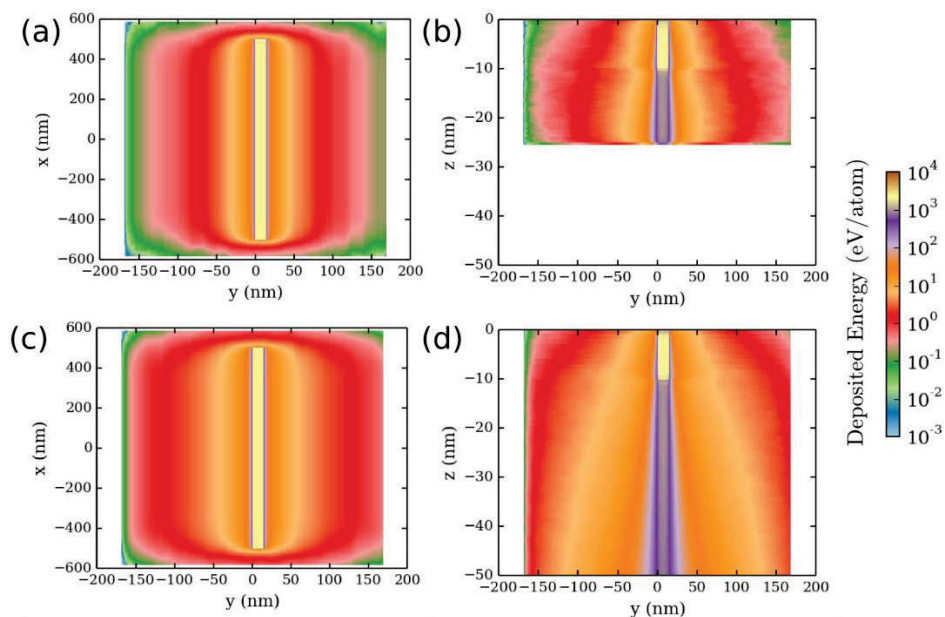


Figure 59. Simulated (a) aerial view (x-y plane) and (b) cross-section (y-z plane) of the deposited nuclear energy, associated with scanning a 25 keV He^+ ion beam on a WSe_2 layer occupying the top 10 nm, with a 15 nm thick carbon layer underneath. The equivalent areal dose is $3.0 \times 10^{17} \text{ He}^+/\text{cm}^2$. The simulation domain and He^+ dose correspond to the experimental conditions used in Figure 58. Note that the plot is on a log scale. (c) Aerial view (x-y plane) and (d) cross-section (y-z plane) of the deposited nuclear energy into 10 nm of WSe_2 on top of a bulk Si substrate. The scan parameters are 15 nm by $1 \mu\text{m}$.

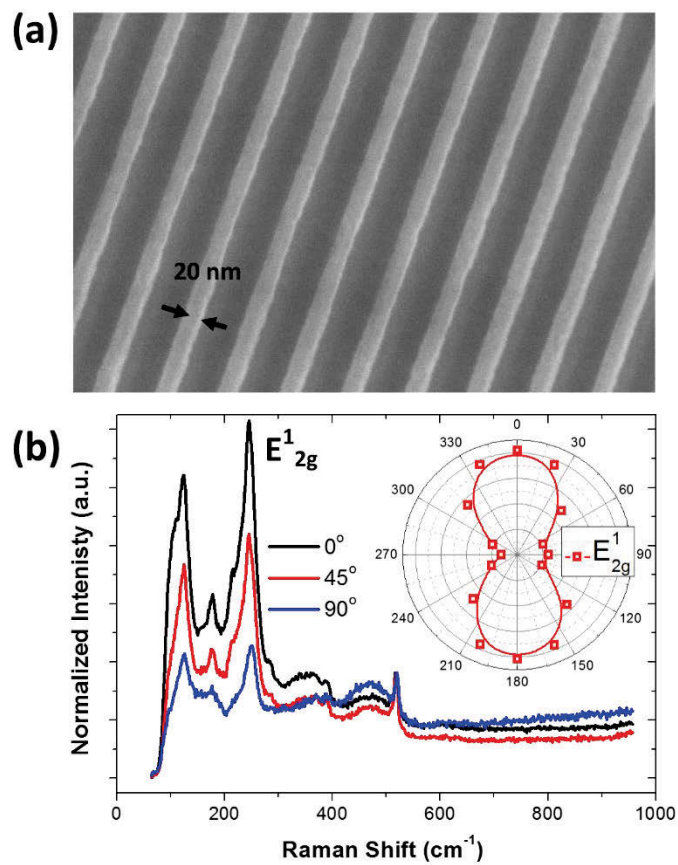


Figure 60. (a) SEM image of an array of 20 nm WNRs. (b) Raman spectra of WNR array normalized to the Si peak as a function of angle between polarization angle of the incident laser spot and the nanoribbon direction. The angular dependence of the Raman anisotropy of the E_{2g}^1 mode is shown in the inset.

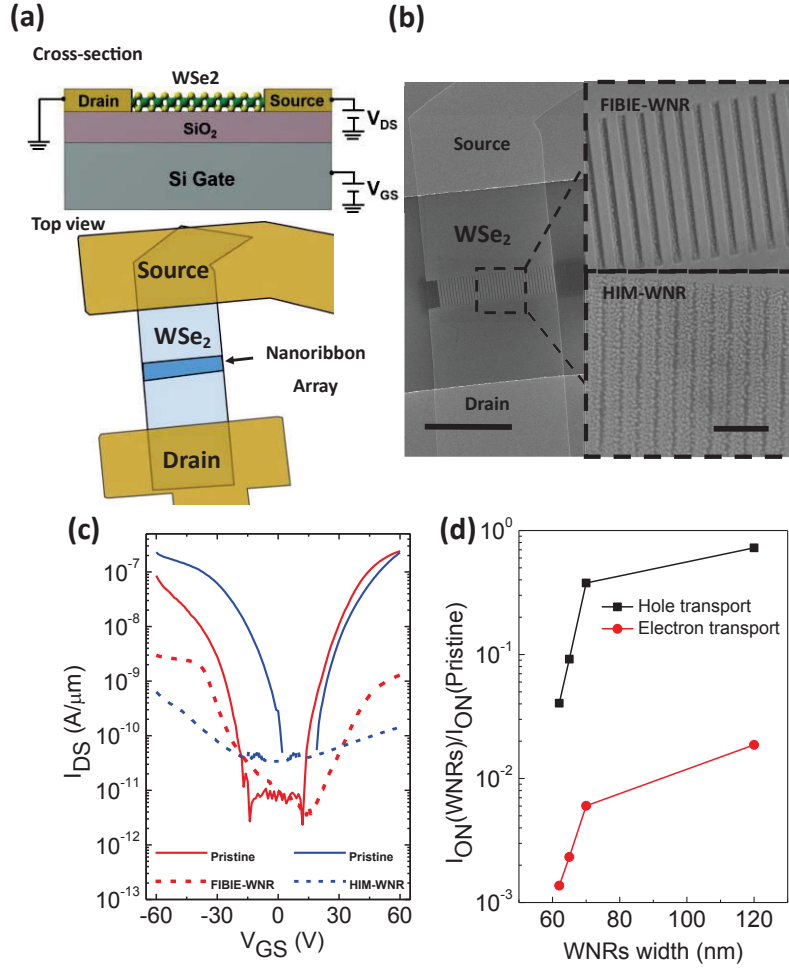


Figure 61. (a) Schematic of WNR TFT from side and top view. (b) SEM image of a FET device fabricated with an array of WNRs which are 1 μm long. Scale bar is 3 μm. Inset are SEM images of WNR devices fabricated using standard He⁺ milling (HIM-WNR) and the FIBIE process (FIBIE-WNR). Scale bar is 300 nm. (c) Normalized channel currents as a function of gate bias (I_{DS} vs V_{GS}) for pristine WSe₂ (solid curves) and HIM-WNR and FIBIE-WNR (dotted curves) devices. The effective channel width of FIBIE-WNR devices are normalized to fill factor. (d) Ratio of ON state currents of the FIBIE-WNRs to that of pristine WSe₂ devices as a function WNRs widths for both electron transport (red) and hole transport (black). The ON state currents for electron are measured at +60 V gate bias, while for hole are measured at -60 V gate bias with 1.0 V source-drain excitation.

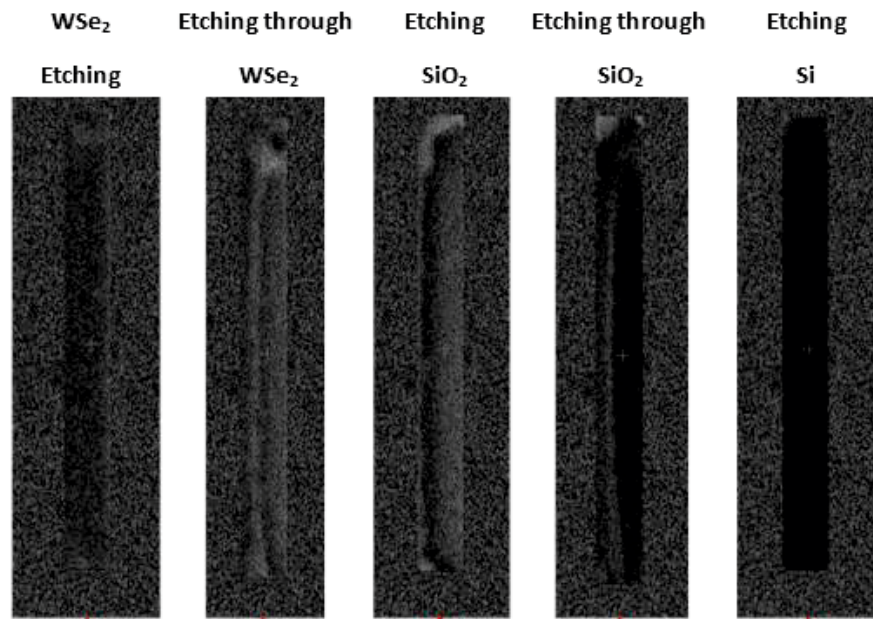


Figure 62. Helium ion microscope images of frames from video recorded during FIBIE to monitor etch progress. Timestamp of frames are used to determine etch dose and hence etch yield.

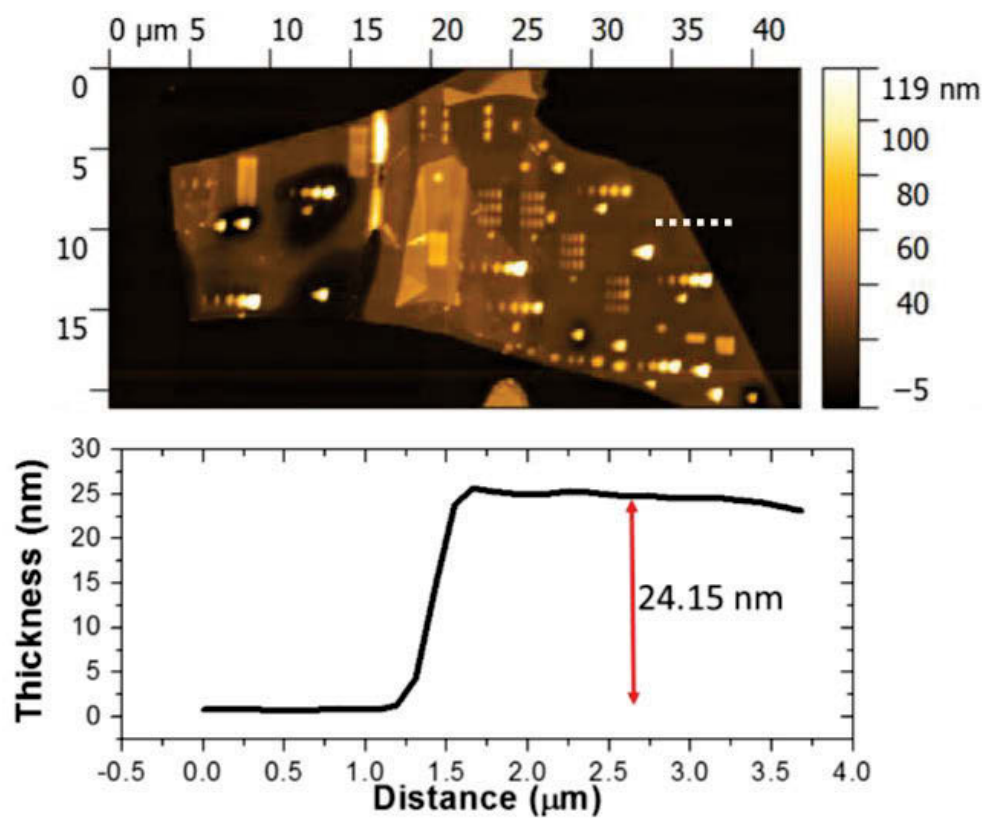


Figure 63. AFM image of flake where milling experiments were conducted. A thickness line profile is displayed which shows that flake thickness was approximately 24.15 nm.

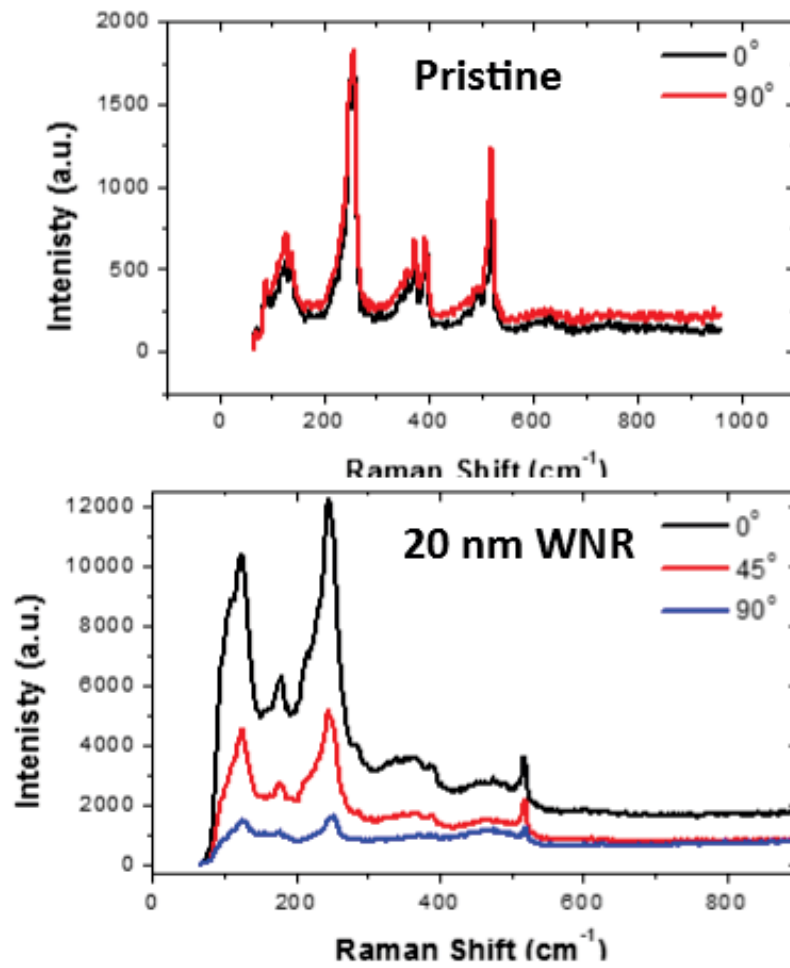


Figure 64. Raman spectra for a pristine WSe₂ flake as well as Raman spectra for 20 nm WNRs as different orientations to the polarized laser source axis. Significant Raman anisotropy is observed for the WNRs but not for the pristine WSe₂.

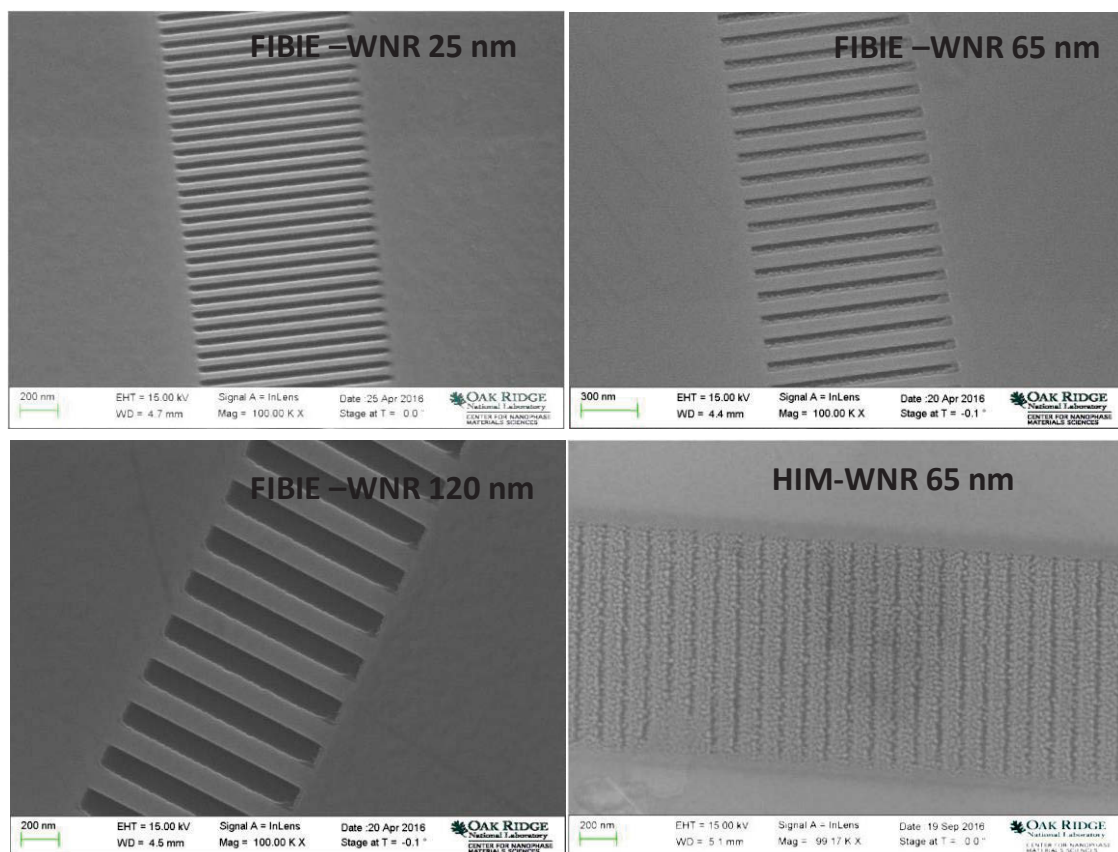


Figure 65. SEM images of three FIBIE-WNR devices and a HIM-WNR device. The nanoribbon widths shown here are 120, 65, and 25 nm.

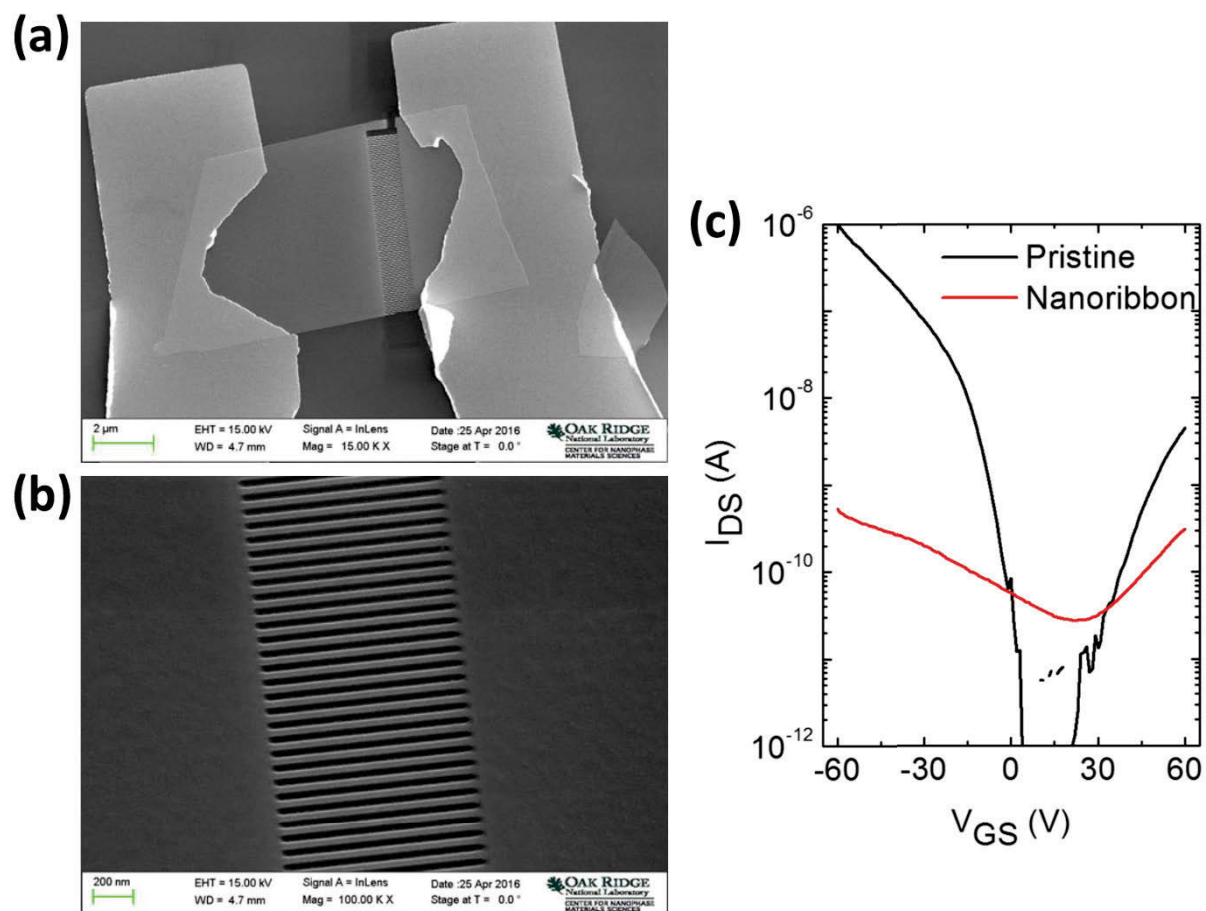


Figure 66. (a) SEM image of a WNR device composed of an array of 25 nm WNRs. (b) SEM image of the WNR array. (c) Transfer curve of the transistor before (pristine) and after the fabrication of the 25 nm aligned WNR array.

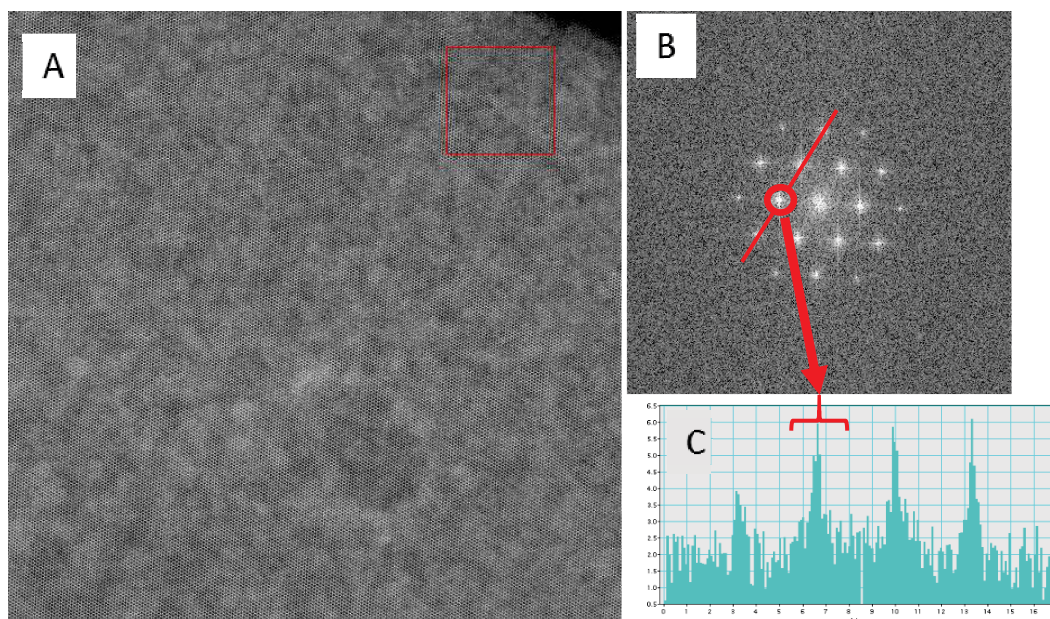


Figure 67. (a) 64 nm x 64 nm HAADF image analyzed for the disorder measurements. The red square, 10nm x 10 nm, is arbitrarily placed and represents the sub-area used to find specific spatial information from within the total image. (b) Fast Fourier transforms (FFT) of the sub-area with the -110 reflection circled and the red line marking the path of the intensity profile. (c) FFT Intensity profile. The width of these peaks are used as the measure of material order/disorder.

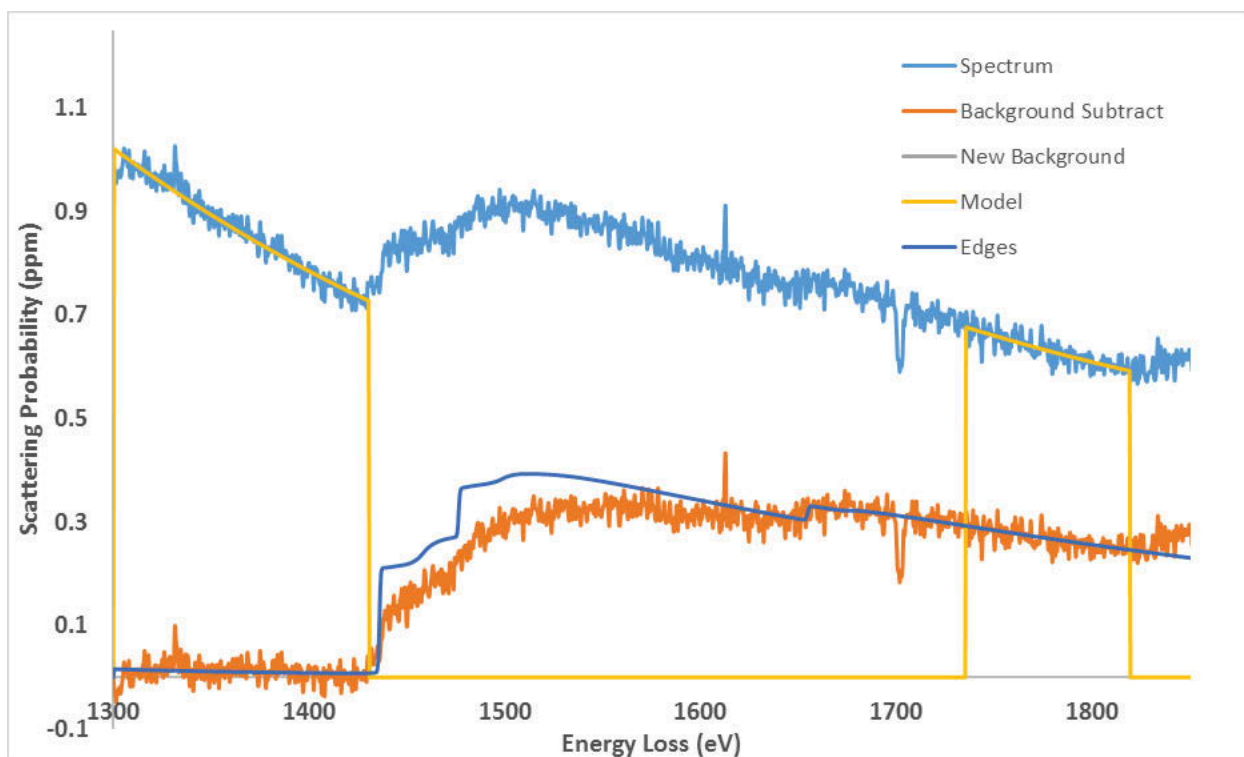


Figure 68. EELS from the WNR on amorphous carbon membrane. Integrating under the Se $L_{2,3}$ Edge we get that Se is 712 Se atoms/nm² and Se in WSe₂ with P6/mmc symmetry has a volume density of 65.9 Se atoms/nm³. The layer density is 44.8 Se atoms/nm². It was determined the WSe₂ flake thickness shown in STEM images was approximately 10 nm.

2.3.6.3 Tables

Table 7. Estimated XeF₂ and He⁺ parameters for FIBIE processes with 30 μs and 100 ns dwell times with a 0.25 nm pixel pitch and for a FIBIE process with a 100 ns dwell time and a 4.0 nm pixel pitch.

	30 us dwell, 0.25 nm pitch	100 ns dwell, 0.25 nm pitch	100 ns dwell, 4.0 nm pitch
Localized XeF ₂ flux	1.6x10 ¹⁷ cm ² s ⁻¹	1.6x10 ¹⁷ cm ² s ⁻¹	1.6x10 ¹⁷ cm ² s ⁻¹
Monolayer coverage time	8.4x10 ³ μs	8.4x10 ³ μs	8.4x10 ³ μs
Refresh time (loop time)	1.2x10 ⁷ μs	4.0x10 ⁴ μs	1.6x10 ² μs
Ions per pixel per pass	320 ions	1.1 ions	1.1 ions
Ions per WSe ₂ surface site per pass	380 ions	1.3 ions	4.9x10 ⁻³ ions
Ions per nm ³ etched	730 ions	210 ions	120 ions

Table 8. the doses required to etch through the WSe₂ and SiO₂ at various dwell times. These values were extracted by analysis of the VEM as well as correlation with recorded videos of the etch process.

Dwell time	WSe ₂ etch dose (He/cm ²)	SiO ₂ etch dose
100 ns	5.50E+17	1.79E+18
1 us	8.70E+17	2.23E+18
10 us	1.80E+18	2.40E+18
30 us	2.00E+18	2.80E+18

CHAPTER III
TUNABLE MATERIAL PROPERTIES VIA DEFECT ENGINEERING IN
2D MATERIALS BY ION BEAM IRRADIATION

3.1 Focused Helium-Ion Beam Irradiation Effects on Electrical Transport Properties of Few-Layer WSe₂: Enabling Nanoscale Direct Write Homo-junctions

A version of this chapter was originally published by M. G. Stanford et al.:

Stanford, M. G.; Pudasaini, P. R.; Belianinov, A.; Cross, N.; Noh, J. H.; Koehler, M. R.; Mandrus, D. G.; Duscher, G.; Rondinone, A. J.; Ivanov, I. N.; et al. Focused Helium-Ion Beam Irradiation Effects on Electrical Transport Properties of Few-Layer WSe₂: Enabling Nanoscale Direct Write Homo-Junctions. *Sci. Rep.* 2016, 6, 27276.

Michael G. Stanford conducted experiments and performed analysis reported in this work. Michael G. Stanford also wrote the manuscript. Pushpa Pudasaini fabricated electrical devices and performed characterization. Kyle Mahady conducted Monte Carlo simulations. Nicholas Cross and Gerd Duscher perform scanning transmission electron microscopy. David Mandrus synthesized the WSe₂. All co-authors contributed to manuscript revisions.

3.1.1 Abstract

Atomically thin transition metal dichalcogenides (TMDs) are currently receiving significant attention due to their promising opto-electronic properties. Tuning optical and electrical properties of mono and few-layer TMDs, such as tungsten diselenide (WSe₂), by controlling the defects, is an intriguing opportunity to synthesize next generation two dimensional material opto-electronic devices. Here, we report the effects of focused helium ion beam irradiation on the structural, optical and electrical properties of few-layer WSe₂, via high resolution scanning transmission electron microscopy, Raman spectroscopy, and electrical transport measurements. By controlling the ion irradiation dose, we selectively introduce precise defects in few-layer WSe₂ thereby locally tuning the resistivity and transport properties of the material. Hole transport in the few layer WSe₂ is degraded more severely relative to electron transport after helium ion irradiation. Furthermore, by selectively exposing material with the ion beam, we demonstrate a simple yet highly tunable method to create lateral homo-junctions in

few layer WSe₂ flakes, which constitutes an important advance towards two dimensional optoelectronic devices.

3.1.2 Introduction

Two-dimensional transition-metal dichalcogenides (TMDs) have recently garnered interest due to their novel electronic and optoelectronic properties and provide promise for next generation device technologies. TMDs belong to the MX₂ family where M = W, Mo, or Nb and X = Se, S, or Te.^{184,185} Much of the interest in TMDs is fueled by the presence of a band gap, which enables the creation of atomically thin semiconductor devices that are otherwise difficult to fabricate from intrinsically gapless materials such as graphene.

Single layer WSe₂ has a direct band gap of ~1.67 eV¹⁸⁶ and an indirect band gap of ~1.2 eV¹⁸⁷ in the bulk, which is in the visible spectrum. High quality WSe₂ films can be easily fabricated by mechanical exfoliation from single crystal down to a single, or a few layers. Exfoliated WSe₂ layers have been successfully used in thin-film transistors¹⁸⁸, electrostatically gated light emitting diodes^{189,190}, and electrostatically gated photodiodes¹⁹¹ to name a few. Chemical vapor deposition (CVD) growth has been used to create large area synthesis of TMD monolayers¹⁹² as well as lateral heterojunctions between TMDs of different composition.¹⁹³ This advance has allowed the realization of devices with precisely controlled thicknesses to be functionalized by lateral junctions^{193,194}.

Tuning of defects within TMD devices serves as an alternative method to vary electronic and optoelectronic properties. Irradiation with charged particle beams allows precise control of defect generation by altering beam conditions and exposure dose. Kim et al. demonstrated the use of a high energy proton beam to introduce trap states in the back gate dielectric of a MoS₂ thin-film transistor¹⁹⁵. Tongay et al. have used α -particle irradiation to generate vacancies in TMDs, which introduce new emission peaks and enhance photoluminescence intensity¹⁹⁶. Fox et al. have demonstrated the use of a focused helium-ion beam to pattern MoS₂ as well as preferentially sputter sulfur atoms.¹⁹⁷ The local tuning of opto-electronic properties of mono and few-layer TMDs can provide an excellent opportunity to realize sharp homo-junctions similar to conventional p-n, p-i-n, or p-n-p junctions, which are critical to many device architectures. The p-n junction diodes are particularly important because the built-in potential at the junction separates the photo-generated electron-hole pairs, which subsequently migrate to the respective

electrodes, leading to higher photo-current at zero bias. Both vertical and lateral, homo- and hetero- p-n junctions have been realized in many TMDs by chemical doping^{198,199}, electrostatic doping^{189–191}, and material engineering.^{193,200,201} However, chemical doping may require capping layers, or additional lithographic steps, adding complexity to device fabrication, whereas the electrostatic doping brings many challenges for nanoscale modification.

In this study, we selectively introduced defects in few-layer WSe₂, including chalcogen vacancies, by irradiation with a focused He⁺ beam. Signatures of induced disorder are apparent in the measured electronic and optoelectronic properties. Specifically, He⁺ irradiation of WSe₂ causes a semiconductor – insulator – metallic transition with increasing dose due to induced disorder and preferential sputtering of selenium atoms. Ambipolar conduction of WSe₂ transistors is quenched at an exposure dose of 1×10^{15} He⁺/cm², thus the defects generated by He⁺ exposure effectively act as a highly tunable method to direct write n-type dopants. We have demonstrated selective He⁺ irradiation within a few-layer WSe₂ flake as a novel method to introduce an optically active homo-junction, similar to a conventional p-n junction.

3.1.3 Results and Discussion

Figure 69a illustrates Raman spectra for exfoliated few-layer WSe₂. The longitudinal acoustic (LA) mode at the M point of the Brillouin zone (LA(M)) is particularly interesting as this peak is associated with defect generation and disorder within the lattice,^{202,203} analogous to the D band in graphene. As the He⁺ irradiation dose increases, the intensity of the LA(M) peak increases and also shifts from ~ 118 cm⁻¹ to 124 cm⁻¹, thus indicating defect generation in the WSe₂. A spatially resolved Raman map of the LA(M) peak intensity is shown superimposed on an optical micrograph in **Figure 69b**. The rise in intensity of the LA(M) peak confirms direct-write defect generation in WSe₂ by He⁺ irradiation. **Figure 69c** is a line plot of the LA(M) peak intensity across the WSe₂ flake. The intensity of the LA(M) peak correlates with the irradiation dose and indicates that greater He⁺ doses introduces greater disorder within the flake. Due to resolution limits of micro-Raman, the generated exposure patterns were relatively large (> 4 μm) relative to the resolution limits of the He⁺ microscope (1 nm). Thus, direct-write defect generation on the nanoscale straightforward, though proximal disorder from the backscattered ion beam, in the case of supported samples, must be considered^{115,11}. Additional Raman spectra and peak assignments may be found in the Supporting Information.

Figure 70 shows HAADF STEM images of suspended few-layer WSe₂ irradiated with various doses of He⁺. **Figure 70a**, shows that a dose of 2×10^{13} ions/cm² has little effect on the single crystal structure of the exfoliated WSe₂, which appears relatively free of point defects. As the dose increases to 1×10^{15} and 1×10^{16} ions/cm² in **Figure 70b-c**, signs of disorder in the film become evident and result in a semi-crystalline WSe₂ film. When the dose is increased to 1×10^{17} ions/cm² (**Figure 70d**), the films becomes significantly disordered. Additional STEM images can be found in the Supporting Information. Inset SAED patterns show broadening of diffraction spots with increasing He⁺ dose, however the position of the distinct spots did not change indicating that the overall orientation and phase of the WSe₂ did not change. Results from Z-contrast imaging and SAED both show a trend towards increasing disorder of the lattice structure as ion dosage is increased. This disorder can be considered an increased amount of point defects, consistent with the Raman spectra. However, only the 1×10^{17} He⁺/cm² SAED pattern has significant contributions from random scattering events and broadened Bragg spots, which suggest increased disorder in the crystalline periodicity. This indicates a significant change in crystal structure with a 1×10^{17} He⁺/cm² exposure dose. This is likely due to increasing selenium vacancies degrading short-range order in the material, which is confirmed by EDS chemical composition analysis detailed in Supporting Information, and agrees with previous work¹⁹⁷. It is worth noting that backscattered He⁺ will have a negligible effect on the defect generation in the suspended WSe₂, since the ions pass through the film and into vacuum. In contrast, substrate-supported WSe₂ will experience collisions from backscattered ions, which expedites the formation of the point defects.

The effects of He⁺ irradiation on electrical transport properties of mechanically exfoliated few-layer WSe₂ films were studied using a field effect transistor (FET) configuration. **Figure 71a** shows a schematic of a WSe₂ FET device on SiO₂/Si substrate with symmetric Ti/Au contacts. **Figure 71b** is an optical image of a fabricated device. The AFM micrograph and height profile of one of the devices are shown in **Figure 71c**. Few-layer WSe₂ FET devices with flake thicknesses ranging from 7 – 26 nm were used in this study. The devices were irradiated with different He⁺ doses ranging from 1×10^{13} to 1×10^{17} He⁺/cm² with the Zeiss ORION NanoFab He/Ne ion microscope with the beam conditions as described in the experimental section. **Figure 71d** shows the transfer curves at two different drain-source voltages (black curves for $V_{DS} = -0.1$

V and red curves for $V_{DS} = -1.1$ V) before (solid curves) and after (dotted curves) the He^+ irradiation at a dose of 1.5×10^{15} ions/cm². The measured transfer characteristics clearly show the ambipolar characteristics of the WSe₂ FET device prior to He^+ irradiation, consistent with previous reports.^{204,205} The source-drain current (I_{DS}) increases with an increase in V_{GS} both with positive and negative bias almost symmetrically reaching an ON state current >1 μA , leading the current ON/OFF ratio in excess of 10^6 . The device after He^+ irradiation (dotted curves) has a degraded hole conduction with a six orders of magnitude decrease in ON state current at negative gate bias, while the ON state current for the positive gate bias (electron conduction) decreases by approximately three orders of magnitude. For clarity, a single voltage sweep of the transfer curve (I_{DS} vs V_{GS}) was plotted, however we observed a small hysteresis both before and after He^+ irradiation in WSe₂ FET device (see Supporting Information file **Figure 82**). The field effect mobility of the pristine device (prior to He^+ exposure) shows thickness dependence which agrees with the literature.¹ The maximum field effect hole mobility of 64.13 cm²/Vs was determined for a 9 nm thick device (see Supporting Information **Figure 83** for thickness dependent mobility). The field effect hole mobility of the same device after He^+ ion irradiation was almost negligible (0.0052 cm²/V.s), while there is still small electron conduction. Furthermore, He^+ irradiation effects as a function of WSe₂ film thickness was also studied at a particular dose of 1×10^{15} ions/cm². I-V measurements reveal that irrespective to the WSe₂ channel thickness, both hole and electron conductivity were suppressed. However, hole conduction decreased more than electron conduction, and it shows slightly n-type behavior (increase in channel current with the increase in gate voltage) (see Supporting Information file **Figure 84**). The 25 keV He^+ used in this study is very energetic and easily penetrates the entire thickness of the few-layer WSe₂ channel. We performed EnvizION ion-solid Monte Carlo simulations illustrating the distribution of displaced atoms in WSe₂ films of varying thickness (see Supporting Information file **Figure 85**). The thickest few layer films we tested were 26 nm thick and thus significantly thinner than the He^+ penetration depth which has a peak implant depth of ~ 120 nm in bulk WSe₂. While the energy is slightly dissipated and thus the electronic and nuclear stopping power slightly changed from top to bottom, it is negligible and thus we expect a fairly uniform defect distribution within the material.

Figure 71e is a plot of the resistivity evolution of the mechanically exfoliated few-layer WSe₂ on SiO₂/Si supported architecture as a function of He⁺ dose. We observe three distinct regimes as a function of the He⁺ dose. The initial semiconducting nature of the material changes to insulating behavior with a two order of magnitude increase in resistivity at the He⁺ dose of $\sim 1 \times 10^{14}$ ions/cm² and more than four orders of magnitude increase in resistivity at 1×10^{15} ions/cm². As the dose increases, the resistivity of the device decreases sharply and reaches approximately two orders magnitude lower resistivity than the initial pristine device. At the highest dose, (1×10^{17} ions/cm²) the WSe₂ device completely loses its semiconducting behavior (see the inset in **Figure 71e**) as the current is no longer sensitive to the gate voltage. Similar semiconductor-insulator-metal transitions have been previously reported for MoS₂ layered materials with the He⁺ exposure.¹⁹⁷ An increase in electrical resistivity in layered MoS₂ due to high energy proton beam irradiation has also been reported¹⁹⁵. The electrical resistivity changes of the proton-irradiated MoS₂ was attributed to induced traps, including positive oxide-charge traps, in the underlying SiO₂ gate insulator layer, and the trap states at the interface between the MoS₂ channel and SiO₂ layer. However, in contrast to proton irradiated MoS₂ where the current recovered almost to its original values after five days, our He⁺ irradiated WSe₂ devices do not recover even after a month (see Supporting Information file **Figure 86**).

The observed electrical changes due to the He⁺ irradiation can be understood by considering the structural changes in the few-layer WSe₂ under the He⁺ irradiation. EDS analysis (**Figure 80**) and a previous study¹⁹⁷, show that He⁺ irradiation results in the preferential sputtering of chalcogen atoms. Density Functional Theory calculations suggests that chalcogen vacancies in TMDs result in unsaturated electrons which surround the transition metal atoms and act as electron donors²⁰⁶. In the case of MoS₂, S vacancies act as deep donor states. These states demonstrate high electron mass and strong localization within a 3 Å radius surrounding the vacancy. This results in a nearest-neighbor hopping transport mechanism at room temperature. This is in stark contrast to delocalized electrons in the valence band which are dominated by Mo 4d orbitals.

Analogously, Se vacancies in WSe₂ act as electron donors, and thus an n-type dopant. When irradiated with relatively low He⁺ dose ($1 \times 10^{13} - 5 \times 10^{15}$ ions/cm²), Se vacancies are formed through knock-on collisions. These vacancies create highly localized states which serve

as hole traps. This accounts for the reduced hole conduction in devices which were irradiated with He^+ . Since the near mid gap Se vacancy states are highly localized, electron conduction is not significantly enhanced by He^+ irradiation and scattering at defect sites can explain the slight degradation in electron conduction and increased resistivity. Thus, direct-write introduction of Se vacancies through He^+ irradiation serves as a method to selectively quench hole conduction while permitting electron conduction. At high He^+ dose ($> 1 \times 10^{16}$ ions/cm²), selective Se sputtering greatly increases the W atomic percentage. This enables metallic bonding between neighboring W which increases electron delocalization, hence producing a large drop in electrical resistivity (**Figure 71e**). It is worth noting, oxygen substitution into Se vacancy sites under room temperature ambient conditions may occur, but the rate is slow without supplying additional thermal energy²⁰⁷. We conclude that oxidation of Se vacancy sites does not play a dominant role in influencing the electrical behavior of He^+ irradiated WSe_2 flakes, since device behavior shows minimal changes with time, and Raman spectra do not show signatures of oxidation²⁰⁸.

The selective suppression of hole transport in ambipolar WSe_2 flakes due to He^+ irradiation can generate a homo-junction similar to a conventional p-n junction. The ability to quickly create this structures in a simple, robust, and tunable manner is critical to realizing many opto-electronics devices. Therefore, we selectively irradiated half of the channel area of WSe_2 FET devices. **Figure 72a** shows a schematic of an irradiated device, in which selective introduction of defects are used to create a homo-junction within the WSe_2 flake. **Figure 72b** shows a spatially resolved Raman map of this device, which plots the integrated peak area ratio of the LA(M) peak (which is associated with He^+ induced disorder) to the in-plane E_{2g}^1 main peak. It is clear that He^+ irradiation successfully induced a junction within the material, as revealed by Raman, although the optical micrograph (see inset in **Figure 72b**) shows no visual signature of the irradiation. The electrical transfer characteristic curves of the corresponding device, before and after He^+ irradiation, are shown in **Figure 72c-d**, respectively. Consistent with the previous observation, the hole transport in the material decreased by almost four orders in magnitude. For example, the device ON current was measured as 1.86 μA , at $V_{\text{DS}} = -1.1$ V and $V_{\text{GS}} = -60$ V, prior to He^+ irradiation; whereas after He^+ irradiation, the current was measured as 0.26 nA under the same measurement conditions. In contrast, the transistor ON

current, corresponding to the electron transport in the device, decreases by less than an order of magnitude.

Figure 73a shows a Kelvin Probe Force Microscopy (KPFM) image of a WSe₂ TFT with a homo-junction created within the flake by exposing half of the channel with a dose of 5×10^{14} He⁺/cm². The homo-junction is visible within the channel and the interface is sharp. The junction indicates clear band bending in the vacuum level and represents the difference in work function (Φ) of the exposed and pristine WSe₂. It is worth noting that the scale of the surface potential is offset due to charging effects related to poor grounding of the device, therefore the magnitude of potential differences at the interfaces should be noted as opposed to the absolute magnitude.

Figure 73b is a tapping mode topography AFM image of the same WSe₂ device. The topography of the WSe₂ flake shows no signs of surface alteration as a result of the He⁺ exposure. Hence, the structural integrity of the device remains intact, while the electronic structure is tuned by precisely controlling the exposure dose. **Figure 73c** illustrates a KPFM line scan, along the black dotted line in **Figure 73a**, which shows band bending across the WSe₂ homo-junction. The work function difference between the exposed and pristine regions is ~ 55 mV for a junction created with a dose of 5×10^{14} He⁺/cm². **Figure 73d** depicts a proposed band diagram of the homo-junction created within the WSe₂ device. The exposed region takes on n-type behavior, which limits hole transport, and is experimentally observed in the transport properties (**Figure 72d**). The electrical properties and hence band bending at the homo-junction is tunable by controlling He⁺ dose, as indicated by changes in transport properties with dose (**Figure 71e**).

The photo-response of the lateral homo-junction created in layered WSe₂ due to selective He⁺ irradiation was investigated by utilizing (exposing) a standard microscope white light source. **Figure 74a** shows a log plot for the current-voltage (I_{DS} vs V_{DS}) curves at zero gate bias of the homo-junction without (black) and with (red) white light exposure. Significant improvement in channel current is observed due to the built-in electric potential at the junction. A photovoltaic effect with open circuit voltage of 220 mV is observed (see **Figure 74b**), which is comparable with the lateral homo-junction⁹ and hetero-junction^{11,12} in mono and few-layer WSe₂ and MoS₂ devices, respectively. No significant photovoltaic effect is observed in the pristine WSe₂ device without He⁺ irradiation (see the Supporting Information **Figure 87**). This

confirms the presence of homo-junction in few-layer WSe₂ due to the selective defect introduction from irradiation with He⁺.

To further investigate the effect of He⁺ irradiation on hole transport in few-layer WSe₂, we also fabricated an asymmetric electrode (Pd in one and Ti/Au in the other) device with the favorable energy band alignment for hole collection by minimizing the Schottky barrier between the valence band of the WSe₂ and fermi level of Pd metal electrode. We carried out the electrical transport measurements before (**Figure 75a** and **Figure 75c**) and after (**Figure 75b** and **Figure 75d**) He⁺ irradiation for two different ion doses (1×10^{14} ions/cm² – upper panel and 1×10^{15} ions/cm² – lower panel, respectively). Preferential hole injection in the WSe₂ channel is clearly observed in the asymmetric nature of I_{DS} – V_{DS} curves (see **Figure 75a** and **Figure 75c**) due to the Ohmic contact between the Pd electrode and valence band of WSe₂ flake relative to the apparently small Schottky barrier for the Ti/Au contact. The hole transport is still significantly suppressed compared to electron transport (see **Figure 75b** and **Figure 75d**) in the WSe₂ channel after He⁺ irradiation. For instance, the device ON current decreased from 30 nA (pristine device) to 10 pA at V_{DS} = -1 V and V_{GS} = -60 V, due to He⁺ irradiation at the dose of 1×10^{15} ions/cm².

3.1.4 Conclusions

In summary, we report the effects of focused helium-ions beam irradiation on opto-electronic properties of few-layer WSe₂ devices. Precise defects were selectively introduced in mechanically exfoliated few-layer WSe₂ by controlled dose of He⁺ irradiation, and its effects on structural, optical and electrical properties were investigated via STEM, Raman spectroscopy, and transport measurements. With increasing dose, point defects and local disorder of WSe₂ flake were observed, thereby tuning the electrical transport of the material, and allowing control over semiconductor-insulator-metal like transitions with more than six order change in resistivity. Hole transport in WSe₂ was significantly suppressed compared to electron transport for the same dose of He⁺ irradiation. This presents the unprecedented opportunity to create direct –write lateral junctions in the materials. By selective He⁺ irradiation, we demonstrate a lateral homo-junction, like a conventional p-n junction, with a calculated built-in potential as high as 220 mV, which constitute an important advance towards two dimensional opto-electronic devices.

3.1.5 Methods

3.1.5.1 Helium Ion Irradiation

Helium ion exposures were performed with a Zeiss ORION Nanofab He/Ne ion microscope. An accelerating voltage of 25 keV was used for all exposures. Beam currents were varied from 0.3 – 6.0 pA in order to enable a large range of exposure doses ($1 \times 10^{12} - 1 \times 10^{17}$ ion/cm²). All patterns in this study were exposed with a constant 1 μ s dwell time, whereas the pixel spacing was varied with the desired dose. For low dose exposures ($< 1 \times 10^{14}$ ions/cm²), larger pixel spacing (4 - 40 nm) with beam defocus was utilized to supply a uniform dose to the patterning area. For higher doses ($> 1 \times 10^{14}$ ion/cm²), a pixel spacing of 2 nm was used. Patterns were generated using Fibics NPVE pattern generating software and hardware scan controller.

3.1.5.2 WSe₂ Device Fabrication and Characterization

Polycrystalline WSe₂ was synthesized from a stoichiometric mixture of W (Alfa-Aesar, 99.999%) and Se (Alfa-Aesar, 99.999%) powders. The starting materials were sealed in silica tubes under vacuum, and then slowly heated to 900 °C. The ampoules remained at 900 °C for seven days, and then were allowed to furnace cool to room temperature. Single crystals of WSe₂ were then grown using the polycrystals as starting material and iodine as a transport agent. The silica tubes containing phase-pure powder and iodine were sealed under vacuum and placed in a tube furnace with a 50 °C temperature gradient from the hotter end of the tube containing the charge (1050 °C) to the colder end where growth occurs (1000 °C). The iodine concentration within the tube was ~ 17.5 mg/cm³. Crystals in the form of shiny silver plates with typical size $5 \times 5 \times 0.1$ mm³ grew over the course of 5 days. WSe₂ flakes were exfoliated onto SiO₂ (290 nm)/Si (heavily doped Si which also serves as a bottom gate electrode) substrate from a bulk single crystal by the ‘Scotch tape’ micromechanical cleavage technique and were identified by their optical contrast. The thicknesses of the exfoliated WSe₂ flakes were measured using Atomic Force Microscope (AFM). Kelvin probe force microscopy (KPFM) measurements were performed using an Asylum Research Cypher AFM with a Pt-Ir coated cantilever. Standard e-beam lithography followed by e-beam evaporation was employed to create the source/drain electrodes for electrical measurements. The contacts consisted of Ti/Au (5/30 nm) metals deposited and subsequently patterned via a lift-off process. The fabricated devices were subjected to He⁺ exposures with different doses ranging from 1×10^{12} to 1×10^{17} ions/cm². The

electrical characteristics of the fabricated WSe₂ devices before and after the He⁺ exposure were measured using an Agilent semiconductor parametric analyzer (Agilent Tech B1500 A).

3.1.5.3 Raman Spectroscopy

Raman spectroscopy and mapping were performed in a Renishaw inVia micro-Raman system using a 532 nm excitation laser. A 100X magnification objective was used for spectral acquisition with a 5 second acquisition time. Maps were generated using a 0.6 - 1 μm step size. Data analysis and maps were constructed with the WIRE v3.4 software.

3.1.5.4 Energy Dispersive X-ray Spectroscopy

Energy dispersive X-ray spectroscopy (EDS) was conducted in a Zeiss MERLIN Scanning Electron Microscope (SEM) equipped with a Bruker EDS system. For the EDS measurements, a map acquisition of the He⁺ irradiated WSe₂ film was taken over a $\sim 6 \times 8 \mu\text{m}$ area with a 15 min collection time. A beam energy of 4 keV and beam current of 0.7 nA were used to excite the sample and generate the X-ray spectra.

3.1.5.5 Microscopy

Atomic resolution images of WSe₂ were acquired using a Nion UltraSTEM100 scanning transmission electron microscope with fifth-order aberration correction. STEM was operated at 60 kV with a spatial resolution of 1.1 angstrom. High angle annular dark-field (HAADF) Z-contrast images of suspended WSe₂ were recorded for regions exposed to He⁺ doses of 2×10^{13} , 1×10^{15} , 1×10^{16} , and 1×10^{17} ions/cm². The WSe₂ flake was exfoliated onto a holey silicon nitride membrane with 2.5 μm holes prior to exposure and imaging. SAED patterns were taken after imaging at the same locations with a Zeiss Libra 200MC operated at 200keV.

3.1.6 Appendix

3.1.6.1 Supporting Information

Raman Spectroscopy

Table 9 lists the Raman peak assignments for few-layer WSe₂. The spectra as a function of various exposure doses can be found in **Figure 76**. It is clear that He⁺ exposure causes a reduction in the E_{12g} and A_{1g} peaks, as well all multiplicity peaks. A sharp rise in the LA(M) peak is observed as the He⁺ exposure dose is increases. This is indicative of selective sputtering and defect introduction within the WSe₂ flake.

STEM

Figure 77 displays high-resolution HAADF STEM images of suspended WSe₂ that was irradiated with He⁺ doses from 2×10^{13} – 1×10^{17} ions/cm². There is a significant increase in disorder with increasing He⁺ dose. Clearly, increasing dose introduces greater amounts of disorder and defects into the WSe₂. An indexed SAED pattern is shown in **Figure 78**. **Figure 79** compares the Z-contrast STEM images, Fourier transformations of each respective Z-contrast image, and selected area electron diffraction patterns that correspond to each He⁺ dose which was studied. The Fourier transformations of the Z-contrast images agree well with SAED results.

EDS

Suspended WSe₂ was irradiated with the 30 keV He⁺ beam at various doses (1×10^{15} – 1×10^{18} ions/cm²) and is displayed in **Figure 80a**. Clearly a dose of greater than 5×10^{17} is sufficient to completely sputter away the entire WSe₂ film. Signs of modification of the film are apparent with exposure down to a dose of 5×10^{16} ions/cm². Chemical composition analysis of the irradiated films were conducted using energy-dispersive X-ray spectroscopy (EDS). In order to qualitatively determine compositional changes in the WSe₂ with He⁺ exposure, the relative peak ratios of W - M (1.774 keV) and Se - L (1.379 keV) were compared and reported in **Figure 80b**. With increasing He⁺ exposure, the W composition relative to Se increases. The chalcogen is preferentially sputtered since its atomic mass is nearly 3x less than that of W, and momentum exchange with the energetic He⁺ is sufficient to eject Se atoms. The preferential sputtering in essence enables selective doping of the WSe₂, by creating direct-write chalcogen deficient regions.

Raw EDS spectra for WSe₂ irradiated with He⁺ at doses from $1 \times 10^{12} - 3 \times 10^{17}$ ions/cm² are shown in **Figure 81a**. The spectra were collected by taking an area scan over the entire region exposed by the He⁺ beam. At a dose of 5×10^{17} ions/cm² the He⁺ irradiation completely sputters away the WSe₂ films. The reduction in overall intensity of the EDS spectra with increasing dose is due to material removal, thus making the EDS response weaker. The W/Se intensity ratio increases with increasing He⁺ dose due to preferentially sputtering of Se as shown in **Figure 80b**. **Figure 81b-e** show EDS area maps from which the raw spectra were acquired.

Hysteresis on Transfer Curves

The transfer curves (I_{DS} vs V_{GS}) of all few layers WSe₂ FET device were collected reversibly (double sweep) with the gate voltage ranging from -60 V to +60 V, at different source-drain voltages (V_{DS}). A small hysteresis on the measured channel current (I_{DS}) was observed for the device before and after the He⁺ ion irradiation. A typical hysteresis collected in one of the device studied is shown below, however, transfers curves with a single voltage sweep were reported throughout the manuscript for clarity.

Mobility Thickness Dependence

Field effect mobility was extracted from FETs fabricated from various thicknesses of exfoliated WSe₂ and reported in **Figure 83**. The maximum field effect mobility of 64.13 cm²/V.s for hole conduction for a device with a 9 nm WSe₂ thickness was recorded. At greater thicknesses, the field effect mobility is significantly reduced.

He⁺ Dose Effect on Electrical Transport Properties of Few Layers WSe₂ as a Function of Thickness

The He⁺ irradiation effect as a function of WSe₂ film thickness was also studied at a common dose of 1×10^{15} ions/cm². I-V measurements reveal that irrespective to the WSe₂ channel thickness, both hole and electron conductivity were significantly suppressed (hole conduction decreased more than electron conduction) and it shows slightly n-type behavior (increase in channel current with the increase in gate voltage). Prior to the He⁺ exposure, the ON state currents for both electron (at + 60 V gate bias) and hole (at -60 V gate bias) were on the order of 1 μ A (normalized to channel W/L ratio). The field effect electron mobility in one of the pristine WSe₂ FET devices prior to the He⁺ irradiation was measured to be 32.80 cm²/V.s, which decreased to 0.08 cm²/V.s after the He⁺ irradiation at a dose of 1×10^{15} ions/cm². It is worth

noting that a full channel exposure at this dose ($1 \times 10^{15} \text{ He}^+/\text{cm}^2$) results in insulating behavior of the film. Although the electron mobility was noticeably decreased, electron conduction after irradiation is still far greater than hole conduction.

EnvizION Ion-Solid Monte Carlo Simulation

EnvizION Monte Carlo simulations¹⁰³ were conducted in order to determine atom displacements created by 25 keV energetic He^+ in WSe_2 (ignoring channeling effects). **Figure 85** shows cross-sections of WSe_2 films of varying thickness which were exposed to a dose of $1 \times 10^{15} \text{ He}^+/\text{cm}^2$. Green pixels represent Se atoms, blue pixels represent W atoms, light green pixels represent displaced Se atoms, light blue pixels represent displaced W atoms, and red pixels represent unfilled vacancies created by sputtering events. The distribution of defect sites are largely uniform over the exposed regions and appear to be independent of film thickness, since the films are much thinner than the penetration depth of 25 keV He^+ in WSe_2 . Table 10 list the sputter yield and Se/W sputter ratio at the three WSe_2 thicknesses which were simulated. The simulations support experimental findings which indicate the Se is preferentially sputtered in comparison to W under He^+ irradiation.

Device Aging

Aging effects on a device exposed with a dose of $1 \times 10^{14} \text{ ions}/\text{cm}^2$ was measured over the course of 30 days and displayed in **Figure 86**. The transistor ON current, with a $V_{\text{DS}} = 1.1 \text{ V}$ and $V_{\text{GS}} = 60 \text{ V}$, remained constant during this time period. The lack of ON current recovery suggest that stable defects were formed within the WSe_2 flake and are not simply due to fixed oxide positive charge induced in the underlying substrate, which exhibits a recoverable ON current¹⁹⁵.

Photoresponse in Unexposed Device

Figure 87 shows the output characteristics of pristine WSe_2 devices under dark and light conditions. Unlike the devices which have a direct-write He^+ exposed junction (**Figure 74a**), there is no open circuit voltage (V_{OC}) under light conditions. Currents are slightly greater with light conditions due additional excited charge carriers, however there is no significant photovoltaic effect.

3.1.6.2 Figures

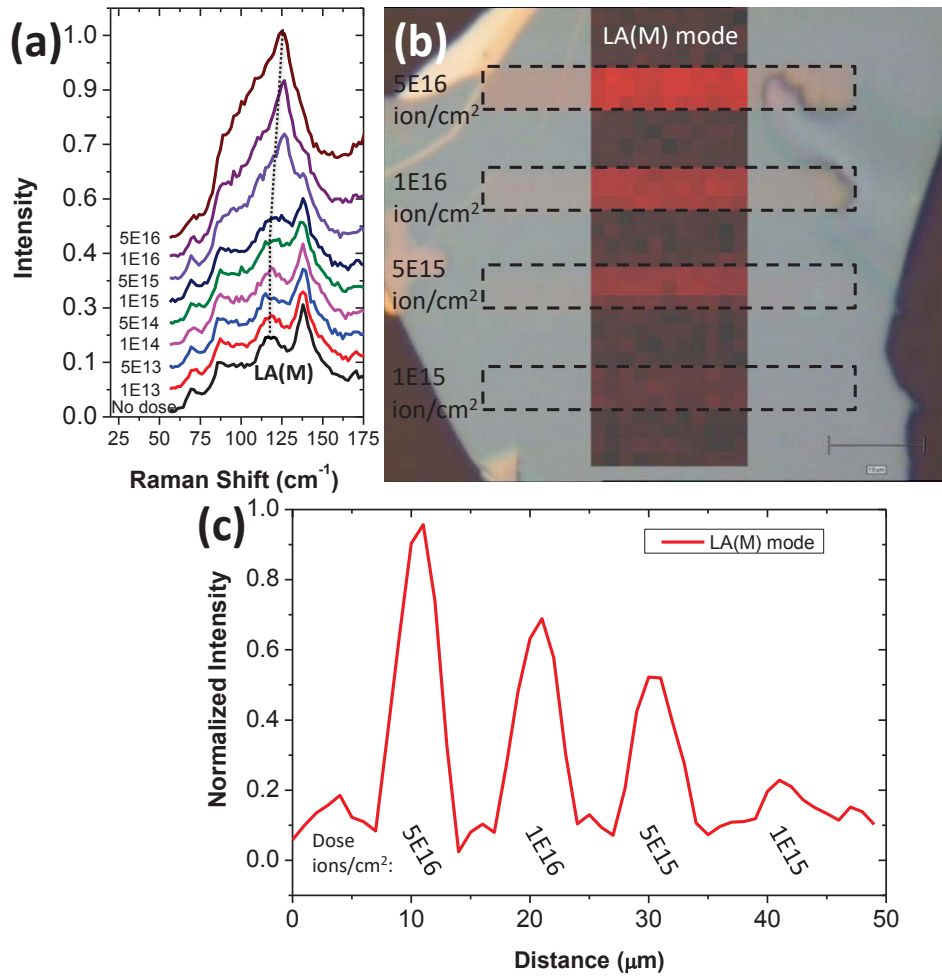


Figure 69. (a) Raman spectra of WSe₂ showing the LA(M) peak at $\sim 118 \text{ cm}^{-1}$. (b) Spatially resolved Raman map of the LA(M) peak superimposed onto an optical micrograph. Rectangular He⁺ exposures on the flake are denoted by inset dotted lines. (c) Normalized intensity of LA(M) mode along a line scan on the patterned WSe₂ flake.

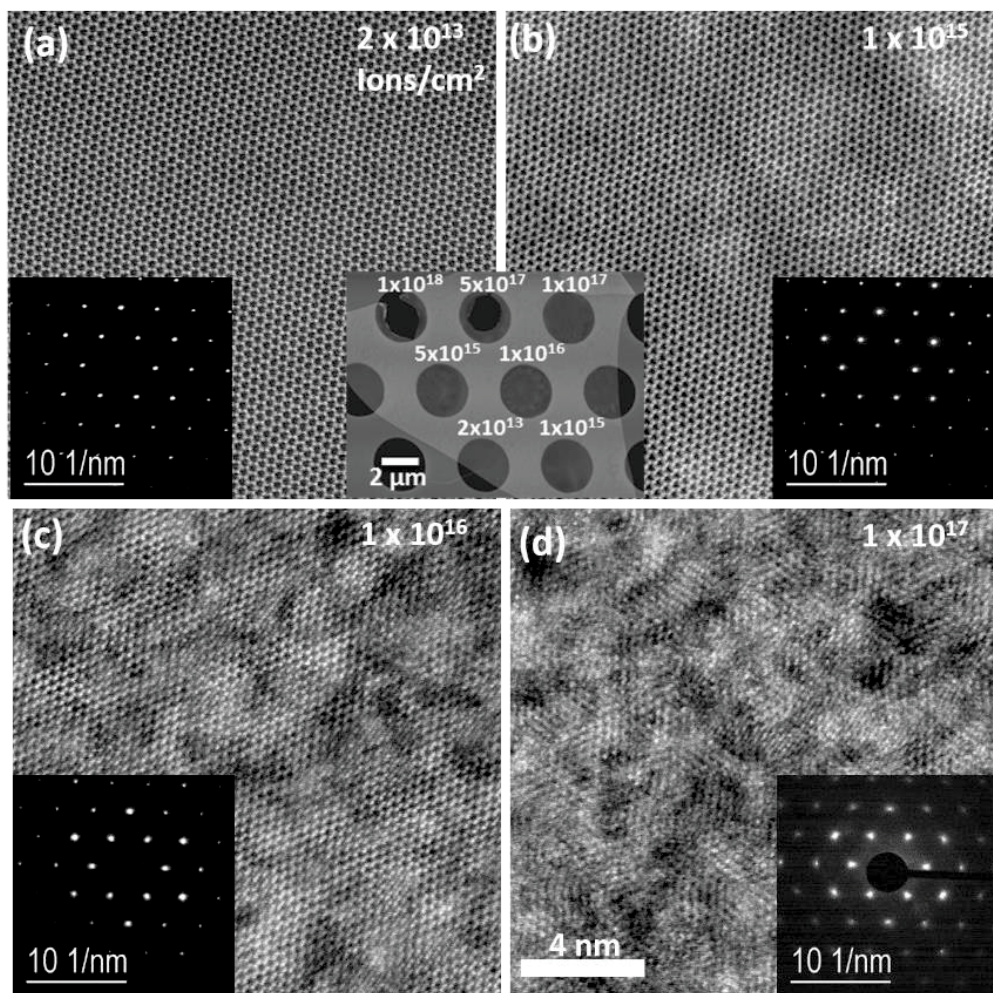


Figure 70. HAADF STEM images of suspended WSe₂ which was irradiated with He⁺ at doses of (a) 2×10^{13} , (b) 1×10^{15} , (c) 1×10^{16} , and (d) 1×10^{17} ions/cm². Field of view is 16 nm. SAED patterns are inset for each exposed dose.

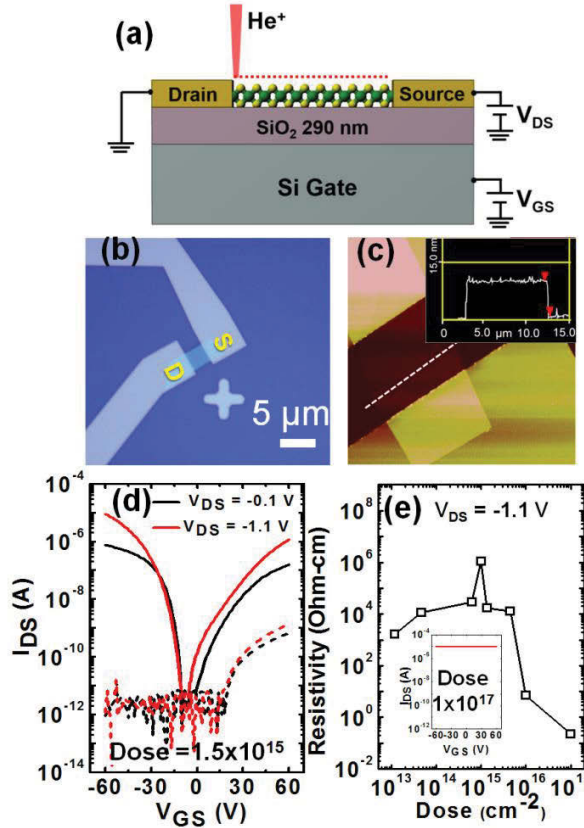


Figure 71. (a) Schematic of the WSe₂ field effect transistor (FET) device irradiated with He⁺. (b) Optical micrograph of the WSe₂ FET on SiO₂/Si substrate. The scale bar is 10 μm. (c) AFM micrograph of the fabricated WSe₂ FET device. The inset represents the height profile along the dotted line shown in the Figure. (d) The transfer characteristics (I_{DS} vs V_{GS}) at two different drain-source voltages (black curves for $V_{DS} = -0.1$ V and red curves for $V_{DS} = -1.1$ V) before (solid curves) and after (dashed curves) He⁺ irradiation at a dose of 1.5×10^{15} ions/cm² on WSe₂ channel region. The measured transfer characteristic clearly shows the ambipolar characteristics of the WSe₂ FET device before He⁺ irradiation, while the device after He⁺ irradiation loses its p-type characteristics. (e) Double log plot of electrical resistivity as a function of He⁺ irradiation dose for mechanically exfoliated few layers WSe₂ flakes on SiO₂/Si substrate. Gradually insulating behavior arose with the initial increasing dose applied, while metallic behavior was observed with the further increase in dose applied. The gate tunability of the WSe₂ device was completely reduced as seen in inset, at a dose of 1×10^{17} ions/cm².

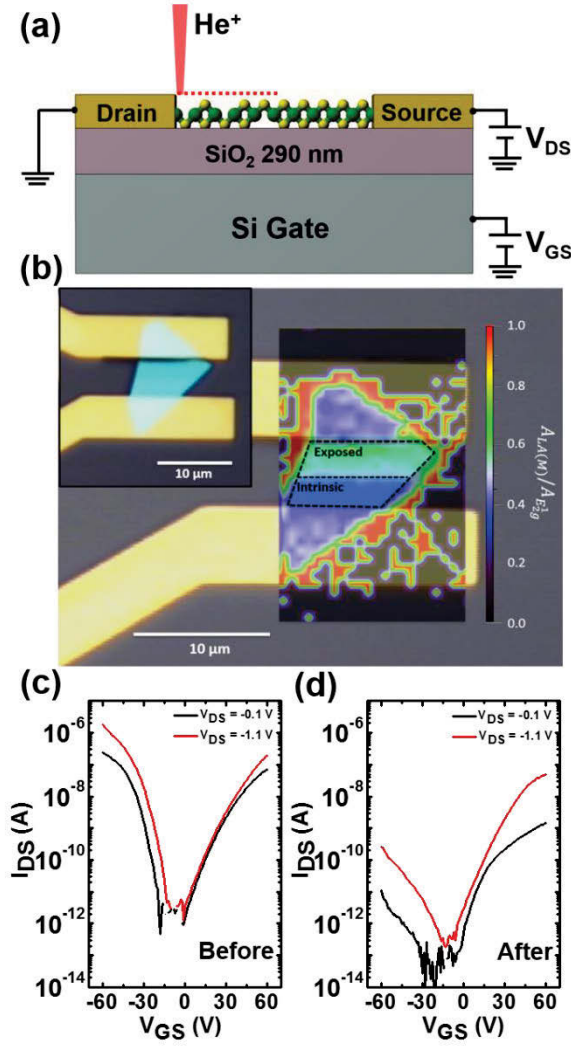


Figure 72. (a) Schematic of the WSe₂ field effect transistor (FET) device irradiated with He⁺ over half of the channel length to induce a homo-junction. (b) Spatially resolved Raman map of He⁺ irradiated junction (1×10^{15} ions/cm²) on a WSe₂ flake. Map shows ratio of integrated peak area of LA(M) (associated with defects) to the main Raman peak E_{12g}. The inset in the upper left corner shows an optical micrograph of WSe₂ device. The measured transfer characteristics of a WSe₂ FET device (c) before and (d) after, He⁺ irradiation was used to create a homo-junction at a dose of 1×10^{15} ions/cm².

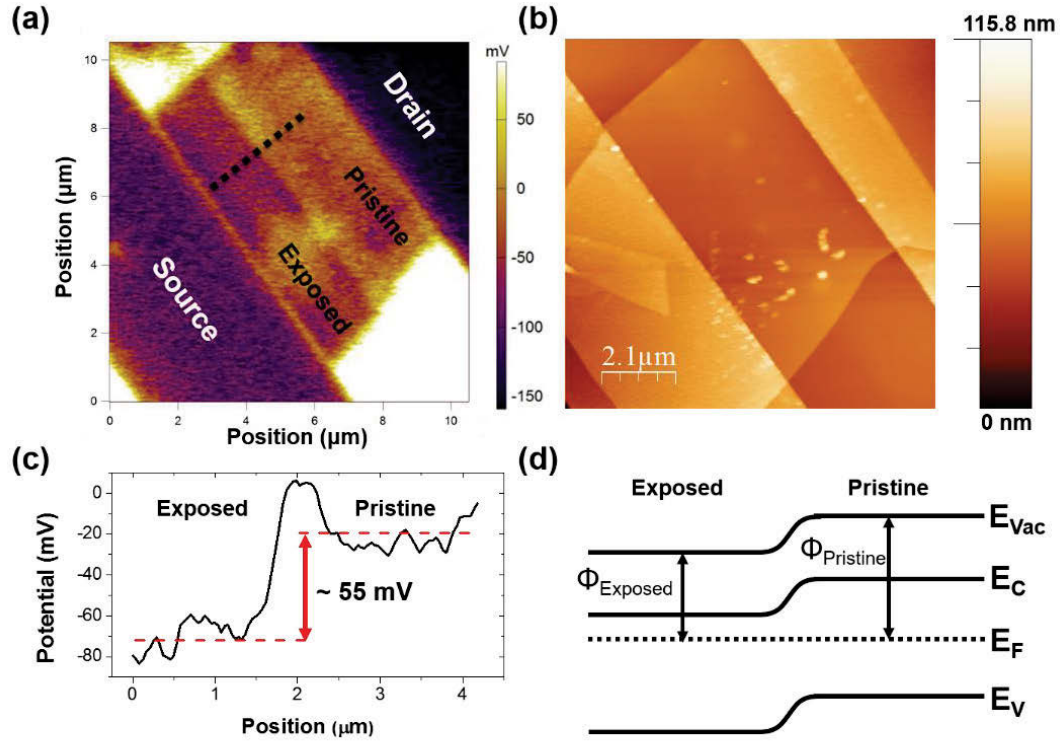


Figure 73. (a) Kelvin Probe Force Microscopy (KPFM) image of a WSe₂ TFT with symmetric Ti/Au electrodes in which half of the channel with exposed with a dose of $5 \times 10^{14} \text{ He}^+/\text{cm}^2$. (b) Tapping mode AFM image of the same exposed WSe₂ TFT, which shows no topographical evidence of exposure. (c) KPFM line scan, denoted by a black dotted line in (a), which shows band bending at the interface of exposed and pristine WSe₂. (d) Band diagram of a WSe₂ flake, which has a junction created by He⁺ exposure.

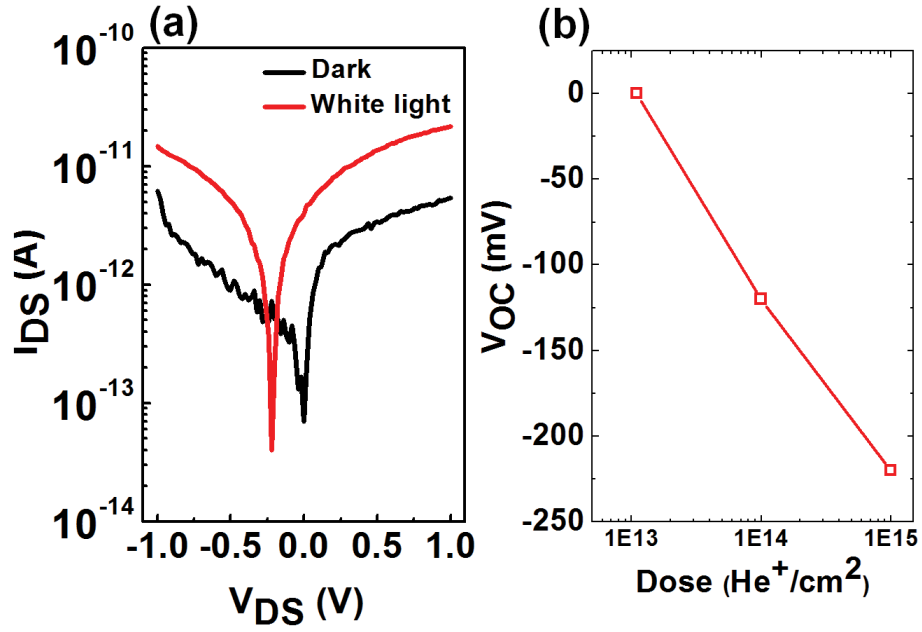


Figure 74. (a) The photoresponse of a device with the lateral homojunction created by a dose of $1 \times 10^{15} \text{ He}^+/\text{cm}^2$ in WSe₂ at zero gate bias. The semi-log plot of I_{DS} vs V_{DS} with and without light exposure shows the photoresponse with noticeable photovoltage as high as 220 mV. (b) Open circuit voltage extracted from devices under light condition as a function of He^+ dose used to create the homo-junction.

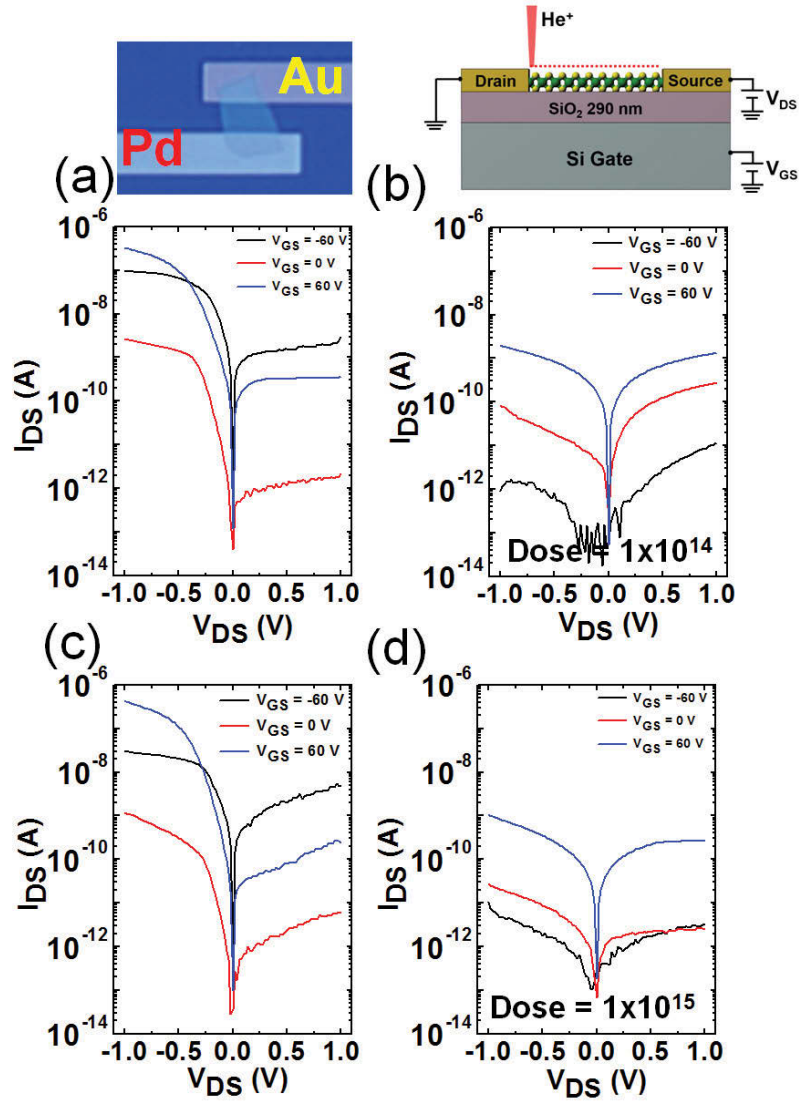


Figure 75. The semi-log plot of output characteristics (I_{DS} vs V_{DS}) of asymmetric electrodes (Pd in one side and Ti/Au in other side) of few-layer WSe₂ devices, before (left panel a & c) and after (right panel b & d) He⁺ irradiations at two different doses (1×10^{14} and 1×10^{15} He⁺/cm², respectively). Preferential hole injection in the WSe₂ channel is clearly seen from the asymmetric nature of $I_{DS} - V_{DS}$ curves (a & c) due to the ohmic contact between the Pd electrode and valence band of WSe₂ flake and a possible Schottky barrier at Ti/Au contact. The hole transport is still significantly suppressed compared to electron transport (Fig. b and d) on WSe₂ channel after the He⁺ irradiation. The images on the top of the Figure depict an optical micrograph (left) and schematic (right) of the device structure studied.

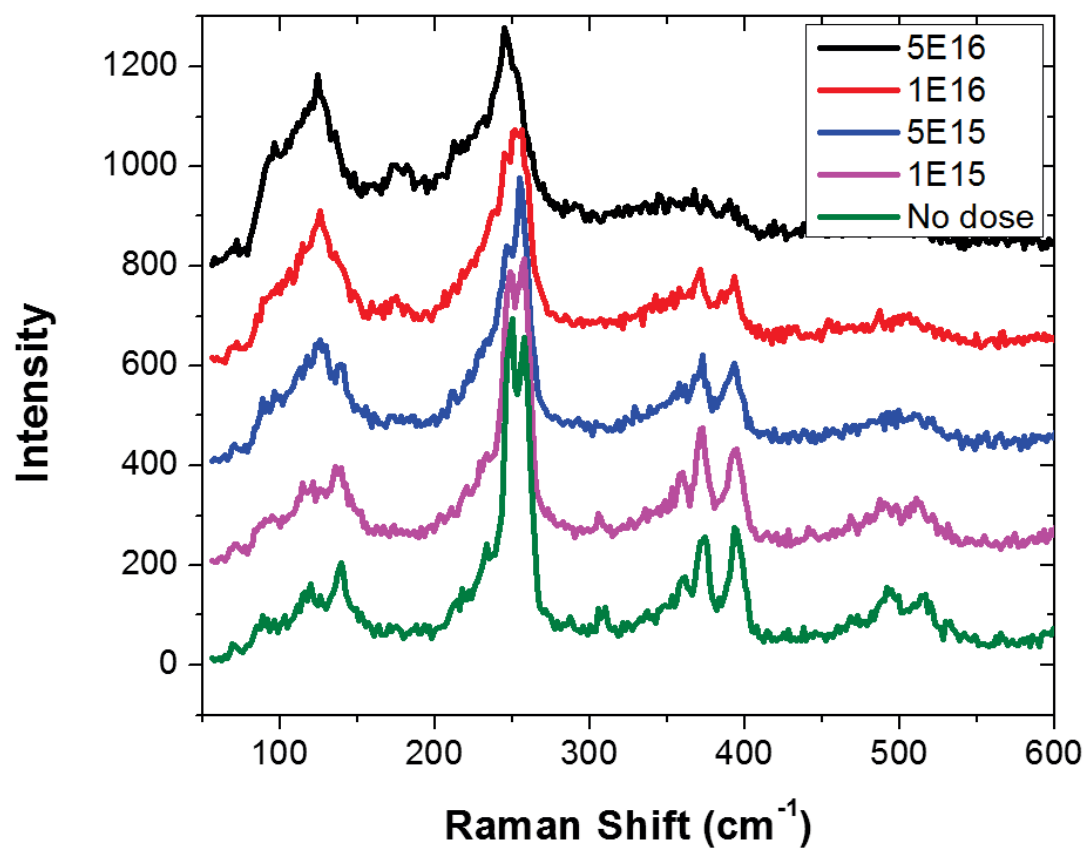


Figure 76. Raman spectra of few-layer WSe₂ at various He⁺ exposure doses.

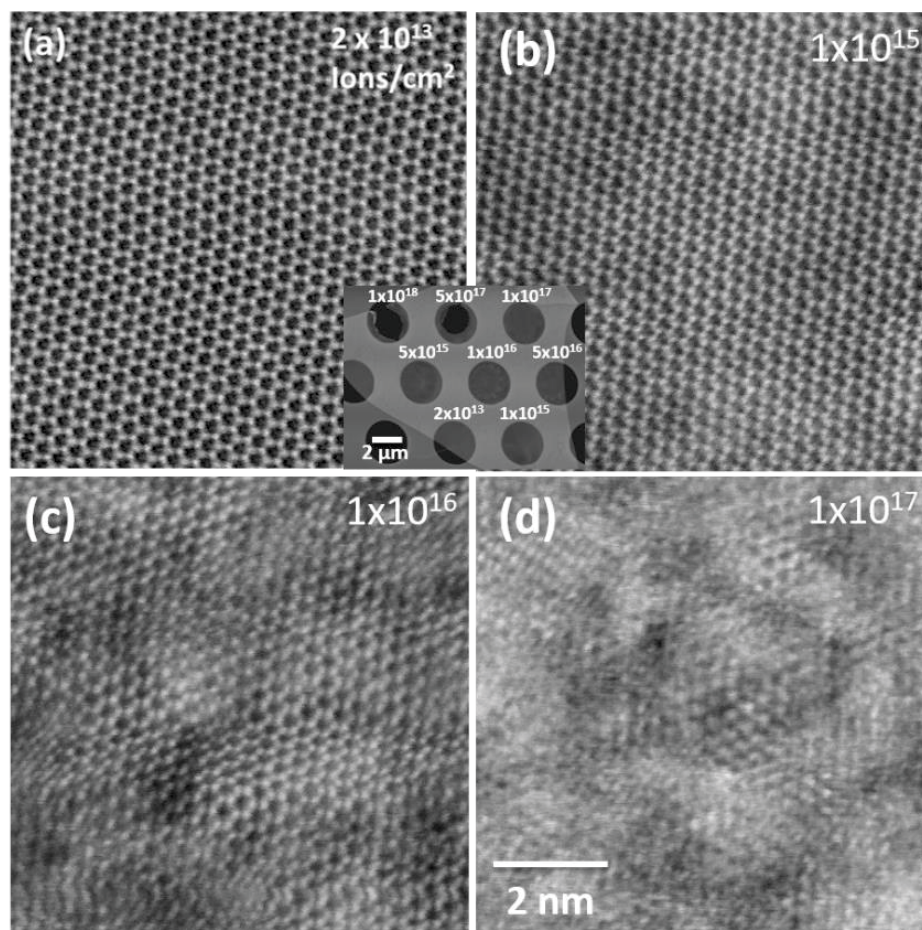


Figure 77. HAADF STEM images of suspended WSe₂ which was irradiated with He⁺ at doses of (a) 2×10^{13} , (b) 1×10^{15} , (c) 1×10^{16} , and (d) 1×10^{17} ions/cm². Images have 8 nm field of view.

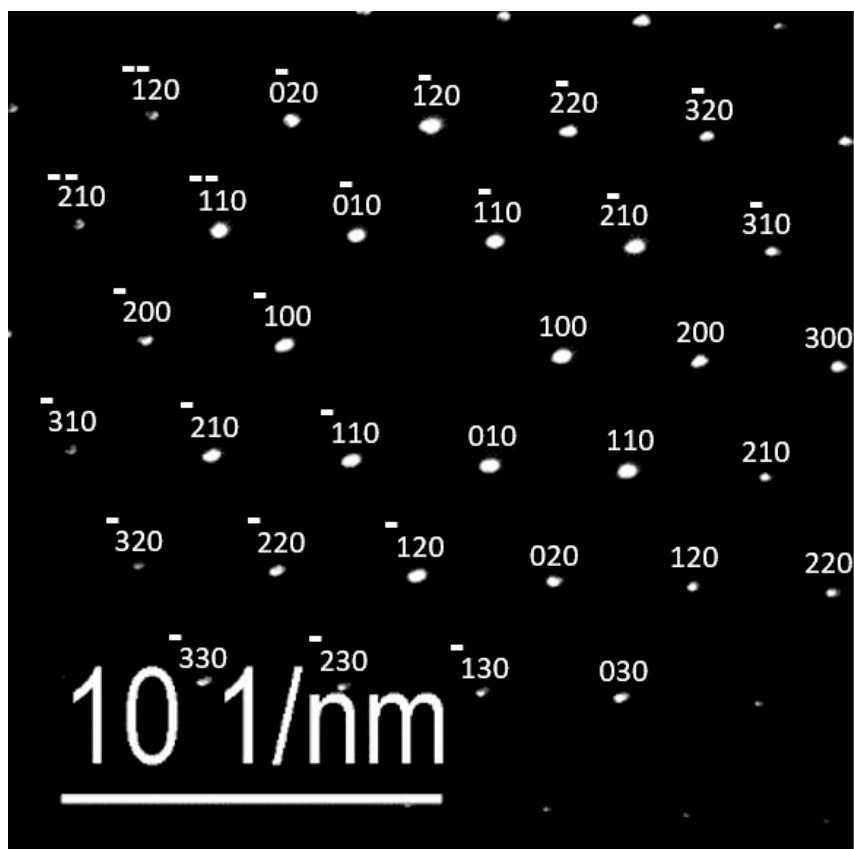


Figure 78. Indexed diffraction pattern taken from WSe₂ flake exposed with a dosage of 2×10^{13} He⁺/cm²

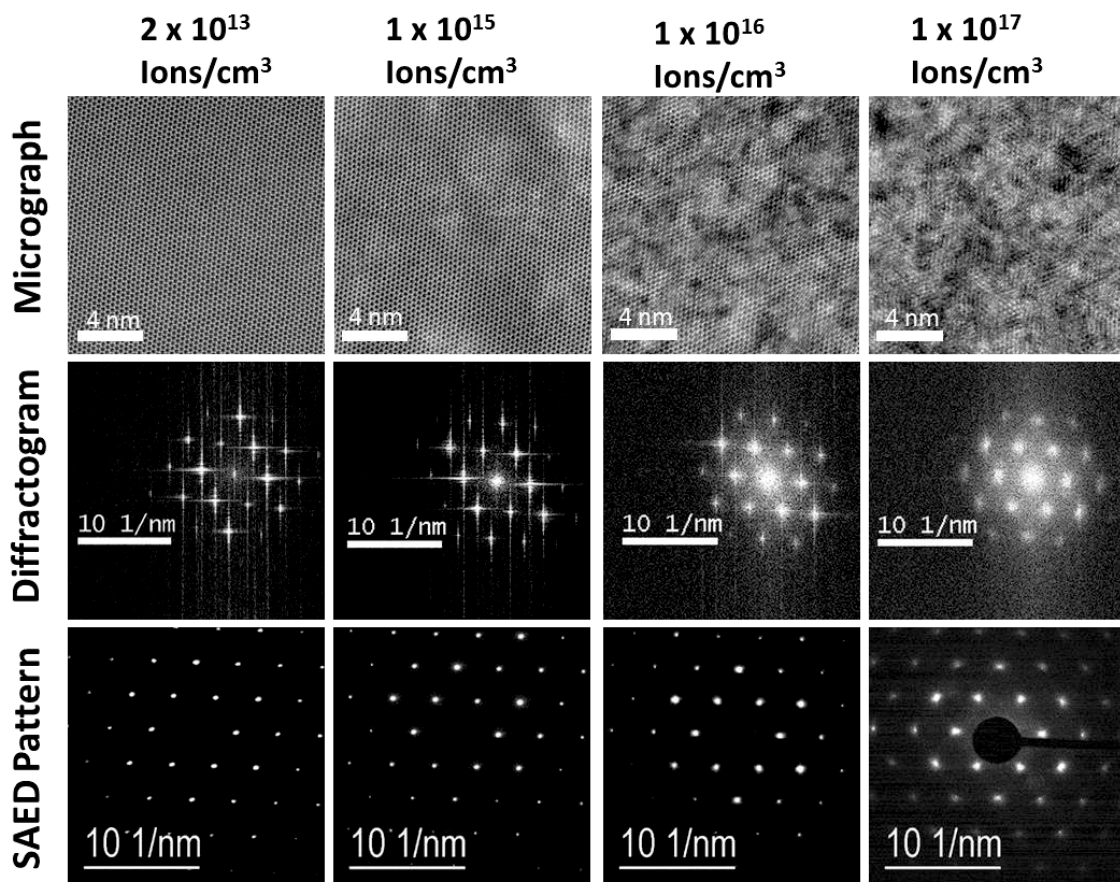


Figure 79. Figure compares the changes in the WSe₂ crystal structure when subjected to varying doses of ion irradiation. This has been done by STEM Z-contrast imaging, Fourier transformations of each respective Z-contrast image, and selected area electron diffraction patterns that correspond to each region. Fourier transformations of the Z-contrast images agree well with SAED results.

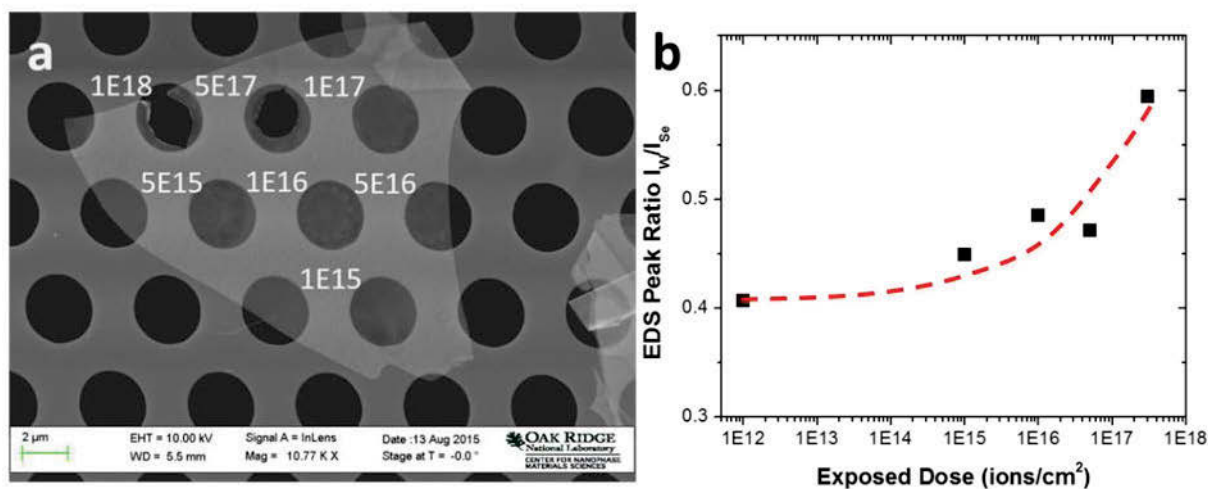


Figure 80. (a) SEM image of a single layer WSe_2 flake on a holey silicon nitride membrane. Inset doses denote the dose applied to each suspended region with units of ions/cm^2 . (b) Plot of the ratio of the relative peaks intensities of W – M and Se – L as a function of He^+ dose.

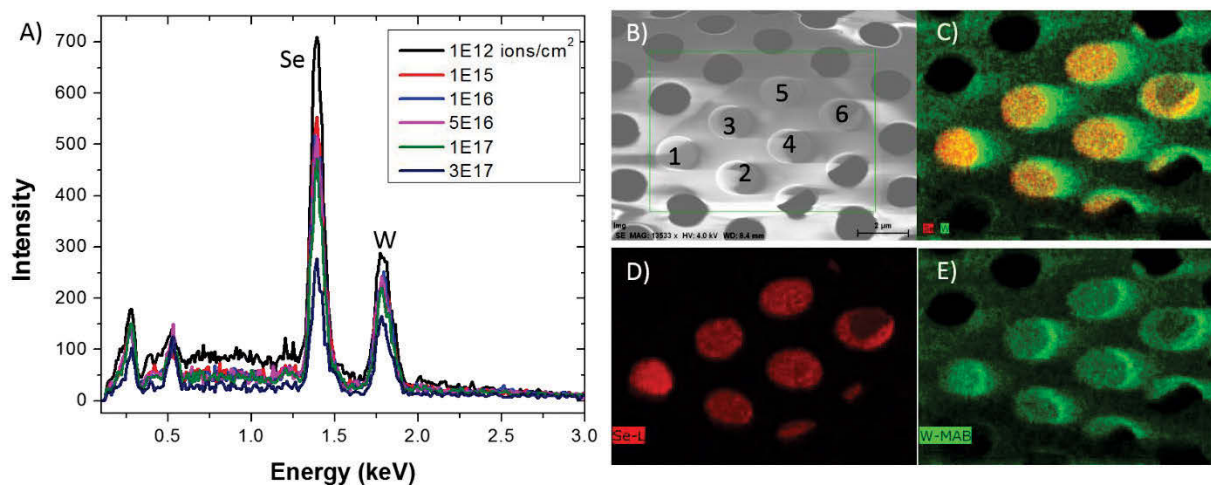


Figure 81. (a) Raw EDS spectra for suspended WSe₂ exposed with He⁺ of various doses. (b) SEM image of the exposed suspended flake on silicon nitride where regions 1-6 were exposed with doses of 1E12, 1E17, 5E16, 1E16, 1E15, and 3E17 respectively. (c-e) EDS maps of Se + W, only Se, and only W respectively.

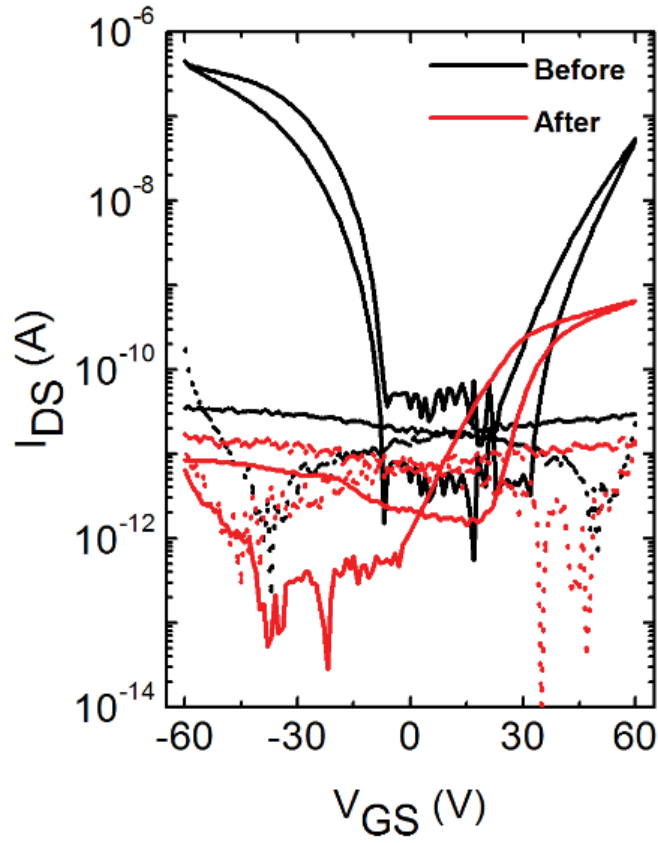


Figure 82. The typical hysteresis in measured I_{DS} vs V_{GS} curves at $V_{DS} = 0.1$ V, before (black) and after (red) He^+ irradiation at the dose of 1.0×10^{15} ions/cm². The corresponding leakage currents (dotted lines) are also plotted in the same graph.

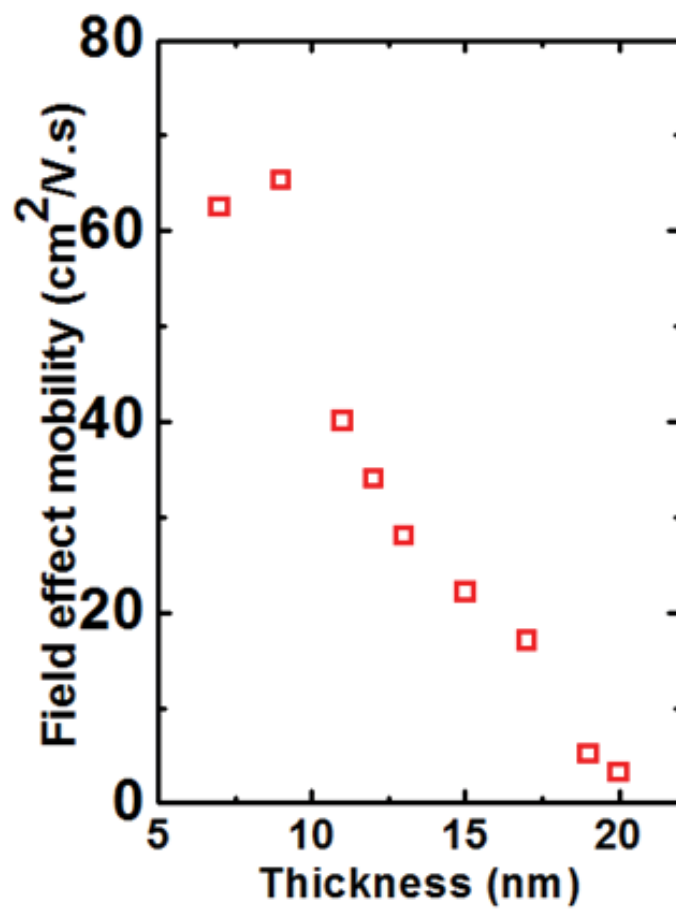


Figure 83. Field effect hole mobility extracted from the transfer characteristic curves for few-layer WSe₂ devices as a function of flake thickness.

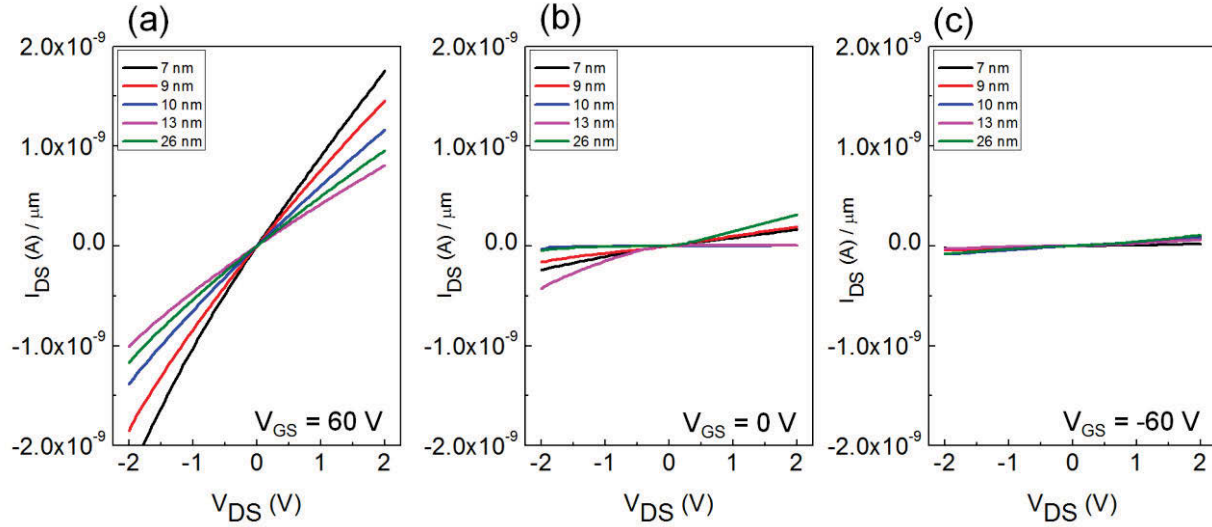


Figure 84. Measured I_{DS} vs V_{DS} normalized to channel W/L ratio, for the different thickness of WSe_2 flakes at three different gate voltages, (a) $V_{GS} = 60$ V, (b) $V_{GS} = 0$ V and (c) $V_{GS} = -60$ V. All flakes were exposed in the channel region with a dose of 1×10^{15} He^+/cm^2 .

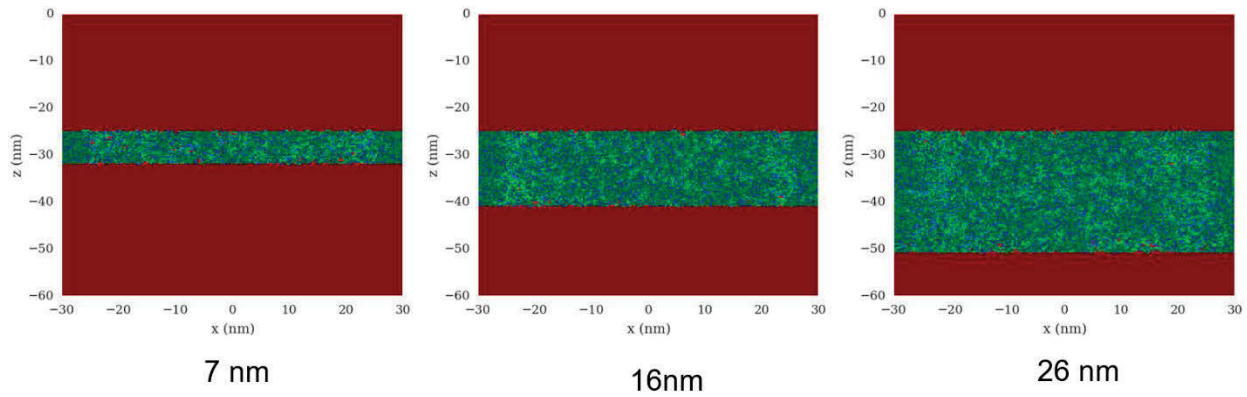


Figure 85. Using our EnvizION¹⁰³ ion-solid Monte Carlo simulation we simulated varying thickness WSe_2 films (7, 16, and 26 nm) which were exposed with 25 keV He^+ to a dose of 1×10^{15} He^+/cm^2 . In this simulation, the WSe_2 is assumed to be amorphous with the stoichiometric W/Se ratio of 1/2 and using the bulk properties of crystalline WSe_2 . The He^+ was simulated as a 25 nm cylindrical beam. Green pixels represent Se atoms, blue pixels represent W atoms, light green pixels represent displaced Se atoms, light blue pixels represent displaced W atoms, and red pixels represent unfilled vacancies created by sputtering events.

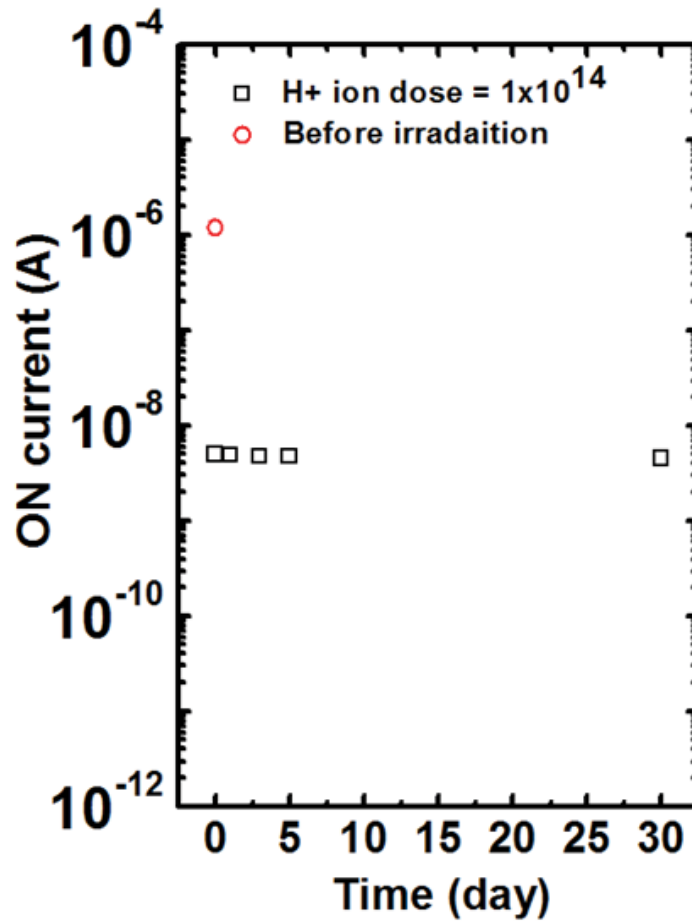


Figure 86. Time dependence of transistor ON current at $V_{DS} = 1.1\text{ V}$ and $V_{GS} = 60\text{ V}$, for few-layer WSe₂ device irradiated with He⁺ ion dose at 1×10^{14} up to 30 days. No recovery on transistor ON currents has been observed by exposing the irradiated sample in ambient conditions. The red open circle represents the channel current prior to He⁺ exposure.

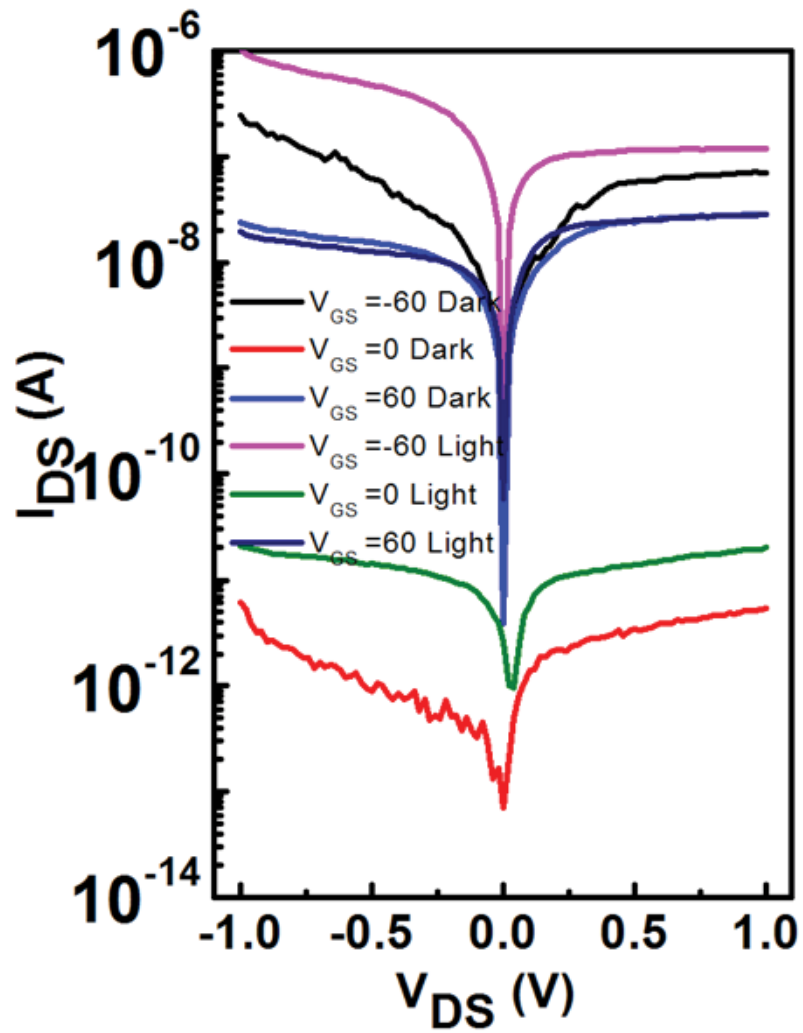


Figure 87. Photo-response of one of the pristine few-layer WSe₂ device (without He⁺ irradiation) at various gate potentials. No significant photovoltaic effect has been observed in few-layer WSe₂ device.

3.1.6.3 Tables

Table 9. Raman peak assignments of few-layer WSe₂.

Peak (cm ⁻¹)	Assignments ²⁰⁹
119	LA(M)
138	A _{1g} -LA
238	2LA(M)
250	E _{2g} ¹ (in plane)
258	A _{1g} (out of plane)
362	2E _{1g}
373	A _{1g} +LA
395	2A _{1g} -LA

Table 10. EnvizION Monte Carlo simulation sputter yields and Se/W sputter ratio for WSe₂ of varying thicknesses.

Thickness (nm)	Yield (atoms/ion)	Ratio (Se/W)
7	0.1	3.9
16	0.11	3.4
26	0.11	3.5

3.2 High Conduction Hopping Behavior Induced in Transition Metal Dichalcogenides by Percolating Defect Networks: Toward Atomically Thin Circuits

A version of this chapter was originally published by M. G. Stanford et al.:

Stanford, M. G.; Pudasaini, P. R.; Gallmeier, E. T.; Cross, N.; Liang, L.; Oyedele, A.; Duscher, G.; Mahjouri-Samani, M.; Wang, K.; Xiao, K.; et al. High Conduction Hopping Behavior Induced in Transition Metal Dichalcogenides by Percolating Defect Networks: Toward Atomically Thin Circuits. *Adv. Funct. Mater.* 2017, 1702829 (DOI: 10.1002/adfm.201702829).

M.G.S, P.R.P., and P.D.R. conceived experiments and prepared the manuscript. M.G.S. conducted He⁺ exposures obtained Raman and PL data. P.R.P. conducted device fabrication and measured electrical properties. N.C. and G.D. carried out STEM imaging. E.T.G and A.B conducted analysis of STEM images. M.M.S, K.W, K.X, and D.B.G. synthesized the WSe₂ and WS₂. L.L and B.G.S. performed DFT modeling. All authors participated in the discussion of results and manuscript revisions.

3.2.1 Abstract

Atomically thin circuits have recently been explored for applications in next-generation electronics and optoelectronics and have been demonstrated with two-dimensional lateral heterojunctions. In order to form true 2D circuitry from a single material, electronic properties must be spatially tunable. Here, we report tunable transport behavior which was introduced into single layer tungsten diselenide and tungsten disulfide by focused He⁺ irradiation. Pseudo-metallic behavior was induced by irradiating the materials with a dose of $\sim 1 \times 10^{16}$ He⁺/cm² to introduce defect states, and subsequent temperature-dependent transport measurements suggest a nearest neighbor hopping mechanism is operative. Scanning transmission electron microscopy and electron energy loss spectroscopy reveal that Se is sputtered preferentially, and extended percolating networks of edge states form within WSe₂ at a critical dose of 1×10^{16} He⁺/cm². First-principles calculations confirm the semiconductor-to-metallic transition of WSe₂ after pore and edge defects were introduced by He⁺ irradiation. The hopping conduction was utilized to direct-

write resistor loaded logic circuits in WSe₂ and WS₂ with a voltage gain of greater than 5. Edge contacted thin film transistors were also fabricated with a high on/off ratio ($> 10^6$), demonstrating potential for the formation of atomically thin circuits.

3.2.2 Introduction

Transition-metal dichalcogenides (TMDs) are layered materials that consist of stacked two-dimensional crystals held together by van der Waals interactions. An individual TMD layer consists of a X-M-X sandwich structure where X is a chalcogen, and M is a transition-metal atom typically of trigonal prismatic coordination for a 2H polytype²¹⁰. TMDs have been shown to exhibit semiconducting properties and have recently been used to create high performance transistors^{211–213} and optical devices^{184,189,190}. Single-layer (1-L) TMDs also exhibit a direct bandgap, typically on the order of 1 - 2 eV depending upon the chemical composition¹⁸⁷.

Defects in TMDs can alter the electronic behavior and band structure in a wide variety of ways. Point defects (0-D), such as vacancies, have been studied extensively for the most commonly synthesized TMDs. For instance, intrinsic chalcogen vacancies in MoS₂ exhibit hopping transport characteristics explained by the Mott formalism²⁰⁶. Mo vacancies can also induce p-type behavior, whereas S vacancies exhibit n-type behavior¹⁸⁰. In WSe₂ and MoS₂, it was shown that chalcogen and transition-metal vacancies introduce mid-gap states into the material^{206,214,215}, a behavior exhibited in many TMDs²¹⁶.

Line defects (1-D), have demonstrated interesting properties with implications on the electrical transport. Different types of 60° grain boundaries, in chemical vapor deposition (CVD) grown TMDs, behave as 1-D metallic wires^{214,217}. It is also predicted that the majority of edge termination states behave metallically for MoS₂^{218,219}. For a review of defect engineering in TMDs see ref²²⁰.

Point defects in TMDs can occur intrinsically; however, a variety of methods have been explored for their control. Nonstoichiometric growth techniques have been used to synthesize MoSe₂ with Se vacancies approaching ~20%²²¹. Plasma treatment has the potential to introduce defects as well as to dope TMDs^{181,222–224}. Electron beam irradiation has been used to introduce a variety of point and extended defects^{7,225}. More recently, a focused helium ion beam has been used to introduce defects into MoSe₂²²⁶, MoS₂¹⁹⁷, and WSe₂²²⁷, controllably tuning the materials' properties. However, the mechanisms in which He⁺ irradiation altered electrical properties was not

thoroughly explored. Molecular dynamics simulations have demonstrated that defects can be introduced into the lattice of TMDs with a high degree of spatial control by tuning the He^+ beam conditions²²⁸.

In this work, a focused He^+ beam was used to introduce defects into single layer WSe_2 . The extent of defects introduction was controlled by adjusting the He^+ exposure dose from 1×10^{14} to $1 \times 10^{17} \text{ He}^+/\text{cm}^2$. We found that a dose of $1 \times 10^{16} \text{ He}^+/\text{cm}^2$ induces metallic-like behavior in the WSe_2 with transport properties independent of gate voltage. Temperature-dependent transport measurements reveal a thermally activated conductivity mechanism consistent with a nearest-neighbor hopping mechanism. Scanning transmission electron microscopy (STEM) suggests that percolating defect networks are formed at a dose of $1 \times 10^{16} \text{ He}^+/\text{cm}^2$, and Se is preferentially sputtered, resulting in the metallic-like behavior. Density functional theory (DFT) calculations were used to model various defect configurations, and confirm that pore and edge defects induced by the high He^+ dose result in many in-gap states in WSe_2 , and the band gap of the defective system is effectively zero. We demonstrate that the metallic-like WSe_2 and WS_2 can be utilized to direct-write logic gates on single TMD flakes and direct-write edge contacted transistors. Our results demonstrate a strategy for generating atomically thin circuitry and show potential for large scale processing via standard ion implantation or plasma exposure.

3.2.3 Results and Discussion

Back-gated, 1L, WSe_2 field effect transistors (FETs) were fabricated on 290 nm SiO_2/Si substrate as described in the Methods section. **Figure 88a** is an optical micrograph of a typical FET device. After fabrication, the channel of the FETs was irradiated with a focused He^+ beam at the beam energy of 25 keV. The He^+ has shown the potential to introduce defects into 2D materials with a high degree of precision^{115,159,229} by generating vacancies, adatoms, and interstitials within the material lattice via nuclear collisions. First-principles studies of native defects reveal the following: (1) Chalcogen vacancies are the most energetically favored point defect; (2) Chalcogen interstitials experience an extremely low diffusion barrier and are thus expected to rapidly annihilate with vacancy sites; (3) It is energetically favorable for interstitial transition metal atoms to form a split-interstitial configuration²³⁰. Therefore, it is expected that most point-defects induced by He^+ irradiation will be in the form of chalcogen vacancies, transition metal vacancies, or transition metal split-interstitials. Minimal amounts of He are implanted within WSe_2 since it is

1L thick, and 25 keV He^+ has an interaction volume and peak implantation of hundreds of nanometers in typical 2D materials and substrates. Photoluminescence and Raman spectra as a function of He^+ dose are reported in the Supporting Information and demonstrate a reduced PL intensity and quenching of the E_{12g} and A_{1g} peaks. **Figure 88b** shows the room temperature transfer curves for FETs in which the channel regions were exposed to varying He^+ doses. The pristine WSe_2 exhibits p-type behavior with an $I_{\text{on}}/I_{\text{off}}$ of 10^8 . At a dose of $1 \times 10^{14} \text{ He}^+/\text{cm}^2$, the device on-current degrades as defects are introduced, and $I_{\text{on}}/I_{\text{off}}$ decreases from 10^8 to 10^5 . Furthermore, at a dose of $1 \times 10^{15} \text{ He}^+/\text{cm}^2$, the back gate modulation no longer has an effect on the device current, however at zero gate voltage the current is two orders of magnitude higher than the pristine/unexposed device. At a dose of $1 \times 10^{16} \text{ He}^+/\text{cm}^2$, the gate modulation is also suppressed, and the zero gate voltage current is approximately 6 orders of magnitude higher than the pristine device. This result is indicative of charge carriers in the absence of a gate applied field. At a dose of $1 \times 10^{17} \text{ He}^+/\text{cm}^2$ and greater, the single layer material is mostly sputtered away, and no current flows. Several devices that demonstrate the same qualitative dose-dependent behavior were measured. **Figure 88c** summarizes the $I_{\text{Exposed}}/I_{\text{Pristine}}$ ratio for devices exposed to varying doses of He^+ at 10 V and -60 V gate voltage, which correspond to the devices “off” and “on” states, respectively. At $V_{\text{GS}} = -60 \text{ V}$, the devices exhibit decreasing current and increasing resistivity as the dose is increased to $1 \times 10^{15} \text{ He}^+/\text{cm}^2$. The resistivity drops sharply at a dose of $1 \times 10^{16} \text{ He}^+/\text{cm}^2$, the point at which metallic behavior is exhibited. However, at $V_{\text{GS}} = 10 \text{ V}$, the current increases with increasing He^+ dose over the entire range studied. This indicates that carrier concentration is increasing as a result of He^+ exposure in the absence of gate induced carrier generation.

To further characterize the conduction mechanism, temperature-dependent transport measurements were conducted on the $1 \times 10^{16} \text{ He}^+/\text{cm}^2$ exposed WSe_2 sample. **Figure 88d** shows the transfer curves ranging from room temperature to 77 K. The device on-current is largely independent of gate modulation for all reported temperatures, and there is a sharp decrease in the conductivity as the temperature decreases. This deviates from the standard metallic behavior where phonon-scattering is reduced at low temperature, thereby increasing conductivity. The temperature-dependent source-drain I-V characteristics of the device exhibit linear behavior and are reported in the Supporting Information. The sheet resistance (R_s) at room temperature is approximately $7.2 \times 10^6 \text{ } \Omega/\text{sq}$ and increases to $3.2 \times 10^9 \text{ } \Omega/\text{sq}$ at 77 K; For reference, the R_s for

graphene has a range from $10^2 - 10^6 \text{ } \Omega/\text{sq}$ ²³¹ at room temperature depending upon the synthesis technique. **Figure 88e** is the Arrhenius plot of the device conductance ($G = I/V$) at the measured temperatures. The behavior can be broken up into a high-temperature (295-125 K) and a low-temperature regime (below 125 K). At high temperature, the transport exhibits an activation behavior associated with a nearest-neighbor hopping (NNH) transport mechanism for which the current is governed by Equation 1:

$$G \propto \exp\left(-\frac{E_a}{k_b T}\right) \quad \text{Eq. (1)}$$

The activation energy (E_a) was determined to be $\sim 36.7 \text{ meV}$, a reasonable value for hopping transport reported in other 2D materials²³². Below a characteristic crossover temperature (T_c) of 125 K, the transport deviates from the Arrhenius behavior. At low temperature, variable range hopping (VRH), which has a $T^{1/3}$ dependence, appears to dominate the transport mechanism over NNH. Due to the temperature range studied, we cannot accurately fit this portion of the plot. The VRH – NNH crossover transport is commonly associated with disordered semiconductors²³³, and has been previously observed in TMDs with intrinsic point defects²⁰⁶. However, the observed behavior differs from other reports due to the independence from gate modulation.

To gain a better understanding of the origin of the He^+ dose dependent transport behavior in the 1L WSe₂, STEM images of exposed WSe₂ were analyzed to reveal signatures of preferential Se sputtering. **Figure 89a** shows a STEM image of WSe₂, which was exposed with a dose of $1 \times 10^{15} \text{ He}^+/\text{cm}^2$. A dose of $1 \times 10^{15} \text{ He}^+/\text{cm}^2$ is reported here because He^+ -induced defects can easily be distinguished, although the WSe₂ is still continuous. K-means cluster analysis, using a Euclidean metric on bond-lengths to a six-member neighborhood for each atom, was conducted on the STEM image and is reported in **Figure 89b**. This approach clusters each atom in the image based on the bond-length to six nearest neighbors (see details in Methods section^{234–236}). This analysis allows automated detection of atoms in varying crystallographic configurations. For instance, pristine lattice atoms with a consistent periodic configuration are labeled blue; atoms neighboring single vacancies are labeled white; and atoms from heavily damaged regions with multiple neighboring vacancies are labeled green. **Figure 89c** shows the real space nearest neighbor distribution for all atoms in the image characterized as pristine (blue) by the k-means analysis. Since the lattice is pristine, all neighboring positions are equally occupied, as indicated

by their similar contrast at each point of the hexagon closest to the center of the image. The real space nearest neighbor distribution for atoms neighboring single vacancies (green) are reported in **Figure 89d**. Nearest neighbor atoms that occupied the downward facing trimer (indicated by inset red arrows) have fewer counts, as indicated by their lighter contrast. This suggests that atoms occupying these sites were preferentially sputtered by the He^+ irradiation in comparison to the other nearest neighbors. Image analysis reveals that the preferentially sputtered atomic species are Se atoms. Therefore, He^+ irradiation results in chalcogen deficiency in irradiated films although some metal atoms are also sputtered. Electron energy loss spectroscopy (EELS) analysis confirms the He^+ irradiation creates Se deficiency within the flakes (see Supporting Information **Figure 97**).

STEM images of the WSe_2 were collected as a function of dose and reported in **Figure 90a** (doses are listed as insets). He^+ irradiation introduces more structural defects into the lattice as a function of increasing dose. At $1 \times 10^{14} \text{ He}^+/\text{cm}^2$, isolated, predominately Se vacancies are generated, which leads to carrier scattering and reduces the field effect mobility from $\sim 16 \text{ cm}^2/\text{Vs}$ for a pristine device to $\sim 1.5 \times 10^{-2} \text{ cm}^2/\text{Vs}$ (Details of field effect mobility calculation can be found in the methods). Notably, at a dose of $1 \times 10^{15} \text{ He}^+/\text{cm}^2$, the Se vacancy concentration increases to a point that the gate-independent NNH transport dominates the conduction relative to the p-type semiconducting behavior of the pristine and $1 \times 10^{14} \text{ He}^+/\text{cm}^2$ samples. At a dose of $1 \times 10^{16} \text{ He}^+/\text{cm}^2$, the defect density is an order of magnitude higher and defects begin coalescing into an extended network percolating throughout the material. Consequently, a greater density of Se vacancies lowers the activation energy and the hopping distance, thereby contributing to an increase in conductivity. A dose of $1 \times 10^{17} \text{ He}^+/\text{cm}^2$ sputters much of the material leaving discontinuous patches. K-means cluster analysis results are reported in **Figure 90b**. Pristine lattice atoms with a periodic configuration of neighboring atoms are labeled as yellow; atoms neighboring vacancies (boundary atoms) are labeled as magenta; and atoms with little or no detectable periodicity are labeled as blue. The boundary states are isolated and reported in **Figure 90c** for clarity. At a dose of $1 \times 10^{14} - 1 \times 10^{15} \text{ He}^+/\text{cm}^2$, there are numerous boundary atoms surrounding pores and point defects, but they are largely isolated from each other. However, at a dose of $1 \times 10^{16} \text{ He}^+/\text{cm}^2$, the boundary atoms form an extended percolating network in the single layer WSe_2 . It is worth noting that the defect concentration in the free-standing WSe_2 induced by a particular He^+ dose is slightly lower than the defect concentration that can be expected for material exposed on a bulk substrate.

This is because the primary He^+ beam energy has a small interaction cross-section with the freestanding WSe_2 ²²⁸ and back-scattered He^+ and recoil atoms contribute significantly toward defect introduction. For atomically thin free-standing material, the vast majority of He^+ transmit or forward-scatter through the material, thus minimizing defects generated from backscattered He^+ . However, recoil atom cascades are still expected to significantly contribute toward defect production. For a more detailed description on how the underlying substrate effects the He^+ -induced defect introduction, interested readers are referred to Ref²³⁷.

Unfortunately, this image analysis does not reveal a single dominant configuration for the edge termination in the percolating network. In context with previous reports, edge states behave metallically for most commonly occurring edge terminations^{218,219}. Therefore, percolating networks of edge states surrounding pores are believed to behave as conductive nanowires and contribute to the high conductivity at $1 \times 10^{16} \text{ He}^+/\text{cm}^2$. To confirm our analysis, first-principles DFT calculations were performed for different defect configurations, as shown in **Figure 91**. Pristine monolayer WSe_2 has a direct band gap of $\sim 1.55 \text{ eV}$ at the K point, according to this level of DFT calculations. For the point defect which is predominately a Se vacancy induced by a low irradiation dose such as $1 \times 10^{14} \text{ He}^+/\text{cm}^2$, this leads to two nearly degenerate in-gap bands above the Fermi level, which are almost dispersionless as their charge densities are well localized around the point defect site (**Figure 91b**)^{206,226}. Thus the point defect lowers the carrier mobility and also the band gap to $\sim 1.17 \text{ eV}$. Although it retains the semiconducting feature, the gap reduction indicates the decreased current on/off ratio, consistent with our experimental observation. With increasing irradiation dose, pore and edge defects are introduced according to the STEM images, giving rise to more in-gap bands. Our calculations suggest that many in-gap states are close to the Fermi level, effectively closing the band gap and rendering the system metallic. This can explain why the back gate modulation no longer has an effect on the device current at doses of 1×10^{15} and $1 \times 10^{16} \text{ He}^+/\text{cm}^2$, and the zero gate voltage current is much higher than that of the pristine device. In other words, both the circular edge surrounding the pore defect (**Figure 91c**) and the straight edge (**Figure 91d**) lead to metallic edge states that behave as conductive nanowires. However, isolated pores, which are prevalent with exposure to a dose of $1 \times 10^{15} \text{ He}^+/\text{cm}^2$, do not coalesce into extended networks and result in lower conduction than material exposed to a dose of $1 \times 10^{16} \text{ He}^+/\text{cm}^2$. Thus, conduction in the material results from percolating 1-D networks of edge states in

series with pockets of Se deficient material. The NNH temperature dependence is a result of the Se deficient material which acts as a bottleneck in the conduction path between high conductivity edge states, as NNH behavior has been demonstrated in TMDs with intrinsic point defects²⁰⁶.

Since gate modulation has a minimal effect on the carrier concentration of the percolating defect networks, the NNH WSe₂ can be utilized to direct write circuitry and logic gates onto a single flake. **Figure 92a** shows a proposed schematic for the structure of a resistor-loaded inverter device (circuit diagram is inset in **Figure 92c**). This logic gate is fabricated as a series of two devices. The channel between the first two electrodes is irradiated with a dose of 1×10^{16} He⁺/cm² in order to induce gate-independent NNH behavior. This region behaves as a resistor due to the linear I-V characteristics. The channel between the second and third electrodes is pristine WSe₂. This device behaves as a standard p-FET with significant gate modulation. An optical micrograph of a fabricated inverter is displayed in **Figure 92b**. The input (V_{in}) – output (V_{out}) characteristics for a back-gated (SiO₂) WSe₂ inverter are shown in **Figure 92c**, and typical inverter behavior of a p-type device is exhibited. In this device, the NNH channel gives a resistance of approximately 5 M Ω . Transfer curves and I-V characteristics of the transistor and resistor in the inverter structure are reported in the Supporting Information **Figure 98** and **Figure 99**. In order to demonstrate the applicability of the NNH defect network in other TMDs, a similar resistor-loaded inverter was fabricated from single layer WS₂. Input-output characteristics are shown in **Figure 92d**; notably, this device shows opposite input-output characteristics since the WS₂ transistor exhibited n-type behavior. Similar to the WSe₂ inverter, the resistor was direct-written with He⁺ irradiation into a single flake by inducing the NNH defect network. The voltage gain (dV_{out}/dV_{in}) in these devices is low since they were back-gated with relatively low-dielectric constant SiO₂ ($\epsilon_r = 3.9$). In order to improve inverter performance, a WSe₂ inverter was top-gated with an ionic liquid (IL) (see supporting information for details) and is reported in **Figure 92e**. V_{DD} was varied from 0.5 V to 1.5 V, and V_{out} was consistently at the level of V_{DD} for positive V_{in} , when the transistor was in an off state. As V_{in} is decreased to a threshold of -1 V, V_{out} rapidly switches to 0 V and displays ideal inverter characteristics. **Figure 92f** reports the voltage gain, which was greater than 5 for V_{DD} equal to 1.5 V. This is a suitable value for implementation of these devices into electronic circuits where a gain greater than 1 is typically desired to drive the input of the next inverter in a circuit.

Furthermore, high conduction NNH behavior induced in the TMD flake can be utilized to create edge contacts for true 2D circuitry, which typically involves a CVD step with a seeding mechanism^{238,239}. **Figure 93a** displays a schematic of an edge contacted transistor fabricated from NNH WS₂ acting as the source and drain along with pristine WS₂, which acts as the channel material. The Raman mapping of the WS₂ 2LA(M) peak in **Figure 93b** shows that a relatively sharp transition can be achieved between defective and pristine material. The 2LA(M) peak is clearly suppressed for the defective WS₂. The transfer curve of the edge contacted device compared to that of a standard WS₂ FET with a Ti/Au source-drain is shown in **Figure 93c**. The introduction of NNH WS₂ edge contact results in a slight reduction in the on-current of the device; however, I_{on}/I_{off} remain greater than 10^6 . Total resistance of a device in its on-state, defined as intrinsic resistance plus contact resistance, increases from $\sim 3.7\text{ M}\Omega$ to $\sim 14.4\text{ M}\Omega$ after the addition of edge contacts. This is likely due to the intrinsic resistivity of the NNH WS₂ and could be reduced by further optimizing the defect concentration. Hence, the induced NNH behavior in TMD flakes can serve as a method to write circuitry and logic devices into the material for atomically thin circuitry and edge contacted devices. The high conduction behavior induced by the formation of extended defect networks can likely be scaled-up via standard lithography of a blocking mask coupled with standard ion implantation or plasma processing.

3.2.4 Conclusions

We have demonstrated that extended networks of defects in WSe₂ and WS₂ can be utilized to induce high conductivity behavior. It is believed, from STEM image analysis, that this behavior arises from the Se deficiency and the formation of extended edge states that percolate throughout the material and behave as 1-D metallic nanowires. DFT simulations confirm that the metallic edge states can be introduced after irradiation. However, temperature-dependent electrical transport suggests that a nearest neighbor hopping transport mechanism is operative within the material, which deviates from standard metallic behavior. The NNH behavior is exhibited due to pockets of chalcogen deficient material which remains between metallic edge states. Networks of defects were induced within single flakes to direct-write inverter devices from WSe₂ and WS₂, devices that demonstrate a voltage gain suitable for electronic circuitry. The NNH material was also utilized to create edge contacts for a transistor that demonstrated an on-off ratio of greater than

10⁶. This enables the formation of atomically thin circuitry without the need for seeding and a CVD step.

3.2.5 Methods

3.2.5.1 Material Synthesis

Monolayer WSe₂ crystals were synthesized on SiO₂/Si substrates by a digital transfer growth method that combines pulsed laser deposition (PLD) and VTG processes²⁴⁰. We employ PLD to first deposit a uniform and precise amount of stoichiometric precursor nanoparticles onto a “source” substrate at room temperature. Specifically, SiO₂/Si source substrates were placed d = 5cm away and parallel to the WSe₂ targets in a vacuum chamber. The WSe₂ targets were prepared by pressing the stoichiometric powder and were ablated by an excimer laser (KrF 248 nm, 20 ns, 1 Jcm⁻²) at 30° angle of incidence with a repetition rate of 1 Hz at the background gas pressure 200 mTorr. This material was then covered by a “receiver” substrate which is placed in contact and on top of the source substrate to form a confined growth system. The source substrate was placed in contact with a button heater at about 900 °C to evaporate the precursor materials on the source substrate. By controlling the background gas pressure, a temperature gradient was established that resulted in condensation of the evaporated precursor materials onto a receiver substrate and growth of WSe₂ monolayer crystals.

High-density WS₂ monolayer crystals were directly grown on SiO₂/Si substrates by chemical vapor deposition. The details were reported in a previous publication²⁴¹.

3.2.5.2 Helium Ion Irradiation

He⁺ exposures were conducted in a Zeiss Orion NanoFab microscope. A constant beam energy of 25 keV was used for all exposures. All exposure patterns were generated using the NanoPatterning and Visualization Engine (NPVE) pattern generator produced by Fibics Inc. TMD field-effect transistors were irradiated after device fabrication. For STEM imaging, the WSe₂ was transferred to a QUANTIFOIL holey carbon grid prior to He⁺ irradiation.

3.2.5.3 Raman and Photoluminescence

Raman spectroscopy and photoluminescence measurements were performed in a Renishaw inVia micro-Raman system using a 532 nm excitation laser. A 100 × magnification objective was used for spectral acquisition with a 10 s acquisition time, and three acquisitions were averaged

together. The laser spot size was approximately 0.6 μm . Data analysis was conducted with the WIRE v3.4 software.

3.2.5.4 Device Fabrication

Single-layer WSe₂ flakes were transferred onto SiO₂ (290 nm)/Si (heavily doped Si, which also serves as a bottom gate electrode). Standard e-beam lithography, followed by e-beam evaporation, was employed to create the source/drain electrodes for electrical measurements. The contacts consisted of Ti/Au (5/30 nm) metals deposited and subsequently patterned via a lift-off process. The electrical characteristics of the fabricated WSe₂ devices were measured using an Agilent semiconductor parametric analyzer (Agilent Tech B1500 A). Field effect mobility was calculated using the following equation, $\mu = (L/W) \cdot (1/C_g V_{DS}) \cdot (dI_{DS}/dV_{GS})$, where L is the channel length, W is the channel width, C_g is the gate capacitance ($\sim 12 \text{ nF/cm}^2$), V_{DS} is 1.1 V, and dI_{DS}/dV_{GS} is the slope from the linear portion of the I_{DS} vs V_{GS} curve.

3.2.5.5 Scanning Transmission Electron Microscope Imaging

All STEM microscopy was carried out using a Nion UltraSTEM 100 operating at an accelerating voltage of 100 kV. Flakes of WSe₂ were exfoliated from a bulk crystal onto films on continuous α -carbon film grids. The 1L WSe₂ images consist of averaging 20 frames each 512 x 512 pixels with a 4 μs dwell time per pixel. The EELS spectra were acquired with a Gatan Spectrometer “Enfina” fitted to the STEM.

3.2.5.6 STEM Image K-Means Cluster Analysis

Quantification of the STEM image data was broken down using the following workflow. First, each atom was located in the image using an atom finding algorithm previously described in Ref 35. Second, vectors describing local 6 member neighborhoods for each atom, based on the six closest atoms, were constructed. These distance vectors served as input into a k-means cluster algorithm, utilizing a Euclidian distance metric, with 1000 iterations to confirm minima convergence. Hierarchical cluster trees (dendrograms) were used to assess the most appropriate number of clusters, and ranges of 2-8 clusters were calculated and analyzed for each image.

3.2.5.7 Density Functional Theory

Plane-wave DFT calculations were performed using the VASP package²⁴² equipped with the projector augmented-wave (PAW) pseudopotentials with a cut-off energy of 300 eV. The exchange-correlation interactions were considered in the generalized gradient approximation

(GGA) using the Perdew-Burke-Ernzerhof (PBE) functional²⁴³. Monolayer WSe₂ was modeled by a periodic slab geometry with 18 Å vacuum separation used in the out-of-plane direction to avoid spurious interactions with periodic images. For the hexagonal unit cell of pristine WSe₂, its optimized in-plane lattice constant is 3.32 Å and 24×24×1 k-point samplings were used in the Monkhorst-Pack scheme. To model the electronic properties of different defect configurations, the point Se vacancy, pores defect and edge defect were considered in a 5×5 supercell with 6×6×1 k-point samplings used. All atoms were relaxed until the residual forces below 0.01 eV/Å.

3.2.6 Appendix

3.2.6.1 Supporting Information

Dose Dependent Transfer Curves

Figure 94a-c reports the transfer curves for devices before and after they were irradiated with He^+ . Devices all display p-type characteristics with an on/off of greater than 10^7 .

Optical Properties of WSe₂

Figure 95a reports Raman spectra for the WSe₂ as a function of He^+ irradiation dose. The pristine material exhibits two strong characteristic peaks attributed to the E_{2g}^1 and A_{1g} peaks. As the He^+ dose increases, the peak intensities decrease, and at a dose of $5 \times 10^{15} \text{ He}^+/\text{cm}^2$ and greater, the E_{2g}^1 and A_{1g} peaks are quenched completely, due to defects and lattice distortions generated from He^+ irradiation. The photoluminescence (PL) spectra of the irradiated WSe₂ are shown in **Figure 95b**. The PL peak at $\sim 1.6 \text{ eV}$ is quenched rapidly at doses of $5 \times 10^{14} \text{ He}^+/\text{cm}^2$ and greater, indicating that even relatively low doses introduce a sufficient number defects to quench emission. Similar quenching behavior has been observed for MoS₂, where plasma was used to induce defects²⁴⁴.

Temperature-Dependent Current-Voltage Characteristics

Figure 96a and **Figure 96b** report the temperature dependent source-drain I-V characteristics of a pseudo-metallic device at $V_{GS} = 80\text{V}$ and -80V , respectively.

Electron Energy Loss Spectra (EELS)

EELS spectra shown in **Figure 97**, contain the selenium $L_{2,3}$ ionization edge at 1436 eV and the W $M_{4,5}$ edge at 1809eV . With increasing dose, the selenium edge decreases while the W edge remains almost constant. Further analysis show that the Se signal is reduced by more than 50% by irradiation with a dose of $1 \times 10^{17} \text{ He}^+/\text{cm}^2$. This indicates that the Se concentration is being reduced by interaction with the He^+ beam. It is concluded that the He^+ preferentially sputters the Se atoms in comparison to W consistent with ion-solid Monte Carlo simulations²²⁷.

Inverter Device Characteristics

Figure 98a-c shows the transfer curves and I-V characteristic for the transistor and resistor portion of the WS₂ logic gate. This device was back-gated by SiO₂, which has a relatively low dielectric constant. This explains the low voltage gain for the inverter. **Figure**

99a,b show the transfer curves and I-V characteristic for the transistor and resistor portion of the WSe₂ logic gate. This device was top-gated with a high dielectric constant ionic liquid.

Details of Ionic Liquid Gating

1-hexyl-3-methylimidazolium bis(trimethylsulfonyl)imide ([hmim][Tf₂N]) was used as a high dielectric constant ionic liquid (IL) to gate the WSe₂ inverter device. A droplet was placed on top of the inverter device in vacuum, and contacted with a probe tip. A schematic of this is shown in **Figure 100**.

3.2.6.2 Figures

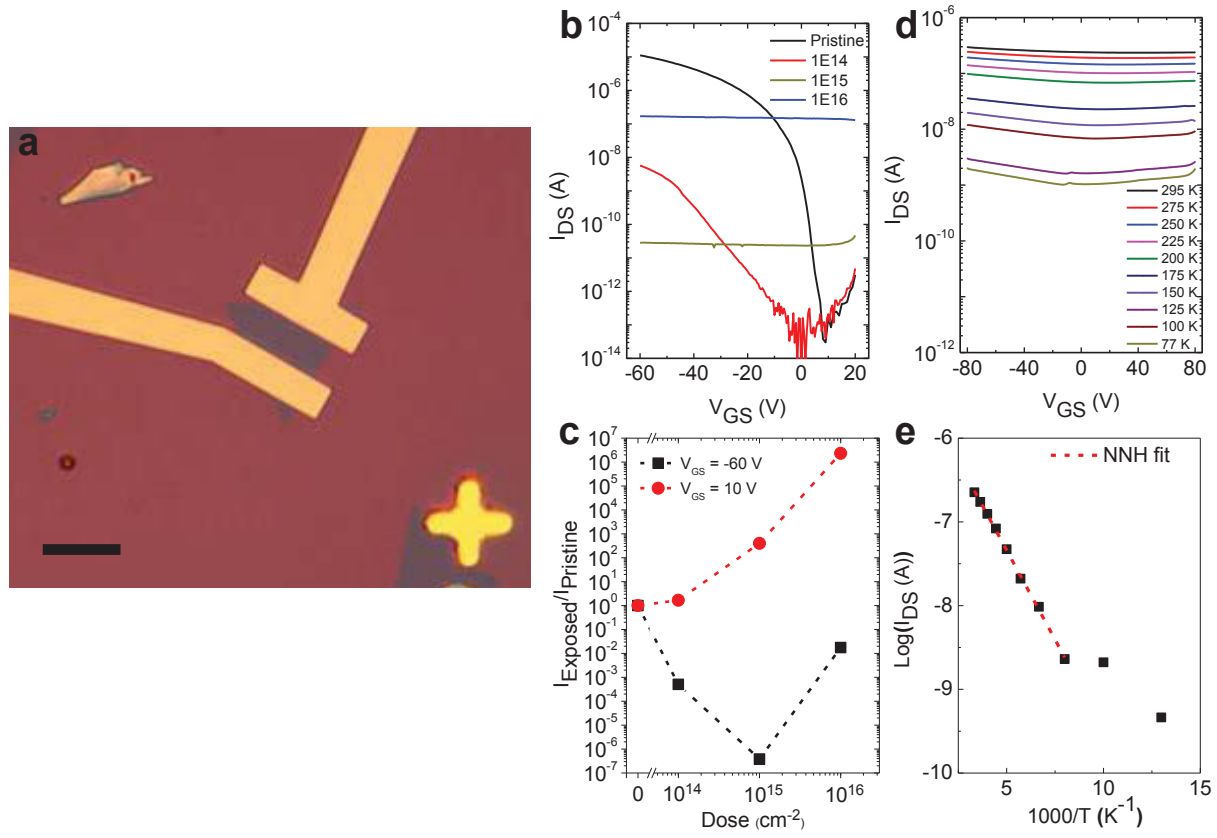


Figure 88. He^+ dose dependent electrical properties. (a) Optical micrograph of a standard WSe_2 FET device. Scale bar is $10\ \mu\text{m}$. (b) Transfer curves for exposed FETs with $V_{\text{DS}} = -1.1\ \text{V}$. (c) Plot of the current ratio: current of the exposed device to current of pristine device at $V_{\text{GS}} = 10$ and $-60\ \text{V}$. (d) Temperature-dependent transfer curves for WSe_2 exposed with a dose of $1 \times 10^{16}\ \text{He}^+/\text{cm}^2$. (e) Arrhenius plot of the device current (I_{DS}) and fitting results of nearest-neighbor hopping model with an activation energy (E_a) of $36.7\ \text{meV}$.

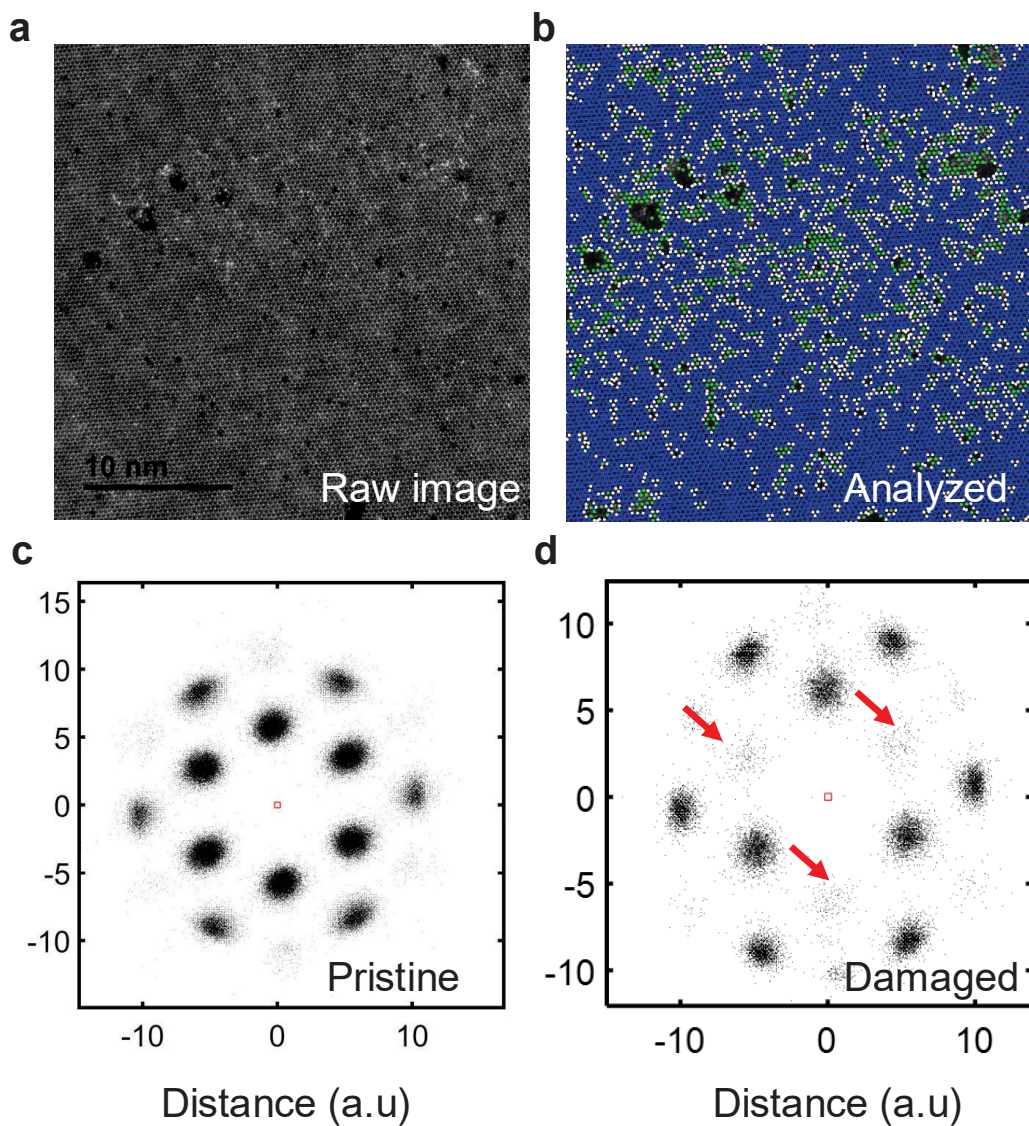


Figure 89. STEM image of exposed WSe₂. (a) HAADF STEM image of WSe₂ which was exposed with a dose of 1×10^{15} He⁺/cm². Field of view is 32 nm. (b) STEM image local crystallography analysis using K-means clustering, on the six-nearest neighbor bond-lengths to each atom. Blue atoms represent a pristine lattice, white atoms are around point defects (light damage), and green atoms are extended defects (heavy damage). Nearest neighbor distribution in real space for (c) pristine (blue) and (d) lightly damaged (white) atoms in the lattice. Lightly damage cluster shows significantly lower counts for neighbors in 'downward pointing' trimer, which corresponds with preferentially sputtered Se.

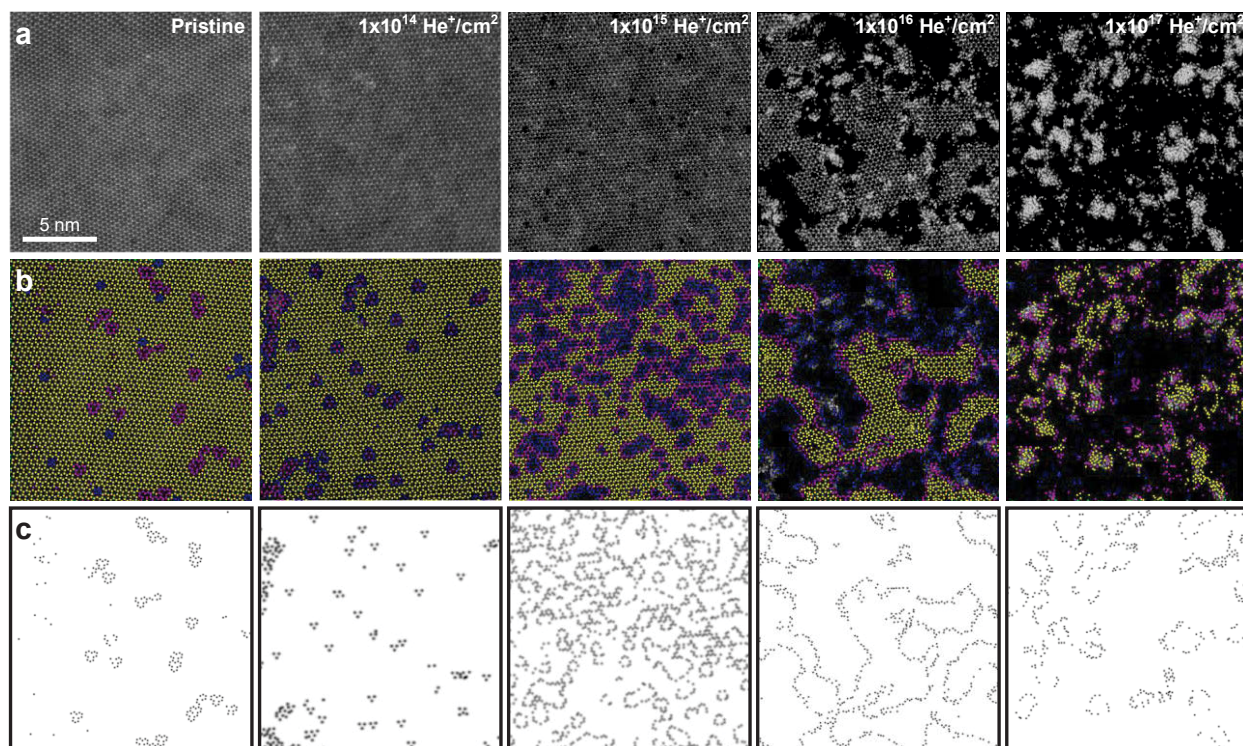


Figure 90. STEM images and analysis. (a) High angle annular dark field (HAADF) STEM images of WSe₂ irradiated with varying doses of He⁺ (text inset in image). (b) K-means cluster analyzed STEM images. (c) Only the vacancy boundary atoms (magenta color in the mid row) from the STEM images (top row).

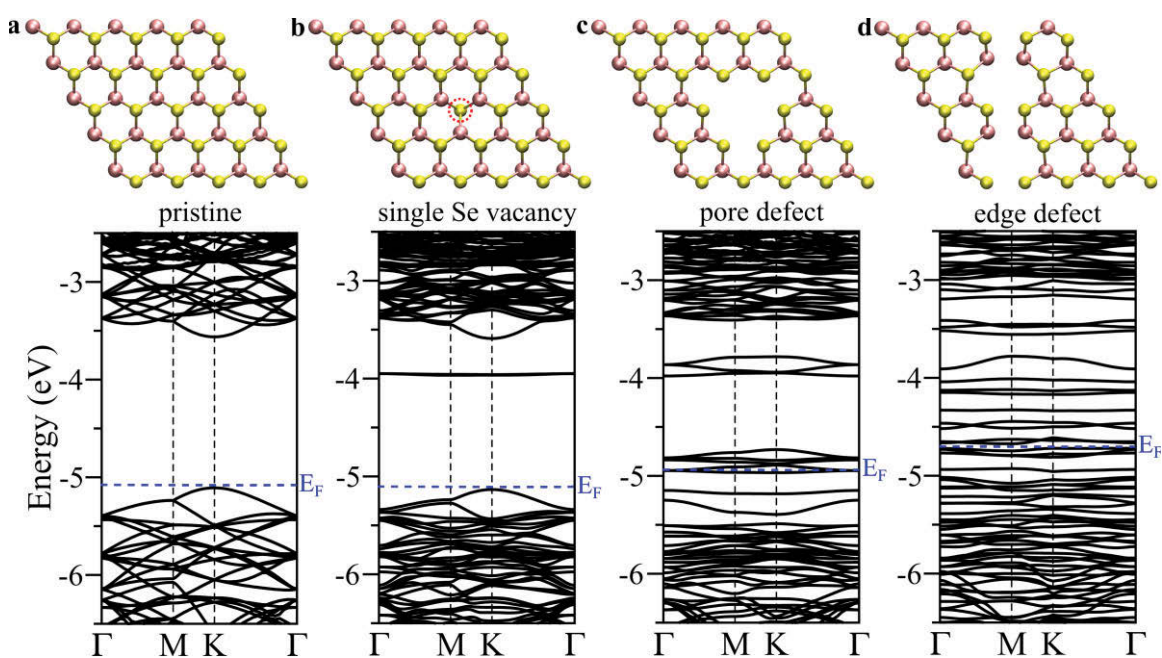


Figure 91. DFT results for pristine and defective single layer WSe₂. Calculated electronic band structures of the 5×5 supercell with (a) no defect, (b) a point defect, (c) a pore defect, and (d) edge defect configurations. All band energies are aligned to the vacuum potential for direct comparison. The Fermi level is set at the valence band maximum for each system, as shown by the blue dashed line. The corresponding atomic structure for each configuration is shown above the band structure. The point defect in (b) corresponds to a single Se vacancy, which is indicated by the red dashed circle.

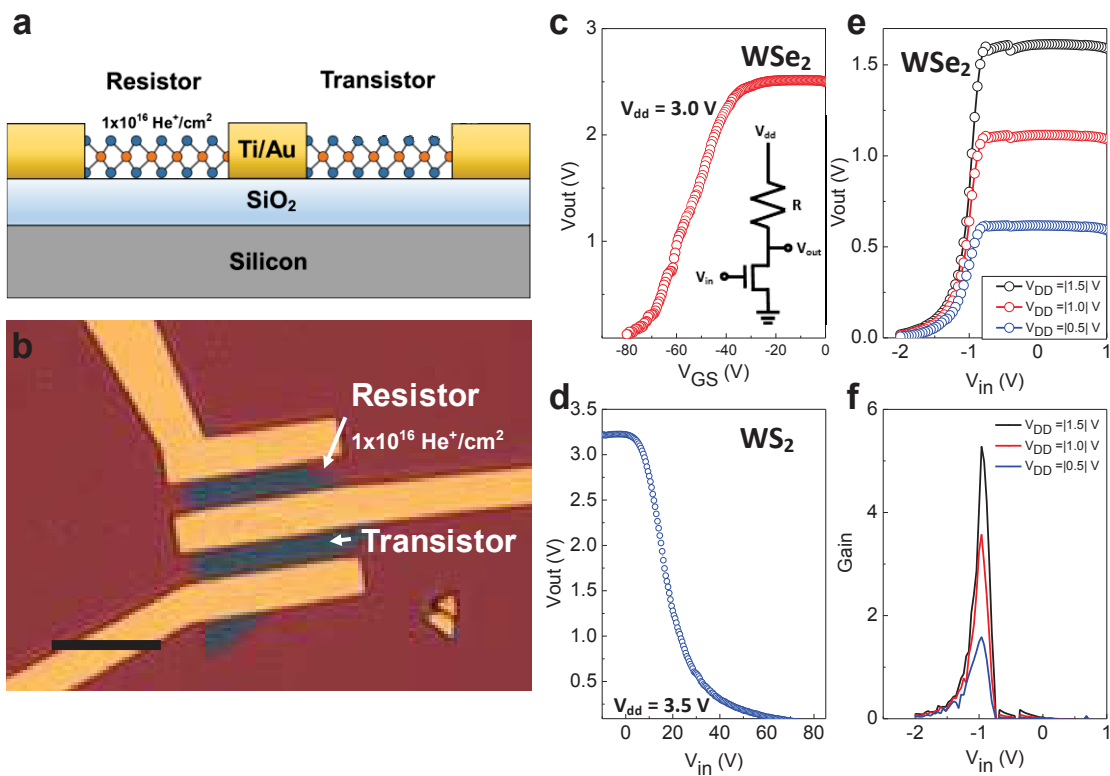


Figure 92. Atomic layer inverters. (a) Schematic of atomic layer inverter created by utilizing exposed and pristine material on a single flake. (b) Optical micrograph of a typical inverter device. Scale bar is 10 μm . (c) Input (V_{in}) – Output (V_{out}) voltage characteristics of a WS₂ atomic layer inverter. Circuit diagram for device is inset. (d) Input (V_{in}) – Output (V_{out}) voltage characteristics of a WSe₂ atomic layer inverter. (e) Input (V_{in}) – Output (V_{out}) voltage characteristics of a WSe₂ atomic layer inverter which was gated with an ionic liquid. (f) Voltage gain ($dV_{\text{out}}/dV_{\text{in}}$) of inverter reported in figure (e).

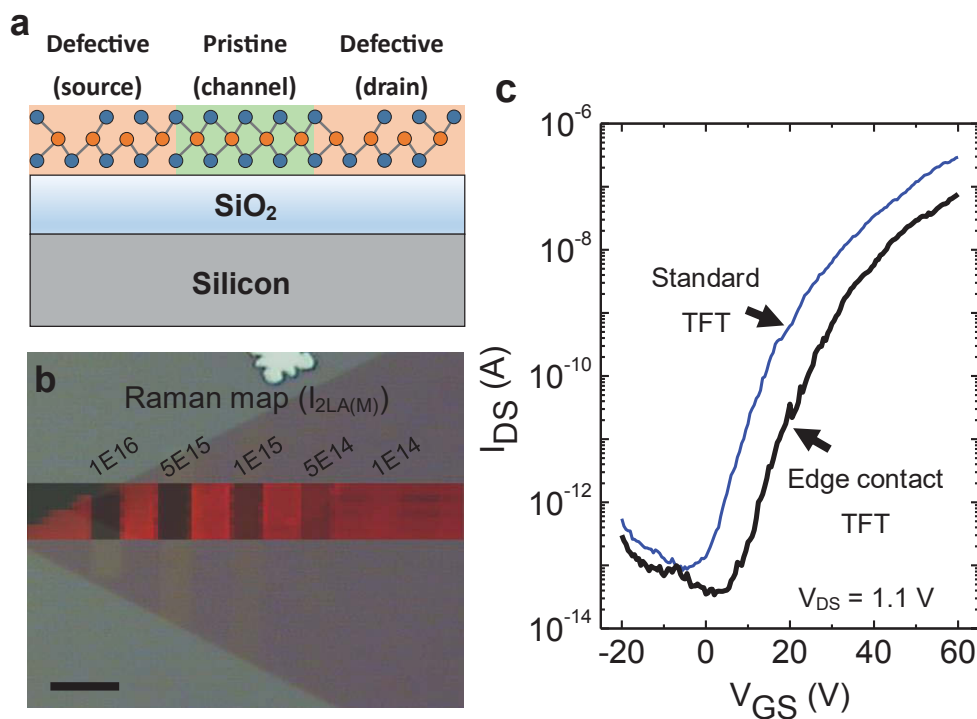


Figure 93. Edge contacts for 2D devices. (a) Schematic of edge contact FET. Source and drain are fabricated from NNH WS₂ (exposed to a dose of 1×10^{16} He⁺/cm²). The FET channel is pristine (unexposed) WS₂. (b) Raman map of a WS₂ flake plotting the intensity of the 2LA(M) peak. The WS₂ flake was exposed to doses varying from 1×10^{14} – 1×10^{16} He⁺/cm² (inset). Scale bar is 10 μ m. Raman map is overlaid on an optical micrograph. (c) Transfer curve for a standard WS₂ FET compared with that of an edge contacted FET in which the source and drain were composed of NNH WS₂.

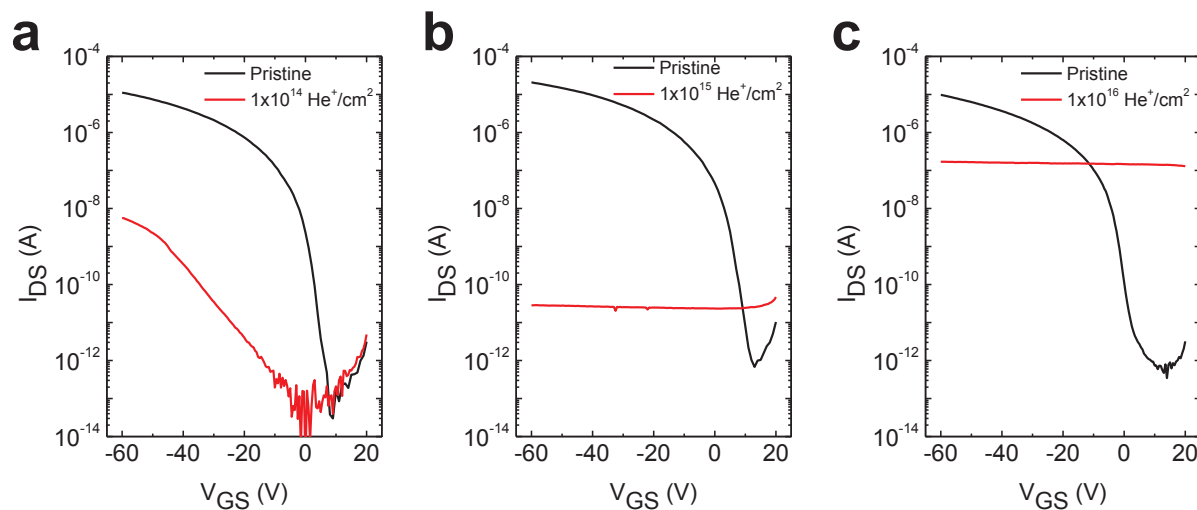


Figure 94. Transfer curves for device before and after irradiation with the He^+ beam. Doses range reported are (a) $1 \times 10^{14} \text{ He}^+/\text{cm}^2$, (b) $1 \times 10^{15} \text{ He}^+/\text{cm}^2$ and (c) $1 \times 10^{16} \text{ He}^+/\text{cm}^2$.

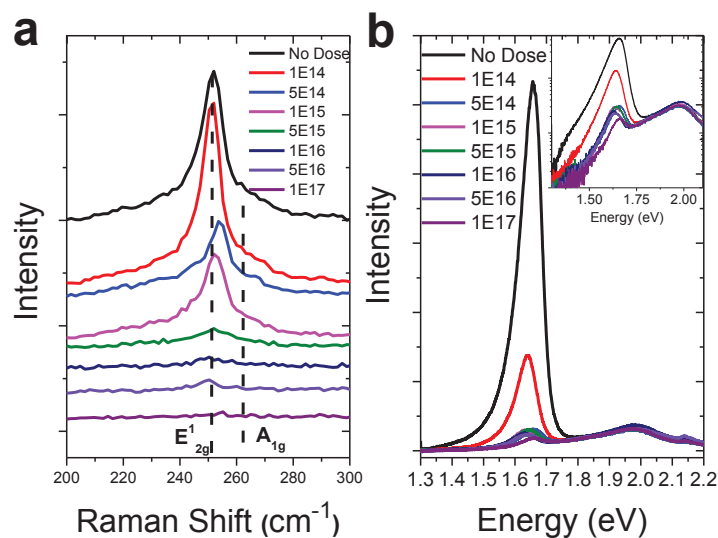


Figure 95. (a) Raman spectra for WSe_2 as a function of He^+ exposure dose. (b) Photoluminescence spectra for WSe_2 as a function of He^+ exposure dose. Log-scale spectra is inset.

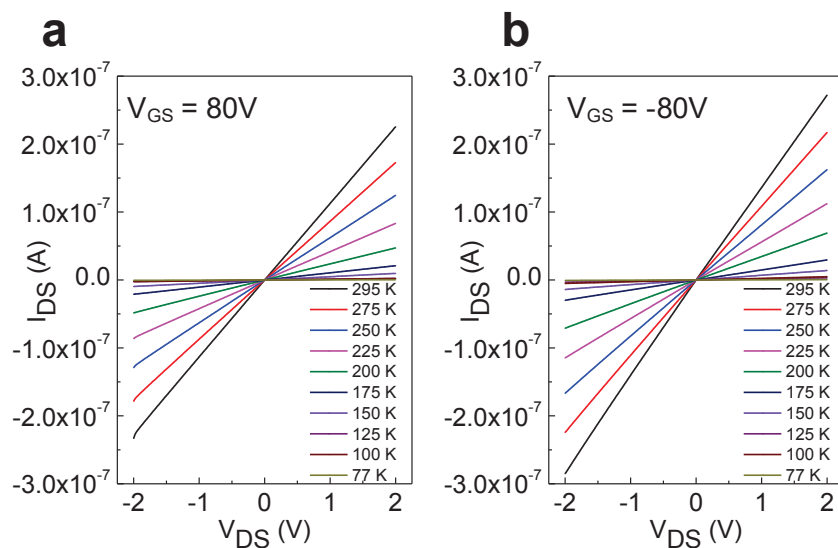


Figure 96. Temperature dependent output curves with a V_{GS} of (a) 80 V and (b) -80 V. The device was exposure with a dose of $1.0 \times 10^{16} \text{ He}^+/\text{cm}^2$ prior to measurement.

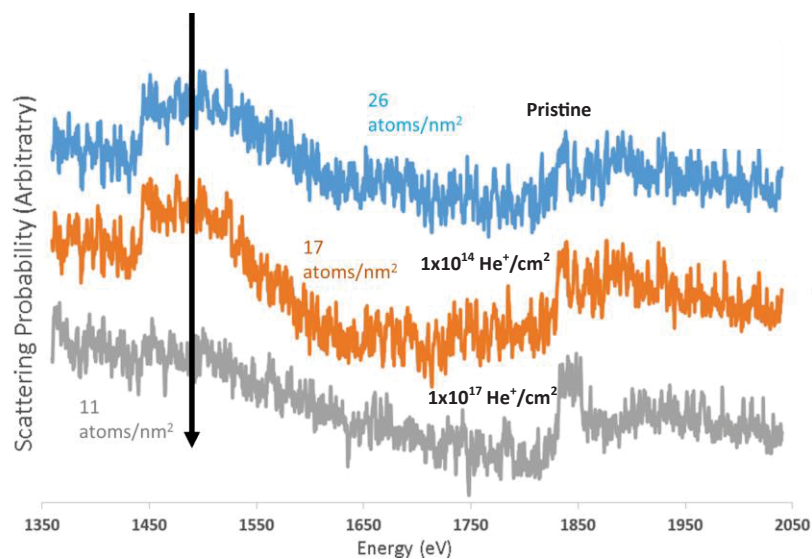


Figure 97. EELS spectra showing a decrease in the area under the selenium $L_{2,3}$ edge with increasing He^+ dose. This is directly correlated to the areal density of the specific element.

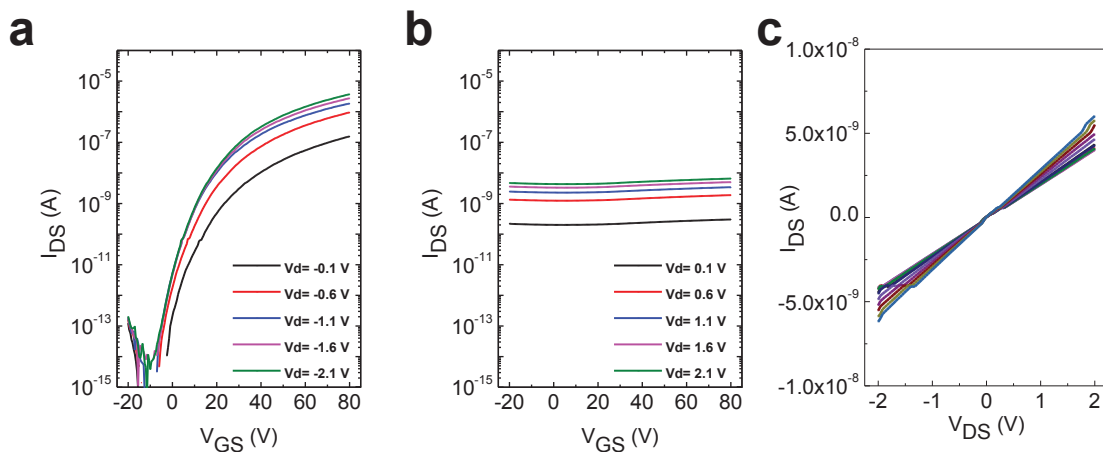


Figure 98. (a) Transfer curves for the WS₂ transistor which was part of the logic gate. (b) Transfer curves of the metallic-like resistor portion of the inverter which demonstrates no effect of gate modulation. (c) I-V characteristic of the resistor.

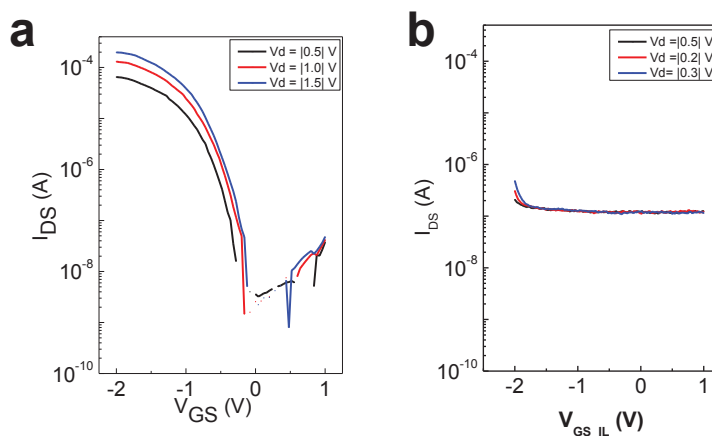


Figure 99. (a) Transfer curves for the WSe₂ transistor which was part of the logic gate. The device was gated with a high dielectric-constant ionic liquid. (b) Transfer curves of the metallic-like resistor portion of the inverter which demonstrates no effect of gate modulation.

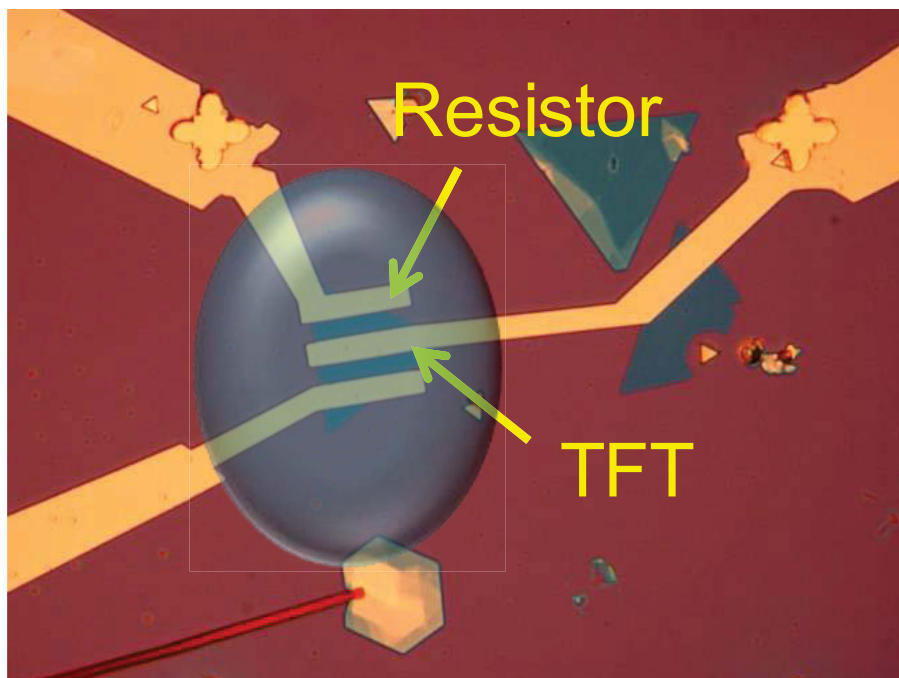


Figure 100. Schematic of a WSe₂ inverter device with IL gating.

CONCLUSION

The results reported in this dissertation represent an advancement in the wide-spread applicability of focused beam induced processing techniques. Chapter I presented laser-assisted techniques to drive the purification of EBID deposits in the SEM chamber. It was demonstrated that O_2 gas as well as inert gas flow can be utilized as a reactive gas in the purification process. An ALD-like process was created which resulted in the high-resolution deposition of pure Pt EBID deposits.

Chapter II presented multiple processing techniques which expand the applicability of the focused He^+ beam as a nanofabrication tool. A laser-assisted He^+ exposure process was used to prevent the formation of subsurface damaged during He^+ processing techniques. This solves a crucial problem which has plagued the He^+ processing community. The focused He^+ beam was also utilized in a laser-assisted etching (LAIBIE) process, which greatly increased the etch rate of Ti while maintaining nanoscale resolution. A similar focused He^+ beam induced etching (IBIE) process was developed to etch WSe_2 . This enabled the formation of highly aligned nanoribbons with sub-10 nm resolution. WSe_2 nanoribbon optical and electronic properties were reported for the first time.

Chapter III reports the effects of focused He^+ beam irradiation on opto-electronic properties of 2D materials, including WSe_2 and WS_2 . Precise defects were selectively introduced in materials by controlled dose of He^+ irradiation, and its effects on structural, optical and electrical properties were investigated via STEM, Raman spectroscopy, and transport measurements. With increasing dose, point defects and local disorder of WSe_2 flake were observed, thereby tuning the electrical transport of the material. A nearest-neighbor hopping transport mechanism was demonstrated and enabled the direct writing of logic gates on a single layer of WSe_2 and WS_2 by defect engineering.

LIST OF REFERENCES

- (1) Randolph, S. J.; Fowlkes, J. D.; Rack, P. D. Focused, Nanoscale Electron-Beam-Induced Deposition and Etching. *Crit. Rev. Solid State Mater. Sci.* **2006**, *31*, 55–89.
- (2) Stanford, M. G.; Lewis, B. B.; Mahady, K.; Fowlkes, J. D.; Rack, P. D. Review Article: Advanced Nanoscale Patterning and Material Synthesis with Gas Field Helium and Neon Ion Beams. *J. Vac. Sci. Technol. B, Nanotechnol. Microelectron. Mater. Process. Meas. Phenom.* **2017**, *35*, 30802.
- (3) Utke, I.; Moshkalev, S.; Russell, P. *Nanofabrication Using Focused Ion and Electron Beams: Principles and Applications*; Oxford University Press, 2012.
- (4) Utke, I.; Hoffmann, P.; Melngailis, J. Gas-Assisted Focused Electron Beam and Ion Beam Processing and Fabrication. *J. Vac. Sci. Technol. B* **2008**, *26*, 1197–1276.
- (5) Spencer, J. A.; Brannaka, J. A.; Barclay, M.; McElwee-White, L.; Fairbrother, D. H. Electron-Induced Surface Reactions of η^3 -Allyl Ruthenium Tricarbonyl Bromide [$(\eta^3\text{-C}_3\text{H}_5)\text{Ru}(\text{CO})_3\text{Br}$]: Contrasting the Behavior of Different Ligands. *J. Phys. Chem. C* **2015**, *119*, 15349–15359.
- (6) Spencer, J.; Rosenberg, S.; Barclay, M.; Wu, Y.-C.; McElwee-White, L.; Howard Fairbrother, D. Understanding the Electron-Stimulated Surface Reactions of Organometallic Complexes to Enable Design of Precursors for Electron Beam-Induced Deposition. *Appl. Phys. A* **2014**, *117*, 1631–1644.
- (7) Komsa, H.-P.; Kotakoski, J.; Kurasch, S.; Lehtinen, O.; Kaiser, U.; Krasheninnikov, A. V. Two-Dimensional Transition Metal Dichalcogenides under Electron Irradiation: Defect Production and Doping. *Phys. Rev. Lett.* **2012**, *109*, 35503.
- (8) Maas, D.; van Veldhoven, E.; Chen, P.; Sidorkin, V.; Salemink, H.; van der Drift, E.; Alkemade, P. Nanofabrication with a Helium Ion Microscope. In *METROLOGY, INSPECTION, AND PROCESS CONTROL FOR MICROLITHOGRAPHY XXIV*; Raymond, C., Ed.; Proceedings of SPIE-The International Society for Optical Engineering; 2010; Vol. 7638.
- (9) Fox, D. S.; Zhou, Y.; Maguire, P.; O'Neill, A.; Ó'Coileáin, C.; Gatensby, R.; Glushenkov, A. M.; Tao, T.; Duesberg, G. S.; Shvets, I. V.; *et al.* Nanopatterning and Electrical Tuning of MoS₂ Layers with a Subnanometer Helium Ion Beam. *Nano Lett.* **2015**, *15*, 5307–5313.

- (10) Fox, D.; Zhou, Y. B.; O'Neill, A.; Kumar, S.; Wang, J. J.; Coleman, J. N.; Duesberg, G. S.; Donegan, J. F.; Zhang, H. Z. Helium Ion Microscopy of Graphene: Beam Damage, Image Quality and Edge Contrast. *Nanotechnology* **2013**, *24*, 1–7.
- (11) Iberi, V.; Vlassiouk, I.; Zhang, X.-G.; Matola, B.; Linn, A.; Joy, D. C.; Rondinone, A. J. Maskless Lithography and in Situ Visualization of Conductivity of Graphene Using Helium Ion Microscopy. *Sci. Rep.* **2015**, *5*, 11952.
- (12) Nanda, G.; Goswami, S.; Watanabe, K.; Taniguchi, T.; Alkemade, P. F. A. Defect Control and N-Doping of Encapsulated Graphene by Helium-Ion-Beam Irradiation. *Nano Lett.* **2015**, *15*, 4006–4012.
- (13) Yang, J.; Ferranti, D. C.; Stern, L. A.; Sanford, C. A.; Huang, J.; Ren, Z.; Qin, L.-C.; Hall, A. R. Rapid and Precise Scanning Helium Ion Microscope Milling of Solid-State Nanopores for Biomolecule Detection. *Nanotechnology* **2011**, *22*, 285310.
- (14) Guo, H.; Dong, S.; Rack, P. D.; Budai, J. D.; Beekman, C.; Gai, Z.; Siemons, W.; Gonzalez, C. M.; Timilsina, R.; Wong, A. T.; *et al.* Strain Doping: Reversible Single-Axis Control of a Complex Oxide Lattice via Helium Implantation. *Phys. Rev. Lett.* **2015**, *114*, 256801.
- (15) Wu, H. M.; Stern, L. A.; Chen, J. H.; Huth, M.; Schwalb, C. H.; Winhold, M.; Porrati, F.; Gonzalez, C. M.; Timilsina, R.; Rack, P. D. Synthesis of Nanowires via Helium and Neon Focused Ion Beam Induced Deposition with the Gas Field Ion Microscope. *Nanotechnology* **2013**, *24*, 175302.
- (16) Melli, M.; Polyakov, A.; Gargas, D.; Huynh, C.; Scipioni, L.; Bao, W.; Ogletree, D. F.; Schuck, P. J.; Cabrini, S.; Weber-Bargioni, A. Reaching the Theoretical Resonance Quality Factor Limit in Coaxial Plasmonic Nanoresonators Fabricated by Helium Ion Lithography. *Nano Lett.* **2013**, *13*, 2687–2691.
- (17) Wang, Y.; Abb, M.; Boden, S. A.; Aizpurua, J.; de Groot, C. H.; Muskens, O. L. Ultrafast Nonlinear Control of Progressively Loaded, Single Plasmonic Nanoantennas Fabricated Using Helium Ion Milling. *Nano Lett.* **2013**, *13*, 5647–5653.
- (18) Scipioni, L.; Ferranti, D. C.; Smentkowski, V. S.; Potyrailo, R. A. Fabrication and Initial Characterization of Ultrahigh Aspect Ratio Vias in Gold Using the Helium Ion Microscope. *J. Vac. Sci. Technol. B* **2010**, *28*, C6P18.

- (19) Cybart, S. A.; Y., C.; J., W.; Wehlin, B. H.; Ma, M. K.; Huynh, C.; C., D. Nano Josephson Superconducting Tunnel Junctions in YBa₂Cu₃O_{7- δ} Directly Patterned with a Focused Helium Ion Beam. *Nat Nano* **2015**, *10*, 598–602.
- (20) Tan, S.; Livengood, R. H.; Hallstein, R.; Shima, D.; Greenzweig, Y.; Notte, J.; McVey, S. Neon Ion Microscope Nanomachining Considerations. In *ISTFA 2011: Conference Proceedings of the 37th International Symposium for Testing and Failure Analysis: November 13-17, 2011, San Jose Convention Center, San Jose, California, USA*; ASM International, 2011; p. 40.
- (21) Tan, S.; Livengood, R.; Hack, P.; Hallstein, R.; Shima, D.; Notte, J.; McVey, S. Nanomachining with a Focused Neon Beam: A Preliminary Investigation for Semiconductor Circuit Editing and Failure Analysis. *J. Vac. Sci. Technol. B* **2011**, *29*, 06F604.
- (22) Botman, A.; Mulders, J. J. L.; Hagen, C. W. Creating Pure Nanostructures from Electron-Beam-Induced Deposition Using Purification Techniques: A Technology Perspective. *Nanotechnology* **2009**, *20*.
- (23) Utke, I.; Friedli, V.; Purrucker, M.; Michler, J. Resolution in Focused Electron- and Ion-Beam Induced Processing. *J. Vac. Sci. Technol. B* **2007**, *25*, 2219–2223.
- (24) Smith, D. A.; Fowlkes, J. D.; Rack, P. D. Understanding the Kinetics and Nanoscale Morphology of Electron-Beam-Induced Deposition via a Three-Dimensional Monte Carlo Simulation: The Effects of the Precursor Molecule and the Deposited Material. *Small* **2008**, *4*, 1382–1389.
- (25) Fowlkes, J. D.; Rack, P. D. Fundamental Electron-Precursor-Solid Interactions Derived from Time-Dependent Electron-Beam-Induced Deposition Simulations and Experiments. *ACS Nano* **2010**, *4*, 1619–1629.
- (26) Rykaczewski, K.; White, W. B.; Fedorov, A. G. Analysis of Electron Beam Induced Deposition (EBID) of Residual Hydrocarbons in Electron Microscopy. *J. Appl. Phys.* **2007**, *101*, 54307.
- (27) Toth, M.; Lobo, C. J.; Hartigan, G.; Knowles, W. R. Electron Flux Controlled Switching between Electron Beam Induced Etching and Deposition. *J. Appl. Phys.* **2007**, *101*, 54309.
- (28) Utke, I.; Hoffmann, P.; Berger, R.; Scandella, L. High-Resolution Magnetic Co Supertips

- Grown by a Focused Electron Beam. *Appl. Phys. Lett.* **2002**, *80*, 4792–4794.
- (29) Noh, J. H.; Nikiforov, M.; Kalinin, S. V.; Vertegel, A. A.; Rack, P. D. Nanofabrication of Insulated Scanning Probes for Electromechanical Imaging in Liquid Solutions. *Nanotechnology* **2010**, *21*.
 - (30) Serrano-Ramon, L.; Cordoba, R.; Alfredo Rodriguez, L.; Magen, C.; Snoeck, E.; Gatel, C.; Serrano, I.; Ricardo Ibarra, M.; Maria De Teresa, J. Ultrasmall Functional Ferromagnetic Nanostructures Grown by Focused Electron-Beam-Induced Deposition. *ACS Nano* **2011**, *5*, 7781–7787.
 - (31) Gavagnin, M.; Wanzenboeck, H. D.; Belic, D.; Bertagnolli, E. Synthesis of Individually Tuned Nanomagnets for Nanomagnet Logic by Direct Write Focused Electron Beam Induced Deposition. *ACS Nano* **2013**, *7*, 777–784.
 - (32) Choo, H.; Kim, M. K.; Staffaroni, M.; Seok, T. J.; Bokor, J.; Cabrini, S.; Schuck, P. J.; Wu, M. C.; Yablonovitch, E. Nanofocusing in a Metal-Insulator-Metal Gap Plasmon Waveguide with a Three-Dimensional Linear Taper. *Nat. Photonics* **2012**, *6*, 837–843.
 - (33) Utke, I.; Jenke, M. G.; Roling, C.; Thiesen, P. H.; Iakovlev, V.; Sirbu, A.; Mereuta, A.; Caliman, A.; Kapon, E. Polarisation Stabilisation of Vertical Cavity Surface Emitting Lasers by Minimally Invasive Focused Electron Beam Triggered Chemistry. *Nanoscale* **2011**, *3*, 2718–2722.
 - (34) Koops, H. W. P.; Schossler, C.; Kaya, A.; Weber, M. Conductive Dots, Wires, and Supertips for Field Electron Emitters Produced by Electron-Beam Induced Deposition on Samples Having Increased Temperature. *J. Vac. Sci. Technol. B* **1996**, *14*, 4105–4109.
 - (35) Yang, X.; Simpson, M. L.; Randolph, S. J.; Rack, P. D.; Baylor, L. R.; Cui, H.; Gardner, W. L. Integrated Tungsten Nanofiber Field Emission Cathodes Selectively Grown by Nanoscale Electron Beam-Induced Deposition. *Appl. Phys. Lett.* **2005**, *86*, 183106.
 - (36) Kolb, F.; Schmoltner, K.; Huth, M.; Hohenau, A.; Krenn, J. R.; Klug, A.; List, E. J. W.; Plank, H. Variable Tunneling Barriers in FEBID Based PtC Metal-Matrix Nanocomposites as a Transducing Element for Humidity Sensing. *Nanotechnology* **2013**, *24*, 305501.
 - (37) Schwalb, C. H.; Grimm, C.; Baranowski, M.; Sachser, R.; Porra, F.; Reith, H.; Das, P.; Mueller, J.; Voelklein, F.; Kaya, A.; *et al.* A Tunable Strain Sensor Using Nanogranular

- Metals. *Sensors* **2010**, *10*, 9847–9856.
- (38) Guan, Y.; Fowlkes, J. D.; Retterer, S. T.; Simpson, M. L.; Rack, P. D. Nanoscale Lithography via Electron Beam Induced Deposition. *Nanotechnology* **2008**, *19*.
 - (39) Mackus, A. J. M.; Thissen, N. F. W.; Mulders, J. J. L.; Trompenaars, P. H. F.; Verheijen, M. A.; Bol, A. A.; Kessels, W. M. M. Direct-Write Atomic Layer Deposition of High-Quality Pt Nanostructures: Selective Growth Conditions and Seed Layer Requirements. *J. Phys. Chem. C* **2013**, *117*, 10788–10798.
 - (40) Rykaczewski, K.; Hildreth, O. J.; Kulkarni, D.; Henry, M. R.; Kim, S. K.; Wong, C. P.; Tsukruk, V. V.; Fedorov, A. G. Mask Less and Resist-Free Rapid Prototyping of Three-Dimensional Structures Through Electron Beam Induced Deposition (EBID) of Carbon in Combination with Metal-Assisted Chemical Etching (MaCE) of Silicon. *ACS Appl. Mater. Interfaces* **2010**, *2*, 969–973.
 - (41) Seki, Y.; Furuta, Y.; Nishikawa, H.; Watanabe, T.; Nakata, T.; Satoh, T.; Ishii, Y.; Kamiya, T. Electroplating Using High-Aspect-Ratio Microstructures Fabricated by Proton Beam Writing. *Microelectron. Eng.* **2009**, *86*, 945–948.
 - (42) Lassiter, M. G.; Liang, T.; Rack, P. D. Inhibiting Spontaneous Etching of Nanoscale Electron Beam Induced Etching Features: Solutions for Nanoscale Repair of Extreme Ultraviolet Lithography Masks. *J. Vac. Sci. Technol. B* **2008**, *26*, 963–967.
 - (43) Liang, T.; Frendberg, E.; Lieberman, B.; Stivers, A. Advanced Photolithographic Mask Repair Using Electron Beams. *J. Vac. Sci. Technol. B* **2005**, *23*, 3101–3105.
 - (44) Noh, J. H.; Stanford, M. G.; Lewis, B. B.; Fowlkes, J. D.; Plank, H.; Rack, P. D. Nanoscale Electron Beam-Induced Deposition and Purification of Ruthenium for Extreme Ultraviolet Lithography Mask Repair. *Appl. Phys. A* **2014**, *117*, 1705–1713.
 - (45) Bret, T.; Afra, B.; Becker, R.; Hofmann, T.; Edinger, K.; Liang, T.; Hoffmann, P. Gas Assisted Focused Electron Beam Induced Etching of Alumina. *J. Vac. Sci. Technol. B* **2009**, *27*, 2727–2731.
 - (46) Makise, K.; Mitsuishi, K.; Shimojo, M.; Shinozaki, B. Microstructural Analysis and Transport Properties of MoO and MoC Nanostructures Prepared by Focused Electron Beam-Induced Deposition. *Sci. Rep.* **2014**, *4*.
 - (47) Winhold, M.; Weirich, P. M.; Schwalb, C. H.; Huth, M. Superconductivity and Metallic

- Behavior in PbxCyO_8 Structures Prepared by Focused Electron Beam Induced Deposition. *Appl. Phys. Lett.* **2014**, *105*.
- (48) Brintlinger, T.; Fuhrer, M. S.; Melngailis, J.; Utke, I.; Bret, T.; Perentes, A.; Hoffmann, P.; Abourida, M.; Doppelt, P. Electrodes for Carbon Nanotube Devices by Focused Electron Beam Induced Deposition of Gold. *J. Vac. Sci. Technol. B* **2005**, *23*, 3174–3177.
- (49) Botman, A.; Hesselberth, M.; Mulders, J. J. L. Improving the Conductivity of Platinum-Containing Nano-Structures Created by Electron-Beam-Induced Deposition. *Microelectron. Eng.* **2008**, *85*, 1139–1142.
- (50) Plank, H.; Gspan, C.; Dienstleder, M.; Kothleitner, G.; Hofer, F. The Influence of Beam Defocus on Volume Growth Rates for Electron Beam Induced Platinum Deposition. *Nanotechnology* **2008**, *19*.
- (51) Gopal, V.; Radmilovic, V. R.; Daraio, C.; Jin, S.; Yang, P. D.; Stach, E. A. Rapid Prototyping of Site-Specific Nanocontacts by Electron and Ion Beam Assisted Direct-Write Nanolithography. *Nano Lett.* **2004**, *4*, 2059–2063.
- (52) Botman, A.; Mulders, J. J. L.; Weemaes, R.; Mentink, S. Purification of Platinum and Gold Structures after Electron-Beam-Induced Deposition. *Nanotechnology* **2006**, *17*, 3779–3785.
- (53) Langford, R. M.; Wang, T. X.; Ozkaya, D. Reducing the Resistivity of Electron and Ion Beam Assisted Deposited Pt. *Microelectron. Eng.* **2007**, *84*, 784–788.
- (54) Stark, T. J.; Mayer, T. M.; Griffis, D. P.; Russell, P. E. FORMATION OF COMPLEX FEATURES USING ELECTRON-BEAM DIRECT-WRITE DECOMPOSITION OF PALLADIUM ACETATE. *J. Vac. Sci. Technol. B* **1992**, *10*, 2685–2689.
- (55) Klein, K. L.; Randolph, S. J.; Fowlkes, J. D.; Allard, L. F.; Meyer III, H. M.; Simpson, M. L.; Rack, P. D. Single-Crystal Nanowires Grown via Electron-Beam-Induced Deposition. *Nanotechnology* **2008**, *19*.
- (56) Fernandez-Pacheco, A.; De Teresa, J. M.; Cordoba, R.; Ibarra, M. R. Magnetotransport Properties of High-Quality Cobalt Nanowires Grown by Focused-Electron-Beam-Induced Deposition. *J. Phys. D-Applied Phys.* **2009**, *42*.
- (57) Tseng, A. A. *Nanofabrication: Fundamentals and Applications*; World Scientific, 2008.
- (58) Langford, R. M.; Ozkaya, D.; Sheridan, J.; Chater, R. Effects of Water Vapour on

- Electron and Ion Beam Deposited Platinum. *Microsc. Microanal.* **2004**, *10*, 1122–1123M3–10.1017/S1431927604883417.
- (59) Perentes, A.; Hoffmann, P. Focused Electron Beam Induced Deposition of Si-Based Materials from SiOxCy to Stoichiometric SiO₂: Chemical Compositions, Chemical-Etch Rates, and Deep Ultraviolet Optical Transmissions. *Chem. Vap. Depos.* **2007**, *13*, 176–184.
 - (60) Mehendale, S.; Mulders, J. J. L.; Trompenaars, P. H. F. A New Sequential EBID Process for the Creation of Pure Pt Structures from MeCpPtMe₃. *Nanotechnology* **2013**, *24*, 145303.
 - (61) Plank, H.; Noh, J. H.; Fowlkes, J. D.; Lester, K.; Lewis, B. B.; Rack, P. D. Electron-Beam-Assisted Oxygen Purification at Low Temperatures for Electron-Beam-Induced Pt Deposits: Towards Pure and High-Fidelity Nanostructures. *ACS Appl. Mater. Interfaces* **2014**, *6*, 1018–1024.
 - (62) Geier, B.; Gspan, C.; Winkler, R.; Schmied, R.; Fowlkes, J. D.; Fitzek, H.; Rauch, S.; Rattenberger, J.; Rack, P. D.; Plank, H. Rapid and Highly Compact Purification for Focused Electron Beam Induced Deposits: A Low Temperature Approach Using Electron Stimulated H₂O Reactions. *J. Phys. Chem. C* **2014**, *118*, 14009–14016.
 - (63) Takeguchi, M.; Shimojo, M.; Furuya, K. Post-Deposition Processes for Nanostructures Formed by Electron Beam Induced Deposition with Pt(PF₃)(4) Precursor. *Appl. Phys. a-Materials Sci. Process.* **2008**, *93*, 439–442.
 - (64) Porrati, F.; Sachser, R.; Schwalb, C. H.; Frangakis, A. S.; Huth, M. Tuning the Electrical Conductivity of Pt-Containing Granular Metals by Postgrowth Electron Irradiation. *J. Appl. Phys.* **2011**, *109*.
 - (65) Roberts, N. A.; Fowlkes, J. D.; Magel, G. A.; Rack, P. D. Enhanced Material Purity and Resolution via Synchronized Laser Assisted Electron Beam Induced Deposition of Platinum. *Nanoscale* **2013**, *5*, 408–415.
 - (66) Roberts, N. A.; Gonzalez, C. M.; Fowlkes, J. D.; Rack, P. D. Enhanced by-Product Desorption via Laser Assisted Electron Beam Induced Deposition of W (CO)₆ with Improved Conductivity and Resolution. *Nanotechnology* **2013**, *24*, 415301.
 - (67) Arnold, G.; Timilsina, R.; Fowlkes, J.; Orthacker, A.; Kothleitner, G.; Rack, P. D.; Plank,

- H. Fundamental Resolution Limits during Electron-Induced Direct-Write Synthesis. *ACS Appl. Mater. Interfaces* **2014**, *6*, 7380–7387.
- (68) Plank, H.; Smith, D. A.; Haber, T.; Rack, P. D.; Hofer, F. Fundamental Proximity Effects in Focused Electron Beam Induced Deposition. *ACS Nano* **2012**, *6*, 286–294.
- (69) Hopf, C.; Schluter, M.; Schwarz-Selinger, T.; von Toussaint, U.; Jacob, W. Chemical Sputtering of Carbon Films by Simultaneous Irradiation with Argon Ions and Molecular Oxygen. *New J. Phys.* **2008**, *10*, 93022.
- (70) Hiratani, M.; Nabatame, T.; Matsui, Y.; Imagawa, K.; Kimura, S. Platinum Film Growth by Chemical Vapor Deposition Based on Autocatalytic Oxidative Decomposition. *J. Electrochem. Soc.* **2001**, *148*, C524–C527.
- (71) Campbell, C. T.; Ertl, G.; Kuipers, H.; Segner, J. A MOLECULAR-BEAM STUDY OF THE ADSORPTION AND DESORPTION OF OXYGEN FROM A PT(111)SURFACE. *Surf. Sci.* **1981**, *107*, 220–236.
- (72) Matsushima, T.; Almy, D. B.; White, J. M. The Reactivity and Auger Chemical Shift of Oxygen Adsorbed on Platinum. *Surf. Sci.* **1977**, *67*, 89–108.
- (73) Sachser, R.; Reith, H.; Huzel, D.; Winhold, M.; Huth, M. Catalytic Purification of Directly Written Nanostructured Pt Microelectrodes. *ACS Appl. Mater. Interfaces* **2014**.
- (74) Roberts, N. A.; Magel, G. A.; Hartfield, C. D.; Moore, T. M.; Fowlkes, J. D.; Rack, P. D. In Situ Laser Processing in a Scanning Electron Microscope. *J. Vac. Sci. Technol. A* **2012**, *30*.
- (75) Botman, A.; Mulders, J. J. L.; Hagen, C. W. Creating Pure Nanostructures from Electron-Beam-Induced Deposition Using Purification Techniques: A Technology Perspective. *Nanotechnology* **2009**, *20*.
- (76) Hoeflich, K.; Yang, R. Bin; Berger, A.; Leuchs, G.; Christiansen, S. The Direct Writing of Plasmonic Gold Nanostructures by Electron-Beam-Induced Deposition. *Adv. Mater.* **2011**, *23*, 2657+.
- (77) Makise, K.; Mitsuishi, K.; Shimojo, M.; Shinozaki, B. Microstructural Analysis and Transport Properties of MoO and MoC Nanostructures Prepared by Focused Electron Beam-Induced Deposition. *Sci. Rep.* **2014**, *4*.
- (78) Winhold, M.; Weirich, P. M.; Schwalb, C. H.; Huth, M. Superconductivity and Metallic

- Behavior in PbxCyO_8 Structures Prepared by Focused Electron Beam Induced Deposition. *Appl. Phys. Lett.* **2014**, *105*, 162603.
- (79) Wnuk, J. D.; Rosenberg, S. G.; Gorham, J. M.; van Dorp, W. F.; Hagen, C. W.; Fairbrother, D. H. Electron Beam Deposition for Nanofabrication: Insights from Surface Science. *Surf. Sci.* **2011**, *605*, 257–266.
- (80) Takeguchi, M.; Shimojo, M.; Furuya, K. Post-Deposition Processes for Nanostructures Formed by Electron Beam Induced Deposition with $\text{Pt}(\text{PF}_3)_4$ Precursor. *Appl. Phys. A Mater. Sci. Process.* **2008**, *93*, 439–442.
- (81) Porrati, F.; Sachser, R.; Schwalb, C. H.; Frangakis, A. S.; Huth, M. Tuning the Electrical Conductivity of Pt-Containing Granular Metals by Postgrowth Electron Irradiation. *J. Appl. Phys.* **2011**, *109*, 63715.
- (82) Belić, D.; Shawrav, M. M.; Gavagnin, M.; Stöger-Pollach, M.; Wanzenboeck, H. D.; Bertagnolli, E. Direct-Write Deposition and Focused-Electron-Beam-Induced Purification of Gold Nanostructures. *ACS Appl. Mater. Interfaces* **2015**, *7*, 2467–2479.
- (83) Villamor, E.; Casanova, F.; Trompenaars, P. H. F.; Mulders, J. J. L. Embedded Purification for Electron Beam Induced Pt Deposition Using MeCpPtMe_3 . *Nanotechnology* **2015**, *26*, 95303.
- (84) Stark, T. J.; Mayer, T. M.; Griffis, D. P.; Russell, P. E. Formation of Complex Features Using Electron-beam Direct-write Decomposition of Palladium Acetate. *J. Vac. Sci. Technol. B* **1992**, *10*, 2685–2689.
- (85) Klein, K. L.; Randolph, S. J.; Fowlkes, J. D.; Allard, L. F.; Meyer III, H. M.; Simpson, M. L.; Rack, P. D. Single-Crystal Nanowires Grown via Electron-Beam-Induced Deposition. *Nanotechnology* **2008**, *19*, 345705.
- (86) Fernandez-Pacheco, A.; De Teresa, J. M.; Cordoba, R.; Ibarra, M. R. Magnetotransport Properties of High-Quality Cobalt Nanowires Grown by Focused-Electron-Beam-Induced Deposition. *J. Phys. D Appl. Phys.* **2009**, *42*, 55005.
- (87) Langford, R. M.; Ozkaya, D.; Sheridan, J.; Chater, R. Effects of Water Vapour on Electron and Ion Beam Deposited Platinum. *Microsc. Microanal.* **2004**, *10*, 1122–1123.
- (88) Martin, A.; McCredie, G.; Toth, M. Electron Beam Induced Etching of Carbon. *Appl. Phys. Lett.* **2015**, (in revision).

- (89) Stanford, M. G.; Lewis, B. B.; Noh, J. H.; Fowlkes, J. D.; Roberts, N. A.; Plank, H.; Rack, P. D. Purification of Nanoscale Electron-Beam-Induced Platinum Deposits via a Pulsed Laser-Induced Oxidation Reaction. *ACS Appl. Mater. Interfaces* **2014**, *6*, 21256–21263.
- (90) Kanarik, K. J.; Lill, T.; Hudson, E. A.; Sriraman, S.; Tan, S.; Marks, J.; Vahedi, V.; Gottscho, R. A. Overview of Atomic Layer Etching in the Semiconductor Industry. *J. Vac. Sci. Technol. A* **2015**, *33*, 20802.
- (91) Mackus, A. J. M.; Leick, N.; Baker, L.; Kessels, W. M. M. Catalytic Combustion and Dehydrogenation Reactions during Atomic Layer Deposition of Platinum. *Chem. Mater.* **2012**, *24*, 1752–1761.
- (92) Xue, Z. L.; Thridandam, H.; Kaesz, H. D.; Hicks, R. F. Organometallic Chemical Vapor Deposition of Platinum. Reaction Kinetics and Vapor Pressures of Precursors. *Chem. Mater.* **1992**, *4*, 162–166.
- (93) Sachser, R.; Reith, H.; Huzel, D.; Winhold, M.; Huth, M. Catalytic Purification of Directly Written Nanostructured Pt Microelectrodes. *ACS Appl. Mater. Interfaces* **2014**, *6*, 15868–15874.
- (94) Fowlkes, J. D.; Geier, B.; Lewis, B. B.; Rack, P. D.; Stanford, M. G.; Winkler, R.; Plank, H. Electron Nanoprobe Induced Oxidation: A Simulation of Direct-Write Purification. *Phys. Chem. Chem. Phys.* **2015**, DOI: 10.1039/C5CP01196E.
- (95) Roberts, N. A.; Magel, G. A.; Hartfield, C. D.; Moore, T. M.; Fowlkes, J. D.; Rack, P. D. In Situ Laser Processing in a Scanning Electron Microscope. *J. Vac. Sci. Technol. A* **2012**, *30*, 41404.
- (96) Kwon, J. H.; Yoon, S. G. Characterization of Pt Thin Films Deposited by Metallorganic Chemical Vapor Deposition for Ferroelectric Bottom Electrodes. *J. Electrochem. Soc.* **1997**, *144*, 2848–2854.
- (97) Knoops, H. C. M.; Mackus, A. J. M.; Donders, M. E.; van de Sanden, M. C. M.; Notten, P. H. L.; Kessels, W. M. M. Remote Plasma ALD of Platinum and Platinum Oxide Films. *Electrochem. SOLID STATE Lett.* **2009**, *12*, G34–G36.
- (98) Aaltonen, T.; Ritala, M.; Tung, Y. L.; Chi, Y.; Arstila, K.; Meinander, K.; Leskela, M. Atomic Layer Deposition of Noble Metals: Exploration of the Low Limit of the Deposition Temperature. *J. Mater. Res.* **2004**, *19*, 3353–3358.

- (99) Arnold, G.; Timilsina, R.; Fowlkes, J.; Orthacker, A.; Kothleitner, G.; Rack, P. D.; Plank, H. Fundamental Resolution Limits during Electron-Induced Direct-Write Synthesis. *ACS Appl. Mater. Interfaces* **2014**, *6*, 7380–7387.
- (100) Maas, D.; van Veldhoven, E.; Chen, P.; Sidorkin, V.; Salemink, H.; van der Drift, E.; Alkemade, P. Nanofabrication with a Helium Ion Microscope. In *Metrology, Inspection, and Process Control for Microlithography XXIV*; Raymond, C., Ed.; Proceedings of SPIE-The International Society for Optical Engineering; 2010; Vol. 7638, pp. 763814-1-763814–10.
- (101) Gonzalez, C. M.; Timilsina, R.; Li, G.; Duschner, G.; Rack, P. D.; Slingenbergh, W.; van Dorp, W. F.; De Hosson, J. T. M.; Klein, K. L.; Wu, H. M.; *et al.* Focused Helium and Neon Ion Beam Induced Etching for Advanced Extreme Ultraviolet Lithography Mask Repair. *J. Vac. Sci. Technol. B* **2014**, *32*, 21602.
- (102) Livengood, R.; Tan, S.; Greenzweig, Y.; Notte, J.; McVey, S. Subsurface Damage from Helium Ions as a Function of Dose, Beam Energy, and Dose Rate. *J. Vac. Sci. Technol. B* **2009**, *27*, 3244–3249.
- (103) Timilsina, R.; Tan, S.; Livengood, R.; Rack, P. D. Monte Carlo Simulations of Nanoscale Focused Neon Ion Beam Sputtering of Copper: Elucidating Resolution Limits and Sub-Surface Damage. *Nanotechnology* **2014**, *25*, 485704.
- (104) Tan, S.; Klein, K.; Shima, D.; Livengood, R.; Mutunga, E.; Vladár, A. Mechanism and Applications of Helium Transmission Milling in Thin Membranes. *J. Vac. Sci. Technol. B* **2014**, *32*, 6FA01.
- (105) Raineri, V.; Saggio, M.; Rimini, E. Voids in Silicon by He Implantation: From Basic to Applications. *J. Mater. Res.* **2000**, *15*, 1449–1477.
- (106) Abrams, K. J.; Hinks, J. A.; Pawley, C. J.; Greaves, G.; van den Berg, J. A.; Eyidi, D.; Ward, M. B.; Donnelly, S. E. Helium Irradiation Effects in Polycrystalline Si, Silica, and Single Crystal Si. *J. Appl. Phys.* **2012**, *111*, 83527.
- (107) Cerofolini, G. F.; Corni, F.; Frabboni, S.; Nobili, C.; Ottaviani, G.; Tonini, R. Hydrogen and Helium Bubbles in Silicon. *Mater. Sci. Eng. R Reports* **2000**, *27*, 1–52.
- (108) Raineri, V.; Fallica, P. G.; Percolla, G.; Battaglia, A.; Barbagallo, M.; Campisano, S. U. Gettering of Metals by Voids in Silicon. *J. Appl. Phys.* **1995**, *78*, 3727.

- (109) Corni, F.; Calzolari, G.; Frabboni, S.; Nobili, C.; Ottaviani, G.; Tonini, R.; Cerofolini, G. F.; Leone, D.; Servidori, M.; Brusa, R. S.; *et al.* Helium-Implanted Silicon: A Study of Bubble Precursors. *J. Appl. Phys.* **1999**, *85*, 1401–1408.
- (110) Brusa, R. S.; Karwasz, G. P.; Tiengo, N.; Zecca, A.; Corni, F.; Calzolari, G.; Nobili, C. He-Implantation Induced Defects in Si Studied by Slow Positron Annihilation Spectroscopy. *J. Appl. Phys.* **1999**, *85*, 2390.
- (111) Oliviero, E.; David, M. L.; Beaufort, M. F.; Barbot, J. F.; van Veen, A. On the Effects of Implantation Temperature in Helium Implanted Silicon. *Appl. Phys. Lett.* **2002**, *81*, 4201–4203.
- (112) Tang, M.; Colombo, L.; Zhu, J.; Diaz de la Rubia, T. Intrinsic Point Defects in Crystalline Silicon: Tight-Binding Molecular Dynamics Studies of Self-Diffusion, Interstitial-Vacancy Recombination, and Formation Volumes. *Phys. Rev. B* **1997**, *55*, 14279–14289.
- (113) Luther, L. C.; Moore, W. J. Diffusion of Helium in Silicon, Germanium, and Diamond. *J. Chem. Phys.* **1964**, *41*, 1018.
- (114) Abbas, A. N.; Liu, G.; Liu, B.; Zhang, L.; Liu, H.; Ohlberg, D.; Wu, W.; Zhou, C. Patterning, Characterization, and Chemical Sensing Applications of Graphene Nanoribbon Arrays Down to 5 nm Using Helium Ion Beam Lithography. *ACS Nano* **2014**, *8*, 1538–1546.
- (115) Hang, S.; Moktadir, Z.; Mizuta, H. Raman Study of Damage Extent in Graphene Nanostructures Carved by High Energy Helium Ion Beam. *Carbon N. Y.* **2014**, *72*, 233–241.
- (116) Roberts, N. A.; Magel, G. A.; Hartfield, C. D.; Moore, T. M.; Fowlkes, J. D.; Rack, P. D. In Situ Laser Processing in a Scanning Electron Microscope. *J. Vac. Sci. Technol. A* **2012**, *30*, 41404.
- (117) Stanford, M. G.; Lewis, B. B.; Noh, J. H.; Fowlkes, J. D.; Rack, P. D. Inert Gas Enhanced Laser-Assisted Purification of Platinum Electron-Beam-Induced Deposits. *ACS Appl. Mater. Interfaces* **2015**, *7*, 19579–19588.
- (118) Stanford, M. G.; Lewis, B. B.; Noh, J. H.; Fowlkes, J. D.; Roberts, N. A.; Plank, H.; Rack, P. D. Purification of Nanoscale Electron-Beam-Induced Platinum Deposits via a Pulsed Laser-Induced Oxidation Reaction. *ACS Appl. Mater. Interfaces* **2014**, *6*, 21256–21263.

- (119) Noh, J. H.; D., F. J.; Timilsina, R.; Stanford, M. G.; Lewis, B. B.; Rack, P. D. Pulsed Laser Assisted Focused Electron Beam Induced Etching of Titanium with XeF₂: Enhanced Reaction Rate and Precursor Transport. *ACS Appl. Mater. Interfaces* **2015**, *7*, 4179–4184.
- (120) Tan, S.; Livengood, R.; Greenzweig, Y.; Drezner, Y.; Shima, D. Probe Current Distribution Characterization Technique for Focused Ion Beam. *J. Vac. Sci. Technol. B* **2012**, *30*, 06F606.
- (121) Wu, H.; Stern, L. A.; Xia, D.; Ferranti, D.; Thompson, B.; Klein, K. L.; Gonzalez, C. M.; Rack, P. D. Focused Helium Ion Beam Deposited Low Resistivity Cobalt Metal Lines with 10 Nm Resolution: Implications for Advanced Circuit Editing. *J. Mater. Sci. Mater. Electron.* **2014**, *25*, 587–595.
- (122) Kalhor, N.; Boden, S. A.; Mizuta, H. Sub-10nm Patterning by Focused He-Ion Beam Milling for Fabrication of Downscaled Graphene Nano Devices. *Microelectron. Eng.* **2014**, *114*, 70–77.
- (123) Sidorkin, V.; van Veldhoven, E.; van der Drift, E.; Alkemade, P.; Salemink, H.; Maas, D. Sub-10-Nm Nanolithography with a Scanning Helium Beam. *J. Vac. Sci. Technol. B* **2009**, *27*, L18–L20.
- (124) Kohama, K.; Iijima, T.; Hayashida, M.; Ogawa, S. Tungsten-Based Pillar Deposition by Helium Ion Microscope and Beam-Induced Substrate Damage. *J. Vac. Sci. Technol. B* **2013**, *31*, 31802.
- (125) Drezner, Y.; Greenzweig, Y.; Fishman, D.; van Veldhoven, E.; Maas, D. J.; Raveh, A.; Livengood, R. H. Structural Characterization of He Ion Microscope Platinum Deposition and Sub-Surface Silicon Damage. *J. Vac. Sci. Technol. B* **2012**, *30*, 41210.
- (126) Lassiter, M. G.; Rack, P. D. Nanoscale Electron Beam Induced Etching: A Continuum Model That Correlates the Etch Profile to the Experimental Parameters. *Nanotechnology* **2008**, *19*, 455306.
- (127) Utke, I.; Hoffmann, P.; Melngailis, J. Gas-Assisted Focused Electron Beam and Ion Beam Processing and Fabrication. *J. Vac. Sci. Technol. B* **2008**, *26*, 1197.
- (128) Gamo, K.; Hamauzu, H.; Xu, Z.; Namba, S. In Situ Development of Ion Bombarded Poly(methylmethacrylate) Resist in a Reactive Gas Ambient. *J. Vac. Sci. Technol. B* **1988**,

- 6, 989.
- (129) Casey, J. D.; Doyle, A. F.; Lee, R. G.; Stewart, D. K.; Zimmermann, H. Gas-Assisted Etching with Focused Ion Beam Technology. *Microelectron. Eng.* **1994**, *24*, 43–50.
 - (130) Stanishevsky, A.; Edinger, K.; Orloff, J.; Melngailis, J.; Stewart, D.; Williams, A.; Clark, R. Testing New Chemistries for Mask Repair with Focused Ion Beam Gas Assisted Etching. *J. Vac. Sci. Technol. B* **2003**, *21*, 3067.
 - (131) Fu, X. L.; Li, P. G.; Jin, A. Z.; Chen, L. M.; Yang, H. F.; Li, L. H.; Tang, W. H.; Cui, Z. Gas-Assisted Etching of Niobium with Focused Ion Beam. *Microelectron. Eng.* **2005**, *78*, 29–33.
 - (132) Santschi, C.; Jenke, M.; Hoffmann, P.; Brugger, J. Interdigitated 50 Nm Ti Electrode Arrays Fabricated Using XeF₂ Enhanced Focused Ion Beam Etching. *Nanotechnology* **2006**, *17*, 2722–2729.
 - (133) Ochiai, Y.; Gamo, K.; Namba, S.; Shihoyama, K.; Masuyama, A.; Shiokawa, T.; Toyoda, K. Temperature Dependence of Maskless Ion Beam Assisted Etching of InP and Si Using Focused Ion Beam. *J. Vac. Sci. Technol. B* **1987**, *5*, 423.
 - (134) Komuro, M.; Watanabe, N.; Hiroshima, H. Focused Ga Ion Beam Etching of Si in Chlorine Gas. *Jpn. J. Appl. Phys.* **1990**, *29*, 2288–2291.
 - (135) Kosugi, T.; Gamo, K.; Namba, S.; Aihara, R. Ion Beam Assisted Etching of GaAs by Low Energy Focused Ion Beam. *J. Vac. Sci. Technol. B* **1991**, *9*, 2660.
 - (136) Young, R. J. Characteristics of Gas-Assisted Focused Ion Beam Etching. *J. Vac. Sci. Technol. B* **1993**, *11*, 234.
 - (137) Edinger, K. Gas Assisted Etching of Copper with Focused Ion Beams. *J. Vac. Sci. Technol. B* **1999**, *17*, 3058.
 - (138) Stark, T. J.; Shedd, G. M.; Vitarelli, J.; Griffis, D. P.; Russell, P. E. H₂O Enhanced Focused Ion Beam Micromachining. *J. Vac. Sci. Technol. B* **1995**, *13*, 2565.
 - (139) Callegari, V.; Nellen, P. M.; Kaufmann, J.; Strasser, P.; Robin, F.; Sennhauser, U. Focused Ion Beam Iodine-Enhanced Etching of High Aspect Ratio Holes in InP Photonic Crystals. *J. Vac. Sci. Technol. B* **2007**, *25*, 2175.
 - (140) Callegari, V.; Nellen, P. M.; Yang, T.; Hauert, R.; Müller, U.; Hernández-Ramírez, F.; Sennhauser, U. Surface Chemistry and Optimization of Focused Ion Beam Iodine-

- Enhanced Etching of Indium Phosphide. *Appl. Surf. Sci.* **2007**, *253*, 8969–8973.
- (141) Schoenaker, F. J.; Córdoba, R.; Fernández-Pacheco, R.; Magén, C.; Stéphan, O.; Zuriaga-Monroy, C.; Ibarra, M. R.; De Teresa, J. M. Focused Electron Beam Induced Etching of Titanium with XeF₂. *Nanotechnology* **2011**, *22*, 265304.
- (142) Mulders, J. J. L.; Belova, L. M.; Riazanova, A. Electron Beam Induced Deposition at Elevated Temperatures: Compositional Changes and Purity Improvement. *Nanotechnology* **2011**, *22*, 55302.
- (143) Stanford, M. G.; Lewis, B. B.; Iberi, V.; Fowlkes, J. D.; Tan, S.; Livengood, R.; Rack, P. D. In Situ Mitigation of Subsurface and Peripheral Focused Ion Beam Damage via Simultaneous Pulsed Laser Heating. *Small* **2016**, *12*, 1779–1787.
- (144) Timilsina, R.; Rack, P. D. Monte Carlo Simulations of Nanoscale Focused Neon Ion Beam Sputtering. *Nanotechnology* **2013**, *24*, 495303.
- (145) Bohmayr, W.; Burenkov, A.; Lorenz, J.; Ryssel, H.; Selberherr, S. Monte Carlo Simulation of Silicon Amorphization during Ion Implantation. *IEEE Trans. Comput. Des. Integr. Circuits Syst.* **1998**, *17*, 1236–1243.
- (146) Fracassi, F.; D’Agostino, R. Chemistry of Titanium Dry Etching in Fluorinated and Chlorinated Gases. *Pure Appl. Chem.* **1992**, *64*, 703–707.
- (147) Ranta, M. Dry Etching of Titanium. *Int. Symp. Plasma Chem.* **1985**, *7*, 966.
- (148) Martin, A. A.; Bahm, A.; Bishop, J.; Aharonovich, I.; Toth, M. Dynamic Pattern Formation in Electron-Beam-Induced Etching. *Phys. Rev. Lett.* **2015**, *115*, 255501.
- (149) Kohlmann, K. T.; Thiemann, M.; Brünger, W. H. E-Beam Induced X-Ray Mask Repair with Optimized Gas Nozzle Geometry. *Microelectron. Eng.* **1991**, *13*, 279–282.
- (150) Ziegler, J. F.; Ziegler, M. D.; Biersack, J. P. SRIM – The Stopping and Range of Ions in Matter (2010). *Nucl. Instruments Methods Phys. Res. Sect. B Beam Interact. with Mater. Atoms* **2010**, *268*, 1818–1823.
- (151) Paddock, C. A.; Eesley, G. L. Transient Thermoreflectance from Thin Metal Films. *J. Appl. Phys.* **1986**, *60*, 285.
- (152) Stojanovic, N.; Jongsin Yun, J.; Washington, E. B. K.; Berg, J. M.; Holtz, M. W.; Temkin, H. Thin-Film Thermal Conductivity Measurement Using Microelectrothermal Test Structures and Finite-Element-Model-Based Data Analysis. *J. Microelectromechanical*

- Syst.* **2007**, *16*, 1269–1275.
- (153) Economou, N. P.; Notte, J. A.; Thompson, W. B. The History and Development of the Helium Ion Microscope. *Scanning* **2012**, *34*, 83–89.
 - (154) Alkemade, P. F. A.; Koster, E. M.; van Veldhoven, E.; Maas, D. J. Imaging and Nanofabrication with the Helium Ion Microscope of the Van Leeuwenhoek Laboratory in Delft. *Scanning* **2012**, *34*, 90–100.
 - (155) Ward, B. W.; Notte, J. A.; Economou, N. P. Helium Ion Microscope: A New Tool for Nanoscale Microscopy and Metrology. *J. Vac. Sci. Technol. B* **2006**, *24*, 2871.
 - (156) Kollmann, H.; Piao, X.; Esmann, M.; Becker, S. F.; Hou, D.; Huynh, C.; Kautschor, L.-O.; Bösker, G.; Vieker, H.; Beyer, A.; *et al.* Toward Plasmonics with Nanometer Precision: Nonlinear Optics of Helium-Ion Milled Gold Nanoantennas. *Nano Lett.* **2014**, *14*, 4778–4784.
 - (157) Rahman, F. H. M.; McVey, S.; Farkas, L.; Notte, J. A.; Tan, S.; Livengood, R. H. The Prospects of a Subnanometer Focused Neon Ion Beam. *Scanning* **2012**, *34*, 129–134.
 - (158) Tan, S.; Livengood, R.; Shima, D.; Notte, J.; McVey, S. Gas Field Ion Source and Liquid Metal Ion Source Charged Particle Material Interaction Study for Semiconductor Nanomachining Applications. *J. Vac. Sci. Technol. B* **2010**, *28*, C6F15.
 - (159) Buchheim, J.; Wyss, R. M.; Shorubalko, I.; Park, H. G. Understanding the Interaction between Energetic Ions and Freestanding Graphene towards Practical 2D Perforation. *Nanoscale* **2016**, *8*, 8345–8354.
 - (160) Fowlkes, J. D.; Rack, P. D. Fundamental Electron-Precursor-Solid Interactions Derived from Time-Dependent Electron-Beam-Induced Deposition Simulations and Experiments. *ACS Nano* **2010**, *4*, 1619–1629.
 - (161) Wu, J.-B.; Zhao, H.; Li, Y.; Ohlberg, D.; Shi, W.; Wu, W.; Wang, H.; Tan, P.-H. Monolayer Molybdenum Disulfide Nanoribbons with High Optical Anisotropy. *Adv. Opt. Mater.* **2016**, *4*, 756–762.
 - (162) Vighier, I.; Liang, L.; Ievlev, A. V.; Stanford, M. G.; Lin, M.-W.; Li, X.; Mahjouri-Samani, M.; Jesse, S.; Sumpter, B. G.; Kalinin, S. V.; *et al.* Nanoforging Single Layer MoSe₂ Through Defect Engineering with Focused Helium Ion Beams. *Sci. Rep.* **2016**, *6*, 30481.

- (163) Stanford, M. G.; Pudasaini, P. R.; Belianinov, A.; Cross, N.; Noh, J. H.; Koehler, M. R.; Mandrus, D. G.; Duscher, G.; Rondinone, A. J.; Ivanov, I. N.; *et al.* Focused Helium-Ion Beam Irradiation Effects on Electrical Transport Properties of Few-Layer WSe₂: Enabling Nanoscale Direct Write Homo-Junctions. *Sci. Rep.* **2016**, *6*, 27276.
- (164) Araujo, E. N. D.; Brant, J. C.; Archanjo, B. S.; Medeiros-Ribeiro, G.; Plentz, F.; Alves, E. S. Patterning Graphene with a Helium Ion Microscope: Observation of Metal-Insulator Transition Induced by Disorder. *Phys. Rev. B* **2015**, *91*, 245414.
- (165) Lemme, M. C.; Bell, D. C.; Williams, J. R.; Stern, L. A.; Baugher, B. W. H.; Jarillo-Herrero, P.; Marcus, C. M. Etching of Graphene Devices with a Helium Ion Beam. *ACS Nano* **2009**, *3*, 2674–2676.
- (166) Abbas, A. N.; Liu, G.; Liu, B.; Zhang, L.; Liu, H.; Ohlberg, D.; Wu, W.; Zhou, C. Patterning, Characterization, and Chemical Sensing Applications of Graphene Nanoribbon Arrays Down to 5 Nm Using Helium Ion Beam Lithography. *ACS Nano* **2014**, *8*, 1538–1546.
- (167) Pan, H.; Zhang, Y.-W. Edge-Dependent Structural, Electronic and Magnetic Properties of MoS₂ Nanoribbons. *J. Mater. Chem.* **2012**, *22*, 7280.
- (168) Botello-Méndez, A. R.; López-Urías, F.; Terrones, M.; Terrones, H. Metallic and Ferromagnetic Edges in Molybdenum Disulfide Nanoribbons. *Nanotechnology* **2009**, *20*, 325703.
- (169) Ataca, C.; Şahin, H.; Aktürk, E.; Ciraci, S. Mechanical and Electronic Properties of MoS₂ Nanoribbons and Their Defects. *J. Phys. Chem. C* **2011**, *115*, 3934–3941.
- (170) Li, Y.; Zhou, Z.; Zhang, S.; Chen, Z. MoS₂ Nanoribbons: High Stability and Unusual Electronic and Magnetic Properties. *J. Am. Chem. Soc.* **2008**, *130*, 16739–16744.
- (171) Rack, P. D.; Randolph, S.; Deng, Y.; Fowlkes, J.; Choi, Y.; Joy, D. C. Nanoscale Electron-Beam-Stimulated Processing. *Appl. Phys. Lett.* **2003**, *82*, 2326–2328.
- (172) Winters, H. F. The Etching of W(111) with XeF₂. *J. Vac. Sci. Technol. A Vacuum, Surfaces, Film.* **1985**, *3*, 700.
- (173) Lassiter, M. G.; Liang, T.; Rack, P. D. Inhibiting Spontaneous Etching of Nanoscale Electron Beam Induced Etching Features: Solutions for Nanoscale Repair of Extreme Ultraviolet Lithography Masks. *J. Vac. Sci. Technol. B* **2008**, *26*, 963.

- (174) Schoenaker, F. J.; Córdoba, R.; Fernández-Pacheco, R.; Magén, C.; Stéphan, O.; Zuriaga-Monroy, C.; Ibarra, M. R.; De Teresa, J. M. Focused Electron Beam Induced Etching of Titanium with XeF₂. *Nanotechnology* **2011**, *22*, 265304.
- (175) Heard, P. J.; Cleaver, J. R. A.; Ahmed, H. Application of a Focused Ion Beam System to Defect Repair of VLSI Masks. *J. Vac. Sci. Technol. B Microelectron. Nanom. Struct.* **1985**, *3*, 87.
- (176) Iberi, V.; Ievlev, A. V.; Vlassiuk, I.; Jesse, S.; Kalinin, S. V.; Joy, D. C.; Rondinone, A. J.; Belianinov, A.; Ovchinnikova, O. S. Graphene Engineering by Neon Ion Beams. *Nanotechnology* **2016**, *27*, 125302.
- (177) Smith, D. A.; Joy, D. C.; Rack, P. D. Monte Carlo Simulation of Focused Helium Ion Beam Induced Deposition. *Nanotechnology* **2010**, *21*, 175302.
- (178) Timilsina, R.; Rack, P. D. Monte Carlo Simulations of Nanoscale Focused Neon Ion Beam Sputtering. *Nanotechnology* **2013**, *24*, 495303.
- (179) Timilsina, R.; Smith, D. A.; Rack, P. D. A Comparison of Neon versus Helium Ion Beam Induced Deposition via Monte Carlo Simulations. *Nanotechnology* **2013**, *24*, 115302.
- (180) McDonnell, S.; Addou, R.; Buie, C.; Wallace, R. M.; Hinkle, C. L. Defect-Dominated Doping and Contact Resistance in MoS₂. *ACS Nano* **2014**, *8*, 2880–2888.
- (181) Chen, M.; Nam, H.; Wi, S.; Ji, L.; Ren, X.; Bian, L.; Lu, S.; Liang, X. Stable Few-Layer MoS₂ Rectifying Diodes Formed by Plasma-Assisted Doping. *Appl. Phys. Lett.* **2013**, *103*, 142110.
- (182) Möller, W.; Eckstein, W. Tridyn — A TRIM Simulation Code Including Dynamic Composition Changes. *Nucl. Instruments Methods Phys. Res. Sect. B Beam Interact. with Mater. Atoms* **1984**, *2*, 814–818.
- (183) Möller, W.; Eckstein, W.; Biersack, J. P. Tridyn-Binary Collision Simulation of Atomic Collisions and Dynamic Composition Changes in Solids. *Comput. Phys. Commun.* **1988**, *51*, 355–368.
- (184) Wang, Q. H.; Kalantar-Zadeh, K.; Kis, A.; Coleman, J. N.; Strano, M. S. Electronics and Optoelectronics of Two-Dimensional Transition Metal Dichalcogenides. *Nat. Nanotechnol.* **2012**, *7*, 699–712.
- (185) Chhowalla, M.; Shin, H. S.; Eda, G.; Li, L.-J.; Loh, K. P.; Zhang, H. The Chemistry of

- Two-Dimensional Layered Transition Metal Dichalcogenide Nanosheets. *Nat. Chem.* **2013**, *5*, 263–275.
- (186) Terrones, H.; López-Urías, F.; Terrones, M. Novel Hetero-Layered Materials with Tunable Direct Band Gaps by Sandwiching Different Metal Disulfides and Diselenides. *Sci. Rep.* **2013**, *3*, 1549.
- (187) Yousefi, G. H. Optical Properties of Mixed Transition Metal Dichalcogenide Crystals. *Mater. Lett.* **1989**, *9*, 38–40.
- (188) Pradhan, N. R.; Rhodes, D.; Memaran, S.; Poumirol, J. M.; Smirnov, D.; Talapatra, S.; Feng, S.; Perea-Lopez, N.; Elias, A. L.; Terrones, M.; *et al.* Hall and Field-Effect Mobilities in Few Layered P-WSe₂ Field-Effect Transistors. *Sci. Rep.* **2015**, *5*, 8979.
- (189) Ross, J. S.; Klement, P.; Jones, A. M.; Ghimire, N. J.; Yan, J.; G., M.; Taniguchi, T.; Watanabe, K.; Kitamura, K.; Yao, W.; *et al.* Electrically Tunable Excitonic Light-Emitting Diodes Based on Monolayer WSe₂ P-N Junctions. *Nat Nano* **2014**, *9*, 268–272.
- (190) Baugher, B. W. H.; Churchill, H. O. H.; Yang, Y.; Jarillo-Herrero, P. Optoelectronic Devices Based on Electrically Tunable P-N Diodes in a Monolayer Dichalcogenide. *Nat Nano* **2014**, *9*, 262–267.
- (191) Pospischil, A.; Furchi, M. M.; Mueller, T. Solar-Energy Conversion and Light Emission in an Atomic Monolayer P-N Diode. *Nat Nano* **2014**, *9*, 257–261.
- (192) Huang, J.-K.; Pu, J.; Hsu, C.-L.; Chiu, M.-H.; Juang, Z.-Y.; Chang, Y.-H.; Chang, W.-H.; Iwasa, Y.; Takenobu, T.; Li, L.-J. Large-Area Synthesis of Highly Crystalline WSe₂ Monolayers and Device Applications. *ACS Nano* **2014**, *8*, 923–930.
- (193) Li, M.-Y.; Shi, Y.; Cheng, C.-C.; Lu, L.-S.; Lin, Y.-C.; Tang, H.-L.; Tsai, M.-L.; Chu, C.-W.; Wei, K.-H.; He, J.-H. Epitaxial Growth of a Monolayer WSe₂-MoS₂ Lateral Pn Junction with an Atomically Sharp Interface. *Science (80-.)*. **2015**, *349*, 524–528.
- (194) Mahjouri-Samani, M.; Lin, M.-W.; Wang, K.; Lupini, A. R.; Lee, J.; Basile, L.; Boulesbaa, A.; Rouleau, C. M.; Poretzky, A. A.; Ivanov, I. N.; *et al.* Patterned Arrays of Lateral Heterojunctions within Monolayer Two-Dimensional Semiconductors. *Nat Commun* **2015**, *6*, 7749.
- (195) Kim, T.-Y.; Cho, K.; Park, W.; Park, J.; Song, Y.; Hong, S.; Hong, W.-K.; Lee, T. Irradiation Effects of High-Energy Proton Beams on MoS₂ Field Effect Transistors. *ACS*

- Nano* **2014**, *8*, 2774–2781.
- (196) Tongay, S.; Suh, J.; Ataca, C.; Fan, W.; Luce, A.; Kang, J. S.; Liu, J.; Ko, C.; Raghunathanan, R.; Zhou, J.; *et al.* Defects Activated Photoluminescence in Two-Dimensional Semiconductors: Interplay between Bound, Charged, and Free Excitons. *Sci. Rep.* **2013**, *3*, 2657.
- (197) Fox, D. S.; Zhou, Y.; Maguire, P.; O'Neill, A.; Ó'Coileáin, C.; Gatensby, R.; Glushenkov, A. M.; Tao, T.; Duesberg, G. S.; Shvets, I. V.; *et al.* Nanopatterning and Electrical Tuning of MoS₂ Layers with a Subnanometer Helium Ion Beam. *Nano Lett.* **2015**, *15*, 5307–5313.
- (198) Li, H.-M.; Lee, D.; Qu, D.; Liu, X.; Ryu, J.; Seabaugh, A.; Yoo, W. J. Ultimate Thin Vertical P–n Junction Composed of Two-Dimensional Layered Molybdenum Disulfide. *Nat. Commun.* **2015**, *6*, 6564.
- (199) Choi, M. S.; Qu, D.; Lee, D.; Liu, X.; Watanabe, K.; Taniguchi, T.; Yoo, W. J. Lateral MoS₂ P–n Junction Formed by Chemical Doping for Use in High-Performance Optoelectronics. *ACS Nano* **2014**, *8*, 9332–9340.
- (200) Lee, C.-H.; Lee, G.-H.; van Der Zande, A. M.; Chen, W.; Li, Y.; Han, M.; Cui, X.; Arefe, G.; Nuckolls, C.; Heinz, T. F. Atomically Thin P–n Junctions with van Der Waals Heterointerfaces. *Nat. Nanotechnol.* **2014**, *9*, 676–681.
- (201) Duan, X.; Wang, C.; Shaw, J. C.; Cheng, R.; Chen, Y.; Li, H.; Wu, X.; Tang, Y.; Zhang, Q.; Pan, A. Lateral Epitaxial Growth of Two-Dimensional Layered Semiconductor Heterojunctions. *Nat. Nanotechnol.* **2014**, *9*, 1024–1030.
- (202) Frey, G. L.; Tenne, R.; Matthews, M. J.; Dresselhaus, M. S.; Dresselhaus, G. Raman and Resonance Raman Investigation of MoS₂ Nanoparticles. *Phys. Rev. B* **1999**, *60*, 2883–2892.
- (203) del Corro, E.; Terrones, H.; Elias, A.; Fantini, C.; Feng, S.; Nguyen, M. A.; Mallouk, T. E.; Terrones, M.; Pimenta, M. A. Excited Excitonic States in 1L, 2L, 3L, and Bulk WSe₂ Observed by Resonant Raman Spectroscopy. *ACS Nano* **2014**, *8*, 9629–9635.
- (204) Chuang, H.-J.; Tan, X.; Ghimire, N. J.; Perera, M. M.; Chamlagain, B.; Cheng, M. M.-C.; Yan, J.; Mandrus, D.; Tománek, D.; Zhou, Z. High Mobility wse₂ P-and N-Type Field-Effect Transistors Contacted by Highly Doped Graphene for Low-Resistance Contacts.

- Nano Lett.* **2014**, *14*, 3594–3601.
- (205) Allain, A.; Kis, A. Electron and Hole Mobilities in Single-Layer WSe₂. *ACS Nano* **2014**, *8*, 7180–7185.
- (206) Qiu, H.; Xu, T.; Wang, Z.; Ren, W.; Nan, H.; Ni, Z.; Chen, Q.; Yuan, S.; Miao, F.; Song, F. Hopping Transport through Defect-Induced Localized States in Molybdenum Disulphide. *Nat. Commun.* **2013**, *4*, 2642.
- (207) Lu, J.; Carvalho, A.; Chan, X. K.; Liu, H.; Liu, B.; Tok, E. S.; Loh, K. P.; Castro Neto, A. H.; Sow, C. H. Atomic Healing of Defects in Transition Metal Dichalcogenides. *Nano Lett.* **2015**, *15*, 3524–3532.
- (208) Liu, Y.; Tan, C.; Chou, H.; Nayak, A.; Wu, D.; Ghosh, R.; Chang, H.-Y.; Hao, Y.; Wang, X.; Kim, J.-S.; *et al.* Thermal Oxidation of WSe₂ Nanosheets Adhered on SiO₂/Si Substrates. *Nano Lett.* **2015**, *15*, 4979–4984.
- (209) Li, H.; Lu, G.; Wang, Y.; Yin, Z.; Cong, C.; He, Q.; Wang, L.; Ding, F.; Yu, T.; Zhang, H. Mechanical Exfoliation and Characterization of Single- and Few-Layer Nanosheets of WSe₂, TaS₂, and TaSe₂. *Small* **2013**, *9*, 1974–1981.
- (210) Sourisseau, C.; Cruege, F.; Fouassier, M.; Alba, M. Second-Order Raman Effects, Inelastic Neutron Scattering and Lattice Dynamics in 2H-WS₂. *Chem. Phys.* **1991**, *150*, 281–293.
- (211) Radisavljevic, B.; Radenovic, A.; Brivio, J.; Giacometti, V.; Kis, A. Single-Layer MoS₂ Transistors. *Nat. Nanotechnol.* **2011**, *6*, 147–150.
- (212) Liu, W.; Kang, J.; Sarkar, D.; Khatami, Y.; Jena, D.; Banerjee, K. Role of Metal Contacts in Designing High-Performance Monolayer N-Type WSe₂ Field Effect Transistors. *Nano Lett.* **2013**, *13*, 1983–1990.
- (213) Yi, Y.; Wu, C.; Liu, H.; Zeng, J.; He, H.; Wang, J. A Study of Lateral Schottky Contacts in WSe₂ and MoS₂ Field Effect Transistors Using Scanning Photocurrent Microscopy. *Nanoscale* **2015**, *7*, 15711–15718.
- (214) Zhou, W.; Zou, X.; Najmaei, S.; Liu, Z.; Shi, Y.; Kong, J.; Lou, J.; Ajayan, P. M.; Yakobson, B. I.; Idrobo, J.-C. Intrinsic Structural Defects in Monolayer Molybdenum Disulfide. *Nano Lett.* **2013**, *13*, 2615–2622.
- (215) Lu, J.; Carvalho, A.; Chan, X. K.; Liu, H.; Liu, B.; Tok, E. S.; Loh, K. P.; Castro Neto, A.

- H.; Sow, C. H. Atomic Healing of Defects in Transition Metal Dichalcogenides. *Nano Lett.* **2015**, *15*, 3524–3532.
- (216) Pandey, M.; Rasmussen, F. A.; Kuhar, K.; Olsen, T.; Jacobsen, K. W.; Thygesen, K. S. Defect-Tolerant Monolayer Transition Metal Dichalcogenides. *Nano Lett.* **2016**, *16*, 2234–2239.
- (217) Komsa, H.-P.; Krasheninnikov, A. V. Engineering the Electronic Properties of Two-Dimensional Transition Metal Dichalcogenides by Introducing Mirror Twin Boundaries. *Adv. Electron. Mater.* **2017**, 1600468.
- (218) Bollinger, M. V.; Lauritsen, J. V.; Jacobsen, K. W.; Nørskov, J. K.; Helveg, S.; Besenbacher, F. One-Dimensional Metallic Edge States in MoS₂. *Phys. Rev. Lett.* **2001**, *87*, 196803.
- (219) Bollinger, M. V.; Jacobsen, K. W.; Nørskov, J. K. Atomic and Electronic Structure of MoS₂ Nanoparticles. *Phys. Rev. B* **2003**, *67*, 85410.
- (220) Lin, Z.; Carvalho, B. R.; Kahn, E.; Lv, R.; Rao, R.; Terrones, H.; Pimenta, M. A.; Terrones, M. Defect Engineering of Two-Dimensional Transition Metal Dichalcogenides. *2D Mater.* **2016**, *3*, 22002.
- (221) Mahjouri-Samani, M.; Liang, L.; Oyedele, A.; Kim, Y.-S.; Tian, M.; Cross, N.; Wang, K.; Lin, M.-W.; Boulesbaa, A.; Rouleau, C. M.; *et al.* Tailoring Vacancies Far Beyond Intrinsic Levels Changes the Carrier Type and Optical Response in Monolayer MoSe₂–X Crystals. *Nano Lett.* **2016**, *16*, 5213–5220.
- (222) Choudhary, N.; Islam, M. R.; Kang, N.; Tetard, L.; Jung, Y.; Khondaker, S. I. Two-Dimensional Lateral Heterojunction through Bandgap Engineering of MoS₂ via Oxygen Plasma. *J. Phys. Condens. Matter* **2016**, *28*, 364002.
- (223) Azcatl, A.; Qin, X.; Prakash, A.; Zhang, C.; Cheng, L.; Wang, Q.; Lu, N.; Kim, M. J.; Kim, J.; Cho, K.; *et al.* Covalent Nitrogen Doping and Compressive Strain in MoS₂ by Remote N₂ Plasma Exposure. *Nano Lett.* **2016**, *16*, 5437–5443.
- (224) Khondaker, S. I.; Islam, M. R. Bandgap Engineering of MoS₂ Flakes via Oxygen Plasma: A Layer Dependent Study. *J. Phys. Chem. C* **2016**, *120*, 13801–13806.
- (225) Komsa, H.-P.; Kurasch, S.; Lehtinen, O.; Kaiser, U.; Krasheninnikov, A. V. From Point to Extended Defects in Two-Dimensional MoS₂: Evolution of Atomic Structure under

- Electron Irradiation. *Phys. Rev. B* **2013**, 88.
- (226) Iberi, V.; Liang, L.; Ievlev, A. V.; Stanford, M. G.; Lin, M.-W.; Li, X.; Mahjouri-Samani, M.; Jesse, S.; Sumpter, B. G.; Kalinin, S. V.; *et al.* Nanoforging Single Layer MoSe₂ Through Defect Engineering with Focused Helium Ion Beams. *Sci. Rep.* **2016**, 6, 30481.
- (227) Stanford, M. G.; Pudasaini, P. R.; Belianinov, A.; Cross, N.; Noh, J. H.; Koehler, M. R.; Mandrus, D. G.; Duscher, G.; Rondinone, A. J.; Ivanov, I. N.; *et al.* Focused Helium-Ion Beam Irradiation Effects on Electrical Transport Properties of Few-Layer WSe₂: Enabling Nanoscale Direct Write Homo-Junctions. *Sci. Rep.* **2016**, 6, 27276.
- (228) Ghorbani-Asl, M.; Kretschmer, S.; Spearot, D. E.; Krasheninnikov, A. V. Two-Dimensional MoS₂ under Ion Irradiation: From Controlled Defect Production to Electronic Structure Engineering. *2D Mater.* **2017**, 4, 25078.
- (229) Yoon, K.; Rahnamoun, A.; Swett, J. L.; Iberi, V.; Cullen, D. A.; Vlassiounk, I. V.; Belianinov, A.; Jesse, S.; Sang, X.; Ovchinnikova, O. S.; *et al.* Atomistic-Scale Simulations of Defect Formation in Graphene under Noble Gas Ion Irradiation. *ACS Nano* **2016**, 10, 8376–8384.
- (230) Komsa, H.-P.; Krasheninnikov, A. V. Native Defects in Bulk and Monolayer MoS₂ from First Principles. *Phys. Rev. B* **2015**, 91, 125304.
- (231) De, S.; Coleman, J. N. Are There Fundamental Limitations on the Sheet Resistance and Transmittance of Thin Graphene Films? *ACS Nano* **2010**, 4, 2713–2720.
- (232) Han, M. Y.; Brant, J. C.; Kim, P. Electron Transport in Disordered Graphene Nanoribbons. *Phys. Rev. Lett.* **2010**, 104, 56801.
- (233) Yildiz, A.; Serin, N.; Serin, T.; Kasap, M. Crossover from Nearest-Neighbor Hopping Conduction to Efros–Shklovskii Variable-Range Hopping Conduction in Hydrogenated Amorphous Silicon Films. *Jpn. J. Appl. Phys.* **2009**, 48, 111203.
- (234) Belianinov, A.; He, Q.; Kravchenko, M.; Jesse, S.; Borisevich, A.; Kalinin, S. V. Identification of Phases, Symmetries and Defects through Local Crystallography. *Nat. Commun.* **2015**, 6, 7801.
- (235) He, Q.; Woo, J.; Belianinov, A.; Guliyants, V. V.; Borisevich, A. Y. Better Catalysts through Microscopy: Mesoscale M1/M2 Intergrowth in Molybdenum–Vanadium Based Complex Oxide Catalysts for Propane Ammoxidation. *ACS Nano* **2015**, 9, 3470–3478.

- (236) Yoon, K.; Rahnamoun, A.; Swett, J. L.; Iberi, V.; Cullen, D. A.; Vlassiouk, I. V.; Belianinov, A.; Jesse, S.; Sang, X.; Ovchinnikova, O. S.; *et al.* Atomistic-Scale Simulations of Defect Formation in Graphene under Noble Gas Ion Irradiation. *ACS Nano* **2016**, *10*, 8376–8384.
- (237) Stanford, M. G.; Pudasaini, P. R.; Cross, N.; Mahady, K.; Hoffman, A.; Mandrus, D. G.; Duscher, G.; Chisholm, M. F.; Rack, P. D. Tungsten Diselenide Patterning and Nanoribbon Formation by Gas-Assisted Focused Helium Ion Beam Induced Etching. *Small Methods* **2017**, *1*, 1600060.
- (238) Zhao, M.; Ye, Y.; Han, Y.; Xia, Y.; Zhu, H.; Wang, S.; Wang, Y.; Muller, D. A.; Zhang, X. Large-Scale Chemical Assembly of Atomically Thin Transistors and Circuits. *Nat. Nanotechnol.* **2016**.
- (239) Ling, X.; Lin, Y.; Ma, Q.; Wang, Z.; Song, Y.; Yu, L.; Huang, S.; Fang, W.; Zhang, X.; Hsu, A. L.; *et al.* Parallel Stitching of 2D Materials. *Adv. Mater.* **2016**, *28*, 2322–2329.
- (240) Mahjour-Samani, M.; Tian, M.; Wang, K.; Boulesbaa, A.; Rouleau, C. M.; Puretzky, A. A.; McGuire, M. A.; Srijanto, B. R.; Xiao, K.; Eres, G.; *et al.* Digital Transfer Growth of Patterned 2D Metal Chalcogenides by Confined Nanoparticle Evaporation. *ACS Nano* **2014**, *8*, 11567–11575.
- (241) Wang, K.; Huang, B.; Tian, M.; Ceballos, F.; Lin, M.-W.; Mahjour-Samani, M.; Boulesbaa, A.; Puretzky, A. A.; Rouleau, C. M.; Yoon, M.; *et al.* Interlayer Coupling in Twisted WSe₂/WS₂ Bilayer Heterostructures Revealed by Optical Spectroscopy. *ACS Nano* **2016**, *10*, 6612–6622.
- (242) Kresse, G.; Furthmüller, J. Efficiency of Ab-Initio Total Energy Calculations for Metals and Semiconductors Using a Plane-Wave Basis Set. *Comput. Mater. Sci.* **1996**, *6*, 15–50.
- (243) Perdew, J. P.; Burke, K.; Ernzerhof, M. Generalized Gradient Approximation Made Simple. *Phys. Rev. Lett.* **1996**, *77*, 3865–3868.
- (244) Kang, N.; Paudel, H. P.; Leuenberger, M. N.; Tetard, L.; Khondaker, S. I. Photoluminescence Quenching in Single-Layer MoS₂ via Oxygen Plasma Treatment. *J. Phys. Chem. C* **2014**, *118*, 21258–21263.

APPENDIX

List of Publications

See [Google Scholar](#) for a complete publication list

1. **Stanford, M. G.**; Noh, J. H.; Ievlev, A. V.; Maksymovych, P.; Ovchinnikova, O. S.; Rack, P. D. Room Temperature Activation of InGaZnO Thin-Film Transistors via He⁺ Irradiation. **2017**, 9, 35125-35132.
2. **Stanford, M. G.**; Pudasaini, P. R.; Gallmeier, E. T.; Cross, N.; Liang, L.; Oyedele, A.; Duscher, G.; Mahjouri-Samani, M.; Wang, K.; Xiao, K.; *et al.* High Conduction Hopping Behavior Induced in Transition Metal Dichalcogenides by Percolating Defect Networks: Toward Atomically Thin Circuits. *Adv. Funct. Mater.* **2017**, 1702829. DOI: 10.1002/adfm.201702829.
3. **Stanford, M. G.**; Lewis, B. B.; Mahady, K.; Fowlkes, J. D.; Rack, P. D. Review Article: Advanced Nanoscale Patterning and Material Synthesis with Gas Field Helium and Neon Ion Beams. *J. Vac. Sci. Technol. B.* **2017**, 35, 30802.
4. **Stanford, M. G.**; Pudasaini, P. R.; Cross, N.; Mahady, K.; Hoffman, A.; Mandrus, D. G.; Duscher, G.; Chisholm, M. F.; Rack, P. D. Tungsten Diselenide Patterning and Nanoribbon Formation by Gas-Assisted Focused Helium Ion Beam Induced Etching. *Small Methods* **2017**, 1, 1600060.
5. **Stanford, M. G.**; Mahady, K.; Lewis, B. B.; Fowlkes, J. D.; Tan, S.; Livengood, R.; Magel, G. A.; Moore, T. M.; Rack, P. D. Laser-Assisted Focused He⁺ Ion Beam Induced Etching with and without XeF₂ Gas Assist. *ACS Appl. Mater. Interfaces* **2016**, 8, 29155–29162.
6. **Stanford, M. G.**; Pudasaini, P. R.; Belianinov, A.; Cross, N.; Noh, J. H.; Koehler, M.; Mandrus, D. G.; Duscher, G.; Rondinone, A. J.; Ivanov, I. N.; *et al.* Focused Helium-Ion Beam Irradiation Effects on Electrical Transport Properties of Few-Layer WSe₂: Enabling Nanoscale Direct Write Homo-Junctions. *Sci. Rep.* **2016**, 6, 27276.
7. **Stanford, M. G.**; Lewis, B. B.; Iberi, V.; Fowlkes, J. D.; Tan, S.; Livengood, R.; Rack, P. D. In Situ Mitigation of Subsurface and Peripheral Focused Ion Beam Damage via Simultaneous Pulsed Laser Heating. *Small* **2016**, 12, 1779-1787. (**Back Cover Article**)

8. **Stanford, M. G.**; Lewis, B. B.; Noh, J. H.; Fowlkes, J. D.; Rack, P. D. Inert Gas Enhanced Laser-Assisted Purification of Platinum Electron-Beam-Induced Deposits. *ACS Appl. Mater. Interfaces* **2015**, 7, 19579–19588. (Cover Article)
9. **Stanford, M. G.**; Lewis, B. B.; Noh, J. H.; Fowlkes, J. D.; Roberts, N. A.; Plank, H.; Rack, P. D. Purification of Nanoscale Electron-Beam-Induced Platinum Deposits via a Pulsed Laser-Induced Oxidation Reaction. *ACS Appl. Mater. Interfaces* **2014**, 6, 21256–21263.
10. **Stanford, M.**; Wang, H.; Ivanov, I.; Hu, B. High Seebeck Effects from Conducting Polymer: Poly(3,4-Ethylenedioxythiophene): Poly(styrenesulfonate) Based Thin-Film Device with Hybrid Metal/polymer/metal Architecture. *Appl. Phys. Lett.* **2012**, 101.
11. Pudasaini, P. R.; **Stanford, M. G.**; Oyedele, A.; Wong, A. T.; Hoffman, A. N.; Briggs, D. P.; Xiao, K.; Mandrus, D. G.; Ward, T. Z.; Rack, P. D. High Performance Top-Gated Multilayer WSe₂ Field Effect Transistors. *Nanotechnology* **2017**, (accepted).
12. Pudasaini, P. R.; Oyedele, A.; Zhang, C.; **Stanford, M. G.**; Cross, N.; Wong, A. T.; Hoffman, A. N.; Xiao, K.; Duscher, G.; Mandrus, D. G.; *et al.* High-Performance Multilayer WSe₂ Field-Effect Transistors with Carrier Type Control. *Nano Res.* **2017**, DOI 10.1007/s12274-017-1681-5.
13. Lewis, B. B.; Winkler, R.; Sang, X.; Pudasaini, P. R.; **Stanford, M. G.**; Plank, H.; Unocic, R. R.; Fowlkes, J. D.; Rack, P. D. 3D Nanoprinting via Laser-Assisted Electron Beam Induced Deposition: Growth Kinetics, Enhanced Purity, and Electrical Resistivity. *Beilstein J. Nanotechnol.* **2017**, 8, 801–812.
14. Iberi, V.; Liang, L.; Ievlev, A. V.; **Stanford, M. G.**; Lin, M.-W.; Li, X.; Mahjouri-Samani, M.; Jesse, S.; Sumpter, B. G.; Kalinin, S. V.; *et al.* Nanoforging Single Layer MoSe₂ Through Defect Engineering with Focused Helium Ion Beams. *Sci. Rep.* **2016**, 6, 30481.
15. Fowlkes, J. D.; Winkler, R.; Lewis, B. B.; **Stanford, M. G.**; Plank, H.; Rack, P. D. Simulation-Guided 3D Nanomanufacturing *via* Focused Electron Beam Induced Deposition. *ACS Nano* **2016**, 10, 6163–6172.

16. Noh, J. H.; D., F. J.; Timilsina, R.; **Stanford, M. G.**; Lewis, B. B.; Rack, P. D. Pulsed Laser Assisted Focused Electron Beam Induced Etching of Titanium with XeF₂: Enhanced Reaction Rate and Precursor Transport. *ACS Appl. Mater. Interfaces* **2015**, *7*, 4179–4184.
17. Fowlkes, J. D.; Geier, B.; Lewis, B. B.; Rack, P. D.; **Stanford, M. G.**; Winkler, R.; Plank, H. Electron Nanoprobe Induced Oxidation: A Simulation of Direct-Write Purification. *Phys. Chem. Chem. Phys.* **2015**, *17*, 18294–18304.
18. Lewis, B. B.; **Stanford, M. G.**; Fowlkes, J. D.; Lester, K.; Plank, H.; Rack, P. D. Electron-Stimulated Purification of Platinum Nanostructures Grown via Focused Electron Beam Induced Deposition. *BEILSTEIN J. Nanotechnol.* **2015**, *6*, 907–918.
19. Gonzalez, C. M.; Slingenbergh, W.; Timilsina, R.; Noh, J.-H.; **Stanford, M. G.**; Lewis, B. B.; Klein, K. L.; Liang, T.; Fowlkes, J. D.; Rack, P. D. Evaluation of Mask Repair Strategies via Focused Electron, Helium, and Neon Beam Induced Processing for EUV Applications. In *SPIE Advanced Lithography; International Society for Optics and Photonics*, **2014**; p. 90480M–90480M.
20. Liu, Q.; Hu, D.; Wang, H.; Stanford, M.; Wang, H.; Hu, B. Surface Polarization Enhanced Seebeck Effects in Vertical Multi-Layer Metal-Polymer-Metal Thin-Film Devices. *Phys. Chem. Chem. Phys.* **2014**, *16*, 22201–22206.
21. Noh, J. H.; **Stanford, M. G.**; Lewis, B. B.; Fowlkes, J. D.; Plank, H.; Rack, P. D. Nanoscale Electron Beam-Induced Deposition and Purification of Ruthenium for Extreme Ultraviolet Lithography Mask Repair. *Appl. Phys. A* **2014**, *117*, 1705–1713.

VITA

Michael Garrison Stanford was born in 1991 in Jackson, TN to the parents of Arvie and Janice Stanford. He attended the University of Tennessee where he obtained his B.S. and M.S. degrees in Materials Science and Engineering in 2013 and 2015, respectively. Michael pursued his Ph.D. in Materials Science under the mentorship of Prof. Philip D. Rack and graduated in December of 2017. During his graduate and undergraduate studies, Michael conducted research at the University of Tennessee, Intel Corporation, and the Center for Nanophase Materials Sciences (CNMS) at Oak Ridge National Laboratory (ORNL). Michael's research interests during his graduate career centered on nanomaterials and nanotechnology. He specifically conducted research on focused ion, electron, and photon beam processing. Michael also studied the application of 2-dimensional materials in electronic devices.